UNIVERSITY OF SOUTHAMPTON

FACULTY OF PHYSICAL SCIENCES AND ENGINEERING

Optoelectronics Research Centre

Integrated planar Bragg grating devices for advanced optical communication systems

by

Chaotan Sima

Thesis for the degree of Doctor of Philosophy

August 2013

UNIVERSITY OF SOUTHAMPTON

ABSTRACT

FACULTY OF PHYSICAL SCIENCES AND ENGINEERING
Optoelectronics Research Centre

Doctor of Philosophy

INTEGRATED PLANAR BRAGG GRATING DEVICES FOR ADVANCED OPTICAL COMMUNICATION SYSTEMS

by Chaotan Sima

This thesis presents theoretical and experimental studies of planar Bragg grating devices for all-optical signal processing. Bragg gratings offer a route to realise many systems for all-optical signal processing including photonic Hilbert transformers. The fabrication of Bragg gratings in a planar format allows monolithic integration with traditional planar components and micro-heaters to realise devices with desired performance.

Photonic Hilbert transformers offer potential for a wide range of applications such as single-sideband modulation, and also provide operational bandwidths and speeds far beyond current electronic technologies. A series of experimental demonstrations of photonic Hilbert transformers based on apodised planar Bragg gratings with phase-shifts are presented. Devices implementing fractional order Hilbert transform are also investigated. Grating structures are synthesised to achieve improved spectral quality including the demonstration of devices with Terahertz bandwidths.

A direct UV grating writing technique based on phase-controlled interferometry is proposed and demonstrated to fabricate arbitrary Bragg gratings in a silica-on-silicon platform. Electro-optic phase modulation of one beam in the interferometer is used to manipulate the fringe pattern and control the parameters of Bragg gratings and waveguides. Along with the unique micron-order writing spot, modulation linearity and translation consistency ensures the desired grating apodisation profile is achieved. Furthermore, the significant improvement in fringe control results in larger grating index contrast, enabling Terahertz bandwidth devices.

Finally, the system utilising the phase controlled UV writing technique is applied to the inscription of fibre Bragg gratings. Various kinds of fibres are experimentally tested in the work. The small writing spot shows potential and significant capability to inscribe arbitrary Bragg gratings into fibre structures.

Contents

Declaration of Authorship **xix**

Acknowledgements **xxi**

1 Introduction **1**
1.1 Integrated optical devices for optical communications . . . 1
1.2 Microwave photonics and radio-over-fibre . . . 1
1.3 Motivation . . . 2
1.3.1 Single-sideband modulation . . . 3
1.3.2 Photonic Hilbert transform . . . 4
1.4 Thesis synopsis . . . 5

2 Background **7**
2.1 Introduction . . . 7
2.2 Definition of Hilbert transform and fractional Hilbert Transform . . . 8
2.3 Causality and realisability . . . 9
2.4 Optical implementation of photonic Hilbert transform . . . 11
2.4.1 Free space . . . 11
2.4.2 Non-grating-based fibre schemes . . . 12
2.4.3 Fibre Bragg grating . . . 14
2.4.4 Photonic integrated circuit . . . 16
2.4.5 Planar Bragg grating . . . 18
2.5 Conclusion . . . 20

3 Bragg grating theory **21**
3.1 Introduction . . . 21
3.2 Wave propagation . . . 21
3.2.1 Maxwell's equations . . . 21
3.2.2 Coupled-mode equations for periodic coupling . . . 24
3.2.3 Schematic of refractive index modulation . . . 26
3.2.4 Solving coupled mode equations . . . 28
3.3 Analytical solutions . . . 31
3.3.1 Transfer matrix method . . . 31
3.4 Bragg gratings responses . . . 33
3.4.1 Apodisation . . . 33
3.4.2 Phase shift . . . 34
3.5 Inverse scattering synthesis . . . 34
3.5.1 Layer-peeling algorithms . . . 34

3.5.2 Accuracy and realisability . . . 36
3.6 Grating structures for optical signal processing . . . 37
3.6.1 Bragg grating for Hilbert transform . . . 37
3.6.2 Integrated all-optical single sideband filter . . . 38
3.7 Summary . . . 41

4 Integrated photonics fabrication background 43
4.1 Introduction . . . 43
4.2 Planar waveguides . . . 44
4.3 Planar silica deposition . . . 46
4.3.1 Plasma enhanced chemical vapour deposition . . . 46
4.3.2 Flame hydrolysis deposition . . . 47
4.4 Photolithography . . . 48
4.5 Photosensitivity . . . 49
4.5.1 Mechanism and dynamics . . . 50
4.5.2 Hydrogen loading . . . 52
4.6 Direct UV laser inscription . . . 52
4.6.1 Direct UV writing into silica-on-silicon . . . 52
4.6.2 Direct UV grating writing . . . 54
4.7 Characterisation methods . . . 55
4.7.1 Optical spectrum analysis . . . 55
4.7.2 Modulation phase-shift technique . . . 56
4.8 Conclusion . . . 58

5 Bragg grating engineering 59
5.1 Introduction . . . 59
5.2 Amplitude modulation method . . . 59
5.2.1 Duty cycle . . . 61
5.2.2 Fluence matching . . . 63
5.3 Piezoelectric actuator based phase control . . . 65
5.3.1 Piezoelectricity background . . . 65
5.3.2 Piezo actuator and the UV writing setup . . . 66
5.3.3 Sawtooth driving voltage . . . 67
5.3.4 Driving circuit design . . . 69
5.3.5 Bragg grating responses . . . 70
5.3.6 Michelson interferometry and piezo hysteresis . . . 71
5.3.6.1 Full range voltage sweep . . . 72
5.3.6.2 Small range voltage with repeat sweep . . . 73
5.3.6.3 Frequency response measurement . . . 75
5.4 Electro-optic modulation based phase control . . . 76
5.4.1 Electro-optic phase modulation background . . . 76
5.4.2 Measurement and calibration using Michelson interferometry . . . 77
5.4.3 High-voltage amplifier driving circuit configuration . . . 79
5.4.4 Direct UV grating writing with electro-optic phase modulation . . . 80
5.4.5 Grating responses analysis . . . 80
5.5 Ultra-wide wavelength detuning . . . 82
5.6 System linearity enhancement . . . 86

5.6.1 Wafer specifications and fluence test . . . 86
5.6.2 Transfer function synthesis . . . 87
5.7 Conclusion . . . 89

6 Integrated photonics Hilbert transform devices 91
6.1 Introduction . . . 91
6.2 Photonic Hilbert transformer . . . 92
6.2.1 Improved grating responses . . . 93
6.3 All-optical SSB filters and microwave photonics operation . . . 94
6.4 Fractional order photonics Hilbert transformers . . . 97
6.5 Terahertz bandwidth photonics Hilbert transformers . . . 101
6.5.1 Linearity enhancement for grating synthesis . . . 104
6.5.2 Ultra-wide all-optical single sideband filters . . . 106
6.6 Conclusion . . . 107

7 Fibre Bragg grating fabrication 109
7.1 Introduction . . . 109
7.2 Fibre Bragg gratings . . . 109
7.2.1 Bragg grating in multimode fibres . . . 111
7.3 Grating engineering . . . 112
7.3.1 Hydrogen loaded fibre . . . 112
7.3.2 Highly photosensitive fibre . . . 112
7.3.3 Writing spot sweep . . . 113
7.3.4 Thermal management . . . 114
7.4 Conclusion . . . 115

8 Conclusions 117
8.1 Conclusions . . . 117
8.2 Future work . . . 119
8.2.1 Direct phase measurement . . . 119
8.2.1.1 Optical vector analyser . . . 119
8.2.1.2 Microwave photonics technique . . . 119
8.2.2 Direct UV grating writing technique . . . 120
8.2.3 Applications of fractional Hilbert transformers . . . 120
8.2.4 Fibre Bragg grating . . . 121
8.2.4.1 Multimode fibre . . . 121
8.2.4.2 Antireflection in high power fibre lasers . . . 121

A Bragg grating derivation 123

B Matlab code 137
B.1 Transfer matrix method . . . 137
B.2 Inverse scattering method . . . 140

C Wafer parameters 143

D Publications 147
D.1 Journals . . . 147

D.2 Conference Contributions 147

References **151**

List of Figures

1.1 An example of integrated optical devices: the planar chip working for quantum-enhanced computation. Picture courtesy of Dr. James Gates. . . . 2

2.1 (a) Theoretical expression of HT (solid line) and FrHT (dashed line) functions; (b) amplitude and (c) phase responses of the HT (solid line) and the ρ order FrHT (dashed line) 10
2.2 Schematic drawing of (a) amplitude and (b) phase responses of physically realisable HT (solid lines) compared to those of ideal HT (dashed lines) in frequency domain. 10
2.3 Block diagram of all-optical SSB modulation system using PHT. DSB: double sideband. An optical variable attenuator and an optical tunable delay line are used in the upper channel to balance signals amplitudes and group delays in the two channels. A phase shifter is used to finely tune the optical signal to optimize the SSB suppression performance. . . . 10
2.4 Optical setup for performing conventional spatial HT and FrHT. (Reprinted from Ref.[29]). 11
2.5 Configuration of non-grating fibre based PHT (a) method combining several fibre-based MZIs to form PHT; (b) impulse response of PHT in (a); (c) experimental setup of optically phase-shifted SSB modulation using (a); (d) SSB signal with 7.8 dB suppression ratio at 10 GHz of system in (c). (Reprinted from Ref.[34]). 12
2.6 (a) System implementation by pre-setting the weights and spacing of the 4 taps; the resulting magnitude response with 3dB ripple(b) and phase response(c). (Reprinted from Ref.[35]). 13
2.7 (a) Sampled FBG design; (b) schematic of optical SSB generation filter; (c) reflection spectral of both arms; (d) sideband suppression characteristic of optical SSB generation. (Reprinted from Ref.[38]). 15
2.8 (a) Example of FBG design using inverse scattering method; (b) reflected power of the fabricated PHT; (c) phase response of the fabricated PHT; (d) SSB signal generation system; (e) generated signals. (Reprinted from Refs.[41, 43]). 16
2.9 Modelling of the apodised Bragg grating:(a) apodisation profile;(b) grating reflectivity;(c) phase response. 16
2.10 (a) Schematic of one ORR with MZI; (b) impulse response of ORR; (c) phase response and (d) power transfer of FrHT using one ORR and another FrHT using two cascaded ORR. ρ indicates the fractional order. (Reprinted from Ref.[55]). 17
2.11 Schematic of proposed integrated SSB modulation device with planar Bragg grating based PHT, located in a single silica-on-silicon chip. 18

3.1 Schematic of the refractive index modulation in Bragg gratings. 27
3.2 The optical fields considering the boundary conditions of the grating section. 29
3.3 Reflectivity (blue line) and group delay (red line) responses for uniform Bragg gratings with (a) $\kappa L = 0.5$ and (b) $\kappa L = 2$. 30
3.4 The concatenation of N grating sections with transfer matrices to form a composite grating, considering boundary conditions. 32
3.5 Reflectivity spectra of a 2mm Gaussian apodised grating (blue line) and a 6mm sinc apodised grating (red line), with maximum $\Delta n = 5 \times 10^{-4}$. . 33
3.6 Reflectivity spectra of a 1mm π phase-shifted Bragg grating (solid line) and a 1mm uniform grating (dotted line), with maximum $\Delta n = 5 \times 10^{-4}$. 34
3.7 The model of discrete grating sections. $\Delta z = L/N$ and N is the number of sections. (Inspired by Ref. [75]). 35
3.8 Modelling using the DLP method: (a) coupling coefficient κ, (b) reflectivity and (c) phase response of a Bragg grating implementing photonic Hilbert transform, with the initial grating spectra (dotted line) and the numerically demonstrated grating spectral responses (solid line). This grating is designed to have a stronger reflectivity via the DLP method, as shown in (b). 36
3.9 Modelling: (a) reflectivity, (b) phase, (c) group delay responses, and (d) the apodisation profile of the Bragg grating implementing a PHT. The grating is design to be 12mm long and with 200GHz ($\sim 0.8nm$) operating bandwidth. 38
3.10 The principle scheme of the integrated all-optical SSB filtering device via thermal tuning. 39
3.11 Modelling and simulation: (a) the PHT and sinc-apodised gratings amplitude spectra; (b) normalized gratings phase spectra; (c)device outputs at port B, with ΔL at $0.2\mu m$ (blue) and $0.4\mu m$ (red); (d) the 3D profile map of the output optical spectra as a function of ΔL. 40

4.1 Basic waveguide geometries: (a) planar waveguide; (b) strip waveguide; (c) optical fibre. 43
4.2 An SEM image of a typical silica-on-silicon wafer, consisting of thin multiple silica layers upon a thick silicon substrate. Sample image obtained by Dr. Christopher Holmes. 45
4.3 PECVD deposition process. 46
4.4 (a) Illustration of flame hydrolysis deposition (FHD) process and (b) the photograph of the working FHD setup. The doped hydrogen oxygen flame passes over the wafers depositing a soot layer. Boron vapour causes the green flame colour. 47
4.5 Colour centre model: a schematic of proposed Ge (or Si) defects of germania-doped silica. Reprinted from [86]. 51
4.6 (a) Illustration of the DGW technique with two crossed beams focused onto the core layer of the silica-on-silicon substrate;(b) a photo of the crossed laser beams in the DGW system. 54
4.7 (a) Standard setup for optical characterisation using OSA; (b) Broadband source spectra of the ASE source and SLED source. DUT: device under test. PM: polarization maintaining. The noise observed near 1400 nm from SLED source corresponds to OH^- absorptions. 55

4.8 Experimental setup of measuring optical device characteristics with modulation phase-shift technique using a vector network analyser. It can be used to measure both transmission or reflection of the device. 57
4.9 (a) The reflected power of a commercial dispersion compensation fibre Bragg grating; (b) the relative group delay spectrum of the FBG. 57

5.1 The schematic diagram of the direct UV grating writing system. PSO: Position synchronized output. 60
5.2 The concept of duty cycle: the time the laser spends in the on state, as a percentage of a complete cycle. 62
5.3 Refractive index variation as a function of duty cycle. 62
5.4 Control of UV writing speed (translation speed) and laser intensity for fluence match between waveguides and the grating section. 64
5.5 Piezoelectric elementary cell: (a) Cubic lattice (above Curie temperature); (b) tetragonal lattice (below Curie temperature). 65
5.6 (a) The applied piezo actuator from Physik Instrumente; (b) the piezo actuator attached with a reflection mirror. 66
5.7 The direct UV grating writing system using piezoelectric phase-control method. 67
5.8 The sawtooth waveform used to drive the piezo mirror for an apodised grating. T is the time interval for a grating period. The offset voltage V_{offset} ($\sim 1V$) is considered to obtain better phase-shift responses of the piezo actuator. 68
5.9 The phase-shift trace image captured from Tektronics™ oscilloscope during the π phase-shift grating writing. 68
5.10 Schematic circuit diagram of the designed integrator. The output voltage is linked to the piezo mirror. A buffer amplifier is used to provide electrical impedance matching. 69
5.11 the photograph of the integrator box in the DGW setup. The tunable resistor R_4 is used to adjust the bias voltage. 69
5.12 Signal traces captured from Tektronics™ oscilloscope and the partially enlarged image showing the slew rate of the system when driving the piezo. 70
5.13 (a) Schematic of a fabricated waveguide channel containing gratings in the chip; (b) reflectivity spectra of the Bragg gratings;(c) the Δn variation with duty cycle. 71
5.14 (a) Schematic of the basic configuration of the Michelson interferometer;(b) a photograph of the experimental setup. 72
5.15 (a) Normalised photo receiver response when an increasing voltage is applied to the piezo transducer; (b) hysteresis curve of the piezo actuator, increasing voltage (blue solid line) and decreasing voltage (red solid line), a straight dashed line is shown for comparison. 73
5.16 Hysteresis curves with slow (1V/s) and fast (5V/s) voltage variation. The insert shows the position shift at the initial point. 74
5.17 (a) The interference pattern intensity as a function of the driving voltage in the small range voltage test; (b) displacements of the piezo mirror at 0V, showing a standard deviation of $\sim 3nm$; (c) displacements of the piezo mirror at 21V, with the standard deviation of $\sim 2nm$. 74
5.18 Frequency responses of the piezo actuator (blue) and background noise (green). 75

5.19 (a)The longitudinal EOM structure using KDP crystal; (b) the EOM used in the experiment. 76
5.20 The experimental free-space Michelson interferometer to test the EOM. The red arrows indicate the route of the laser light. 77
5.21 (a) The normalised photo receiver output voltage; (b) the corresponding optical phase shift with increasing (blue) and decreasing (red) driving voltage, with an effect of phase drift; (c) the amplitude response of the EOM; (d) the phase response of output signals as a function of drive frequency. 78
5.22 (a) The KDP crystal with electrodes;(b) the mounted EOM with purge gas ports;(c) the EOM mounted on the UV writing board with the interferometer structure, blue lines show the route of the UV laser beams. . . . 79
5.23 (a) The overshot issue observed from the oscilloscope; (b) the schematic circuit diagram to solve the problem. 79
5.24 (a) The over shoot issue observed from the oscilloscope; (b) $10M\Omega$ resistance load R_1; (c) a diode in the circuit without R_1; (d) the outcome of the circuit configuration in Fig. 5.23(b). 80
5.25 (a) The experimental setup of phase modulated direct UV grating writing technique; (b) the 3D illustration of the focused writing spot on the silica-on-silicon sample. 81
5.26 (a) EOM drive voltage test with uniform gratings (square) and Gaussian apodised gratings (circle); (b) Duty cycle linearity test using a maximum drive voltage of 4kV, with 2mm Gaussian apodised gratings. 81
5.27 (a) A white-light source image of grating structures in a sample; (b) The reflectivity spectrum of the uniform grating: experimental data (star dot) and modelled data (red line); (c) Gaussian apodised grating; (d) sinc-apodised grating. 82
5.28 Modelling: (a) the refractive index pattern along the grating section; (b) maximum refractive index contrast (Δn) as a function of wavelength detuning ($\Delta\lambda$) with the phase-controlled method; (c) partial enlarged details in (a) present grating period variation showing the effect of wavelength detuning; (d) 1mm uniform grating reflection peaks variation as a function of ($\Delta\lambda$), showing 250nm FWHM (full width at half maximum); (e) the detuning FWHM in (d) as a function of the writing spot diameter. . . 84
5.29 Experimental demonstration: (a) reflectivity spectrum of a series of 1mm uniform gratings from 1250nm to 1600nm, centred at around 1400nm; (b) grating peak reflectivity data (circle). In this case, the UV writing crossing angle was $\theta =\sim 31^{\circ}$, which leads to the centre of the spectral band being located at 1400nm. 85
5.30 Experimental demonstration: (a) reflectivity spectrum of the gratings from 1250nm to 1650nm, centred at 1550nm;(b) grating peak reflectivity data (red dot) and modelled curve (solid line). The UV writing crossing angle was $\theta = 26^{\circ}$, which leads to the centre of the spectral band being located at 1550nm. 85
5.31 Effective indexes versus UV writing fluence, with the NB17/18 sample. . . 86
5.32 The flow chart of the phase-control direct UV grating writing technique, with the cases of normal linear process (blue arrow) and the transfer function process for nonlinear responses (red arrow). 88

5.33 (a) The grating Δn as a function of duty cycle; (b) the transfer function curve of the entire fabrication system, which is the inverse function of the fitting curve in (a). 88

6.1 (a) Spectral simulation of a designed grating response, with the apodisation profile in (b); (c) spectral simulation of the truncated grating response, with the associated truncated apodisation profile in (d); (e) spectral simulation of the grating response with the truncated apodisation profile and 5% phase shift error, with apodisation profile shown in (f); the measured reflection response (g) and group delay (h) of the preliminary 15mm PHT device with 1550.5nm central wavelength. 92

6.2 Experimental data: the reflectivity spectra of the planar Bragg grating implementing a Hilbert transformer (blue line) and that with a sinc apodisation profile(red line). 93

6.3 Simulation: (a) the PHT and sinc apodised gratings amplitude spectra; (b) normalized gratings phase spectra; (c) device outputs with ΔL at $0.2\mu m$ (red) and $0.4\mu m$ (blue); (d) the intensity color map of the output spectra as a function of ΔL. 94

6.4 (a) The fabricated device with electro heating elements and a fibre pigtail; (b) the image of Nichrome heater ($50\mu m$ wide) on top of the waveguide; (c) the experimental setup of the optical SSB modulation system. 95

6.5 (a) Individual grating amplitude responses; (b) device output spectra with 0V (blue) and 14V (red) DC voltages; (c) modelled (line) and experimental data (dot) of output amplitude variations at 50GHz (blue) and -50GHz (red) frequency interval; (d) the SSB suppression ratio with wavelength detuning at 6GHz; (e) the input DSB signal without carrying any data (black dotted line), the output LSB signal (blue solid line) and the output USB signal (red solid line), the data is normalized for comparison. 96

6.6 Simulation:(a)-(c) the left-side-halved apodisation profile of the grating for FrHT, the grating amplitude response, and the optical phase response, and ε denotes the ratio of the maximum index modulation depths Δn in the two sides of the zero-crossing point in the apodisation profile; (d)-(f) the right-side-halved apodisation profile, as well as the grating amplitude and optical phase response; (g) fractional order ρ as a function of the relative ratio ε for the addictive phase shift; (h) ρ as a function of ε for the subtractive phase shift; (i) the grating phase responses implementing same order FrHT but with different operating bandwidths. In the figures showing phase responses the average group-delay was not represented for illustration purposes. 98

6.7 The proposed interferometric structure with FrHTs and push-pull thermal tuning elements. 99

6.8 (a) Measured reflection data (blue solid line) and modelled data (red dashed line) of the grating measured via port C of the proposed structure; (b) measured reflection data (blue solid line) and modelled data (red dashed line) of the other grating measured via port D; (c) modelled data of the output spectra at port B, as a function of propagation length imbalance ΔL; (d) the measured output power spectra (blue line) at port B, with the input power (green line) at port A. 99

6.9 (a) The camera image of the device with heating elements; (b) the microscope image of the Nichrome filament deposited on top of the waveguide channel. . . . 100
6.10 The modelled (red line) and measured (blue line) data of the device output power spectrum from port B, with the Heater1 applied with (a) 0V, (b) 3.5V, (c) 9V and (d) 11V DC voltages. . . . 101
6.11 (a) The measured optical power spectrum with 8V applied to Heater1; (b) the LSB suppression with 6GHz RF signals, with the optical spectrum shown in (a); (c) the measured spectrum with 8V applied to Heater1 and 7V applied to Heater2; (d) the 6GHz RF DSB signals, with the optical spectrum shown in (c); (e) the measured spectrum with 7V applied to Heater2; (f) the 12dB LSB suppression of 6GHz RF signals, with the optical spectrum shown in (e). . . . 102
6.12 (a) The central apodisation profile of the Bragg grating for the THz bandwidth PHTs with increasing Terahertz bandwidths; (b) modelled amplitude responses of PHTs. . . . 103
6.13 Demonstration of fabrication nonlinearity consequences on grating responses. The modelled data (red dot), measured data (blue line) and the corresponding duty cycle profile (black line) are illustrated. (a) shows the grating responses of the initial directly designed PHT with the duty cycle profile in (b); (c) shows the responses of the PHT designed with an arbitrary step function with the duty cycle profile in (d); (e) shows the responses of the PHT designed with a windowing function, with the duty cycle profile in (f). . . . 105
6.14 (a) The measured reflectivity spectra of the fabricated Bragg gratings implementing 1THz, 1.5THz and 2THz bandwidth PHTs; (b) Relative group delay data of the fabricated gratings. . . . 105
6.15 (a) The principle scheme of the integrated all-optical SSB filter device with the planar Bragg grating implementing 1.5THz bandwidth PHT; (b) the measured optical power output spectrum when optical broadband signal is coupled into port A and received from port B. . . . 106

7.1 The schematic of fabricating fibre Bragg gratings using the direct UV grating technique, with the writing spot in $\sim 6\mu m$ diameter. . . . 110
7.2 The schematics of (a) T-groove and (b) V-groove structures, diced within silica slides to hold bare fibres during fabrication. . . . 110
7.3 (a) Reflectivity spectra of a series of 5mm uniform FBGs in a single mode fibre with increased writing fluence (10-100kJ/cm^2); (b) the reflectivity spectra of 5mm uniform FBGs with writing fluence of 100kJ/cm^2, 150kJ/cm^2 and 200kJ/cm^2; (c) the maximum Δn_{ac} as a function of writing fluence; (d) the n_{eff} variation in the two separate sections of fabricated gratings, believed to be due to the different fibre alignment. . . . 111
7.4 (a) The reflectivity spectrum of a 5mm uniform FBG fabricated in a Tm:Ge co-doped multimode fibre (MMF) with fluence of 60kJ/cm^2, showing the higher order mode reflections; (b) the reflectivity spectra of a series of 5mm uniform FBGs in the MMF with increased writing fluence (60-80kJ/cm^2); (c) the maximum grating reflective index modulation depth Δn_{ac} of FBGs with increased fluence; (d) the effective refractive index n_{eff} of FBGs with increased fluence, corresponding to the different modes. 112

7.5 The reflectivity spectra of a series of 1mm uniform FBG fabricated in the photosensitive fibres with increased fluence (5-35kJ/cm^2) and different sweeping rates. The writing spot was simultaneously swept across $\sim 3\mu m$ distance in the perpendicular direction to the fibre core, with different repetition rates and controlled by a piezoelectric mirror in the UV writing setup. 113

7.6 The realtime video capture of the grating reflection spectra (yellow line) compared to the end-facet reflection spectra of the source (white line) from the OSA, during the FBG fabrication in the GF1 photosensitive fibre. The grating spectrum has a sudden change at around 36 seconds (77 seconds as well). This abrupt behaviour and the grating asymmetric spectrum are believed due to the laser induced thermal effect. 114

A.1 Schematic diagram of the refractive index modulation in Bragg gratings. Dashed arrows are about fibre Bragg gratings and solid arrows are in planar Bragg gratings. 129

List of Tables

2.1 Comparisons between current PHT implementations 19

4.1 Key effects of some dopants on silica substrate layer properties [63, 83, 94]. 48

5.1 The piezo actuator technical specification. 67

Declaration of Authorship

I, Chaotan Sima , declare that the thesis entitled *Integrated planar Bragg grating devices for advanced optical communication systems* and the work presented in the thesis are both my own, and have been generated by me as the result of my own original research. I confirm that:

- this work was done wholly or mainly while in candidature for a research degree at this University;
- where any part of this thesis has previously been submitted for a degree or any other qualification at this University or any other institution, this has been clearly stated;
- where I have consulted the published work of others, this is always clearly attributed;
- where I have quoted from the work of others, the source is always given. With the exception of such quotations, this thesis is entirely my own work;
- I have acknowledged all main sources of help;
- where the thesis is based on work done by myself jointly with others, I have made clear exactly what was done by others and what I have contributed myself;
- parts of this work have been published as Appendix D

Signed:.....

Date:.....

Acknowledgements

There are of course many people to whom thanks are due for the help and inspiration they provided me, over the course of my PhD.

I wish to thank: First and foremost, Prof. Peter G. R. Smith and Prof. Michalis N. Zervas, who have supported and advised me throughout my time at the ORC. They have given me erudite suggestions and extensive help to set goals and seek solutions to problems, and have always been encouraging when I came across problems.

I am extremely grateful to all past and present group members including Dr. James Gates, Dr. Chris Holmes, Dr. Corin Gawith, Dr. Ben Snow, Dr. Richard Parker, Dr. Helen Rogers, Dr. Lewis Carpenter, Dr. Sumiaty Ambran, Dr. Dominic Wales, Paolo Mennea, Peter Cooper, and Stephen Lynch, whose enthusiasm and knowledge have been a perpetual inspiration. Particular thanks goes to Dr. James Gates for, among other things, always being caring and patient.

I also thank past and present colleagues at the ORC and dear friends in the university, including: Mrs Eve Smith, Dr. Ping Hua, Prof. Periklis Petropoulos, Dr. Radan Slavík, Dr. Zhenggang Lian, Dr. Liming Xiao, Dr. Jindan Shi, Dr. Jianfa Zhang, Dr. Xin Yang, Mr. Li Shen, Ms. Yang Han, Prof. Ian Castro and his wife Lucy, Dr. Jian Yang, Dr. Deng Pan, and Dr. Sarah Armstrong. All of whom have their unique efforts in assisting and accompanying me throughout the course of my PhD and my life in Southampton.

Thank you to my family for their unwavering support and understanding. Thank you to, my mother Xiaoping Li and father Ming Ma, for providing me with the best educational opportunities, for supporting all my decisions, and for shaping me into a person of integrity, and I sincerely hope they are keeping well.

Finally, thank you to Engineering and Physical Sciences Research Council (EPSRC), UK, and the China Scholarship Council (CSC), China, for supporting me over the past four years of my PhD and giving me the precious experience at the ORC.

Chaotan Sima.

Chapter 1

Introduction

1.1 Integrated optical devices for optical communications

Photonics, the science of light, underpins many recent developments in telecommunications, manufacturing platforms, environmental conservation, consumer electronics, and could also lead to a quantum revolution in computing. Optical communications forms the backbone of global communication networks and the demand for faster devices and new systems concepts grows as bandwidth usage increases.

It has been more than forty years since the publication that introduced the concept of integrated optics [1], which posed the possibility of optical components being integrated into one single substrate. This concept of photonic integrated circuits (PICs) is analogous to integrated microelectronics and likewise exhibits similar benefits of miniaturisation, performance enhancement and usability. Figure 1.1 shows an example of a planar waveguide device, the image is of the 8-cm-long silica-on-silicon photonic chip, recently served as the 3-photon quantum Boson sampling machine for quantum-enhanced computation [2].

During recent years, the PIC technology has made rapid progress in monolithic and hybrid integration, planar waveguides, three dimensional structures, passive and active devices, as well as materials and composites. The implementation of this technology has provided continuing impetus to the development of new integrated optic devices and systems into the 21st century.

1.2 Microwave photonics and radio-over-fibre

In the studies of the interaction between microwave and optical signals, microwave photonics (MWP) has been an interdisciplinary area for applications such as broadband

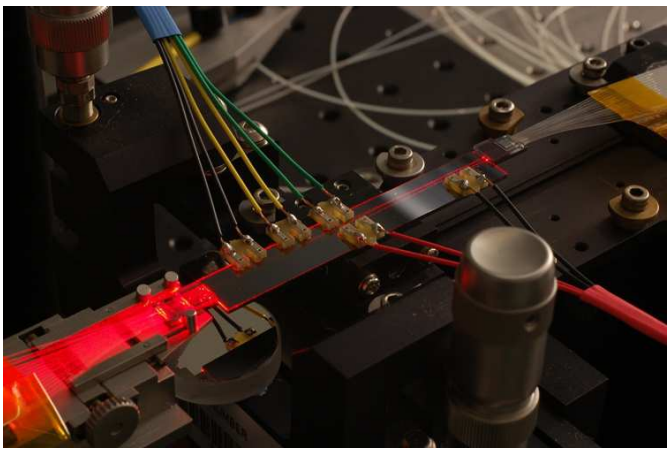

Figure 1.1: An example of integrated optical devices: the planar chip working for quantum-enhanced computation. Picture courtesy of Dr. James Gates.

wireless access networks, sensor networks, radar systems, and satellite communications [3]. One of the main applications of MWP technologies is the radio-over-fibre (RoF) systems, which investigate the transport and distribution of radio or wireless signals over optical fibres, with many advantages such as improvement of radio coverage and capacity, low loss, easy installation, and backhaul of current and next-generation wireless networks [4]. One of the key benefits of RoF systems is that they allow a flexible approach for remotely interfacing to multiple antennas, with the ability to reduce system complexity by using a centralized architecture that incorporates a simplified antenna module located closer to the customer. Therefore, RoF technology is a most suitable candidate for indoor applications such as airport terminals and shopping centers, as well as outdoor applications such as stadiums, underground and motorways [5].

Considerable research effort has been devoted towards developing RoF transport schemes that are either dispersion-tolerant, such as optical single sideband modulation [6], or based on dispersion compensation techniques commonly used in optical networks, such as chirped fibre Bragg grating (FBG) filters [7].

1.3 Motivation

There are many motivations for implementing photonic integrated circuits in optical networks, four key motives and application areas are highlighted below:

- The interconnection within data centres. Data centres around the world deal with giant amount of data information, especially with the concept of cloud computing and storage [8, 9]. The server architecture goes from the I/O inputs through the server hardware to the application stack. The data exchange and interconnection

inside this architecture requires low cost, energy efficiency and highly integrated infrastructure.

- Advanced fibre communication systems use dense-wavelength-division multiplexing (DWDM) technology. The development of high capacity transmission up to 1Tb/s demands compact designs, high density interfaces and modules [10, 11].
- The efficiency for telecom operators. Some functions in the data link layer and physical layer in telecom systems using WDM technology could be shifted to PIC components, so that the installation, service and maintenance of the system can be simplified and the working efficiency is improved [12].
- Intrinsic benefits of waveguide geometry and composite. The advantages of planar devices include potential for high optical gain, low laser threshold, high energy efficiency, thermal management, nonlinear conversion, and system integration, etc [10, 13, 14].

1.3.1 Single-sideband modulation

In microwave photonics, a double-sideband-modulated signal will suffer from a chromatic dispersion induced power penalty, especially for a transmission link operating at high microwave frequency and long distance [3]. The reason for the signal power fading along the fiber is due to the cancellation of the beat signal between the upper sideband and the carrier and the beat signal between the lower sideband and the carrier, since the optical carrier and the two sidebands will travel at different velocities.

The concept of dispersion compensation has been implemented in optical communication systems, using a dispersion compensating fibre or a chirped FBG, a cost-effective and commonly used approach in microwave photonics is to use single sideband (SSB) modulation [3]. Numerous techniques have been proposed to implement SSB modulation, for example, using a dual-drive Mach-Zehnder modulator (MZM) [6, 15] and an optical filter such as an FBG [16, 17] to filter out one of the two sidebands.

It is challenging for MZM devices to operate with bandwidths beyond 100GHz and also have linear frequency responses. The major problem associated with the bandpass filter approach is that the filters such as FBGs should have operating bandwidths, from a few GHz to Terahertz, to effectively and accurately suppress one sideband with signals. Sometimes additional group delay compensation is required.

Thin film optical filters typically consist of multiple alternating layers of high- and low-refractive-index material deposited on a glass substrate, with applications ranging from biomedical and analytical instrumentation to advanced laser systems. Companies have demonstrated commercial thin film bandpass filters ranging from 25GHz to 200GHz [18]. Challenges of designing and manufacturing these filters still exist. Real time optical

monitoring during fabrication often require highly sophisticated optical monitoring algorithms [19].

In electronics, Hilbert transform has many applications such as SSB modulation and image processing in the form of analog or digital filters [20, 21]. The conventional electronic techniques of Hilbert transform suffer the limited bandwidth (below tens of GHz). Considering the analogue microwave signal often contains broadband frequency components when modulated by the optical carrier, it is important to obtain ultra-wide band filters to process these optical signals and achieve linear responses across the full bandwidth ranges. The photonic Hilbert transformer based on Bragg gratings provides a route to overcoming these difficulties and realising such a device.

1.3.2 Photonic Hilbert transform

There are various optical implementations for spatial Hilbert transformers and fractional Hilbert transformers [22–33]. More recently, with the development of optical communication technology and integrated optics, photonic Hilbert transformers (PHTs) have been realised and utilised across the all-optical domain, showing advantages in all-optical signal processing. These include optical fibre schemes [34–44], photonic integrated circuits [45–47], and the programmable Fourier domain optical processor [48]. These devices provide promise in meeting the demand for direct processing of optical signals at high speeds and operational bandwidths, enabling future all-optical high performance networks. The planar Bragg grating based PHT studied in the thesis has some advantages such as ultrawide bandwidth (up to THz), linear frequency responses, low cost, and long-time stability of integrated all-optical SSB filers.

The monolithcally integrated Bragg grating devices implementing PHTs is proposed and demonstrated in this thesis. The past decade has witnessed exciting progress in the field of PHTs with the development of fibre technology and integrated optics. Offering enormous advantages such as operational bandwidths and speeds far beyond current electronic technologies, PHTs have been attracting growing attention in recent years.

Fabrication challenges and system stability issues still remain, particularly considering the need for the high speed operations in all-optical signal processing. The all-optical systems for processing optical signals in terms of optical phase and central wavelength are often rather sensitive to environmental effects. These concerns have raised great challenges and opportunities for future research on integrated PHTs. Grating based structures and systems in integrated formats are practically attractive due to the simple, compact structures, and the preferable choice depends on the fabrication technology. Integrated multi-functional PHT devices are promising and prominent for future implementation and commercialisation. A more detailed discussion about the background and current techniques is provided in the next chapter.

1.4 Thesis synopsis

This PhD thesis is structured as follows:

Chapter 2 reviews the current state of the art in PHTs and related techniques. This will aim to develop an understanding of the principle of Hilbert transforms, the realisation of approaches implementing all-optical Hilbert transformers, and the trend of this technology. This chapter also provides an overview and comparison of current demonstrations and highlights the motivation behind its development. A more theoretically rigorous analysis of the project will be provided in following chapters.

Chapter 3 presents a theoretical understanding of optical waveguide and Bragg grating operation. Developed from Maxwell's equations the chapter examines both analytical and numerical methods of mode solving waveguides with periodic perturbations. The transfer matrix method (TMM) and discrete layer peeling (DLP) based on inverse scattering method are both introduced. Spectral responses of various Bragg grating structures including uniform, apodised and phase-shifted gratings are modelled and simulated, as well as proposed grating based devices for all-optical signal processing.

Chapter 4 provides an overview of fabrication background for the integrated optical components used in this work. Starting from a standard microelectronics industry silicon wafer, the process of fabricating the three-layer silica-on-silicon wafers used extensively throughout this thesis is described briefly. This includes the deposition techniques and the concept and use of photosensitivity in doped silica glasses. Subsequently, descriptions of fabrication processes utilised in producing channel waveguides are given. This includes the unique in-house direct UV grating writing (DGW) system capable of fabricating the aforementioned buried channel waveguides and Bragg gratings simultaneously. The device characterisation techniques used in this thesis are also discussed.

Chapter 5 further develops the concept of DGW and introduces the advanced fabrication techniques for grating engineering. This includes an explanation of the DGW system and how various parameters of this system can be used to affect the resultant waveguides and gratings. The conventional amplitude modulated method and novel phase controlled methods in the DGW setup are discussed. Piezo actuator based phase control and electro-optical phase modulation are both proposed and demonstrated, the latter is chosen to fabricate devices in this work. By using the electro-optical modulator (EOM), ultra wide wavelength detuning for Bragg gratings is achieved. The transfer function of the entire fabrication system is also investigated to enhance grating control linearity and spectral responses.

Chapter 6 presents results on the Bragg grating based PHT devices. PHTs implementing monolithically integrated all-optical SSB filters are proposed, modelled, fabricated and characterised. Localised thermo-optic tuning is also incorporated in the devices. These

initial proof-of-concept devices show sideband suppression ratios at microwave frequency. The PHT is further developed to operate with Terahertz bandwidths and with fractional orders.

Chapter 7 extends the application of the phase-modulated DGW technique to FBGs. FBGs are fabricated and characterised within conventional single mode fibres, photosensitive fibre and multimode fibre. A piezoelectric sweep concept for making FBGs in fibres with large core sizes is discussed. In situ thermal management during the FBG fabrication is also discussed and investigated. The chapter concludes by discussing the challenge of fibre alignment and how the experimental setup needs to be further improved.

Chapter 8 will summarise the work undertaken and the results obtained in this thesis. There will also be a brief discussion on extensions to this work, suggesting possible avenues for further work.

Chapter 2

Background

The background of the Hilbert transform and its all optical implementations are studied in this chapter. The historical development and mathematical definition of the Hilbert transform are introduced and followed with various implementations to realise all-optical Hilbert transform. Some major techniques are reviewed in terms of system performances, fabrication techniques and practical utilisation, etc. Devices based on Bragg gratings within an integrated platform are proposed and discussed, indicating a promising route for the research.

2.1 Introduction

Transform techniques are widely used in various areas of mathematics, science, and engineering, one of which is the principal integral transform perhaps best known as the Fourier transform. The Hilbert transform (HT) sits alongside Fourier transforms among these integral transforms.

David Hilbert studied a pair of integral equations which connected the real and imaginary parts of a analytic function in the unit disc, which leads to the definition of the HT [49, 50]. The definition was believed to be first discussed by G. H. Hardy and named by him in 1924 in honor of contribution from David Hilbert. A detailed historical discussion can be found elsewhere [50]. The definitions of the HT as well as the fractional HT (FrHT) are described in the later section.

Over the decades, Hilbert transformations have had widespread use as they can be applied in the theoretical descriptions of many devices and systems and directly implemented in the form of analog or digital filters (Hilbert transformers) [20, 21]. For example, the analogue microwave signal often contains many frequency components and can be modulated by the optical carrier. It is important to obtain ultra-wide band filters to process the optical signal and achieve a linear response across the bandwidth range.

The conventional electronic techniques suffer the limited bandwidth and probably nonlinear responses. The photonic Hilbert transformer provides a route to overcoming these difficulties and realising such a device.

There are various optical implementations for spatial HTs and FrHTs [22–33]. A spatial HT was first demonstrated in 1950 by Kastler [22] and Wolter [23]. Kastler utilised a HT by interposing an optical system with half-wave plates for image edge enhancement while Wolter used it for spectroscopy [22, 23]. Later, the HT processor was made achromatic [24], two dimensional [25], and angularly isotropic [26]. The achromatic version is based on the detour phase concept, which became the origin of synthetic complex spatial filters [27] and of computer-generated holograms [28]. The spatial FrHT was also demonstrated to improve the performance of the conventional HT and allow an additional degree of freedom [29, 30]. Further applications in spectroscopy and image processing have been reported [31–33].

More recently, with the development of optical communication technology and integrated optics, PHTs have been realised and utilised across the all-optical domain. These include optical fibre schemes [34–44], photonic integrated circuits [45–47], and the programmable Fourier domain optical processor (FDOP) [48]. These devices are rather promising in meeting the demand for direct processing of optical signals at high speeds and operational bandwidths, enabling future all-optical high performance networks.

This chapter reviews the PHT from basic principles to applications. At first, the mathematical definitions of the HT and FrHT, and their physical properties are introduced. Secondly, through a review of recent PHTs, the comparisons between these existing demonstrations in terms of their operating principles, fabrication, system integration, experimental performance and further applications are provided. Fabrication challenges are also discussed to realise the favorable performance of the proposed devices. Then the integrated PHT based on planar Bragg gratings in silica-on-silicon is proposed. The last section gives a brief summary and outlook on PHTs and their future implementations.

2.2 Definition of Hilbert transform and fractional Hilbert Transform

This section defines the HT in the temporal and frequency domain. The definition of HT has also been used in the spatial domain [29, 30].

The conventional HT, $H[g(t)]$, of a one-dimensional real signal $g(t)$ is defined as [20]:

$$H[g(t)] = \hat{g}(t) = g(t) * \frac{1}{\pi t} = \frac{1}{\pi} P \int_{-\infty}^{\infty} \frac{g(\tau)}{t-\tau} d\tau \tag{2.1}$$

where P stands for the Cauchy principal value of the integral to make the defined integral exist, which is obtained by considering a finite range of integration that is symmetric about the point of singularity. Detailed discussion of the Cauchy principal value is presented in [20]. The symbol $*$ denotes the convolution of $g(t)$ and $1/\pi t$. The Fourier transform of the kernel of the HT is:

$$H[g(\omega)] = \hat{g}(\omega) = -jsgn(\omega)g(\omega) \tag{2.2}$$

where ω is the angular frequency. The sign function $sgn(\omega)$ is defined as follows:

$$sgn(\omega) = \begin{cases} 1 & \omega > 0, \\ 0 & \omega = 0, \\ -1 & \omega < 0. \end{cases}$$

Eq. 2.2 can be simplified as:

$$H(\omega) = -jsgn(\omega) \tag{2.3}$$

When a conventional HT is generalized into a FrHT, the frequency version of $H_{Fr}(\omega)$ is given by [50]:

$$\begin{aligned} H_{Fr}(\omega) &= \cos(\varphi) + \sin(\varphi)[-jsgn(\omega)] \\ &= \cos(\varphi) + \sin(\varphi)H(\omega) \end{aligned} \tag{2.4}$$

where $\varphi = \rho\pi/2$ and ρ indicates the fractional order. The formula shows that the FrHT of a signal is a weighted sum of the original signal and its conventional HT. This also expresses that the frequency response of HT has a $(\rho\pi/2)$ phase shift at $\omega = 0$ while the amplitude remains constant. The FrHT becomes the conventional HT when $\rho = 1$ and it offers no modification to the input signal when $\rho = 0$ or $\rho = 2$. The HT can be regarded as a process that phase shifts the input signal by $-\pi/2$ in the temporal domain prior to a defined temporal position and by an angle of $\pi/2$ post this temporal position.

It is conventional to interpret the transform in the frequency domain and Fig. 2.1(a) shows the complex frequency response of the HT and FrHT functions. Figure 2.1(b) illustrates the amplitude (blue solid line) responses of the HT and FrHT functions with Fig. 2.1(c) showing the phase response of the HT (red sold line) and a ρ order FrHT (red dashed line). The amplitude responses of HT and FrHT are identical.

2.3 Causality and realisability

Causality is the relationship between cause and effect [51]. A system is causal if $h(t) = 0$ for $t < 0$, where $h(t)$ denotes the system impulse response. The ideal Hilbert transformer is non-causal and physically non-realisable. In any practical implementation of the HT,

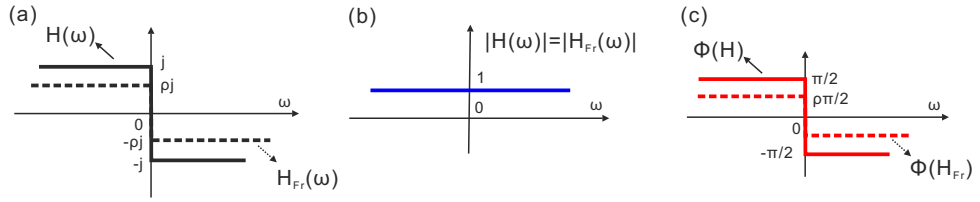

Figure 2.1: (a) Theoretical expression of HT (solid line) and FrHT (dashed line) functions; (b) amplitude and (c) phase responses of the HT (solid line) and the ρ order FrHT (dashed line)

the output signal is a delayed and somewhat altered HT of the input signal. The Paley-Wiener theorem [20] provides the necessary and sufficient conditions that a frequency response characteristic must satisfy, for the resulting filter to be causal and finite. As a consequence the frequency response of the HT will be band-limited with a bandwidth Δf and smooth alteration in phase as illustrated in Fig. 2.2.

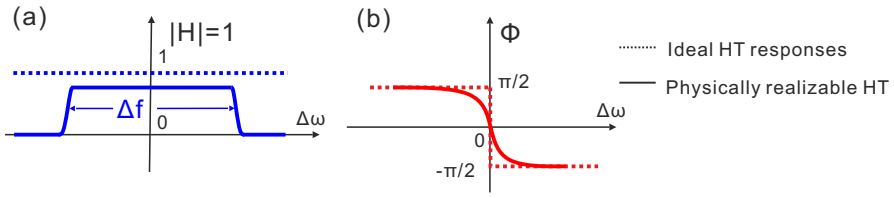

Figure 2.2: Schematic drawing of (a) amplitude and (b) phase responses of physically realisable HT (solid lines) compared to those of ideal HT (dashed lines) in frequency domain.

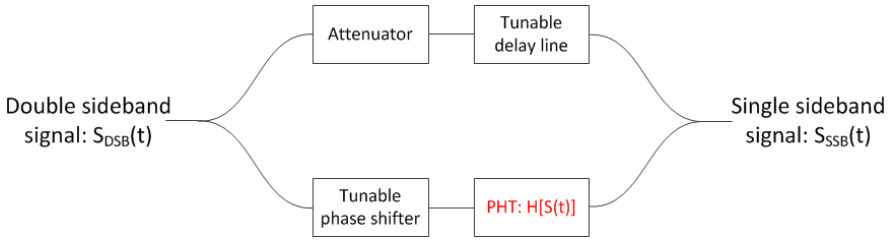

Figure 2.3: Block diagram of all-optical SSB modulation system using PHT. DSB: double sideband. An optical variable attenuator and an optical tunable delay line are used in the upper channel to balance signals amplitudes and group delays in the two channels. A phase shifter is used to finely tune the optical signal to optimize the SSB suppression performance.

Consequently, the physically realisable HT filter is a practical band-pass filter with a π phase shift (fractional π for FrHT) in the central frequency $\Delta\omega = 0$. Apart from electronic Hilbert transformers [20], different theoretical and experimental approaches of PHTs are discussed and analysed in the next sections. Figure 2.3 shows the block diagram of the interferometric all-optical SSB modulation system, a crucial application of PHT, which were experimentally demonstrated in fibre schemes [34, 37, 38, 43]. An optical attenuator, delay line and a phase shifter are incorporated in the system to balance the optical path and signal phases for coherent operations.

2.4 Optical implementation of photonic Hilbert transform

In the past half century, various research groups have published investigations and utilizations of PHTs for spectroscopy, optical signal processing, microwave photonics and radio over fibre systems, etc. These efforts have produced PHTs and FrHTs in free space objects [22–26, 28, 29], optical interferometers and delay lines [34–37], sampled FBGs [38], and phase-shifted FBGs with apodisation profiles [39–44], integrated platforms [45–47]and the FDOP wave-shaper [48]. Considering the PHT implementations in signal processing, SSB modulation is a well-known technique for improving performance in terms of required power, enhancing spectral efficiency and reducing fading [43]. Electronically, Hilbert transformers have been widely used in terms of analytical functions in SSB modulation applications with analog and digital format [20]. In this section, the characteristics of these demonstrations and examples on SSB applications are briefly reviewed.

2.4.1 Free space

Early demonstrations of PHT have been reported since 1950 using free space lenses and plates [22–26, 28, 29]. Figure 2.4 shows the original optical setup used by Kastler [22] and Wolter [23]. They employed a conventional optical spatial filter that consisted of a glass plate half covered by a π phase-shifting layer. The output image $O(x)$ was the Hilbert transformation of the input image $I(x)$ that had a π phase-shift at $s > 0$ and remained unmodified at $s \leq 0$.

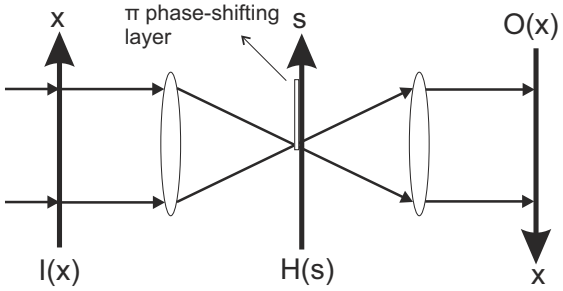

Figure 2.4: Optical setup for performing conventional spatial HT and FrHT. (Reprinted from Ref.[29]).

As mentioned above, the FrHT of a signal is a weighted sum of the original signal and its conventional HT. Here, the weighting parameters $\cos(\varphi)$ and $\sin(\varphi)$ in Eq.2.4 are varied simply if the object signal is linearly polarized at 45°, if the filter consists of two pieces of a quarter-wave plate (oriented at 0° for $\omega \geq 0$ and at 90° otherwise). The output polarizer is oriented at angle φ, the magnitude of which controls the weighting parameter. Furthermore, Lohmann et al. proposed some other approaches which combined HTs with fractional Fourier transforms [29] and realising two dimensional FrHTs [30]. The free-space implementation of PHTs has been proposed in many application areas,

such as spectroscopy and image processing [31–33]. However, for signal processing and telecommunications, the PHT and FrHT in free space setups are not suitable, as they suffer from several limitations such as bandwidth, response time, and system stability. With the development of fibre technology and integrated optics, alternative approaches have been investigated in the last decade.

2.4.2 Non-grating-based fibre schemes

In fibre-related schemes, HTs as well as FrHTs have been proposed and demonstrated via: Mach-Zehnder Interferometers (MZIs) with optical delay lines [34], transversal filters with wavelength division multiplexing (WDM) techniques [35, 36], and photonic microwave delay-line filters [37].

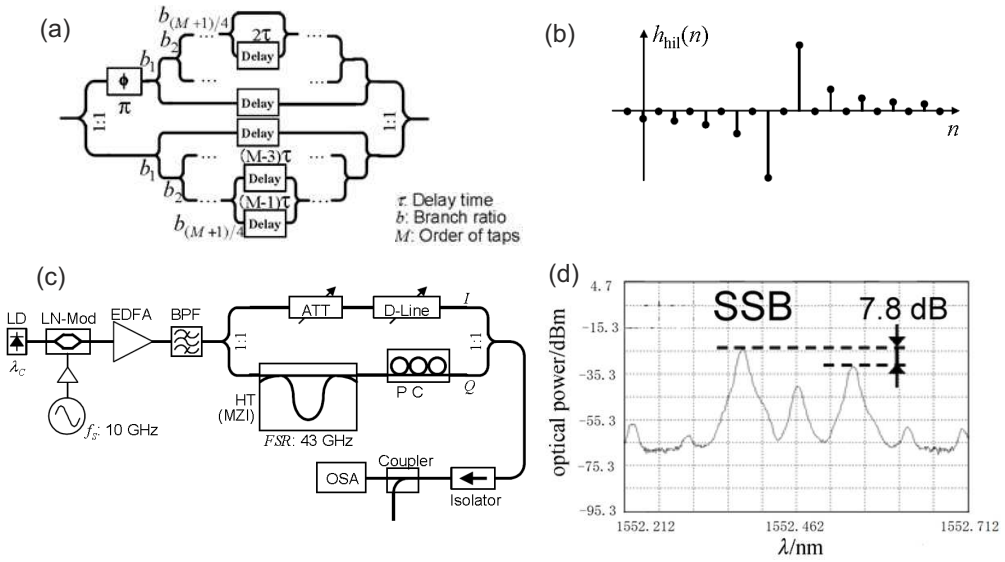

Figure 2.5: Configuration of non-grating fibre based PHT (a) method combining several fibre-based MZIs to form PHT; (b) impulse response of PHT in (a); (c) experimental setup of optically phase-shifted SSB modulation using (a); (d) SSB signal with 7.8 dB suppression ratio at 10 GHz of system in (c). (Reprinted from Ref.[34]).

Figure 2.5 presents the impulse responses of HTs and configurations of the proposed all-optical HT by Takano et al. [45]. Their all-optical different order (viz. fractional) Hilbert transformers were realised by combinations of several fibre-based MZIs and optical delay lines, shown in Fig. 2.5(a). Different delays of optical signals resulted in the corresponding impulse responses which were rotated at the tap center, as shown in Fig. 2.5(b). Figure 2.5(c) shows the fibre-based system using the HT system in (a) for SSB implementations. The sideband suppression function with 7.8dB ratio was exhibited in Fig. 2.5(d). The SSB suppression ratio was defined as the ratio between the power of the unwanted sideband and the desired one. This work demonstrated the first PHTs used for single sideband applications in an all-optical scheme. It was realised by

the concatenation of MZIs, tunable delay lines (D-line), the optical attenuator (ATT), the polarization controller (PC), optical couplers as well as phase shifters, resulting in a complex optical system, which cannot be easily integrated or put in a compact form.

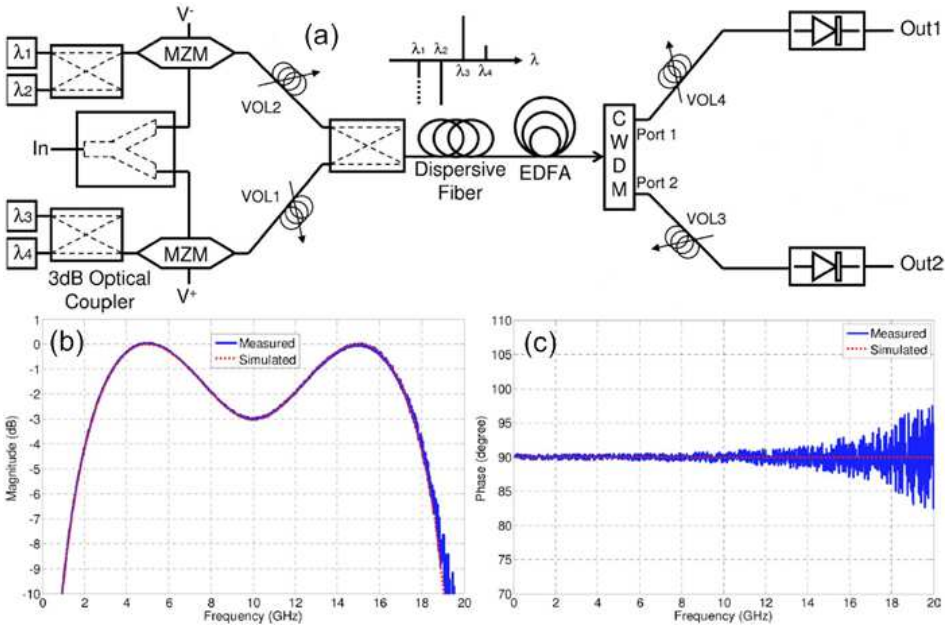

Figure 2.6: (a) System implementation by pre-setting the weights and spacing of the 4 taps; the resulting magnitude response with 3dB ripple(b) and phase response(c). (Reprinted from Ref.[35]).

In 2008, Emami et al. demonstrated a RF HT using all-optical schemes with a four-tap transversal filter and a coarse WDM coupler [35, 36]. The PHT configuration and RF generation are shown in Fig. 2.6. Measured and simulated data of PHT responses were shown in Figs. 2.6(b) and 2.6(c). The amplitudes and delay times of optical signals (wavelengths of $\lambda_1 - \lambda_4$) were empirically adjusted and located at desired wavelength intervals, with necessary time spacing [35]. A 90^o phase shift with 3dB of amplitude ripple was obtained within a $2.4 - 17.6$GHz bandwidth. However, some degradation of the performance above 20GHz was apparent. This system was modified into a two-tap transversal filter with an additional reference tap, providing two orthogonal DC measurements to perform simultaneous frequency and power measurement [36]. The manipulation of signals with different wavelengths was critical and challenging. In such a system, the operational bandwidth and adaptability were inevitably restricted.

In 2011, Huang et al. applied the programmable FDOP (Finisar™ WaveShaper) and high-speed photodiodes as a PHT for a microwave photonic quadrature filter [48]. The wave-shaper is a wavelength selective switch, and also permits reconfigurable per-channel dispersion trimming. Advantageous responses were reported with $< 0.23dB$ amplitude and $< 0.5^o$ phase imbalances. Nonetheless, the wave-shaper system is costly and the operating temperature is limited to 15°C-35°C.

In 2012, Li et al. reported microwave delay line filters for PHTs, whose spectral features function as first-order temporal optical differentiators [37]. These ultra-fast differentiators were also demonstrated by Slavík using long period gratings [52]. Li et al. experimentally demonstrated $\sim 24GHz$ bandwidth PHTs with some advantages of arbitrary wavelength operation and tunable fractional order Hilbert transform. For wider bandwidth operation, the chromatic dispersion of the signal in the dispersive fibre requires consideration [37]. The system needs extra temperature compensation setup for stable implementations in an optical network.

In view of operation principles and demonstrations, there are some similarities among the non-grating-based fibre schemes mentioned above. Precise control of the magnitude and delay time of each wavelength tap are essential for the PHT operation. Various components, such as MZIs, fibre couplers, optical delay lines and dispersive fibres, are necessary and require individual adjustment for optimal performance. In these systems, coupling loss, environmental effects, high system costs, thermal and mechanical stability as well as adjustability limit the performance and practicality of these approaches.

2.4.3 Fibre Bragg grating

FBGs have been developed as key components for many applications in fibre-optic communication and sensor systems [53]. The spectral characteristics of FBGs transform the amplitude and phase modulation of the input optical signal, which could incorporate HT features all optically. Since 2009, PHTs designed with sampled FBGs [38], using the space-to-frequency-to-time mapping algorithm (SFTM) [39, 40] and inverse scattering methods (also called discrete layer peeling, DLP) [41, 44] were reported consecutively.

In 2009, Wang et al. reported experimental demonstrations of PHTs with sampled FBGs [38]. Figure 2.7 shows the design of the sampled FBG, grating responses, the schematic of the optical SSB generation filter and the SSB response. Besides the sampled FBG, a uniform FBG (UFBG) was introduced in one arm of the couplers. The optical attenuator (ATT), tunable delay line (TDL) and the polarization maintaining couplers were included in the PHT schemes. The sideband suppression ratio about 10dB with a bandwidth of 15GHz was obtained. The ratio was lower than the simulated data due to the non-ideal responses of the various optical components [38]. The bandwidth of the system was limited as a consequence of the discrete apodisation envelope; this is difficult to overcome using conventional phase mask FBG inscription techniques. The authors comment in the paper that the SSB filter performance is sensitive to the optical phase and state-of-polarization of the interrogation source. This is likely to originate from the imbalanced nature of the interferometer, which when using discrete fibre components is challenging to overcome.

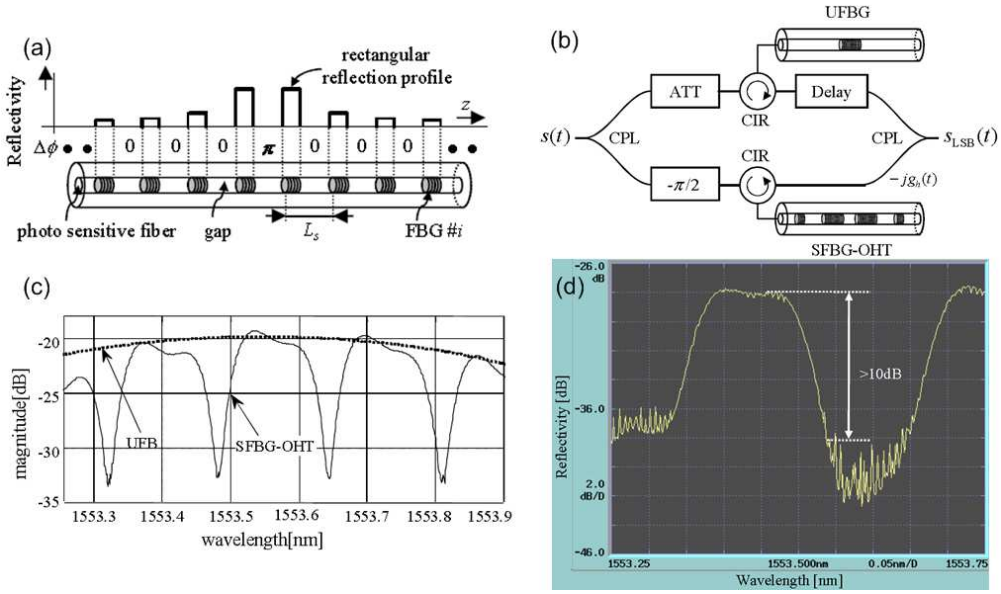

Figure 2.7: (a) Sampled FBG design; (b) schematic of optical SSB generation filter; (c) reflection spectral of both arms; (d) sideband suppression characteristic of optical SSB generation. (Reprinted from Ref.[38]).

In 2010, Li et al. presented the theoretical design and experimental results of a FBG-based PHT using the inverse scattering method [41, 42]. Later in 2011, they reported PHT implementation in an optical SSB suppression system [43]. The FBGs were fabricated with apodisation profiles and appropriate phase shifts, which were derived using the inverse scattering method. Figure 2.8 shows the FBG design (Fig. 2.8(a)), the fabricated grating responses (Figs. 2.8(b) and 2.8(c)), the optical SSB modulation system setup (Fig. 2.8(d)), and the generated optical SSB signals at different microwave frequencies (Fig. 2.8(e)). The TDL, the polarization controller (PC), the couplers and the ATT are necessary in the setup. $15-20dB$ suppression ratios were achieved in the frequency bandwidth of 20GHz. Performance degradation was commented by the authors and was believed due to the non-ideal and not easily controllable $\pi/2$ phase shift in the upper MZI arm and the limited long-term stability owing to the wavelength drift of the FBG and the MZI [43]. Extra temperature compensation would be necessary in the setup.

By means of the SFTM algorithm, Asghari and Azaña simulated the conventional PHT [39] and Cuadrado extended it to fractional orders [40]. Grating apodisation profiles were derived via inverse Fourier transform and SFTM, the HT temporal and frequency responses were presented, and will be further discussed in the next chapter. Figure 2.9(a) shows an example of the grating apodisation profile (refractive index change envelope) of the proposed Bragg grating. The (b) reflectivity and (c) phase responses are also illustrated.

Currently, the presented FBG-based PHT implementations suffer from rather small operation bandwidths (tens of GHz), imposed by the FBG bandwidths. To overcome

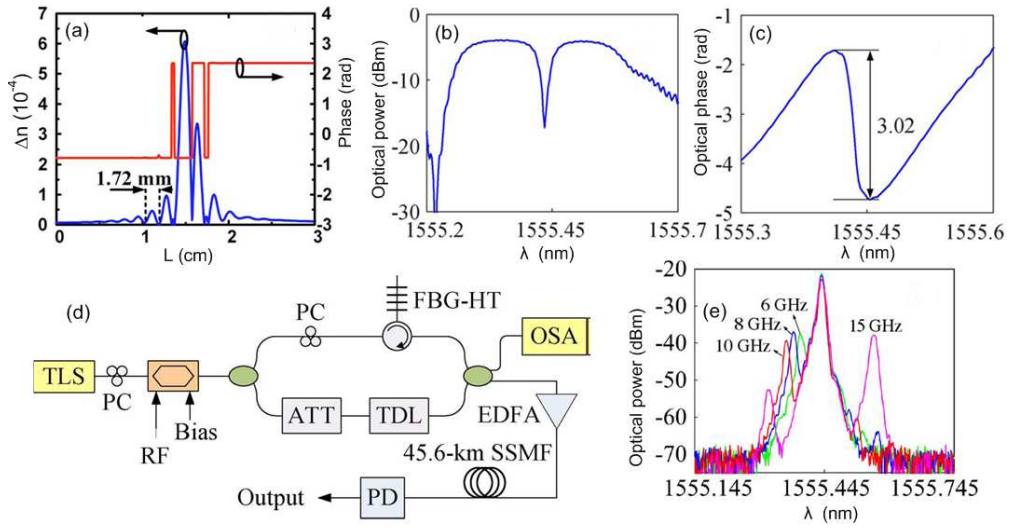

Figure 2.8: (a) Example of FBG design using inverse scattering method; (b) reflected power of the fabricated PHT; (c) phase response of the fabricated PHT; (d) SSB signal generation system; (e) generated signals. (Reprinted from Refs.[41, 43]).

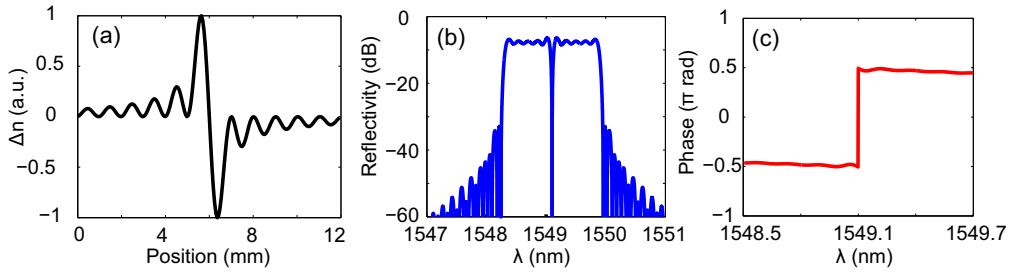

Figure 2.9: Modelling of the apodised Bragg grating:(a) apodisation profile;(b) grating reflectivity;(c) phase response.

this limitation, long period gratings were proposed and numerically designed to perform Terahertz bandwidth PHTs [44]. Apodised gratings with a $430\mu m$ period and a single π phase-shift in the standard single-mode fibre Corning™ SMF-28 platform were simulated using inverse scattering methods [54], giving device operation bandwidths up to 18.372 THz. The device operates via the coupling between cladding mode and fibre core mode, nevertheless, the complexity of the modal interaction is challenging to realise practically.

2.4.4 Photonic integrated circuit

Despite the performance improvements and experimental topology simplifications, efficient FBG incorporation into all optical PHT implementations still require optical circulators, fine optical and polarization adjustments. To solve some of these problems, photonic integrated circuits as well as planar Bragg gratings have been experimentally demonstrated in the planar waveguide format and implemented into photonic signal processing.

Compared to fibre based schemes, planar waveguide devices can significantly reduce the system complexity, increase long-term stability, and meet with the additional demands of volume manufacture, compactness, ruggedness and low cost, all of which are essential for practical PHT implementations. Tanaka et al. theoretically proposed the planar structure PHT with branching waveguides for SSB signal suppression [45], while Takano et al. experimentally demonstrated this concept in all fibre systems [34], as previously shown in Fig. 2.5. The transformer was constructed by an optical phase shifter, three optical delay lines and branching waveguides including asymmetric structures.

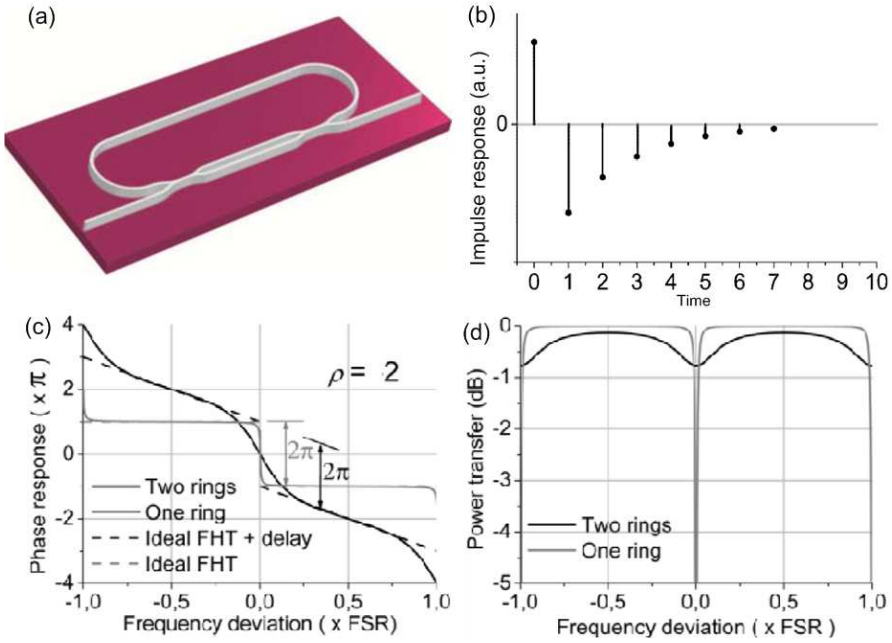

Figure 2.10: (a) Schematic of one ORR with MZI; (b) impulse response of ORR; (c) phase response and (d) power transfer of FrHT using one ORR and another FrHT using two cascaded ORR. ρ indicates the fractional order. (Reprinted from Ref.[55]).

In 2012, Zhuang et al. proposed and experimentally demonstrated a photonic on-chip implementation of FrHT using optical ring resonator (ORR) structures [46, 55]. The ORR and a MZI were used to implement PHTs, schematically shown in Fig. 2.10(a). The MZI was structured to close the ring path, which served as a practical tunable power coupler. The impulse response of the ORR was illustrated in Fig. 2.10(b). The phase response and the power transfer of the fabricated device are shown in Figs. 2.10(c) and 2.10(d), respectively. This device has the advantages of the variable and arbitrary FrHT, space efficiency and compatibility for large-scale integration. Nevertheless, the fabrication of such devices requires high precision to ensure the correct phase and operation wavelength, in reality heater assemblies are used to post trim the devices. Some of the disadvantages of the ORR device come from the intrinsic material properties which result in high sensitivity to environment conditions, such as temperature and mechanical stress. As a consequence, these devices suffer the drawbacks of limited long-term stability and mass reproducibility.

2.4.5 Planar Bragg grating

To overcome the complexity and increased environmental sensitivity of fibre-based implementations and previously reported integrated circuits, we proposed a silica based integrated circuit employing Bragg gratings and directional coupler structures, as shown in Fig. 2.11. It is a monolithically integrated all-optical SSB filter device on silica-on-silicon substrate, composed of an X-coupler, a PHT, flat top reflector and a micro heater. The PHT is implemented using a planar Bragg grating with appropriate apodisation profile and a π phase shift within the grating. A sinc-apodised Bragg grating is utilised as the flat top reflector. The reflected optical signal from the two gratings undergoes constructive and destructive interference, thereby suppressing one side band and enhancing the other. The relative optical phase of the two signals will be determined by the relative position of the gratings which is further fine-tuned by a small micro heater located on one arm of the device. The direct UV grating writing technique (DGW)would be used to fabricate the devices [56, 57].

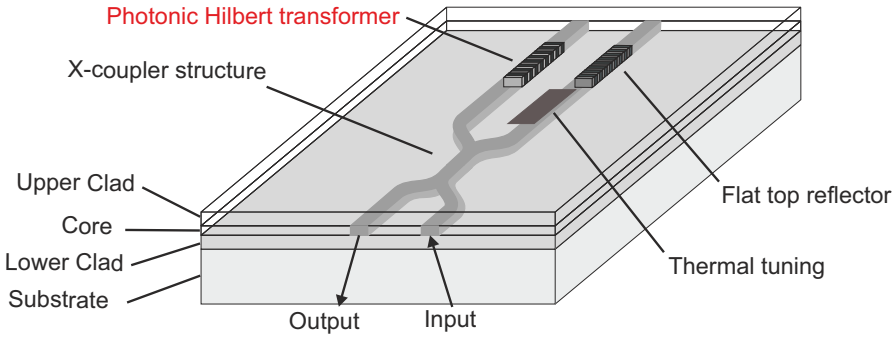

Figure 2.11: Schematic of proposed integrated SSB modulation device with planar Bragg grating based PHT, located in a single silica-on-silicon chip.

This device has the benefits of integrated single structures, direct thermal tuning, balanced optical path, fibre compatibility, long-term thermal stability and could be used alongside conventional etched silica-on-silicon devices. The approach has a advantage of extending to Terahertz bandwidth. However, there are some limitations including: bandwidth limited by photosensitivity, tunability is not particularly large (e.g., $11pm/^oC$ thermal), and the need to match to channels, also the planar devices show birefringence and require fibre pigtail. Experimental data of the fabricated devices will be discussed in Chapter 6.

Researchers	Operation principle	Device performance	Operation bandwidth	Fabrication simplicity	System stability	Application
Takano et al. [34]	MZI+delay line	✓	10 GHz	✓	✓	SSB ratio: 7.8 dB
Emami et al. [35, 36]	transversal filter+ coarse WDM coupler	✓	20 GHz	✓	✓	RF signal measurement
Wang et al. [38]	sampled FBGs	✓✓	15 GHz	✓	✓	SSB ratio>10 dB
Huang et al. [48]	FDOP+photo diodes	✓✓✓	100 GHz	N/A	✓	quadrature RF signal generation
Li et al. [37]	photonic microwave delay-line filter	✓✓	24 GHz	✓✓✓	✓	optical temporal differentiator
Li et al. [42, 43]	single FBG	✓✓	100 GHz	✓✓	✓	SSB ratio$\leq$ 20dB
Zhuang et al. [46, 55]	MZI+optical ring resonator	✓✓✓	10 GHz	✓✓✓	✓✓	quadrature RF signal generation
Sima et al.	planar Bragg grating	✓✓✓	in THz	✓✓✓	✓✓✓	integrated all-optical SSB filter

N/A: not applicable

Table 2.1: Comparisons between current PHT implementations

2.5 Conclusion

Major experimental implementations of PHTs are summarised and listed in Table 2.1. The device operating bandwidths, fabrication simplicity and system stability are evaluated from the literature. In the literature [48], the key component, FDOP, is a commercial product, Finisar™ WaveShaper, for which a description of fabrication process is not applicable.

The past decade has witnessed exciting progress in the field of PHTs with the development of fibre technology and integrated optics. Owning to their enormous advantages such as operational bandwidths and speeds far beyond current electronic technologies, PHTs have been attracting increasingly attention in recent years. However, fabrication challenges and system stability issues still remain, particularly considering the high speed operations in all-optical signal processing. For those in optical communications and optical computing, processed optical signals in terms of optical phase and central wavelength are known to be rather sensitive to environmental effects. These concerns have raised great challenges and opportunities for future research on PHTs. Grating based and non-grating based systems in integrated formats are both attractive due to simple and compact structures, and the preferable choice depends on the fabrication technology. Integrated multi-functional PHT devices are promising and prominent for future implementation and commercialisation.

Chapter 3

Bragg grating theory

3.1 Introduction

The focus of this thesis is the simulation, fabrication and analysis of integrated optical devices, and specifically for this project Bragg gratings in integrated structures. This chapter will present some theoretical derivation and modelling of the grating structures and devices. To begin to understand the propagation of light in these optical structures, the basic concepts and equations of electrodynamic theory are presented in Section 3.2. The transfer matrix method is employed to solve the coupled-mode equations [58, 59], described in Section 3.3. Bragg gratings are periodic (or aperiodic) modulations in refractive index. They have several spectral attributes that can be modified and these will be described and modelled in Section 3.4. Section 3.5 presents the inverse scattering method (discrete layer peeling, DLP) to design the grating coupling coefficients to achieve the target grating responses. Some examples of proposed grating structures for optical signal processing are also provided in Section 3.6.

3.2 Wave propagation

3.2.1 Maxwell's equations

The basic constitutive relations in physics and materials are:

$$\vec{D} = \varepsilon\vec{E} = \varepsilon_0 n^2 \vec{E}, \tag{3.1}$$

$$\vec{B} = \mu\vec{H} \tag{3.2}$$

where $\vec{E}$, $\vec{D}$, $\vec{B}$ and $\vec{H}$ denote the electric field, electric displacement, magnetic induction, and magnetic intensity, respectively. ε represents the dielectric permittivity of the medium, μ represents the magnetic permeability and n is the medium refractive

index. ε_0 and μ_0 are the free space dielectric permittivity and magnetic permeability respectively.

For nonmagnetic materials which normally constitute an optical waveguide, the magnetic permeability μ is very nearly equal to the free-space value μ_0, thus here we assume $\mu = \mu_0$ for convenience. For an isotropic $\nabla \cdot \vec{D} = 0$, linear, nonconducting $\vec{J} = 0$, and non-magnetic $\nabla \cdot \vec{B} = 0$ medium, **Maxwell's equations** are:

$$\nabla \times \vec{E} = -\frac{\partial \vec{B}}{\partial t} = (-\mu_0 \frac{\partial \vec{H}}{\partial t}), \tag{3.3}$$

$$\nabla \times \vec{H} = \frac{\partial \vec{D}}{\partial t} = \varepsilon_0 n^2 \frac{\partial \vec{E}}{\partial t}. \tag{3.4}$$

Taking the curl of Eq.(3.3) and substituting Eq.(3.4) with Eq.(3.2), we get

$$\begin{aligned} \nabla \cdot \vec{D} &= \varepsilon_0 \nabla \cdot (n^2 \vec{E}) = \varepsilon_0 (\nabla n^2 \cdot \vec{E} + n^2 \nabla \cdot \vec{E}) = 0. \\ \nabla \cdot \vec{E} &= -\frac{1}{n^2} \nabla n^2 \cdot \vec{E}. \end{aligned}$$

So we arrive at the electromagnetic wave equation:

$$\nabla^2 \vec{E} - \mu_0 \varepsilon_0 n^2 \frac{\partial^2 \vec{E}}{\partial t^2} + \nabla (\frac{1}{n^2} \nabla n^2 \cdot \vec{E}) = 0. \tag{3.5}$$

Similarly for the magnetic field,

$$\nabla^2 \vec{H} - \mu_0 \varepsilon_0 n^2 \frac{\partial^2 \vec{H}}{\partial t^2} + \frac{1}{n^2} \nabla n^2 \times (\nabla \times \vec{H}) = 0. \tag{3.6}$$

The scalar wave equation for a homogeneous medium becomes

$$\nabla^2 E - \mu_0 \varepsilon_0 n^2 \frac{\partial^2 E}{\partial t^2} = 0. \tag{3.7}$$

When the electric field $\vec{E}$ can be expressed as sinusoidal functions in time domain, it is often presented as complex amplitudes [14]. For example, the electric field vector $\vec{E}$ is expressed as

$$\vec{E}(r,t) = |E\vec{(r)}| \cos(\omega t + \phi) = Re\{E\vec{(r)} e^{i\omega t}\} = \frac{1}{2}(E\vec{(r)} e^{i\omega t} + E\vec{(r)}^* e^{-i\omega t}) \tag{3.8}$$

where $|\vec{E}|$ is the amplitude, ϕ is the phase, r is the radius, and $*$ denotes the complex conjugate. $\vec{E}(r,t)$ is represented by $\vec{E}(t)$ for illustration purpose and the term $e^{-i\beta r}$ will be considered later in this section. Defining the complex amplitude of $\vec{E}(t)$ by

$\vec{E} = |\vec{E}|e^{j\phi}$, we will define $\vec{E}(t)$ by

$$\vec{E}(t) = \vec{E}e^{i\omega t} \tag{3.9}$$

instead of by Eq.(3.8).

To be noted, this expression is not strictly correct, and when using this phasor expression it is to be noted that Eq.(3.9) means the real part of $\vec{E}e^{i\omega t}$ [14]. In most mathematical manipulations, such as addition, subtraction, differentiation and integration, this replacement of Eq.(3.8) by the complex form Eq.(3.9) poses no problems. Nevertheless, extra consideration should be taken account in the manipulations that involve the product of sinusoidal functions. In these cases we must use the real function or complex conjugates in Eq.(3.8). For example, in the reference [53], $\vec{E}e^{i\omega t} + cc.$ is chosen for the electric field expression, the same as that in Eq.(3.8).

For the practical single mode fibres, silica-on-silicon substrates and planar Bragg gratings structures, the refractive indices in the core and cladding are nearly equal. The longitudinal components of the electric and magnetic fields are usually negligible in comparison to the corresponding transverse components, which is referred as the **weakly guiding approximation**.

When the refractive index varies only in the transverse direction, that is $n^2 = n^2(x, y)$, Eq.(3.5) and Eq.(3.6) can be separated into the time and z space parts. Thus the solutions of Eq.(3.5) and Eq.(3.6) can be written as

$$\vec{E}(x, y, z, t) = \vec{E}(x, y, t)e^{-i\vec{\beta}z} \tag{3.10}$$

$$\vec{H}(x, y, z, t) = \vec{H}(x, y, t)e^{-i\vec{\beta}z} \tag{3.11}$$

Furthermore, the total electric field is

$$\vec{E}(x, y, z, t) = \vec{\Psi}(x, y, z)e^{i\omega t} = \vec{\psi}(x, y)e^{-i\vec{\beta}z}e^{i\omega t} \tag{3.12}$$

where $\Psi(x, y, z)$ is the space component of the electric field, $\psi(x, y)$ is the transverse component of the electric field, and $\vec{\beta}$ is the propagation vector constant. For planar waveguide structures, the refractive index variation is simplified to be $n^2 = n^2(x)$ in one dimension. Substituting Eq.(3.12) into Eq.(3.3)and Eq.(3.4), and taking out the x, y

and z components, we obtain the following equations

$$\begin{aligned} i\beta E_y &= -i\omega\mu_0 H_x \\ \frac{\partial E_y}{\partial x} &= -i\omega\mu_0 H_z \\ -i\beta H_x - \frac{\partial H_z}{\partial x} &= i\omega\varepsilon_0 n^2 E_y \\ i\beta H_y &= i\omega\varepsilon_0 n^2 E_x \\ \frac{\partial H_y}{\partial x} &= i\omega\varepsilon_0 n^2 E_z \\ -i\beta E_x - \frac{\partial E_z}{\partial x} &= -i\omega\mu_0 H_y \end{aligned}$$

The first three equations involve only E_y, H_x, and H_z. This set of equations corresponds to the modes with E_z vanishing and that implies no electric field component along the propagation direction, and so describes transverse electric (TE) modes. Similarly, the last three equations correspond to transverse magnetic (TM) modes. These indicate the two polarization states of light propagation in the planar waveguide, also known as birefringence.

Substituting (3.12) into (3.7), we have

$$e^{-i\beta z}e^{i\omega t}[(\nabla^2 - \frac{\partial^2}{\partial z^2})\psi(x,y) + \mu_0\varepsilon_0 n^2\omega^2\psi(x,y) - \beta^2\psi(x,y)] = 0$$

So the transverse component $\psi(x,y)$ satisfies the following scalar **wave equation**:

$$\nabla_t^2\psi + [\beta_0^2 n^2(x,y) - \beta^2]\psi = 0. \tag{3.13}$$

where $\nabla_t^2 = \nabla^2 - \partial^2/\partial z^2$, t is the transverse subscript, $\beta_0 = \omega\sqrt{\mu_0\varepsilon_0}$, $\omega = 2\pi\nu$ is angular frequency, and ν is the optical frequency.

It is acknowledged that $\beta = |\vec{\beta}|$ is the phase propagation constant or the wave number, given as:

$$\beta = |\vec{\beta}| = n\beta_0 = \frac{n\omega}{c} = \frac{2\pi}{\lambda}$$

where c is the light speed in vacuum.

3.2.2 Coupled-mode equations for periodic coupling

Considering a planar waveguide with a refractive index profile $n(x,y)$ in which there is a periodic z-dependent perturbation $\Delta n(z)$, $\psi_1(x,y)$ and $\psi_2(x,y)$ are two modes to be coupled in the waveguide with the same $n^2(x,y)$ and different propagation constant β_1,

β_2. From Eq.(3.13), β_1 and β_2 satisfy the following equations:

$$\nabla_t^2\psi_1 + [\beta_0^2 n^2(x,y) - \beta_1^2]\psi_1 = 0 \tag{3.14}$$

$$\nabla_t^2\psi_2 + [\beta_0^2 n^2(x,y) - \beta_2^2]\psi_2 = 0 \tag{3.15}$$

The orthogonality condition is also satisfied:

$$\int_{-\infty}^{\infty}\int_{-\infty}^{\infty} \psi_1^*(x,y)\psi_2(x,y)dxdy = 0$$

The total electric field in the waveguide at any value of z is given as

$$E(x,y,z,t) = \Psi(x,y,z)e^{i\omega t} = [A(z)\psi_1(x,y)e^{-i\beta_1 z} + B(z)\psi_2(x,y)e^{-i\beta_2 z}]e^{i\omega t} \tag{3.16}$$

where $A(z)$ and $B(z)$ are amplitudes of the two input modes and are z-dependent. Referring to Eq.(3.7), the wave equation satisfied by $\Psi(x,y,z)$ is:

$$\nabla^2\Psi + \beta_0^2[n^2(x,y) + 2n(x,y)\Delta n(z)]\Psi = 0 \tag{3.17}$$

In the literature, there are two different definitions for the periodic perturbation of permittivity $\Delta\varepsilon$. For example, in the reference [60], the perturbation of permittivity was defined as $\varepsilon_r + \Delta\varepsilon = n^2(x,y) + \Delta n^2(z)$ and $\Delta n^2(z)$ was expressed as a periodic or almost-periodic function, while a different expression was used in [53]. In the reference [53], the perturbation of permittivity was defined as $\varepsilon_r + \Delta\varepsilon = [n(x,y) + \Delta n(z)]^2 = n^2 + 2n\Delta n + \Delta n^2$ and Δn (not Δn^2) was expressed as a periodic or almost-periodic function. In the latter case, assuming $\Delta n \ll n$ and thus ignoring Δn^2, we have $\varepsilon_r + \Delta\varepsilon \approx n^2 + 2n\Delta n$. These two expressions may lead to same results, through some approximations. Since it is more apparent from the reference [61] that uses Δn for the periodic perturbation, the same definition is utilised here.

Substituting Eq.(3.16) into Eq.(3.17), and by applying the slowly varying envelope approximation and the orthogonality condition Eq.(3.2.2), we get:

$$\frac{dA}{dz} = -ic_{11}A - ic_{12}Be^{i\Delta\beta z} \tag{3.18}$$

$$\frac{dB}{dz} = -ic_{22}B - ic_{21}Ae^{-i\Delta\beta z} \tag{3.19}$$

where $\Delta\beta = \beta_1 - \beta_2$, and c_{11}, c_{12}, c_{21} and c_{22} denote the coupling coefficients given as:

$$\begin{aligned} c_{11}(z) &= \frac{\beta_0^2}{\beta_1}\frac{\iint \psi_1^* n(x,y)\Delta n(z)\psi_1 dxdy}{\iint \psi_1^*\psi_1 dxdy} \\ c_{12}(z) &= \frac{\beta_0^2}{\beta_1}\frac{\iint \psi_1^* n(x,y)\Delta n(z)\psi_2 dxdy}{\iint \psi_1^*\psi_1 dxdy} \\ c_{22}(z) &= \frac{\beta_0^2}{\beta_2}\frac{\iint \psi_2^* n(x,y)\Delta n(z)\psi_2 dxdy}{\iint \psi_2^*\psi_2 dxdy} \\ c_{21}(z) &= \frac{\beta_0^2}{\beta_2}\frac{\iint \psi_2^* n(x,y)\Delta n(z)\psi_1 dxdy}{\iint \psi_2^*\psi_2 dxdy} \end{aligned} \tag{3.20}$$

Eq.(3.18) and Eq.(3.19) are the well-known **coupled-mode equations** with z-dependent perturbation. More detailed study on coupled-mode equations could be found in the references [58, 59] and Appendix A.

3.2.3 Schematic of refractive index modulation

For Bragg gratings with a periodic z-dependent perturbation, the refractive index modulation is given as:

$$\Delta n(x,y,z) = \Delta n_{dc}(z) + \Delta n_{ac}(x,y)\Delta\tilde{n}(z)\cos[\frac{2\pi}{\Lambda}z + \phi(z)] \tag{3.21}$$

where,

- $\Delta n_{dc}(z)$: the average refractive index change ('dc' offset);
- $\Delta n_{ac}(x,y)$: the maximum value of refractive index change (modulation depth);
- $\Delta\tilde{n}(z)$: the grating apodisation profile (*e.g.* Gaussian);
- Λ : the perturbation period (Bragg grating period);
- $\phi(z)$: related to the grating chirp.

The following section discusses the components of the refractive index modulation function, Eq.(3.21), in context of the integrated photonics fabrication platform which will be discussed in the next chapter.

1. The first component $\Delta n_{dc}(z)$ is the average index change of the grating section, unvarying part of index modulation. The planar Bragg gratings in this work are generally fluence matched, which implies the average refractive index change is designed to be equal to the UV induced index increase $\Delta n_{dc}(z)$ of the waveguide channel and $\Delta n_{dc}(z) \approx 0$.

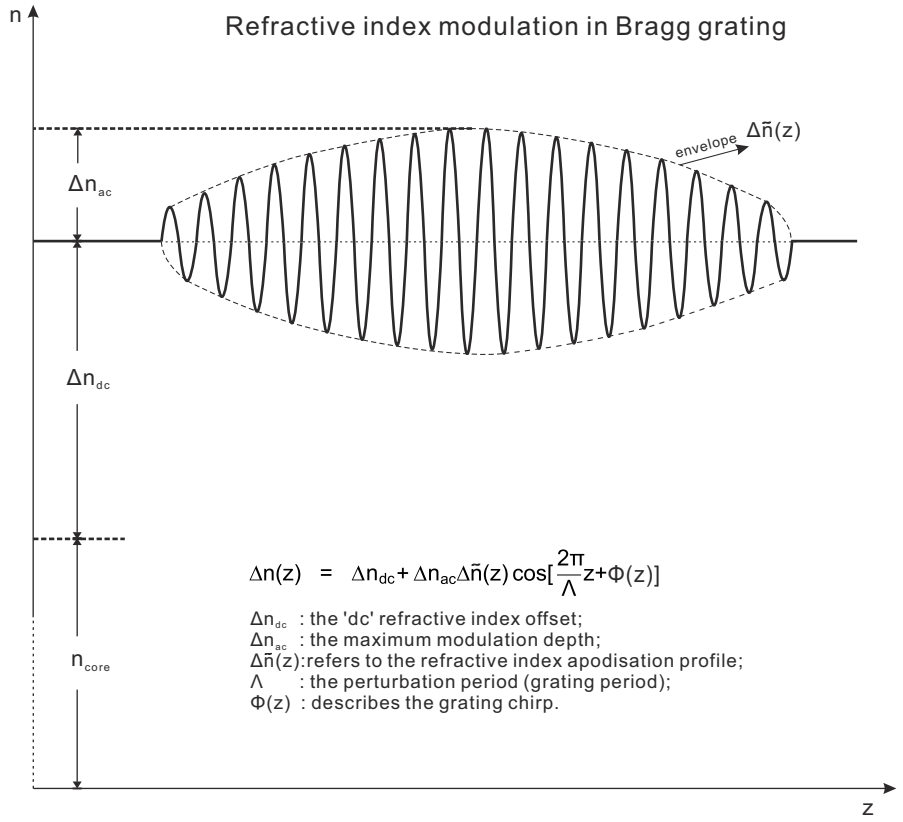

Figure 3.1: Schematic of the refractive index modulation in Bragg gratings.

2. The second component of $\Delta n(x, y, z)$ has been predefined to be constant, as $\Delta n_{ac}(x, y) = \Delta n_{ac}$.

3. In this thesis, Δn denotes the grating maximum refractive index change Δn_{ac} for simplicity.

Hence, for these planar Bragg gratings, the refractive index modulation illustrated in Fig. 3.1 becomes:

$$\Delta n(z) = \Delta n_{ac} \Delta \tilde{n}(z) \cos[\frac{2\pi}{\Lambda} z + \phi(z)] \tag{3.22}$$

Considering the theory of fibre Bragg gratings in the reference [61], it is conventional to describe to refractive index perturbation as

$$\Delta n_{(}z) = \overline{\Delta n}(z)\{1 + v \cos[\frac{2\pi}{\Lambda} z + \phi(z)]\}, \tag{3.23}$$

where v is the fringe visibility of the index change. The schematic of refractive index modulation in Bragg gratings is shown in Fig. 3.1.

The coupled-mode theory mentioned above assumes that the mode fields of the unperturbed waveguide remain unchanged in the presence of weak perturbation. This approach provides a set of first-order differential equations Eq.(3.18) and Eq.(3.19) for

the change in the amplitude of the fields along the waveguide, which have analytical solutions for uniform sinusoidal periodic perturbations.

Substituting Eq.(3.22) into Eq.(3.18) and Eq.(3.19), and considering the **synchronous approximation** [60], we find coupling occurs predominantly between those modes with propagation constant β_1 and β_2 satisfying the Bragg condition:

$$\Delta\beta = \beta_1 - \beta_2 \approx \pm\frac{2\pi}{\Lambda} = \frac{2\pi}{\lambda_0}\Delta n_{eff}$$

Coupling to other modes is negligible. Δn_{eff} is the effective index difference between the modes, approximately the refractive index difference between the core and cladding. For the counter-propagating identical modes in Bragg gratings, $\beta_1 = -\beta_2 = 2\pi n_{eff}/\lambda_B$, it is simplified to be:

$$\lambda_B = 2n_{eff}\Lambda \tag{3.24}$$

which is called the **Bragg wavelength**.

3.2.4 Solving coupled mode equations

Considering the set of Equations (3.20) represents overlap integral of the various modes and the index perturbation, and the c_{ij} parameters and same order (identical) modes in coupled mode equations Eq. (3.18) and Eq. (3.19), if we introduce two new parameters [61]:

$$\begin{aligned}
\kappa_{dc}(z) &= \frac{\omega\varepsilon_0}{2} n_{eff}\Delta n_{dc} \\
\kappa_{ac}(z) &= \frac{\omega\varepsilon_0}{4} n_{eff}\Delta n_{ac}\Delta\tilde{n}(z)\iint_{core}\psi_1^*\psi_2 dxdy
\end{aligned}$$

where κ_{dc} is a 'dc' (period-averaged) coupling coefficient and κ_{ac} is an 'ac' coupling coefficient. As previously discussed, $\Delta n_{dc} = 0$ leads to $\kappa_{dc} = 0$ for the planar samples. But we keep it in the derivation here for generality. Hence, Eq. (3.18) and Eq. (3.19) can be written as:

$$\begin{aligned}
\frac{dA(z)}{dz} &= -i\kappa_{dc}A(z) - i\kappa_{ac}B(z)e^{i[(\Delta\beta-\frac{2\pi}{\Lambda})z-\phi(z)]} \\
\frac{dB(z)}{dz} &= i\kappa_{dc}B(z) + i\kappa_{ac}^*A(z)e^{i[(\Delta\beta-\frac{2\pi}{\Lambda})z-\phi(z)]}
\end{aligned}$$

Although the mode amplitude functions $A(z)$ and $B(z)$ vary slowly, the two exponential functions may fluctuate rapidly. To minimize the effect of rapid fluctuations, we introduce two auxiliary functions $R(z)$ and $S(z)$ [62]:

$$\begin{aligned}
R(z) &= A(z)e^{\frac{-i}{2}[(\Delta\beta-\frac{2\pi}{\Lambda})z-\phi(z)]} \\
S(z) &= B(z)e^{\frac{i}{2}[(\Delta\beta-\frac{2\pi}{\Lambda})z-\phi(z)]}
\end{aligned}$$

Thus we have

$$A(z) = R(z)e^{\frac{i}{2}[(\Delta\beta-\frac{2\pi}{\Lambda})z-\phi(z)]} \tag{3.25}$$

$$B(z) = S(z)e^{\frac{-i}{2}[(\Delta\beta-\frac{2\pi}{\Lambda})z-\phi(z)]} \tag{3.26}$$

Substituting Eq. (3.25) and Eq. (3.26) into coupled mode equations, and defining the detuning parameter as

$$\delta = 2\pi n_{eff}(\frac{1}{\lambda} - \frac{1}{\lambda_D})$$

where δ is wavelength depend, and the "dc" self-coupling coefficient is [61]

$$\hat{\delta} = \delta + \kappa_{dc} - \frac{1}{2}\frac{d\phi}{dz}$$

We obtain the equations

$$\frac{dR(z)}{dz} = -i\hat{\delta}R(z) - i\kappa_{ac}S(z) \tag{3.27}$$

$$\frac{dS(z)}{dz} = i\hat{\delta}S(z) + i\kappa^*_{ac}R(z) \tag{3.28}$$

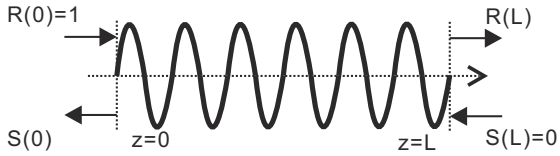

Figure 3.2: The optical fields considering the boundary conditions of the grating section.

These equations are not exactly the same as those in the reference [61], with the $'\pm'$ notation difference, but have the same solutions [53]. If the grating is a simple uniform Bragg grating along z direction, then Δn_{dc} is a constant and $d\phi/dz = 0$, thus, Eq.(3.27) and Eq.(3.28) are coupled first-order ordinary differential equations with constant coefficients, for which closed-form solutions can be found when appropriate boundary conditions are specified. The reflectivity of a uniform grating of length L can be found by assuming a forward-going wave incident at $z = 0$ is unity therefore $R(0) = 1$, and that no backward-going wave exists at $z = L$ therefore $S(L) = 0$, as shown in Fig. 3.2. Defining $\kappa = \kappa_{ac}$, the solutions of the coupled-mode equations are:

$$R(z) = \frac{i\delta\sinh[\sqrt{\kappa^2-\hat{\delta}^2}(L-z)] + \sqrt{\kappa^2-\hat{\delta}^2}\cosh[\sqrt{\kappa^2-\hat{\delta}^2}(L-z)]}{i\delta\sinh(\sqrt{\kappa^2-\hat{\delta}^2}L) + \sqrt{\kappa^2-\hat{\delta}^2}\cosh(\sqrt{\kappa^2-\hat{\delta}^2}L)} \tag{3.29}$$

$$S(z) = \frac{-i\kappa\sinh[\sqrt{\kappa^2-\hat{\delta}^2}(L-z)]}{i\delta\sinh(\sqrt{\kappa^2-\hat{\delta}^2}L) + \sqrt{\kappa^2-\hat{\delta}^2}\cosh(\sqrt{\kappa^2-\hat{\delta}^2}L)} \tag{3.30}$$

Assuming $\phi(0) = 0$ for simplicity, the reflection coefficient ρ is:

$$\rho = \frac{B(0)}{A(0)} = \frac{S(0)}{R(0)} e^{-i\phi(0)} = \frac{-i\kappa \sinh[\sqrt{\kappa^2 - \hat{\delta}^2} L]}{\sqrt{\kappa^2 - \hat{\delta}^2} \cosh[\sqrt{\kappa^2 - \hat{\delta}^2} L] + i\delta \sinh[\sqrt{\kappa^2 - \hat{\delta}^2} L]} \tag{3.31}$$

The grating reflectivity $r = |\rho|^2$ is

$$r = \frac{\sinh^2(\sqrt{\kappa^2 - \hat{\delta}^2} L)}{\cosh^2(\sqrt{\kappa^2 - \hat{\delta}^2} L) - \frac{\hat{\delta}^2}{\kappa^2}} \tag{3.32}$$

When $\hat{\delta} = 0$ or $\lambda = (1 + \frac{\Delta n_{dc}}{n_{eff}})\lambda_D$, the maximum reflectivity occurs with

$$r_{max} = \tanh^2(\kappa L)$$

If denoting $\theta_\rho = phase(\rho)$, the average group delay τ_ρ (in picoseconds) for the optical signal reflected from the grating is

$$\tau_\rho = \frac{d\theta_\rho}{d\omega} = -\frac{\lambda^2}{2\pi c} \frac{d\theta_\rho}{d\lambda} \tag{3.33}$$

The grating group delay characteristic is investigated in later chapters. It is also related to the dispersion parameter d_ρ in optical fibre communications, which is used to describe the chromatic dispersion in units of picoseconds per nanometer and kilometer (ps/(nm*km)):

$$d_\rho = \frac{d\tau_\rho}{d\lambda} = \frac{2\tau_\rho}{\lambda} - \frac{\lambda^2}{2\pi c} \frac{d^2\theta_\rho}{d\lambda^2} = -\frac{2\pi c}{\lambda^2} \frac{d^2\theta_\rho}{d\omega^2} \tag{3.34}$$

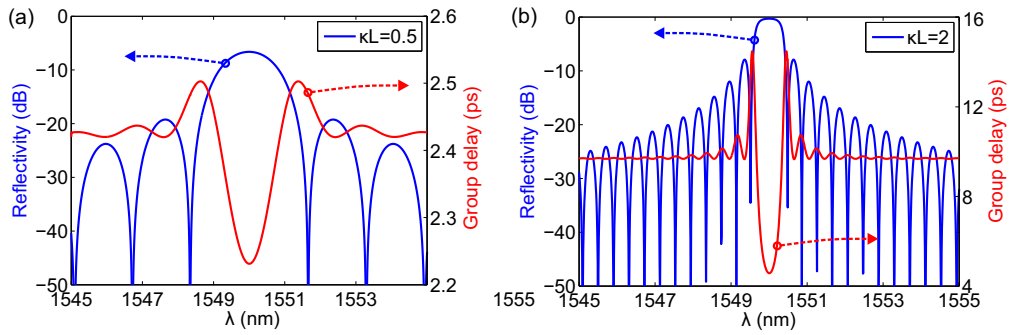

Figure 3.3: Reflectivity (blue line) and group delay (red line) responses for uniform Bragg gratings with (a) $\kappa L = 0.5$ and (b) $\kappa L = 2$.

Figure 3.3 shows the modelling of reflectivity and group delay spectra of uniform Bragg gratings with $\kappa L = 0.5$ and $\kappa L = 2$, by using Eq.(3.32) and Eq.(3.33).

3.3 Analytical solutions

There are some techniques for solving the transfer function of complex Bragg gratings, for example, by the application of a scheme for a multilayered dielectric thin film [53]. The method relies on the calculation of the reflected and transmitted fields at an interface between two dielectric slabs of dissimilar refractive indexes. Its equivalent reflectivity and phase then replace the slab.

Alternatively, the computational grating model could also be established using an ordinary differential equation (ODE) solver and implementing adaptive step-size 4th order Runge-Kutta numerical integration to directly solve the coupled mode equations Eq. 3.27 and Eq. 3.28. More detailed work on this Runge-Kutta method can be found in the work of the previous student in the group [63].

Here we use the transfer matrix method to model Bragg gratings and devices, which will be discussed in the next subsection.

3.3.1 Transfer matrix method

The transfer matrix method has been widely used for analysing the propagation of electromagnetic waves in layered mediums [58]. For Bragg grating structures, the transfer matrix method was also proposed in 1987 [64], for the approximation of solutions of ordinary differential equations calculating the coupling coefficients of the light propagation. The method is also employed in this thesis. The program is written in Matlab™ and the code is provided in Appendix B.

A simple uniform Bragg grating has an analytical solution; a complex grating may be considered to be a concatenation of several small sections, each of constant period and unique refractive index modulation. Thus, the modelling of the transfer characteristics of the Bragg gratings becomes a relatively simple clear and fast technique for analyzing more complex structures.

The coupled-mode equations Eq. 3.27 and Eq. 3.28 are used to calculate the output fields of a short grating section for which the grating parameters (*e.g.* an arbitrary coupling constant and grating chirp) are assumed to be constant (uniform gratings, *e.g.* in Fig. 3.2 and Fig. 3.3). Each may possess a unique and independent functional dependence on the spatial parameter. For such a grating with an integral number of periods, the analytical solution results in the amplitude reflectivity, transmission, and phase. These quantities are then used as the input parameters for the adjacent section of the grating.

The input and output fields of a single grating section are shown in Fig. 3.2. The grating may be regarded as a four-port device with four fields: forward fields $R(0)$ and $R(l_1)$, and the backwards fields $S(0)$ and $S(L_1)$. A transfer matrix F^1 represents the grating

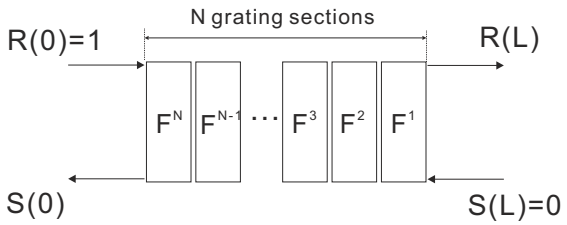

Figure 3.4: The concatenation of N grating sections with transfer matrices to form a composite grating, considering boundary conditions.

amplitude and phase response. Consequently, the fields on the right-hand-side (RHS), $R(l_1)$ and $S(l_1)$ are now the new fields on the RHS that can be transformed again by another matrix F^2 for the adjacent grating section, and so on, so that for the entire grating after the Nth section, where $L = \sum_{i=1}^{N} l_i$, is

$$\begin{bmatrix} R(0) \\ S(0) \end{bmatrix} = F \times \begin{bmatrix} R(L) \\ S(L) \end{bmatrix} \tag{3.35}$$

Where the matrix $F = F^N \times F^{N-1} \times F^{N-2} \times \cdots \times F^1$. A schematic of the sectioned gratings with transfer matrix is shown in Fig. 3.4.

For the reflection gratings discussed in the report, the input field amplitude $R(0)$ is normalized to unity, and the reflected field amplitude at the output of the grating $S(L)$ is zero, since there is no perturbation beyond the end of the grating section. By writing the matrix elements and applying the boundary conditions into Eq.(3.35), the reflection coefficient ρ can be derived as:

$$\rho = \frac{R(0)}{S(0)} = -\frac{F_{21}}{F_{11}} \tag{3.36}$$

The grating reflectivity r is given as:

$$r = \left|\frac{R(0)}{S(0)}\right|^2 = \left|\frac{F_{21}}{F_{11}}\right|^2 \tag{3.37}$$

The elements of the transfer matrix F are:

$$\begin{bmatrix} F_{11} & F_{12} \\ F_{21} & F_{22} \end{bmatrix} = \begin{bmatrix} \cosh(\alpha\Delta z) - i\frac{\hat{\delta}}{\alpha}\sinh(\alpha\Delta z) & -i\frac{\kappa}{\alpha}\sinh(\alpha\Delta z) \\ i\frac{\kappa}{\alpha}\sinh(\alpha\Delta z) & \cosh(\alpha\Delta z) + i\frac{\hat{\delta}}{\alpha}\sinh(\alpha\Delta z) \end{bmatrix} \tag{3.38}$$

where $\alpha = \sqrt{\kappa^2 - \hat{\delta}^2}$. The transfer matrix elements have been derived from Eq.(3.29) and Eq.(3.30). We use this transfer matrix method to calculate Bragg grating responses in the next section. The Matlab code is provided in Appendix B.

3.4 Bragg gratings responses

As discussed in Section 3.2, if we modify any of the parameters in Eq. (3.22), different grating structures, *e.g.* apodised, chirped and phase-shifted gratings, could be achieved. For example, chirped FBGs were utilised for dispersion compensations in optical communication networks [7, 65]. In this work, we focus on introducing an apodisation profile and phase shifts into the Bragg gratings to realise photonic Hilbert transformers.

3.4.1 Apodisation

Apodisation literally means "removing the foot" [66]. In optics, it was originally meant to help with side-lobe suppression, *e.g.* for optical reflectors and filters [67]. In Bragg gratings, this is apodisation of the refractive index change, *i.e.* $\Delta\tilde{n}(z)$ in Eq. (3.22). The term apodisation generally refers to the grading of the refractive index to approach zero at the ends of the grating. Apodised gratings offer significant improvement in side-lobe suppression while maintaining reflectivity and a narrow bandwidth. The two functions we studied here are the Gaussian and sinc functions.

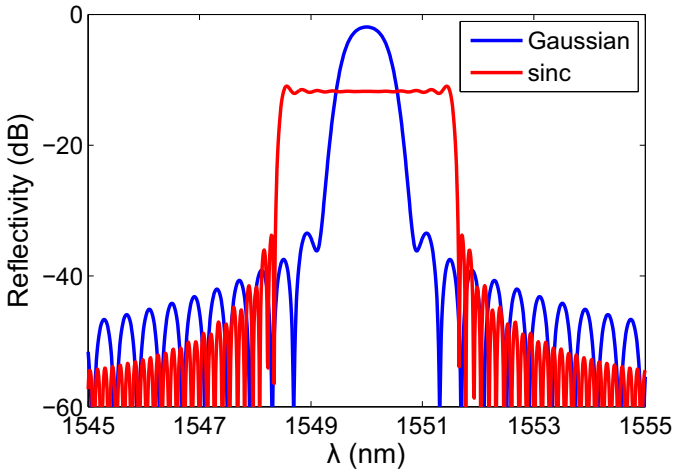

Figure 3.5: Reflectivity spectra of a 2mm Gaussian apodised grating (blue line) and a 6mm sinc apodised grating (red line), with maximum $\Delta n = 5 \times 10^{-4}$.

Figure 3.5 shows the reflectivity responses of a 2mm Gaussian apodised grating (blue line) and a 6mm sinc apodised grating (red line), with maximum $\Delta n = 5 \times 10^{-4}$. The Gaussian apodised grating has a sidelobe suppression ratio of $> -30dB$. The Gaussian apodisation for Bragg gratings is widely used, for example, to expand the capacity of optical fibre networks using the dense wavelength division multiplexing (DWDM) techniques [61] or to enhance the sensitivity and accuracy of grating based sensor technology [68, 69]. The sinc apodised grating has a flat top reflection spectrum with ripples $< 2dB$ and frequently used to generate flat top and dispersion-less reflectors [70].

3.4.2 Phase shift

It is often useful and necessary to incorporate phase jumps within a distributed grating structure [53]. The phase jump opens up a band-gap within the reflection bandwidth, creating a narrow-band transmission filter. This procedure has been applied to distributed feedback (DFB) lasers [71] and wavelength demultiplexers [72]. Figure 3.6 shows the reflectivity spectra of 1mm long uniform Bragg gratings with and without a π phase-shift. A phase shift is accomplished in the transfer matrix method (discussed in Section 3.3) by multiplying the reflectivity of the certain section by matrix elements containing only phase terms.

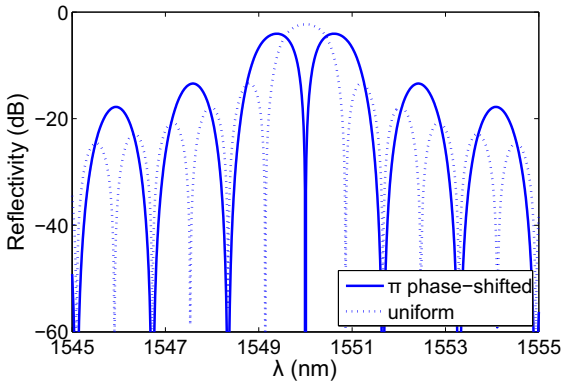

Figure 3.6: Reflectivity spectra of a 1mm π phase-shifted Bragg grating (solid line) and a 1mm uniform grating (dotted line), with maximum $\Delta n = 5 \times 10^{-4}$.

3.5 Inverse scattering synthesis

Grating synthesis is a significant tool to reconstruct the grating structure from the reflection spectrum. A simple and direct synthesis approach based on differential inverse scattering algorithms was first proposed in 1999 at the ORC [54], for the design of complex fibre Bragg gratings. This method was further developed both for design and also for characterisation of fabricated devices [73, 74]. The method relies on the synthesis of the impulse response of the grating by means of a DLP algorithm. The algorithm developed takes into account all the multiple reflections inside the grating, giving an exact solution to the inverse scattering problem. The layer-peeling methods are efficient in the sense that they require one or two order less complexity then previous inverse scattering methods, and well suited for parallel computation [54].

3.5.1 Layer-peeling algorithms

The DLP method is based on causality and the fact that the leading edge of the reflection impulse response corresponds directly to the coupling coefficient of the first grating layer.

Thus one can identify the first layer from the desired response, and remove its effect by propagating the fields to the next layer.

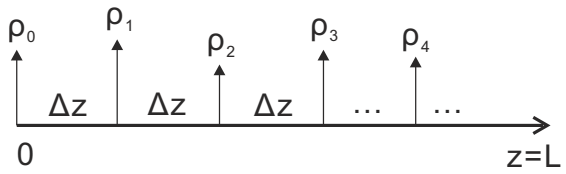

Figure 3.7: The model of discrete grating sections. $\Delta z = L/N$ and N is the number of sections. (Inspired by Ref. [75]).

Instead of making the piecewise uniform discretisation in Fig. 3.4, we can discretise the grating into a stack of complex, discrete reflectors, shown in Fig. 3.7. It is convenient to use the convention that the grating is represented as a stack of $N+1$ complex reflectors j for $j = 0, 1, 2 \cdots N$, separated by N propagation sections $\Delta z = L/N$, see Fig. 3.7. Assuming no chirp and $\Delta n_{dc} = 0$ for simplicity, the jth transfer matrix F_j is then replaced by $F_{\Delta z} \times F_{\rho_j}$, where

$$F_{\Delta z} = \begin{bmatrix} e^{i\delta\Delta z} & 0 \\ 0 & -e^{i\delta\Delta z} \end{bmatrix} \tag{3.39}$$

is the pure propagation matrix obtained from Eq. (3.38) by letting $\kappa \to 0$, and

$$F_{\rho_j} = (1 - |\rho_j|^2)^{-1/2} \begin{bmatrix} 1 & -\rho_j^* \\ -\rho_j & 1 \end{bmatrix} \tag{3.40}$$

is the discrete reflector matrix obtained by letting $\kappa \to \infty$ holding $\kappa\Delta z$ constant in Eq. (3.38). Hence, by substituting Eq. (3.39) and Eq. (3.40) in to Eq. (3.36), the discrete reflection coefficient is given by

$$\rho_j = -\tanh(|\kappa_j|\Delta z)\frac{\kappa_j^*}{|\kappa_j|}$$

By using the transfer matrix as $F_{\Delta z} \times F_{\rho_j}$ in Eq. (3.38), we have the relation between adjacent complex reflectors as:

$$r(z + \Delta z, \delta) = e^{-2i\delta\Delta z}\frac{r(z,\delta) - \kappa_j}{1 - \kappa_j^* r(z,\delta)} \tag{3.41}$$

Based on Eq.(3.41), the discrete layer-peeling algorithm in frequency domain can be described as follows [73]:

1. Start with a physically realisable reflection spectrum, with $j = 0$ and $r_0(\delta) = r(\delta)$;

2. Compute the coupling coefficient $\kappa(j\Delta z)$ of the jth layer with the Fourier transform of $r_j(\delta)$;

3. Propagate the spectrum with Eq. (3.41) and obtain $r_{j+1}(\delta)$;

4. Increase j and repeat step 2 until the entire grating structure is determined.

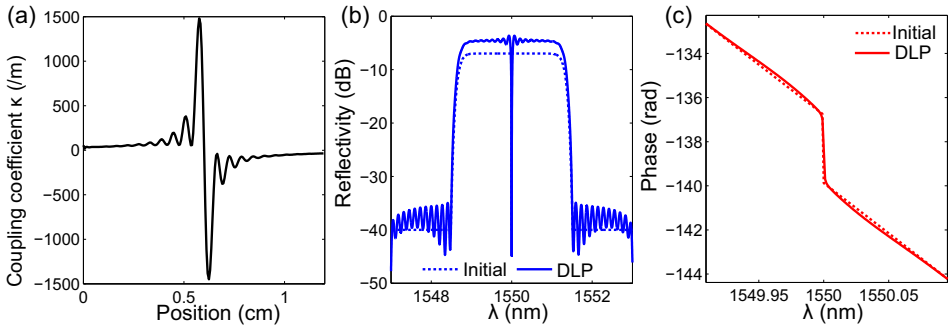

Figure 3.8: Modelling using the DLP method: (a) coupling coefficient κ, (b) reflectivity and (c) phase response of a Bragg grating implementing photonic Hilbert transform, with the initial grating spectra (dotted line) and the numerically demonstrated grating spectral responses (solid line). This grating is designed to have a stronger reflectivity via the DLP method, as shown in (b).

The DLP algorithm has been used to design to synthesis FBGs with different characteristics, *e.g.* square dispensionless filters, 2^{nd} and 3^{rd} order dispersion compensators [54], and Gaussian gratings [76]. Figure 3.8 shows an example of a 12mm Bragg grating implementing 300GHz PHT, with (a) coupling coefficient κ, (b) reflectivity and (c) phase response respectively. The super Gaussian windowing function is employed in the modelling and the reflectivity spectrum shows a strong and flat response within the operation bandwidth, similar to the demonstrations in the reference [41]. The DLP method is used to improve the grating response, generating a greater reflectivity compared to the initial grating response [54], as shown in Fig. 3.8(b). The phase response agrees perfectly with target spectrum, showing a π phase shift in the central wavelength.

The DLP algorithm (inverse scattering method) is numerically demonstrated here; nevertheless, this method was not further practically applied to grating infrastructures due to the time limitation of the PhD course, and could be implemented in the future work.

3.5.2 Accuracy and realisability

The DLP method has been demonstrated to be effective and efficient to design strong Bragg gratings, and with significant accuracy [54, 73]. An important characteristic of the method is its computation efficiency [77]. The efficiency of this algorithm is superior to that of the iterative GLM method [78] and the processing time consumed for each iteration of the GLM method was twice the total execution time of the layer-peeling algorithm, with examples in the reference [77].

A main problem with inverse scattering algorithms is that not all reflection spectrum functions are realisable. It is not sufficient to require that the spectrum is a causal filter function with absolute value less than unity. Thus, inverse scattering algorithms cannot always be applied directly for design since the target spectrum is not necessarily realisable. A common way to make the target spectrum approximately realisable is to specify a spectrum which corresponds to an impulse response of finite duration. This is achieved with conventional methods for design of finite impulse response (FIR) filters using windows [51]. A super-Gaussian windowing function was employed in the modelling here. This procedure gives good results, shown in Fig. 3.8. Once the physically realisable spectrum is obtained, the DLP algorithm can be used to determine the grating structures.

3.6 Grating structures for optical signal processing

The technique of applying photonic technologies to process signals in the all-optical domain has the ability to overcome the inherent speed limitations of electronic signal processors. All-optical signal processing based on FBGs and multiple wavelength techniques open up new possibilities for the realisation of high resolution, wide-band and adaptive processing of the optical signals traveling along the fibre [79].

The project focuses on the Bragg grating devices for PHT in all-optical signal processing. Through the theoretical derivation and modelling discussion in the previous sections, we are able to simulate the proposed Bragg grating structures for PHTs.

3.6.1 Bragg grating for Hilbert transform

The π-phase shift which is the primary function of a Hilbert transformer is simply induced by placing a π-phase shift in the refractive index modulation of the Bragg grating. The practical Bragg device could incorporate an apodisation profile with the necessary π-phase shift, similar to the simple weak-coupling uniform FBG in [39]. The grating apodisation profile is:

$$\Delta n(z) \propto \frac{\sin^2[\pi n_{eff} \Delta f(z - z_0)]}{n_{eff} \Delta f(z - z_0)} \tag{3.42}$$

where, $0 < z < L$ for L is the total grating length, n_{eff} is the effective refractive index of the mode, c is the light speed in vacuum, and z_0 is the zero-crossing point in the apodisation function, here set in the centre of the grating length for simplicity, and Δf is the operating bandwidth.

The grating apodisation profile requires a single π-phase shift along the grating length, as previously shown in Fig. 2.9(a). Through simple mathematical calculation, it is demonstrated that the zero-to-zero width of the side lobe Δn in the apodisation profile is directly related to the operating bandwidth Δf, with $\Delta f = c/(n_{eff}\Delta z)$. Negative Δn value results from a π-phase shift in the apodisation profile.

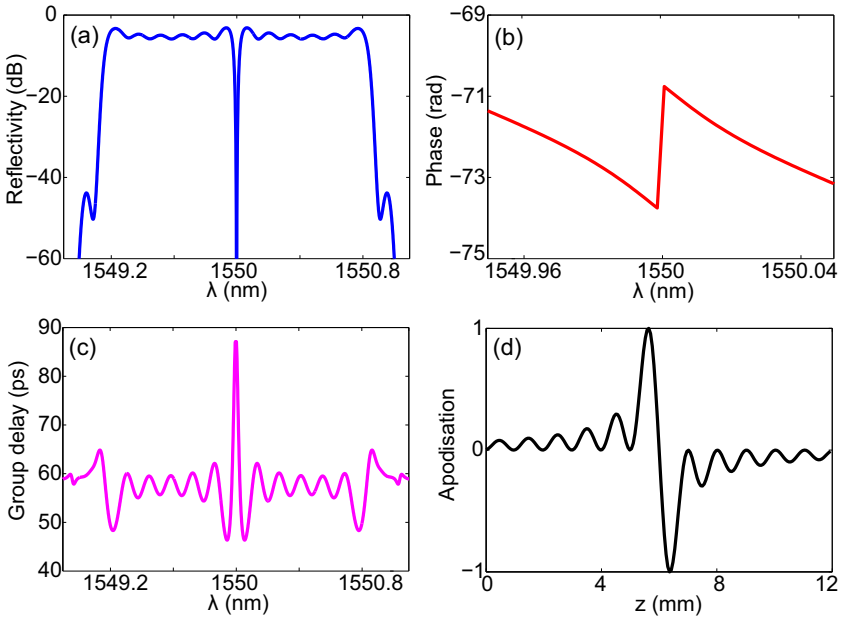

Figure 3.9: Modelling: (a) reflectivity, (b) phase, (c) group delay responses, and (d) the apodisation profile of the Bragg grating implementing a PHT. The grating is design to be 12mm long and with 200GHz ($\sim 0.8nm$) operating bandwidth.

With the transfer matrix method discussed in Section 3.3, we did some simulation work on the proposed gratings, with data shown in Fig. 3.9. The program code is written using Matlab™. The Bragg grating is $12mm$ in length; the designed Bragg wavelength is $1550nm$; the effective refractive index is set to $n_{eff} = 1.44852$ (which is the typical number of planar samples used in this fabrication process) with the maximum refractive index change $\Delta n = 7 \times 10^{-4}$; the intentional bandwidth is set to $200GHz(\sim 0.8nm)$.

As anticipated, the amplitude response is a nearly flat top with $< 3dB$ fluctuation and phase response presents an abrupt π-phase jump. The spectral bandwidth is about $1.6nm$ ($\sim 200GHz$), which agrees with the input bandwidth value.

3.6.2 Integrated all-optical single sideband filter

The integrated all-optical SSB filter discussed in Chapter 2 is composed of an X-coupler, PHT, flat top rectangular reflector, and a micro heating filament. The PHT is implemented using an appropriate apodised planar Bragg grating with a π-phase shift in the grating length discussed above. The sinc-apodised Bragg grating is utilised as a flat top

rectangular reflector with the same bandwidth as the PHT. By applying DC voltage to the micro Ni-chrome filament on one arm of X-coupler, thermal tuning in terms of phase trimming is achieved. All structures are located in a single chip, schematically shown in Fig. 3.10.

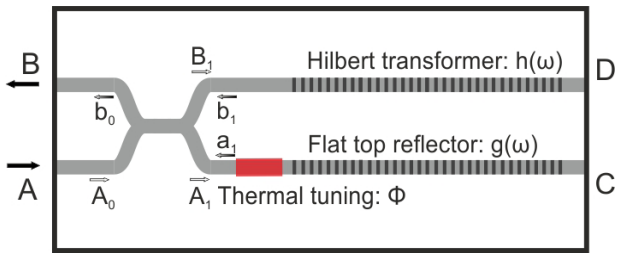

Figure 3.10: The principle scheme of the integrated all-optical SSB filtering device via thermal tuning.

We consider the case in which light is coupled into port A and received from port B, and assume that both arms have identical waveguide structures. From the waveguide coupler theory [14], we have

$$A_1 = A_0 \cos(\kappa l) \tag{3.43}$$

$$B_1 = -iA_0 \sin(\kappa l) \tag{3.44}$$

where κ is the coupling coefficient and l is the coupling length. After reflection from the gratings, optical fields a_1 and b_1 become

$$a_1 = A_1 g(\Delta\omega) e^{i(2\phi-\beta l)} = A_0 \cos(\kappa l) g(\Delta\omega) e^{i(2\phi-\beta l)} \tag{3.45}$$

$$b_1 = B_1 h(\Delta\omega) e^{i(-\beta l)} = -iA_0 \sin(\kappa l) h(\Delta\omega) e^{i(-\beta l)} \tag{3.46}$$

where $-\beta L$ is the phase shift due to propagation in two arms, β is the wave number and ϕ is the extra phase shift due to thermal tuning. $\phi = \beta\Delta L$ and ΔL is the optical path length difference between the two arms. The extra phase shift of light in one round trip is 2ϕ. $h(\Delta\omega)$ and $g(\Delta\omega)$ are reflection coefficients of the PHT and the flat top reflector respectively. $\Delta\omega = \omega - \omega_0$ where ω is the frequency parameter and ω_0 is the central frequency. The device output b_0 is the superposition of the electric fields a_1 and b_1 as:

$$b_0 = -iA_0 \sin(\kappa l) \cos(\kappa l) e^{-i\beta L} [h(\Delta\omega) + g(\Delta\omega) e^{2i\phi}] \tag{3.47}$$

The Hilbert transform grating response function in the frequency domain is given as:

$$h(\Delta\omega) = -isgn(\Delta\omega) \prod(\Delta\omega) \rho_0 \tag{3.48}$$

which is similar to that in Eq. (2.3). $sgn(\Delta\omega)$ is the sign function (which is $+1$ for $\Delta\omega > 0$ and -1 otherwise), $\prod(\Delta\omega)$ is the rectangular function (window function), and

ρ_0 is the maximum reflection coefficient. The PHT has a π phase shift at $\Delta\omega = 0$, whereas the amplitude remains constant other than $\Delta\omega = 0$.

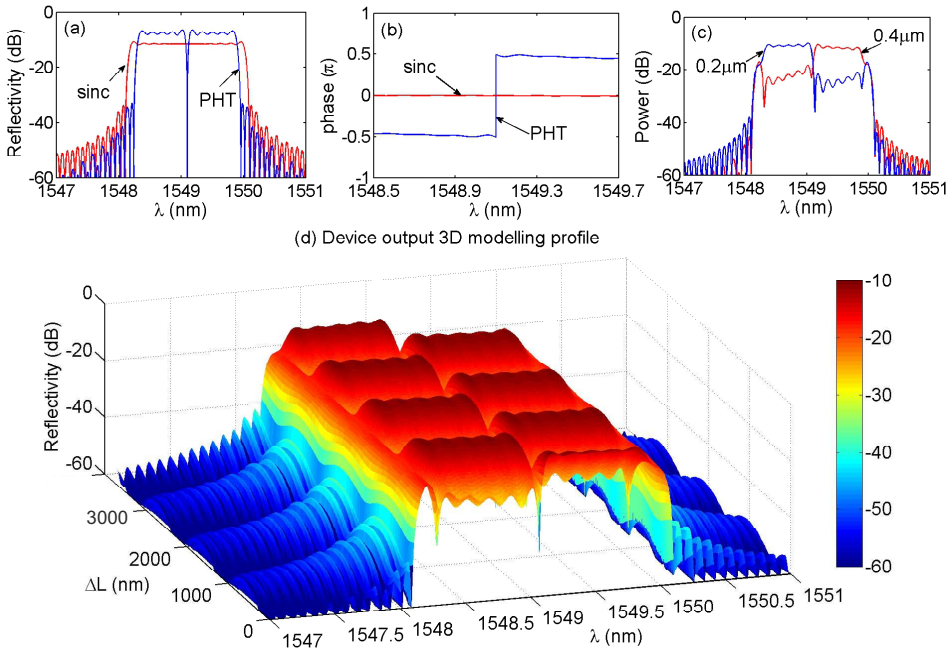

Figure 3.11: Modelling and simulation: (a) the PHT and sinc-apodised gratings amplitude spectra; (b) normalized gratings phase spectra; (c)device outputs at port B, with ΔL at $0.2\mu m$ (blue) and $0.4\mu m$ (red); (d) the 3D profile map of the output optical spectra as a function of ΔL.

Sinc-apodisation of Bragg gratings are used to generate flat top and dispersion-less reflectors [14]. In this case a sinc-apodised grating design is used to obtain similar bandwidth and amplitude responses as the PHT. The grating frequency response is:

$$g(\Delta\omega) = \prod(\Delta\omega)\rho_0 \tag{3.49}$$

The grating apodisation profile is given as:

$$\Delta n(z) \propto \frac{\sin[\pi(z - z_0)]}{z - z_0} \tag{3.50}$$

A transfer matrix method is employed for the calculation of the expected device output by calculating the fields in Eq. (3.47). Figure 3.11 illustrates the reflectivity and phase spectra of individual gratings, the device output at port B with ΔL (e.g. $0.2\mu m$ and $0.4\mu m$), and a 3D profile of the spectra from port B as a function of ΔL. Figures 3.11(a) and 3.11(b) demonstrate the similarity of the sinc-apodised grating response to that of the PHT, except the π phase-shift at the central wavelength. Figure 3.11(c) shows the resulting interfered output from the device for two optical path difference scenarios, where the opposite side lobes are suppressed. Figure 3.11(d) presents the effect of optical

path difference over an extended range showing a periodic variation. The experimental data will be presented and discussed in Chapter 6.

3.7 Summary

In this chapter, light propagation in anisotropic media has been discussed, starting from Maxwells equations. This has followed into waveguides and Bragg grating structures, many of which have been fabricated and characterised during this thesis. Analytical solutions for simple Bragg grating geometries have been developed from coupled-mode equations to explain optical properties. Transfer matrix method and the DLP based on inverse scattering method have been discussed and used for computational analysis for more complex grating structures. The concepts and importance of apodised and phase-shifted gratings have been introduced and grating spectral profiles have been computed using the author's code. Finally, models of the proposed devices for PHTs and all-optical SSB filtering have been established and simulated, and these results indicated a promising route for the project.

Chapter 4

Integrated photonics fabrication background

4.1 Introduction

Devices in this thesis are fabricated via state-of-the-art integrated photonics facilities at the ORC. This chapter gives a brief introduction of the fabrication platform and some related techniques. The planar waveguide substrates, deposition methods, photolithography, photosensitivity and waveguide and grating inscription techniques, are discussed consecutively. Some measurement techniques are demonstrated with examples of device characterisation.

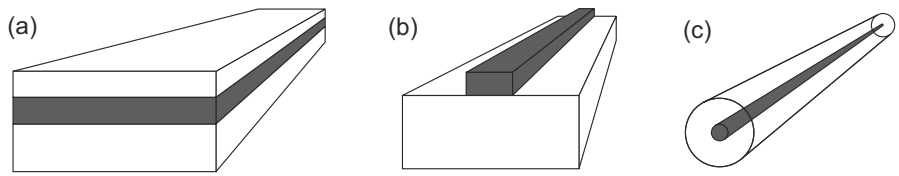

Figure 4.1: Basic waveguide geometries: (a) planar waveguide; (b) strip waveguide; (c) optical fibre.

The optical waveguide is the fundamental element that interconnects the various devices of an optical integrated circuit. Figure 4.1 shows some examples of basic structures for the most common waveguide geometries. In a planar waveguide of Fig. 4.1(a), light is trapped in a film (grey region), and the film must have a refractive index greater than the refractive indices corresponding to the upper and lower media. These are usually referred to as the cladding layer and the substrate, respectively, and the film is called the core, because that is where most of the optical energy is concentrated. In a strip waveguide of Fig. 4.1(b) the light propagates within a rectangular area (grey region) which is embedded in a planar substrate. This type of waveguide has been widely used for fabricating integrated photonic devices *e.g.* gratings and modulators [13]. Finally,

Fig. 4.1(c) shows the geometry of an optical fibre, which can be considered as a cylindrical channel waveguide. The central region of the optical fibre or core is surrounded by a material called the cladding. The core should have a higher refractive index than the cladding for achieving total internal reflection.

In both Fig. 4.1(b) strip waveguides and Fig. 4.1(c) optical fibres the confinement of optical radiation takes place in two dimensions, in contrast to Fig. 4.1(a) planar waveguides where there is only light confinement in a single direction. This fact allows light in planar waveguides to diffract in the plane of the film, whereas in the case of strip waveguides and fibres diffraction is avoided, forcing the light propagation to occur only along the structures main axis [13].

4.2 Planar waveguides

A wide range of materials including glasses, crystals and semiconductors can be used to fabricate optical waveguides. In particular, the platforms most commonly used are glasses, lithium niobate, silicon, silica-on-silicon, III-V semiconductor compounds and polymers [13]. Each type of material has its own advantages and disadvantages, and the choice of a specific substrate depends on the particular application of the photonic device. Nowadays there exists a great variety of devices based on each of these materials.

The glass-based integrated optical devices have the great advantages of the low cost of the starting material, low loss, low nonlinearity and the capability of rare earths incorporation to different implementations. With all these devices it is the deposition method what limits the cost.

Lithium niobate ($LiNbO_3$) is another widely used material, due to several physical characteristics, for example, valuable acousto-optic, electro-optic and piezo-electric effects, and high non-linear optical coefficients [80]. A great variety of devices based on $LiNbO_3$ substrates, mainly in the field of optical communications [81], are now commercially available.

The III/V semiconductor compounds (*e.g.* GaAs and InP) are the substrates with greatest impact and have a promising future in this field. They offer the possibility of a high level of monolithic integration. InP is a very versatile platform that promises large-scale integration of active components (lasers and detectors), passive components, and also electronics. The main problem concerning this technology has its roots in the relatively high losses of waveguides made of these materials [13].

Among the suitable materials, polymers occupy a special position, due to the fact that they exhibit some useful physical properties, low-cost, high ruggedness and chemical and biological potential, well potential for large scale mass production [82].

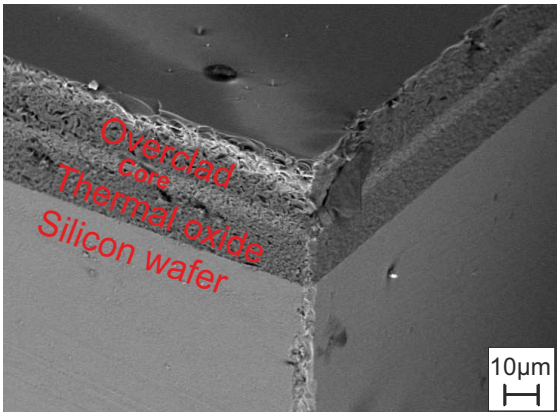

Figure 4.2: An SEM image of a typical silica-on-silicon wafer, consisting of thin multiple silica layers upon a thick silicon substrate. Sample image obtained by Dr. Christopher Holmes.

The material used in this work is the silica-on-silicon platform or $SiO_2 : Si$; an example is shown in Fig. 4.2. The substrate is silicon, upon which a thermal oxide layer is grown to produce an underclad. Thermal oxide growth is achieved by placing the silicon wafers in a furnace at $\sim 1100^oC$ containing water vapour. The oxide thicknesses required are generally up to a hundred times thicker than those encountered in the microelectronics industry and so typically take several weeks to grow the desired thickness, of up to $14\mu m$. Upon the thermal oxide, doped silica can be deposited using Plasma Enhanced Chemical Vapour Deposition (PECVD) and Flame Hydrolysis Deposition (FHD), both of which have been studied by previous members of the research group [83–85] and will be further discussed in later sections. Finally an overclad is deposited using again FHD or PECVD. There is inherent compatibility between this platform and optical fibres as both use silica as the guiding medium. $SiO_2 : Si$ platforms also have the potential to accommodate optical and electronic functions on the same integrated optical device [86].

An SEM image of a completed silica-on-silicon wafer is shown in Fig. 4.2. The $\sim 17\mu m$ thick overclad and $\sim 6\mu m$ core layer are consolidated onto the $\sim 17\mu m$ thick thermal oxide layer, grown on the base silicon wafer. The wafers used in this PhD thesis were fabricated using an FHD process by the in-house facilities. Specifications of the wafers used in this work are included in the Appendix C. For completeness both PECVD and FHD process, with their relative advantages and disadvantages shall be described in the following sections.

4.3 Planar silica deposition

4.3.1 Plasma enhanced chemical vapour deposition

The first demonstration of direct UV writing into planar silica-on-silicon utilised plasma enhanced chemical vapour deposition (PECVD) for silica deposition [87]. The PECVD utilises energy provided by RF or microwaves to dissociate the reactants, creating a high energy plasma that facilitates thin film deposition. The main advantage of this technique is that depositions can be carried out at low temperatures due to the additional energy provided by the plasma [88]. A schematic diagram of the PECVD deposition chamber and process is shown in Fig. 4.3.

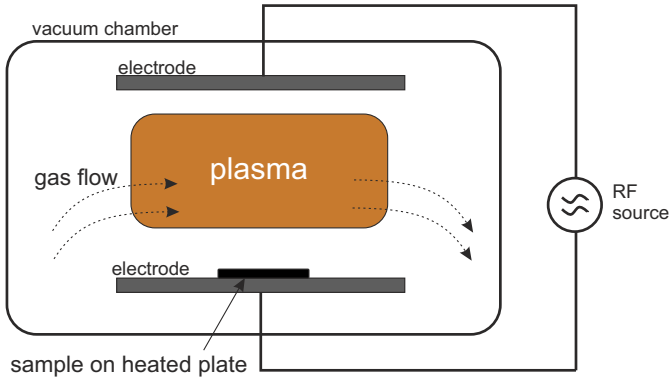

Figure 4.3: PECVD deposition process.

Target substrates are placed into a vacuum chamber which is fed volatile precursors, typically SiH_4, N_2O and a carrier gas, for example N_2, Ar or He [63]. The gases decompose and react to deposit a film on the substrate. PECVD utilises RF electrical fields to ionize the gases, forming a plasma. This allows decomposition and reaction at lower temperatures than some CVD techniques. Glass layers formed by PECVD often contain substantial amount of hydrogen and nitrogen. Their associated bonds in the glass network cause absorption in the near-IR which are issues for telecommunication devices. N-H, Si-H and O-H bonds all contribute to absorption losses in the spectral region of the C-band (1525-1565nm) [89]. PECVD layers can also produce layers with defects and voids that cause scattering losses, while also making the material susceptible to water ingress. These problems can be reduced by extra processes such as annealing at high temperatures [90].

As PECVD does not require a halide precursor, a wider choice of dopants can be used. However, PECVD is limited by the possible deposition thickness. Typically only a few μm can be deposited in any one step, whereas FHD can deposit the required $15\mu m$ in a single step. Greater thickness deposition in a single step can cause blistering and delamination [85]; this is primarily caused by hydrogen being hindered in its escape from

the glass layer as it is being consolidated. Thus the PECVD technique can become more expensive and time consuming than FHD.

4.3.2 Flame hydrolysis deposition

An alternative to PECVD is the flame hydrolysis deposition (FHD) process, which is used to fabricate the photosensitive core and index-matched overclad layers of wafers in this thesis. It is a common process used to deposit glass layers onto planar substrates [91]. This is because it has the advantages of high deposition rates, low loss layers and can form layers with low stresses.

The layers used in this thesis were designed at the ORC, and fabricated on FHD systems designed by the Centre for Integrated Photonics (CIP), UK. Early fabrication work was carried out on a system at CIP, whilst installation of an equivalent system was undertaken at the ORC to replace a system designed within the group [83], but destroyed by fire in 2005. The silica-on-silicon wafers used to create the devices and techniques described in this thesis were designed and fabricated by the group at the ORC [92]. The specifics of layers used for individual devices are detailed in the appropriate chapters and referenced appendices.

Figure 4.4 shows (a) the schematic of the deposition step of the flame hydrolysis deposition procedure where the soot is subsequently thermally treated to form a glassy layer, and (b) a camera image of the working FHD setup. A silica soot is first deposited on to a substrate, followed by a high temperature consolidation step during which the low density soot is converted into a dense glass layer.

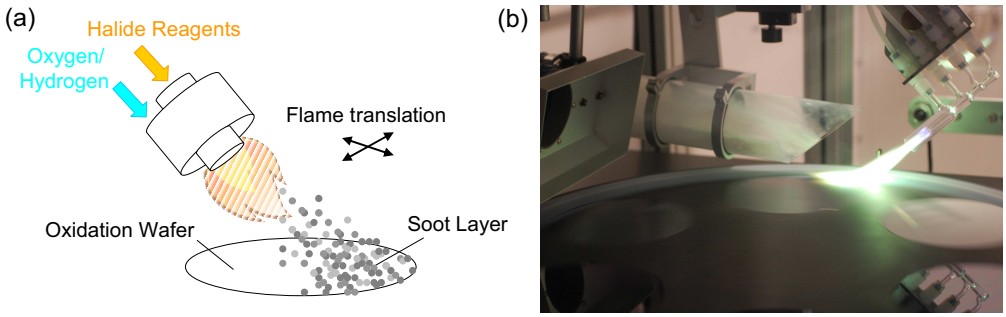

Figure 4.4: (a) Illustration of flame hydrolysis deposition (FHD) process and (b) the photograph of the working FHD setup. The doped hydrogen oxygen flame passes over the wafers depositing a soot layer. Boron vapour causes the green flame colour.

The silica soot is produced by burning a silicon tetrachloride vapour in an oxygen-hydrogen flame. The precursors for FHD are required to be halide based. For silica deposition this halide precursor is silicon tetrachloride ($SiCl_4$). For temperatures below 1200^oC the principle reaction is hydrolysis [93]. Silica soot is formed principally through

the direct oxidation of $SiCl_4$ at the centre of the flame, where temperatures reach 2000^oC. The hydrolysis and direct oxidation reactions for SiCl4 are as follow:

- (Hydrolysis, $< 1200^oC$): $SiCl_4 + 2H_2O \rightarrow SiO_2 + 4HCl$
- (Direct oxidation, $\geq 1200^oC$): $SiCl_4 + O_2 \rightarrow SiO_2 + 2Cl_2$

Deposited layers can be selectively added with dopants with controlled concentrations by using the relevant halide. Germanium, phosphorus and boron are often used as additives and their respective oxides are also formed by either hydrolysis or oxidation [83]. Dopants affect particular properties of each layer, notably refractive index, and photosensitivity, thermal expansion coefficient and melting point. These effects are summarised in Table 4.1.

The refractive index profile determines the waveguide characteristics of devices fabricated in the substrate, while the photosensitivity determines the ability to define buried channel waveguides and Bragg gratings using UV inscription techniques.

Dopant	Refractive index	photo-sensitivity	Melting point	Thermal expansion
Germanium	+	+	-	+
Phosphorous	+	-	-	+
Boron	-	+	-	+

Table 4.1: Key effects of some dopants on silica substrate layer properties [63, 83, 94].

A example of a fabricated FHD sample is previously shown in Fig. 4.2. The core layer contains germanium to increase the photosensitivity to UV radiation. The importance of this will be explained in the later section. In this work the core layer is typically $5 - 7\mu m$ thick for the single mode operation, whereas the cladding layers are typically $15\mu m$ for the fundamental mode trapping efficiency.

To create these channel waveguides and Bragg gratings, an extra fabrication step is required. For the UV writing process three planar layers are used, whereas for photolithographic devices the core is etched before cladding deposition. The direct UV grating writing techniques are powerful fabrication tools which allow for simultaneous definition of both the waveguides and gratings in a single process. These UV writing techniques will be further discussed in Chapter 5.

4.4 Photolithography

In this work, photolithography was used to fabricate heating assemblies on top of the UV written waveguide, to achieve thermal tuning capability. Photolithography (or optical

lithography) is a technique that has been used for many years in the manufacture of semiconductor integrated circuits and has made the transition into the field of planar waveguide fabrication [84]. It is the processes of transferring geometric shapes from a transmission mask into a photoresist layer spun onto a substrate. The photoresist is a polymer sensitive to UV light, which causes the exposed polymer to crosslink. The photoresist is spun onto the sample creating a thin film that is exposed to the mask pattern through a mask-aligner.

The photolithography has been widely used for etched waveguides generally. Nevertheless, in this thesis, this technique was employed to make micro-heaters on top of fabricated waveguides, achieving thermal tuning capability. The process was described in detail as follows.

Waveguide structures in the sample was created in advance by the direct UV writing technique, which will be discussed later in Section 4.6. A mask aligner (Karl-Suss™ MA6 double-sided mask aligner) exposed the sample through the mask to a weak UV source imprinting the mask structure into the resist. The resist can consequently be developed and the un-exposed resist washed away. In this work, the electron beam metal evaporator (Edwards™ Auto 500) was used subsequently to deposit a Nichrome thin layer onto the waveguide surface. The incorporation with a printed circuit board (PCB) allowed it to work as the micro heater. This process is employed to add thermal tuning capability to optical devices, which will be discussed in Chapter 6.

Photolithographic techniques are suitable for mass production, which can be low costs and are regularly used in the definition of integrated optical devices. They also do not require photosensitive layers for waveguide definition. However, masks, mask aligners and associated clean room facilities become costly, especially when making prototypes and small batches. Photolithography also is more susceptible to roughness at the sides of the waveguide, and waviness or inconsistent waveguide thickness. Sidewall roughness can be a result of the etching process which can induce scattering loss. This can have negative consequences, especially in complex grating structures where fine control of grating structures is critical in this work.

4.5 Photosensitivity

Photosensitivity in silica waveguide refers to a permanent refractive index change of the core when exposed to light with characteristic wavelength and intensity that depends on the core material [94]. This physical effect forms the basis of all the work involving direct UV writing in this thesis and directly determines the device performance. Hence, it is crucial to discuss the mechanism, dynamics and enhancement of the photosensitivity. Nevertheless, the physical mechanisms underlying photosensitivity are yet to be

completely understood and are considered to be a combination of photochemical, photomechanical and thermochemical effects, and are material dependent [86]. The current consensus on the mechanism of photosensitivity in silica glass is the formation of colour centres that gives way to compaction of UV irradiated glass [94]. Another model also suggested that the UV-light induces compaction or stress changes in the glass leading to refractive index changes [95–97].

Photosensitivity in optical waveguides was first observed by launching a 488 nm laser into the core of germanium-doped optical fibre [98]. After that, the development of FBGs was discussed and reviewed in the literature [53, 61, 99, 100]. FBGs were defined using a 244nm UV laser radiation and the transverse holographic method [101]. Hydrogen loading was used to further increase the photosensitivity and was another significant step in progressing with the filed [102]. They are further discussed in the next subsections.

4.5.1 Mechanism and dynamics

As discussed previously the precise mechanism leading to the refractive index increase of a material irradiated with UV sources is yet to be fully understood. As for the germanium-doped silica used in this work, the two main models for this case are the defect centre (or colour centre) model and the glass compaction (or stress change) model. It is most likely that the index increase results from the combination of both these effects [53, 86].

The colour centre model argues that the colour or defect centres within the material are responsible for changes in the UV absorption spectrum of the glass, creating index change in the IR region via the causality principle. This increased value can be quantified by obtaining the effective refractive index change via Bragg grating reflectivity data. When germanium is incorporated into glass matrix, incorrect bonds such as $Ge - Si$ and $Ge - Ge$ are formed producing Ge^{2+} centres (also known as GeO). These are linked to the 240-250 nm absorption band and their centres are known as germanium oxygen-deficient centres (GODCs), schematically shown in Fig. 4.5. Detailed information about the defects and centres could be found elsewhere [53, 94]

The glass compaction model is based on laser-irradiation induced density changes that result in refractive index changes [94]. This compaction is thermally reversible and is combination of structural volume changes and the volume of oxygen ions present in the glass. UV excitation leads to bond breaking which, in turn, results in a volume change. This model has been verified as it is found that density modulation occurs in germanosilicate glass irradiated with UV [103]. Further experimental data shows the densification model explains 40% the photosensitivity in non-hydrogen loaded germanosilicate while the colour centre model accounts for a large part of the photosensitivity in the hydrogen loaded germanosilicate samples [96].

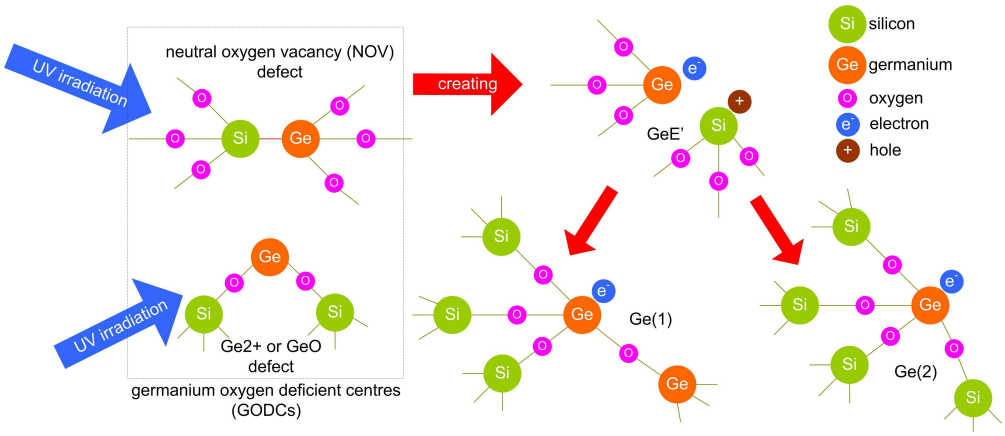

Figure 4.5: Colour centre model: a schematic of proposed Ge (or Si) defects of germania-doped silica. Reprinted from [86].

Another effect exploited during UV writing, particulary during alignment is photoluminescence. It was reported that the luminescence signal from a germanosilicate glass graded-index fibre preform followed the index profile of the glass fibre at low excitation power and was bleached at higher powers above a certain Ge-concentration threshold [104]. Within this work this observation was used as a basic way of testing the photosensitivity of samples, and subsequently determining suitable UV fluence levels.

Considering the grating formation in the germanium-doped silica with the UV exposure dosage, refractive index changes in UV irradiated samples are mainly classified into three types: Type I, Type IIA and Type II. The final grating type depends upon the initial writing conditions (*e.g.*laser power and wavelength, CW or pulsed energy delivery) and substrate properties [94].

- Type I: the effective refractive index and the reflective index modulation depth increases monotonically with moderate UV radiation dosage. This is the regime that is used in most writing experiments. Further increasing the UV intensity would lead to the partial or complete erasure of the formed gratings and the formation of a new spectrum, into the Type IIA regime.

- Type IIA: Following erasure of Type I gratings, another set of gratings with difference index change mechanisms is formed. Type IIA gratings appear to have similar spectral characteristics as Type I gratings, but are with considerably improved temperature stability.

- Type II: The final phase, a Type II grating, is formed via ablation (physical damage) by using very high intensity light which is usually pulsed. Shorter wavelengths launched into these devices are strongly coupled into the cladding which is a distinct feature in the transmission spectra [105].

4.5.2 Hydrogen loading

Hydrogen loading is used in this work to achieve strong and better defined spectral responses of the proposed planar Bragg gratings. This technique was first reported in 1993 [102] and showed that the refractive index change of germanosilica glass could be enhanced by an order of magnitude through hydrogen loading the samples at high pressures ($\sim 120bar$) prior to UV exposure. One disadvantage of this technique is that the hydroxyl species formed have an OH^- absorption band near 1400nm, which may cause optical losses for telecom operation. An improvement to this would be using deuterium loading, where the OD^- group would have an absorption band at 1900nm, away from the wavelength region of interest.

Nevertheless, at room temperature and pressure the in-diffused hydrogen/deuterium will out-diffuse and thus the level of photosensitivity will reduce as a function of time. In this work, this effect is minimised by quickly putting the removed sample into a transport flask containing liquid nitrogen which keeps temperatures below -30^oC [106], significantly increasing this time constant.

Prior to direct UV writing the germanium doped silica wafers in this work were hydrogenated. Hydrogen was selected over deuterium as the reduction in absorption did not justify the increase in cost. Photosensitivity in the hydrogenated FHD wafers used in this work was observed to induce a maximum index change of 5×10^{-3}, but refractive index changes of 10^{-2} have been observed in bulk samples [102]. This give the ability to direct UV write weak guiding waveguides and gratings. The theory and methodology of direct UV writing shall be described in the following section.

4.6 Direct UV laser inscription

This section gives a brief introduction to the fabrication techniques used in this work, including Direct UV Writing (DUW) and Direct Grating Writing (DGW). Detailed discussion of the DGW technique and the phase-control method to improve the current DGW technique for complex grating writing is included in Chapter 5.

4.6.1 Direct UV writing into silica-on-silicon

The technique used to define buried channel waveguides is known as Direct UV Writing (DUW). DUW exploits the UV photosensitivity of the hydrogen loaded FHD samples as mentioned in the previous section. The technique was developed by Svalgaard in the 1990's [87], and has demonstrated the fabrication of integrated devices such as optical splitters and attenuators [107].

Direct UV writing (DUW) uses a frequency doubled argon-ion laser operating at 244 nm (in this case a Lexel™ 95-SHG laser), which spectrally overlaps with the absorption resonance of the photosensitive Ge-doped core as discussed previously. The argon-ion laser has good spatial coherence, with a coherence length suitable for writing Bragg gratings with an interferometric technique [56]. They also have good beam pointing stability such that devices requiring extended exposure times are possible.

Focussing the laser beam into the Ge-doped core of a three-layer substrate causes a local refractive index change. When the sample is translated underneath the static focussed laser writing spot, a structure with two-dimensional confinement can be produced. For a typical three-layer substrate, this technique produces a buried channel waveguide whose height is governed by the thickness of the photosensitive core layer and width by the diameter of the writing spot. The sample is translated using high precision air-bearing stages (Aerotech™ ABL 9000) under computer control.

The refractive index contrast between the written and unwritten substrate is typically of the order 10^{-3}. The refractive index change is proportional to the intensity and duration of the UV exposure, until the index change saturates. These UV exposure parameters are summarised succinctly by the concept of fluence [85], which quantifies the energy illuminating the sample. It is dependent on the laser intensity and also the translation speed of the sample. Fluence is defined as:

$$F = \frac{I_{UV} \times d}{v_{trans}} \tag{4.1}$$

Where I_{UV} is the average power density of the focussed laser spot (here in kW/cm^2), d is the spot diameter in cm and v_{trans} is the sample translation speed in cm/s. Fluence is typically measured in units of kJ/cm^2.

Direct UV writing has several advantages over photolithography-based waveguide definition. As mentioned in the previous sections, variations of etched waveguide structures can primarily lead to changes of the propagation constant of waveguides, which can cause varication of Bragg grating structures. The UV writing technique suffers less from this problem as the width of the guide is exclusively defined by the laser fluence. This is an important point for the device fabrication in this work. It does not require any additional processing steps, aside from the hydrogen loading for increased UV sensitization. Devices are ready to use once the writing process is complete meaning fabrication for small numbers of devices are time efficient. As DUW does not require masks there is far more flexibility in waveguide design, which is crucial for this project. Consecutive samples can have completely different UV written patterns, with little or no extra setup time or cost. Also, as the waveguide roughness is defined by the FHD deposition and not by post-processing, the waveguides are intrinsically optically uniform.

4.6.2 Direct UV grating writing

The DGW technique is an extension of the DUW writing technique discussed above. It is a technique that allows for simultaneous definition of both channel waveguides and Bragg grating structures [56]. DGW uses a similar setup to that used by DUW and also requires a precision air-bearing stage system, with additional components to transform it into an interferometric system. These components comprise an optical modulator, a beam splitter, reflection mirrors and focusing lenses to create an interferometer. The precision air-bearing stage system is used to translate the sample underneath the beams, and, if no modulation is used, produces producing channel waveguides or Bragg gratings if the fringe pattern is modulated, as shown in Fig. 4.6.

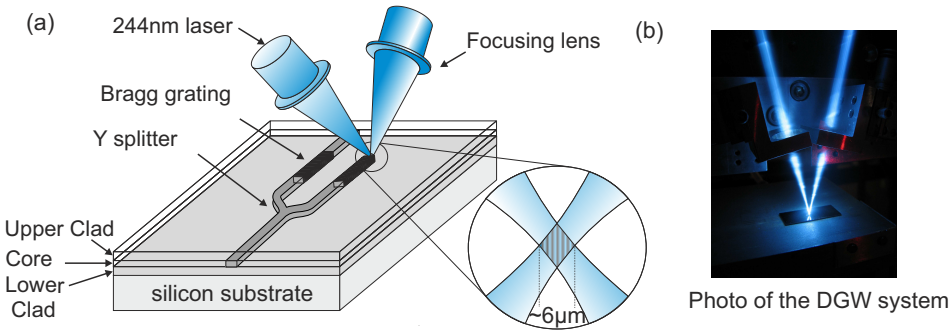

Figure 4.6: (a) Illustration of the DGW technique with two crossed beams focused onto the core layer of the silica-on-silicon substrate;(b) a photo of the crossed laser beams in the DGW system.

Figure 4.6(a) illustrates the DGW technique involving focusing two crossed laser beams ($\lambda = 244nm$) into the photosensitive core of a planar sample. Figure 4.6(b) shows a camera image of the DGW system. UV irradiation increases the refractive index in this layer. Precise translation of the sample and modulation of the fringe pattern both defines the channel waveguide and simultaneously the creation of grating structures. This spot size is approximately $6\mu m$ in diameter, providing the unique ability over traditional FBG to manipulate the grating structures at the micron level. This ability allows precise engineering of the amplitude and phase responses of the proposed gratings in this project.

To increase the flexibility of this technique for arbitrary grating structures, two methods have been demonstrated: use of an Acousto-Optic modulator (AOM) prior to the interferometer to regulate the laser intensity directly [84], or an Electro-Optic modulator (EOM) to change the phase difference of the two coherent beams inside the interferometer to adjust the fringe pattern intensity. The prior one, named as 'amplitude modulation method', has been developed by the previous members of the research group [84–86]. The latter novel method, named as 'phase-control method', benefits from energy and time efficiency, linear refractive index control, and simplified optical layout, etc, and is the significant part of this thesis and presented in Chapter 5.

4.7 Characterisation methods

The transfer characteristics of a grating are of primary importance for a number of applications, for example, Bragg grating sensors [68]. The bandwidth, reflection profile, and phase response of gratings require special measurement techniques for proper characterisation. This section introduces some characterisation methods used in this work to measure grating parameters such as reflectivity and transmission spectra, and group delay spectra, etc.

4.7.1 Optical spectrum analysis

The reflectivity spectra of fabricated devices are examined using an optical spectrum analyser (OSA) characterisation setup as shown in Fig. 4.7(a). An amplified spontaneous emission source (ASE AFC™ BBS 1550 A-TS) with optical output over the telecom C-band (1525-1565 nm), or a combined multi super-luminescent diode source (SLED, Amonics™ ASLD-CWDM-5-B-FA) covering 1235-1645 nm, are used with the UV-written Bragg gratings designed for these wavelengths. The light is then fed into a circulator whose following port connects to the grating and the final port connects to an OSA (ANDO™ AQ6317B). The OSA acquires and displays spectral responses which can be connected to a computer using General Purpose Interface Bus (GPIB) hardware for data acquisition. A Gaussian fitting algorithm is applied to the spectra, as well as the central wavelength of each grating obtained. For transmission measurements no circulator is required as the light is transmitted through the waveguide and observed at the output with the OSA. The OSA parameters such as wavelength resolution and power sensitivity can be adjusted for the purpose.

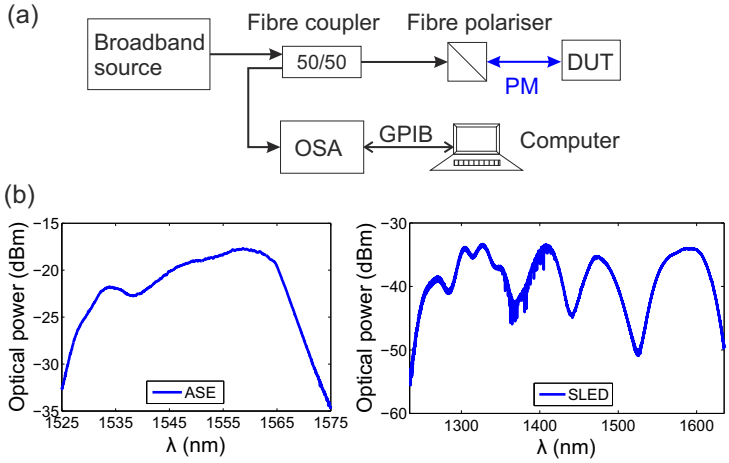

Figure 4.7: (a) Standard setup for optical characterisation using OSA; (b) Broadband source spectra of the ASE source and SLED source. DUT: device under test. PM: polarization maintaining. The noise observed near 1400 nm from SLED source corresponds to OH^- absorptions.

The polarization maintaining (PM) fibre is also used in the setup. Typical planar samples have birefringence, measured to be with Δn of $2-4\times10^{-4}$, which is believed primarily due to the material stress in the planar samples. Figure 4.7(b) includes the optical output spectra from the broadband ASE source and the broadband SLED source used in this work respectively. They do exhibit spectral features within their useable bandwidth. The coupling loss in the system also needs to be compensated. Several methods are used to normalise grating spectra.

- One way is taking the data from the broadband Fresnel reflection from the end-facet of the launched fibre. The spectrum is taken by disconnecting the sample from the circulator, leaving the fibre unconnected, and recording the $\sim 4\%$ Fresnel reflected spectrum with the OSA. The spectrum can then be used to normalize the background power for Bragg gratings. Fresnel reflected background spectra are also useful for exposing poor optical connections, or contaminated connectors. This method can then be used to produce the reflectivity of the device
- The second way is employing a saturated uniform grating for reference. The reference grating is located out of the useful spectral band and should have a $\sim 100\%$ flat-top reflection spectrum, *e.g.* the grating with $\kappa l = 2$ in Fig. 3.3. The grating spectrum should remain the 100% flat-top feature in the experiment hence the external loss can be estimated.
- The combination of these two methods will allow an accurate and convincing measurement of reflectivity and transmission spectra for the fabricated devices.

This measurement setup has been further investigated by the members of the research group, to measure and analyse the loss and dispersion characteristics of planar waveguide samples [108, 109]. More details about this technique can be found elsewhere [92].

4.7.2 Modulation phase-shift technique

The modulation phase-shift technique [110] is used to measure the relative group delay of the devices, with the setup schematically shown in Fig. 4.8. A tunable laser source (Agilent™ 81600B-201 Tunable Laser Source, TLS) is used to provide a polarized continuous source wavelength which can be swept over the region of interest spectra. The signal optical intensity is modulated by a sinusoid waveform at radio frequency (RF) through an EOM. The optical signal passing through the device under test (DUT) is detected by a high bandwidth photodiode (PD) and then sent for signal processing. The received RF waveform can be measured and compared with the original modulation waveform by using a RF vector network analyser (VNA, Agilent™ 8753ES S-parameter). PM fibre components are used throughout due to the birefringent effect of planar waveguide devices.

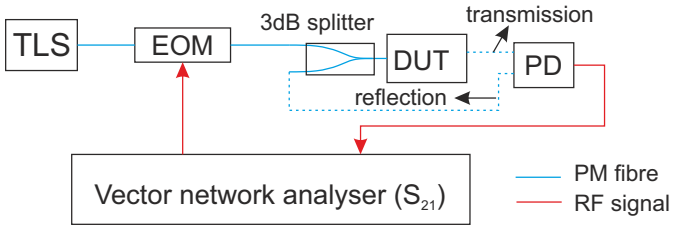

Figure 4.8: Experimental setup of measuring optical device characteristics with modulation phase-shift technique using a vector network analyser. It can be used to measure both transmission or reflection of the device.

The experimental setup shown in Fig. 4.8 is able to measure both the intensity transfer function and the relative optical group delay as functions of wavelength set by the tunable laser. Smaller wavelength tuning step-size ensures good frequency resolution of the measurement and the TLS is able to provide 0.1pm tuning step size in the 1260-1640nm wavelength range. In terms of measurement accuracy of the optical group delay response, a high modulation frequency would create a larger relative RF phase shift for a certain group delay difference. Therefore a high modulation frequency generally helps to ensure optical group delay measurement accuracy. However, since the measured group delay using modulation phase shift technique is an averaged value across the doubled modulation bandwidth, if the group delay varies significantly within this frequency window, the measured results will not be accurate [110]. In this work, the proposed device has an optical phase shift response which results in the steep optical group delay peak. Hence, an appropriate modulation frequency should be considered, and the effect on some measured results will be discussed in Chapter 6.

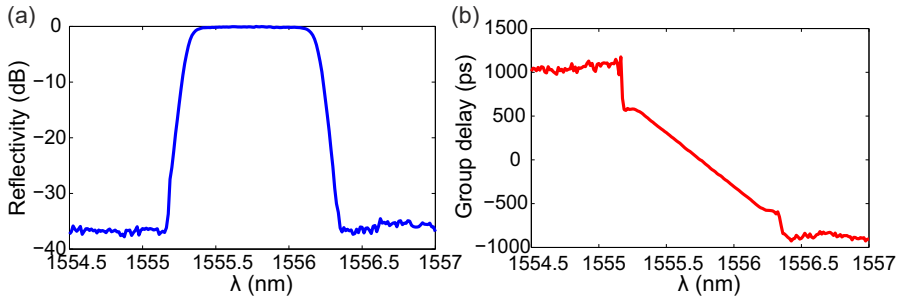

Figure 4.9: (a) The reflected power of a commercial dispersion compensation fibre Bragg grating; (b) the relative group delay spectrum of the FBG.

Figure 4.9 presents an example using the modulation phase-shift technique, the measured data of a commercial SPI™ dispersion compensation FBG. The reflected power of the FBG was shown in Fig. 4.9(a) with a flat top reflective window while the relative group delay data was illustrated in Fig. 4.9(b) with the dispersion rate around $-1300ps/nm$. The FBG devices have been widely used for dispersion compensation in the optical communication systems [7].

4.8 Conclusion

The background of the fabrication platform for planar integrated optical devices has been presented in this chapter. The planar waveguide structures and some materials are introduced. To fabricate the silica-on-silicon substrates in this work, PEVCD and FHD deposition processes are discussed. The photosensitivity mechanisms and enhancement via hydrogen loading are described, which is exploited by both the DUW and DGW techniques to define buried channel waveguide and Bragg grating structures. Advanced grating structures including apodised and phase-shifted gratings can be fabricated. The measurement techniques used to obtain device characteristics are also discussed. Further explanation of the specific DGW fabrication processes will be given in Chapter 5.

Chapter 5

Bragg grating engineering

5.1 Introduction

This chapter will explain the grating engineering work using direct UV grating writing (DGW) techniques. Explained in detail is the novel phase-controlled method of the DGW system which is an important part of the work in this thesis. The previous amplitude modulation method is reviewed with the interaction between control software, laser modulation and substrate translation described. To realise the novel phase-controlled method, a piezoelectric actuator was initially employed, and Bragg gratings were fabricated and characterised. Due to intrinsic artifacts of the piezo effect, electro-optic modulation was utilised as an alternative route to achieve the linear and accurate control in the arbitrary Bragg grating fabrication. This significant improvement of the UV writing technique also allows simpler, faster and more linear fabrication process of the entire system.

5.2 Amplitude modulation method

The DGW technique allows for the simultaneous definition of both channel waveguides and Bragg grating structures. The prior DGW setup comprises of an Acousto-Optic modulator (AOM) used to modulate the beam intensity, and a beam splitter and additional optics to create an interference pattern [84], as shown in Fig. 5.1. The precision air-bearing stage system is used to translate the sample underneath the beams, producing channel waveguides if no modulation is used, or Bragg gratings if the beam intensity is modulated.

The DGW system is controlled by a computer using a FireWire™ interface. The computer contains software that uses a set of programming language called 'G-code', which is part of the Computer Numerical Control (CNC) machine tool language. G-code controls

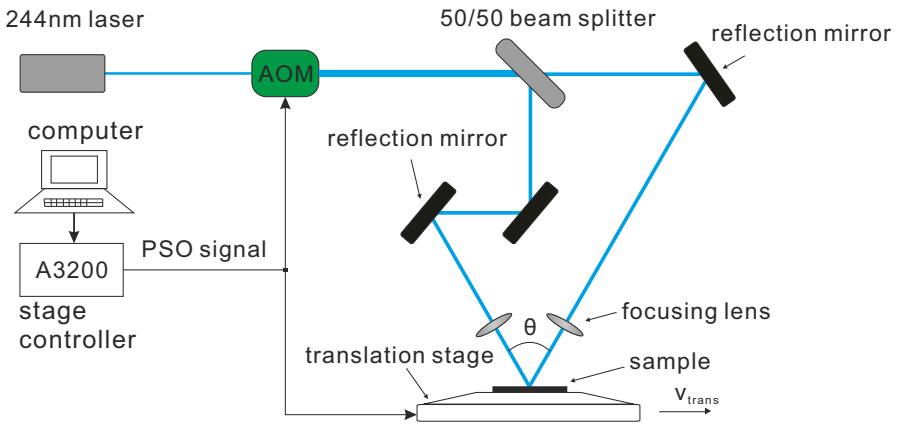

Figure 5.1: The schematic diagram of the direct UV grating writing system. PSO: Position synchronized output.

both the AOM and the movement of the stages holding the sample. These must be linked properly in order to define Bragg grating structures.

The computer program contains commands for both the movement of the stages and the firing positions for the AOM. These positions are uploaded as an array to an Aerotech™ A3200-npaq multi-axis machine controller prior to writing. Firing positions are where the Position Synchronized Output (PSO) from the A3200 changes state. In order to correlate the firing positions with the movement of the stages, as is needed for grating inscription, the A3200 acquires the position of the stage from a linear glass encoder on the Aerotech™ ABL9000 series air-bearing stage system. It then compares the current position to the positions defined in the array that was uploaded prior to writing. Once the positions correlate, the PSO output from the stage controller changes state. The PSO output is linked to the AOM and thus the AOM changes state. This allows the AOM to modulate the beam intensity as a function of stage position whilst the stages are being translated. The AOM diffracts the beam when switched on and leaves it unaltered when switched off. The changing of the stage's translation velocity can cause instability of the system.

In this setup the first order diffraction of AOM is used. Although the first order diffraction only diffracts a maximum of $\sim 80\%$ of the incoming beam power, it allows almost complete extinction of the beam when the diffraction is switched off. This is preferable to using the zero order which provides the maximum transmitted power but provides reduced contrast as it cannot fully extinguish the beam. The laser power is pulsed by the AOM which determines when the sample is illuminated with the interference pattern. The interference pattern is created by recombining the two beams after being split by an equally weighted beam splitter. One arm of the interferometer contains two mirrors in order to invert the beams pattern in that arm. This ensures that when the beams are recombined the interference patterns overlap, such that the spatial distributions of both patterns correlate. This produces an interference pattern onto the core layer of the

sample whose period is determined by the wavelength of light and the angle between the beams:

$$\Lambda_{spot} = \frac{\lambda_{UV}}{2\sin(\theta/2)} \tag{5.1}$$

with a writing wavelength of 244nm, and a crossing angle θ between the beams of about 26^o, the resultant spot has interference fringes with $\Lambda_{spot} = 542nm$. Therefore a focussed spot diameter of order $\sim 6\mu m$ would contain about 10 periods. The angle is chosen to allow fabrication of gratings that reflect around the standard telecom wavelength band. Comparatively, phase-mask based writing techniques used in FBG fabrication typically use the $\sim 100\mu m$ writing spot. Thus the DGW technique provides greater scope for modifying grating parameters, *e.g.*Bragg wavelength, when engineering a grating structure.

For the purpose of Bragg grating inscription, the AOM is pulsed at the correct period that produces an aligned overlap of successive interference fringes. However, as discussed earlier, if the angle between the beams is fixed and only perfectly aligned overlap is used, there will be only one possible writing wavelength. Therefore the interference pattern is slightly shifted such that the grating period is not fixed by the interference pattern period [84]. Detuning (central wavelength shifting) is achieved by slightly altering the AOM firing position with respect to the sample translation speed. Detuning of interference fringes causes a weakened grating contrast, but not sufficiently so as to cause significant degradation of the grating response [111]. This is because the beam diameter and therefore the number of fringes in the beam are small (~ 10). The range of detuning will be discussed later.

5.2.1 Duty cycle

Duty cycle provides a control of grating index contrast. In the amplitude modulation system, this is analogous to pulse width, as shown in Fig. 5.2. Duty cycle represents the ratio of laser on time to laser off time for a single grating period. Consider a grating to be made up of alternating high and low index grating planes. The duty cycle is a measure of the width of the high index planes relative to the low. For a uniform grating the frequency of the UV modulation is constant but the proportion of time that the laser is on during each modulation may be varied. The duty cycle is the fraction of each modulation period that the laser is on. Therefore, a 100% duty cycle is equivalent to the laser always on and 0% results in the laser remaining off. All values between these extremes produce a modulation of refractive index.

Prior work [63, 84] has shown that the grating index perturbation and spectral bandwidth can be controlled through the variation of duty cycle. For a given UV exposure level, higher percentage duty cycles provide greater refractive index change whilst lower values result in a reduced index perturbation.

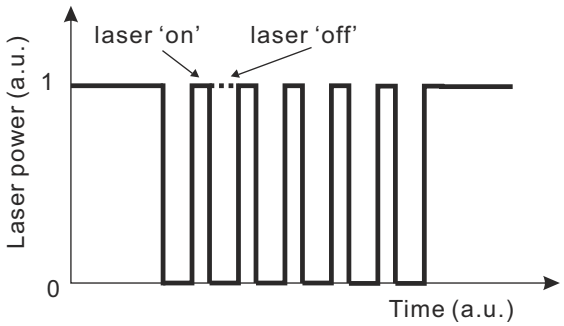

Figure 5.2: The concept of duty cycle: the time the laser spends in the on state, as a percentage of a complete cycle.

In fact, the refractive index contrast does not have an exactly linear variation with the duty cycle change. To explore this, more experiments have been done in this work, with some data show in Fig. 5.3. A series of 18 waveguide channels were fabricated in a single W5 wafer chip (the term W5 means the serial number of wafers and specifics are included in Appendix C); each waveguide contains a 0.5mm uniform grating with duty cycle changing from 0.1 to 0.9 and the same reference grating. Introducing the reference grating is to diminish the adverse effects from coupling loss in the characterisation and non-uniform materials in the samples. The reflection curves of these uniform gratings were fitted to Matlab™ code for Bragg gratings and from the peak reflectivity the Bragg grating maximum refractive index change Δn values were calculated. The relationship between Δn and duty cycle is shown in Fig. 5.3. The measured value of refractive index change intimately depends on to the DGW setup and samples.

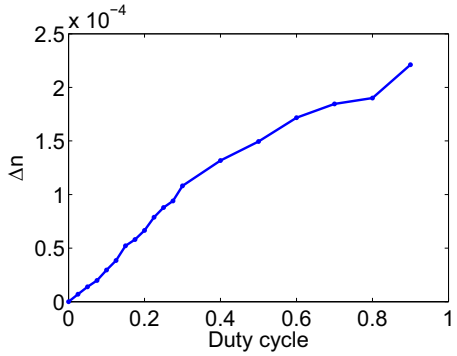

Figure 5.3: Refractive index variation as a function of duty cycle.

The nonlinearity curve shown in Fig. 5.3 is a critical issue for this work. The AOM modulates the beam intensity as a function of stage position (PSO signal) whilst the stages are being translated. The AOM diffracts the beam when switched on and leaves it unaltered when switched off (duty cycle). When creating the apodised gratings, the duty cycle alters rapidly and subtly during the writing process. It's not absolutely certain that the output modulated laser after AOM will exhibit the same duty cycle value, because of instability in the diffraction strength due to thermal fluctuations, and

the voltage-diffraction strength response of the AOM being non-linear and containing hysteresis [63]. The nonlinearity may also originate from the fluence matching in the system, which is discussed in the next subsection.

5.2.2 Fluence matching

The system has demonstrated the ability to write both buried channel waveguides and Bragg gratings simultaneously. However, as the grating uses pulsed illumination for the grating and continuous illumination for the waveguide the two sections will be exposed to different average light intensities. Due to the photosensitivity of the germanium doped sample this leads to different average refractive index changes. This issue is known as a 'fluence mismatch'.

Fluence mismatch will cause undesirable grating responses. One of the fundamental properties governing a grating's response is the effective refractive index, not only of the grating but also of the channel waveguides leading to the grating. Gratings have a channel waveguides attached to either end to provide coupling, ideally there should be no abrupt transition between the two components to avoid unwanted Fresnel reflections. As explained by Fourier theory, the spatial components of a waveguide structure can be converted into their corresponding frequency components. Bragg gratings are defined by their spectral response which is determined by the spatial properties of the grating planes. When the laser power is pulsed to produce gratings, the effective fluence reduces because the substrate is not continuously exposed. Therefore if all other parameters are identical for both waveguides and gratings, the effective refractive index will not be constant and there would be a fluence mismatch causing unwanted spectral features, similar to FBGs with a nonuniform 'dc' index change [61, 112].

Due to the discussion above, the gratings therefore need to be fluence matched to the waveguides such that both components have the same effective refractive index. In the previous DGW fabrication setup, fluence matching was achieved by adjusting the diffraction strength of the AOM. The AOM would be fed digital data determining the on/off firing positions, and an analogue signal to control the diffraction strength. However, this method is slow as the AOM is continually fed analogue data along the grating length. Other problems included instability in the diffraction strength due to thermal fluctuations, and the voltage-diffraction strength response of the AOM being non-linear and containing hysteresis. An alternative way was the system controlled the translation speed to change the fluence. This also avoids any impedance mismatch between waveguide and grating, and also reduces error in the grating strength profile. An example of impedance control is shown in Fig. 5.4. With the writing power normalized to unity for a channel waveguide, it can be seen that the average writing power is 50% for a fully modulated beam (duty cycle 0.5) during grating inscription. The translation speed would therefore reduce to 50% in order to obtain fluence matching.

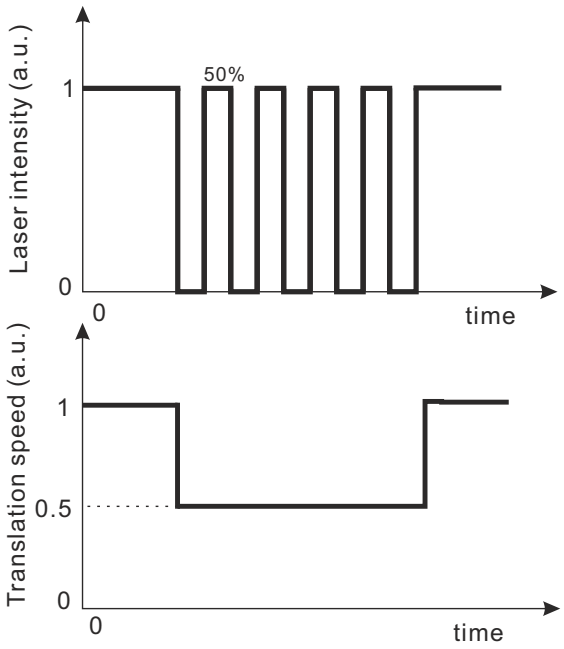

Figure 5.4: Control of UV writing speed (translation speed) and laser intensity for fluence match between waveguides and the grating section.

As mentioned above, The key component in the conventional method for grating engineering is the AOM. Advanced grating properties such as chirp, phase shifts, and apodisation were introduced by adjusting the duty cycle and phase offset of AOM, in terms of the writing laser intensity and the writing speed. But there are several drawbacks in this method:

1. The apparent modulation linearity. PSO signals control translation stage speed and the AOM state (which determines the beam intensity) simultaneously. When creating complex gratings, the duty cycle and PSO will alter rapidly and subtly during the writing process. Often the UV laser density exposed to certain area of samples will not exhibit the same performance as designed. That is because of thermal fluctuations from RF heating, hysteretic and nonlinear features of AOM and the vibration ($\sim 10nm$) of stage calibration. This issue could lead to the nonlinear results shown in Fig. 5.3.

2. The fabrication process is time /energy consuming. In the past, fluence matching was achieved by adjusting the diffraction strength of the AOM and the stage velocity. The first order diffraction beam with less than 80% power was used. The AOM was fed digital data determining the on/off firing positions, and an analogue signal to control the diffraction strength. The average writing speed was slow as the AOM was continually fed analogue data along the process.

3. Variation of the instantaneous writing speed. When the duty cycle is small for slight refractive index change, the writing speed becomes correspondingly low due

to the need to fluence match. In this case, the precision of the air-bearing stage may be degraded because of the cumulative effect of the inevitable stage fluctuation. In addition longer writing time causes out gasing problems with hydrogen loading.

4. Heating of samples. As the sample translation speed changes so does the injected energy hence temperature, this also degrades grating performance.

This work in this chapter presents and demonstrates a novel method that overcomes these problems by introducing the phase-control method into the current DGW setup, the interference pattern intensity is exclusively controlled by the phase differences between the two coherent arms of the laser beam. Similar concepts were elsewhere proposed [113–115], which related to the fabrication of advanced FBGs.

5.3 Piezoelectric actuator based phase control

The first route attempted to implement phase control used piezoelectric actuators.

5.3.1 Piezoelectricity background

The piezoelectric effect was discovered by Jacques and Pierre Curie in 1880. They found that if certain crystals were subjected to mechanical strain, they became electrically polarized and the degree of polarization was proportional to the applied strain. The Curies also discovered that these same materials deformed when they were exposed to an electric field. This has become known as the inverse piezoelectric effect. The history of piezoelectric developments could be found elsewhere [116].

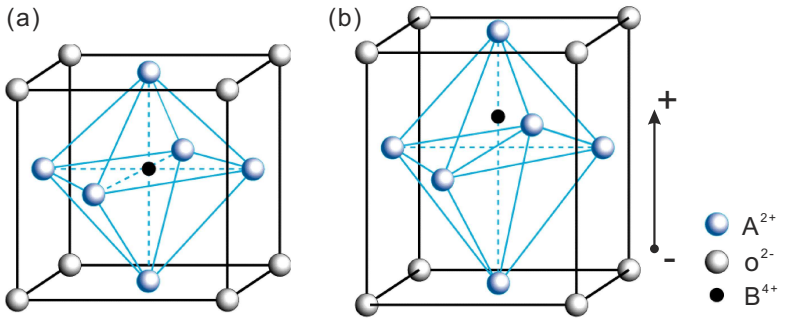

Figure 5.5: Piezoelectric elementary cell: (a) Cubic lattice (above Curie temperature); (b) tetragonal lattice (below Curie temperature).

Simply speaking, the piezoelectric effect is exhibited by a number of naturally-occurring crystals, *e.g.* quartz and tourmaline, and these have been used for many years as electromechanical transducers. For a crystal to exhibit the piezoelectric effect, its structure should have no centre of symmetry. A stress (tensile or compressive) applied to such

a crystal will alter the separation between the positive and negative charge sites in each elementary cell leading to a net polarization at the crystal surface. The effect is practically linear, *i.e.* the polarization varies directly with the applied stress, and direction-dependent, so that compressive and tensile stresses will generate electric fields and hence voltages of opposite polarity. The mechanism is also reciprocal. If the crystal is exposed to an electric field, it will experience an elastic strain causing its length to increase or decrease according to the field polarity.

Besides the crystals mentioned above, an important group of piezoelectric materials are the piezoelectric ceramics. These are poly-crystalline ferroelectric materials with the perovskite crystal structure - a tetragonal/rhombahedral structure very close to cubic, shown in Fig. 5.5. They have the general formula $A^{2+}B^{4+}O^{2-}$, in which A denotes a large divalent metal ion such as barium or lead, and B denotes a tetravalent metal ion such as titanium or zirconium. Above a temperature known as the Curie point, these crystallites exhibit simple cubic symmetry, the elementary cell of which is shown in Fig. 5.5(a). This structure is centrosymmetric with positive and negative charge sites coinciding, so there are no dipoles present in the material [117]. Below the Curie point, however, the crystallites take on tetragonal symmetry in which the positive and negative charge sites no longer coincide (Fig. 5.5(b)), so each elementary cell then has a built-in electric dipole which may be reversed, and also switched to certain allowed directions by the application of an electric field. Such materials are termed ferroelectric because this electrical behavior presents a physical analogy with the magnetic behavior of ferromagnetic materials [117].

5.3.2 Piezo actuator and the UV writing setup

In this work, the P-016.10 PICA™ stack actuator from Physik Instrumente (PI) was purchased and implemented. The piezo actuator was glued with a reflection mirror and fitted into our interferometric UV writing board.The image was shown in Fig. 5.6.

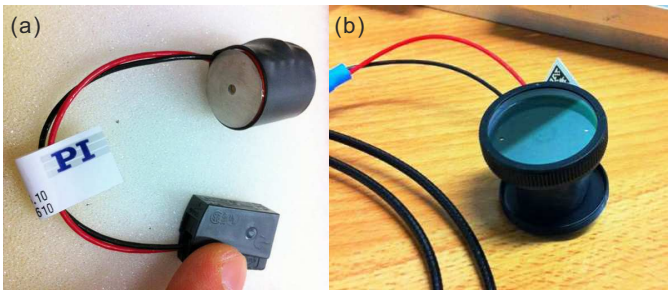

Figure 5.6: (a) The applied piezo actuator from Physik Instrumente; (b) the piezo actuator attached with a reflection mirror.

The PICA™ piezo actuator was chosen due to the maturity of products and was specifically designed for high duty-cycle applications [117]. The combination of high displacement and low electrical capacitance provides for excellent dynamic behaviour with reduced driving power requirements. The device specifications are listed in Table 5.1. To accomplish the phase modulation, a reflection mirror in one beam path in Fig. 5.1 is

No.	Displacement	Diameter	Length	Blocking force	Stiffness	Capacitance	Resonant frequency
P016.10	$15\mu m$	$16mm$	$17mm$	$4600N$	$320N/\mu m$	$180nF$	$59kHz$

Table 5.1: The piezo actuator technical specification.

replaced by the piezo mirror in the UV interferometer and the AOM is excluded. Driven by the applied voltage, a translation of the piezo mirror, introduces a phase shift between the interfering beams, which shifts the fringe pattern intensity at the focus point. The experimental setup is illustrated in Fig. 5.7. In this configuration the writing stage will move in a constant fast speed during the whole waveguide channel, including any Bragg gratings which alleviates the drawbacks such as sampling heating, the stage vibration and time/energy consumption.

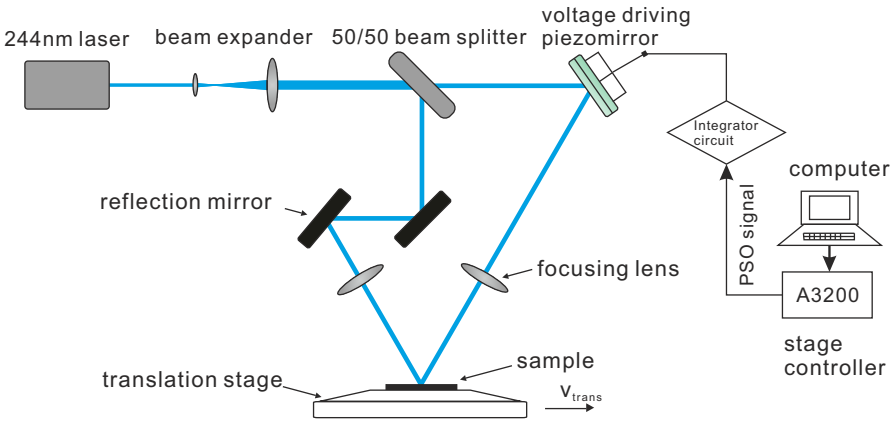

Figure 5.7: The direct UV grating writing system using piezoelectric phase-control method.

5.3.3 Sawtooth driving voltage

Since the piezo elements cannot move a long distance, they are fed with a sawtooth signal so that the fringes follow the sample over a certain distance, typically one grating period, schematically shown in Fig. 5.8. At the end of the voltage ramp in each period the fringes jump back to the original position. During this short moment the sample is evenly exposed, giving a slight increase in dc index change. Each new period of the sawtooth signal results in a new sub-exposure of the sample, corresponding to the new sub-grating in earlier sequential methods. Similar concepts were implemented for FBG fabrication [113].

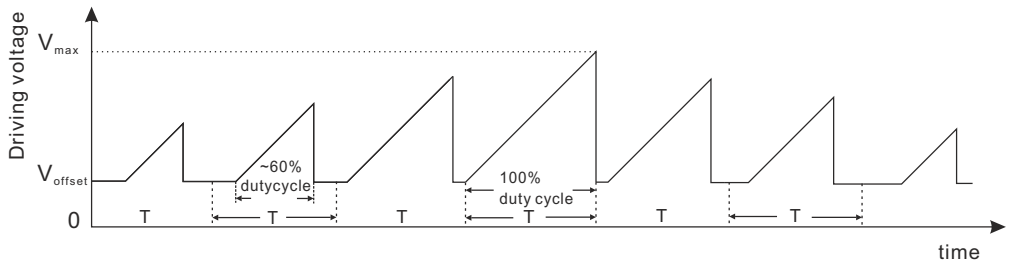

Figure 5.8: The sawtooth waveform used to drive the piezo mirror for an apodised grating. T is the time interval for a grating period. The offset voltage V_{offset} ($\sim 1V$) is considered to obtain better phase-shift responses of the piezo actuator.

For simple un-chirped and un-apodised gratings all exposed fringes are in phase and the sawtooth jumps appear at the same integral number of grating pitches throughout the writing process. Advanced grating properties including chirp, phase shifts, and apodisation could be implemented by changing the piezo voltage. Adding a (positive) phase shift, *e.g.* for distributed-feedback structures, merely corresponds to delaying the jump somewhat. The interference pattern will then follow the sample a little bit longer than otherwise at the position of the phase shift and make a correspondingly larger jump back. Figure 5.9 illustrates an example of the instant change of the piezo driving voltage for writing the π phase-shift Bragg grating, captured from the Tektronics™ oscilloscope. The signal channel 1 (the bottom trace) is the applied voltage signal, which is controlled by the PSO signal (the upper trace).

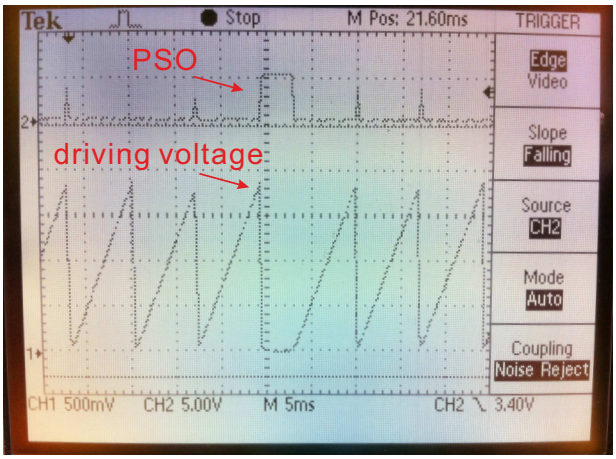

Figure 5.9: The phase-shift trace image captured from Tektronics™ oscilloscope during the π phase-shift grating writing.

As for the apodised grating, the sawtooth triangle pattern will alter for each period, shrunk to some extent compared to the full period pattern (Fig. 5.8). The diminished ratio is determined by the value of apodisation profile (duty cycle value). The firing position (central ramp position) should remain the same in each period; otherwise the grating period will have local variation and would lead to unwanted grating chirp.

The piezo mirror is located such that a small translation will change the path length of the interferometer arm. However, the consequence of retaining the simple optical arrangement in Fig. 5.7 is that the beam will also undergo a lateral translation. The displacement of the focused point on the sample becomes few nanometers, which is ignorable compared to the interference fringe period of $\sim 530nm$.

5.3.4 Driving circuit design

The entire grating structure is determined by the positions of the ramps, *i.e.* the sign reversions of the sawtooth signal. These positions are calculated in advance by the computer and fed into the electronics control hardware (the PSO system) that produces a digital signal when the desired positions are reached. To convent the digital signal to a ramp, an electronic integrator is utilised [118].

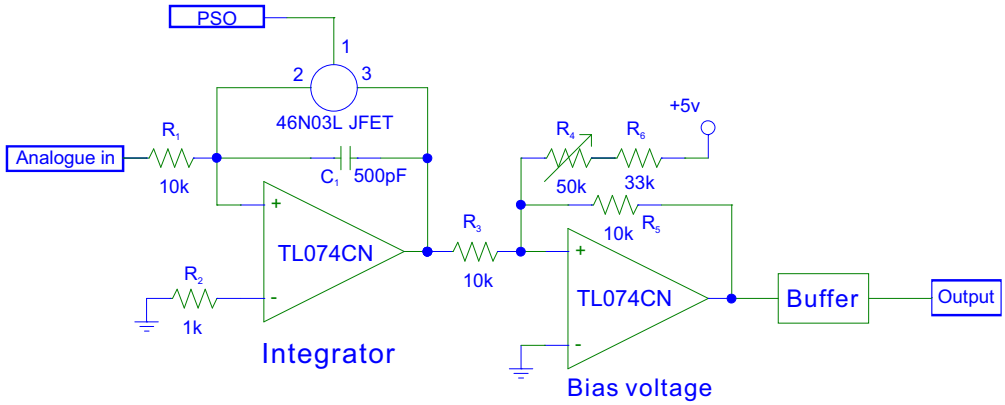

Figure 5.10: Schematic circuit diagram of the designed integrator. The output voltage is linked to the piezo mirror. A buffer amplifier is used to provide electrical impedance matching.

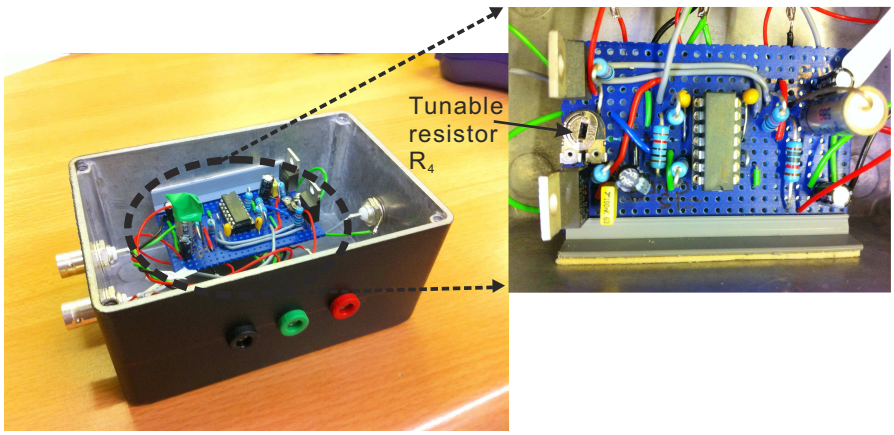

Figure 5.11: the photograph of the integrator box in the DGW setup. The tunable resistor R_4 is used to adjust the bias voltage.

Figure 5.10 shows schematic circuit diagram for the integrator and Fig. 5.11 shows photographs of the integrator circuit used in the DGW setup. The TL074CN Quad Low-Noise JFET-Input operational amplifier was used in the circuit. The bias voltage was set to 1V, and could be adjusted by the tunable resistor R_4. Both the PSO signal and the input analogue signal are generated by the Aerotech™ A3200 controller. The JFET switch in Fig. 5.10 discharges the capacitor C_1 when the PSO signal is on. A buffer amplifier is also used to supply sufficient current from a first circuit, having a high output impedance level, to a second circuit with a low input impedance level. The interposed buffer amplifier prevents the second circuit from loading the first circuit unacceptably and interfering with its desired operation [119].

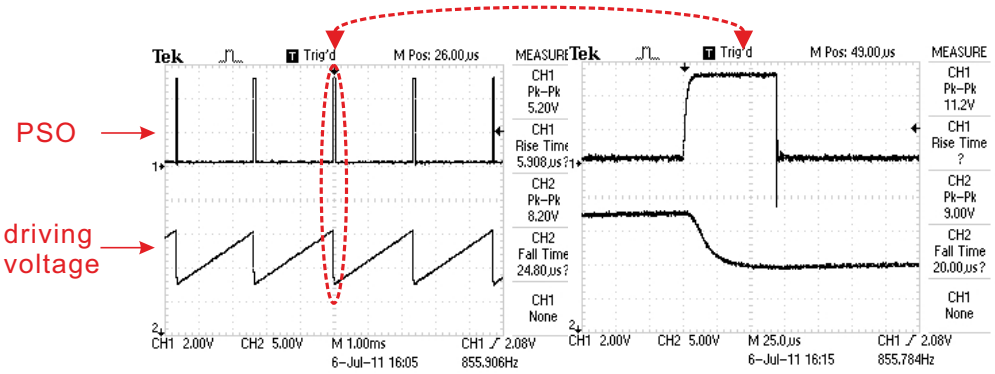

Figure 5.12: Signal traces captured from Tektronics™ oscilloscope and the partially enlarged image showing the slew rate of the system when driving the piezo.

Figure 5.12 shows captured images from Tektronics™ oscilloscope. The capacitor C_1 was $\approx 500pF$ to provide a suitable time constant for the 0-10 volts analogue signal from the PSO.

5.3.5 Bragg grating responses

This setup was utilised to make uniform and apodised gratings, and the variation of Δn with duty cycle curve was investigated, similar to the duty cycle test in Section 5.2. The W5 sample wafer and fluence of $10kJ/cm^2$ were selected in this experiment (specifics in Appendix C). Figure 5.13(a) illustrates the schematic of a waveguide channel in the chip. A 0.5mm uniform grating with the central wavelength of $\sim 1530nm$ is included for characterisation reference, a 12mm phase-shifted and apodised grating with the central wavelength of $\sim 1550nm$ is implemented for the PHT, and a 0.5mm uniform grating with the central wavelength of $\sim 1570nm$ was utilised for duty cycle test. The grating reflection spectra are shown in Fig. 5.13(b). This measurement was taken by comparison with the 4% end facet reflection, as described in Section 4.7. Fig. 5.13(c) shows the grating maximum refractive index change as a function of duty cycle.

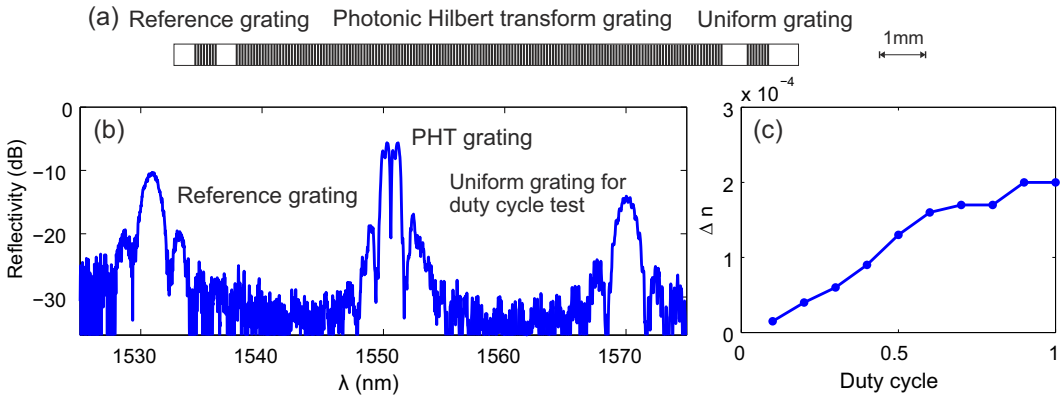

Figure 5.13: (a) Schematic of a fabricated waveguide channel containing gratings in the chip; (b) reflectivity spectra of the Bragg gratings;(c) the Δn variation with duty cycle.

The uniform gratings yielded smooth symmetric spectra with sidelobe features as expected. Unfortunately, the more complex grating (*e.g.* PHT) did not work so well, displaying large side lobes and ripples on the expected flat-top response. The suspected cause was a nonlinear relationship between the designed apodisation profile and the translation of the interference intensity pattern. Using the peak reflectivity of the uniform grating the transfer function of the fabrication system was obtained, as shown in Fig. 5.13(c), and confirmed the suspicion. Consequently, a Michelson interferometry experiment was conducted to calibrate the translation of the piezo actuator.

5.3.6 Michelson interferometry and piezo hysteresis

In a free-space Michelson interferometer [110], a partially reflecting mirror (50/50) is used to split the input optical beam into two parts. After traveling a distance, each beam is reflected back to recombine at the partial reflection mirror. The interference between these two beams is detected by the photo-detector. The mirror with piezo actuator is used as one of the retro-reflecting mirrors and can be scanned to vary the interference pattern, shown in Fig. 5.14. Figure 5.14(a) shows the basic configuration of the free-space Michelson interferometer and Fig. 5.14(b) shows the experimental setup on an optical table.

Assuming that the input optical field is E_i, the power-splitting ratio of the coupler is α, and the optical lengths are L_1 and L_2 for the two arms, then the optical field reaches the receiving photo detector is

$$\begin{aligned} E_0 &= \sqrt{1-\alpha}\sqrt{\alpha}E_i[e^{j(2\beta L_1+\varphi_1)} + e^{j(2\beta L_2+\varphi_2)}]e^{j\omega t} \\ &= 2\sqrt{1-\alpha}\sqrt{\alpha}E_i e^{j[\beta(L_1+L_2)+\frac{\varphi_1+\varphi_2}{2}]}e^{j\omega t}\cos(\beta\Delta L + \frac{\varphi_1-\varphi_2}{2}) \end{aligned} \tag{5.2}$$

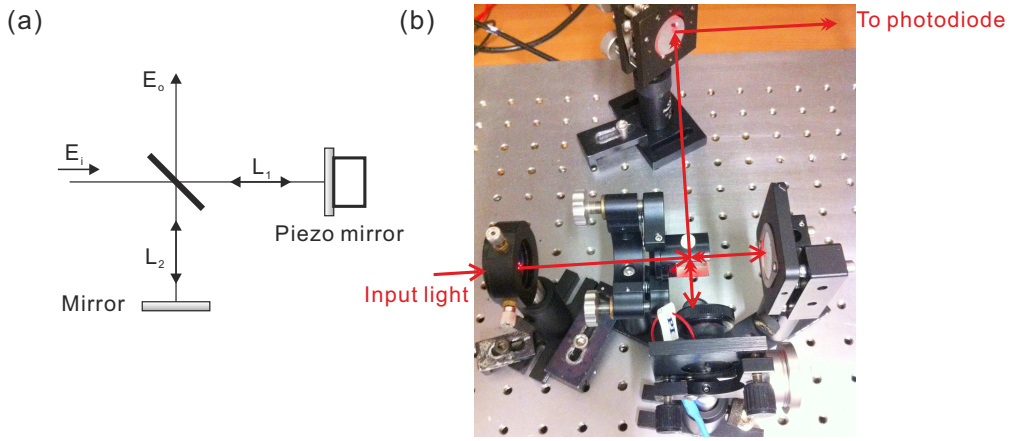

Figure 5.14: (a) Schematic of the basic configuration of the Michelson interferometer;(b) a photograph of the experimental setup.

where $\beta = 2\pi n/\lambda$ is the propagation constant, n is the refractive index, $\Delta L = L_1 - L_2$ is the path length difference between the two arms, and ω is the optical frequency. φ_1 and φ_2 are the initial phase shift of the two arms, which can be introduced by the beam splitter as well as the reflecting mirrors.

Since the photodiode is a square-law detection device, the photo-current generated by the photodiode is directly proportional to the optical power:

$$I = \mathcal{R}|E_0|^2 = 2\alpha(1-\alpha)P_i\mathcal{R}[1+\cos(2\beta\Delta L + \Delta\varphi)] \tag{5.3}$$

where $\mathcal{R}$ is the detector responsivity and $\Delta\varphi = \varphi_1 - \varphi_2$ is the initial phase difference between the two arms when $\Delta L = 0$. Obviously, if the path length of one of the two arms is variable, the photo-current changes with ΔL.

In the experimental setup in Fig. 5.14(b), a He-Ne laser ($\lambda = 638nm$) is used and the piezo actuator is driven by a signal generator (Tektronics™ AFG 3021B). The intensity at a particular position of the interference pattern is received by the photo receiver and displayed on an electronic oscilloscope (ISO-TECH™ ISR635). In some of the frequency response measurement experiments below, a Lock-in Amplifier (STANFORD RESEARCH SYSTEM™ Model SR830 DSP LIA) is also used to reduce the measurement noise. A LabVIEW™ programme is used to control the signal generator, collect and analyse the data from the photo receiver. A range of experiments were conducted to investigate the properties of the piezo actuator.

5.3.6.1 Full range voltage sweep

To obtain the relationship between the piezo translation and driving voltage, a DC voltage (0-150 Volts) was applied to the piezo actuator and the intensity was monitored.

Fig. 5.15 shows the observed sine-like curve from the photo receiver. It can be seen that the period of the curve changed a small amount with the driven voltage. To analyse the data the photo-receiver responses were normalised and the photo diode voltage was converted to a displacement. The resulting data in Fig. 5.15(b) illustrates displacement as a function of the applied piezo voltage and clearly shows hysteresis of the response. This hysteresis curve is similar to the open loop hysteresis data of piezo actuators [117].

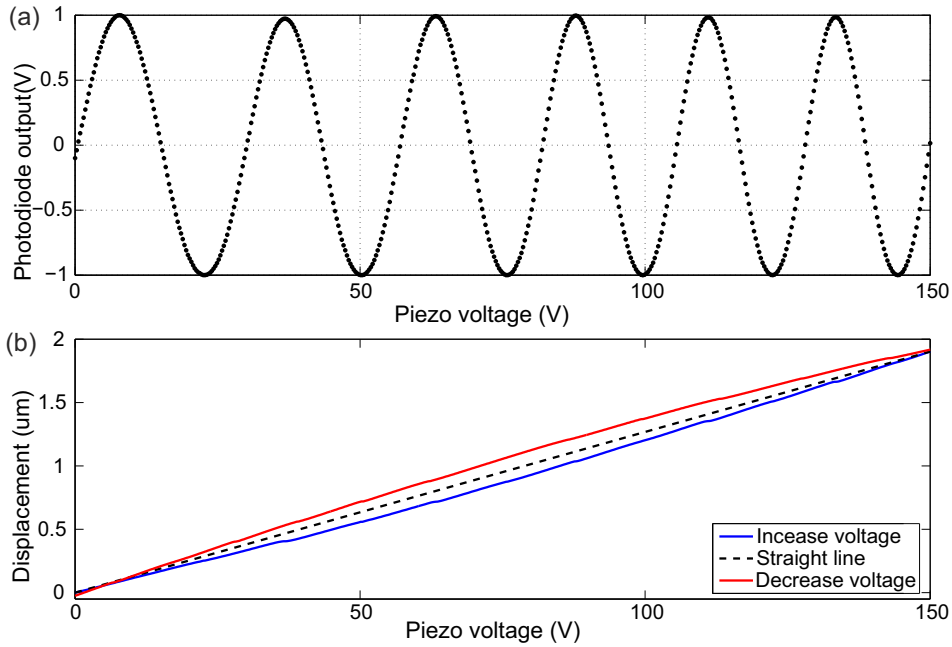

Figure 5.15: (a) Normalised photo receiver response when an increasing voltage is applied to the piezo transducer; (b) hysteresis curve of the piezo actuator, increasing voltage (blue solid line) and decreasing voltage (red solid line), a straight dashed line is shown for comparison.

Furthermore, this experiment was repeated by changing the speed of the applied voltage shown in Fig. 5.16. The response exhibited was very similar although small changes can be observed at the minimum and maximum voltages. This indicated a ramp dependent hysteresis effect [117].

5.3.6.2 Small range voltage with repeat sweep

In order to test the translation precision and stability of the piezo actuator in the interferometer, a small voltage range (0-21V) was applied and repeatedly tested ten times. It is calculated that the piezo displacement introduced by this similar range of driving voltages can lead to full period fringe modulation in the interferometric UV writing setup. Fig. 5.17(a) shows the interference pattern intensity plotted as a function of the driving voltage. Fig. 5.17(b) and (c) plot the displacements of the piezo mirror at the starting point (0V) and at the ending point (21V) respectively. The standard

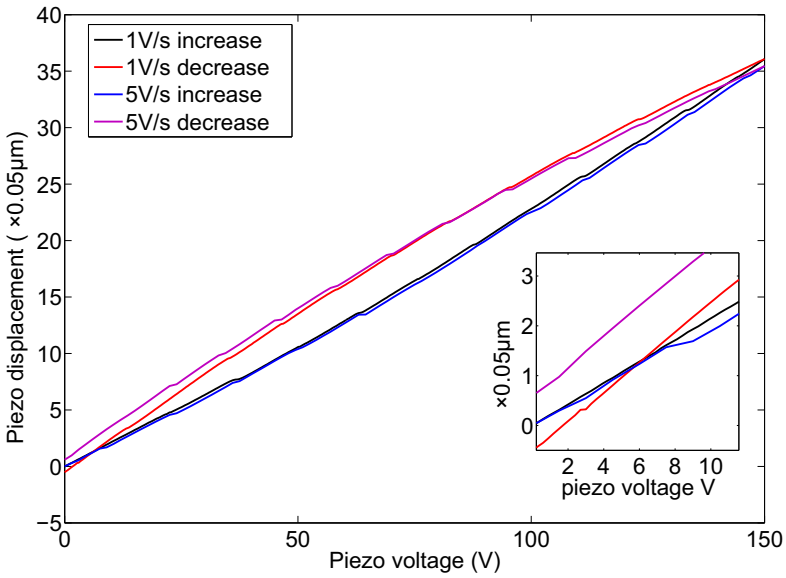

Figure 5.16: Hysteresis curves with slow (1V/s) and fast (5V/s) voltage variation. The insert shows the position shift at the initial point.

deviation of the piezo translations in this test is in order of few nanometers. As for the current Michelson interferometer in this experiment, the positional error of the piezo actuator is subtle.

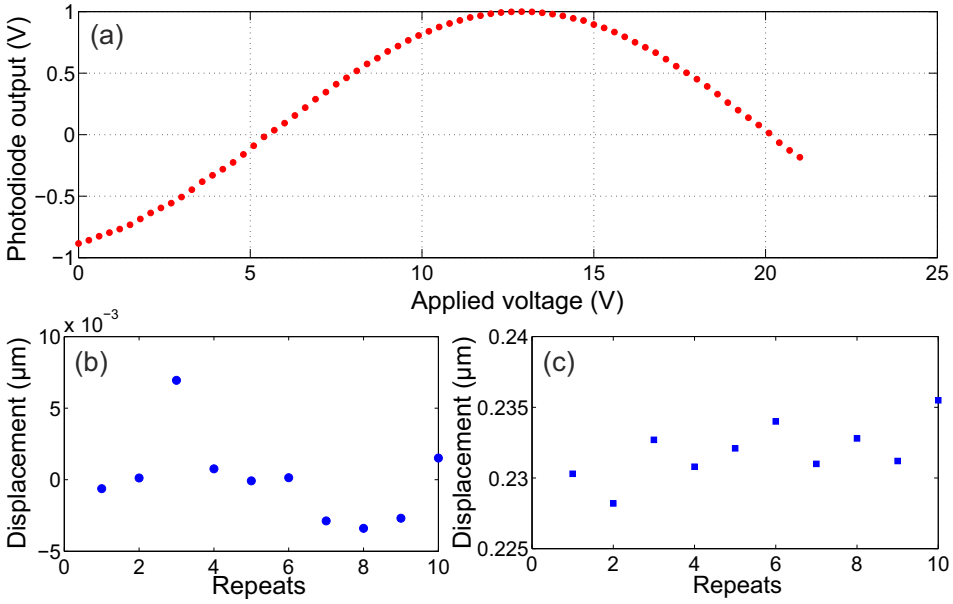

Figure 5.17: (a) The interference pattern intensity as a function of the driving voltage in the small range voltage test; (b) displacements of the piezo mirror at 0V, showing a standard deviation of $\sim 3nm$; (c) displacements of the piezo mirror at 21V, with the standard deviation of $\sim 2nm$.

5.3.6.3 Frequency response measurement

The frequency response of the piezo actuator was measured, and the results are shown in Fig. 5.18. The piezo actuator has a series of resonance responses due to the intrinsic features of the piezo ceramic, stacking structures and the mirror mount. The background noise response was also measured for comparison. In the phase-control DGW setup, the applied voltage is a sawtooth pattern, which contains many frequency components.

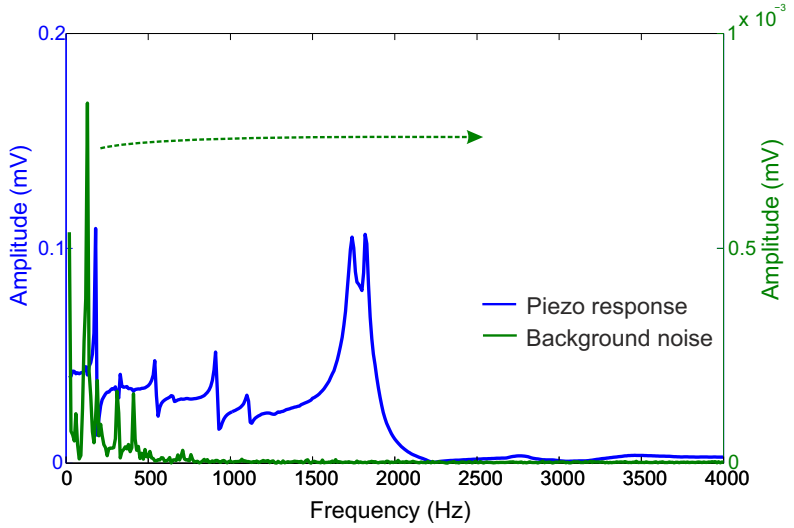

Figure 5.18: Frequency responses of the piezo actuator (blue) and background noise (green).

From the above experiments and analysis, we arrive at some conclusions.

- The current piezo actuator was fitted into the interferometric UV writing board, to modulate the optical path length of one arm and thus interference fringe intensity.
- The piezo mirror also has crosstalk with effects of the tilting, and pitch and yaw of the piezo mirror mount.
- The piezo actuator working currently under the open-loop control exhibits hysteresis and causes nonlinearity in the phase-control fabrication technique.
- The closed-loop piezo control provides elimination of hysteresis and creep effects, and good linearity of the piezo translation. However, it will reduce the operating bandwidths and add cost to the fabrication system.

Due to the above investigation and conclusions, the open-loop piezo based phase-control method does not meet with the requirements of this work. An alternate approach based on an EOM was proposed and demonstrated, and is discussed in the next section.

5.4 Electro-optic modulation based phase control

5.4.1 Electro-optic phase modulation background

A device is considered to be a modulator if its primary function is to impress information on a light wave by temporally varying one of its properties [10]. The fundamental phenomenon that accounts for the operation of most electro-optic modulators is the change in index of refraction produced by the application of an electric field. In the most general case this effect is non-isotropic, and contains both linear (Pockels effect) and nonlinear (Kerr effect) components. In crystalline solids, the change in refractive index produced by the linear electro-optic effect can be most conveniently characterised by the change in the components of the optical indices matrix [120].

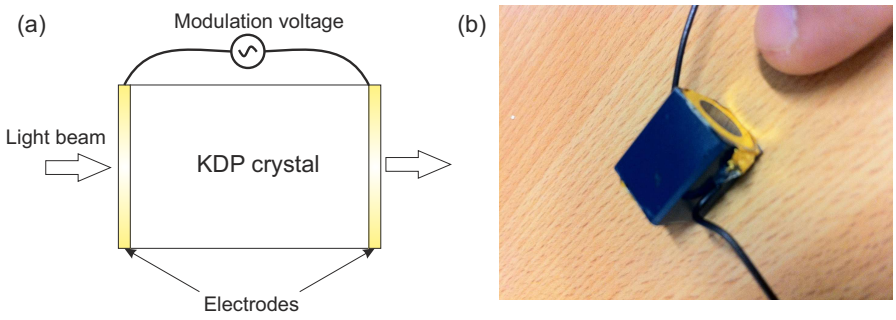

Figure 5.19: (a)The longitudinal EOM structure using KDP crystal; (b) the EOM used in the experiment.

In this work, the longitudinal phase modulator using Potassium Dihydrogen Phosphate (KH_2PO_4, KDP) is a common and simple electro-optic modulator, shown in Fig. 5.19. It consists of the crystal mounted between parallel electrodes at the optical path facets. Here, an electric field is applied along the KDP crystal z-axis. Light propagated along the z-direction experiences an index of refraction change, hence an optical path length change, that is proportional to the applied electric field. These modulators allow the use of large electric fields between the electrodes while simultaneously providing a long interaction length to accumulate phase shift. The phase of the optical field exiting from the crystal therefore depends on the applied electric field. Due to the symmetries of the KDP crystal uniaxial structure, the electro-optic tensor r_{ij} has only three non-zero elements.

For this to be used as a phase modulator the light must be polarized along the x or y axis. The phase shift due to the change in the refractive index is [120]:

$$\Delta\phi = \frac{\pi}{\lambda} n_0^3 r_{63} V L \tag{5.4}$$

where V is the applied voltage and L is the length of the modulator in the z-direction. Electro-optic and optical properties(r_{41}, r_{63} and n_0) of the KDP crystal can be found in

literature [121]. The half wave voltage V_P is also considered, which refers to a relative spatial displacement of one-half a wavelength, which is equivalent to a phase difference of π [120]. The measurement and characterisation of the EOM are presented in the following section.

5.4.2 Measurement and calibration using Michelson interferometry

Figure 5.20 shows a Michelson interferometer similar to that described in Section 5.3. In this arrangement the mirrors are all stable and the EOM is placed across one light beam of the setup. A He-Ne laser ($\lambda = 638nm$) is used and the EOM is driven by a high voltage amplifier (Trek™ 610E) which could provide DC voltage up to 10kV. The equipment proceed remains similar to the previous piezo actuator test.

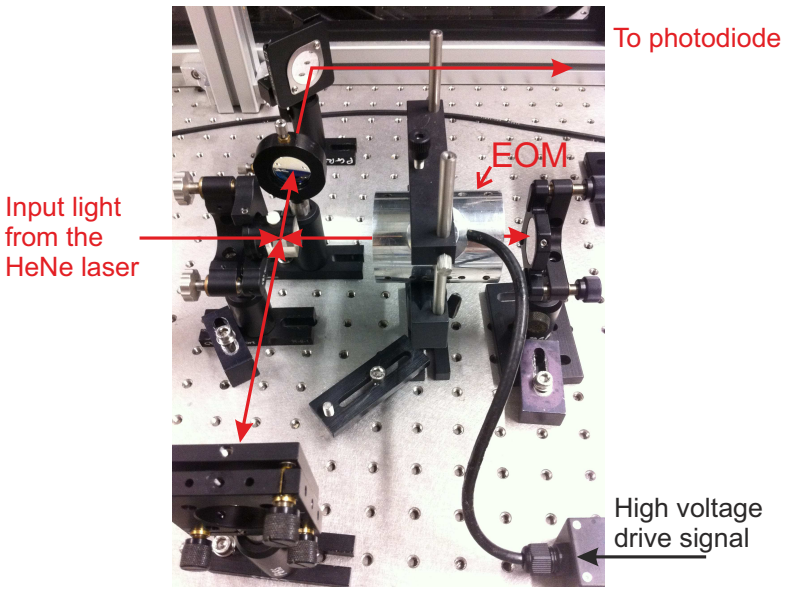

Figure 5.20: The experimental free-space Michelson interferometer to test the EOM. The red arrows indicate the route of the laser light.

For the longitudinal Pockels cell in its mount, the input laser polarization axis is aligned with the crystal principle axis. The isogyre pattern was observed during the rotation of the crystal along the UV light propagation direction and caused by interference of the divergent light at angles corresponding to directions at which an additional wavelength of path difference has been added by the birefringence of the crystal [122]. When the pattern is centered with a good extinction of the laser beam, the cell is axially aligned. If the pattern is off centre, the cell must be adjusted in altitude and azimuth until the pattern is centered.

Measurement results are shown in Fig. 5.21. The normalised output voltages of the photo receiver are plotted in Fig. 5.21(a) with the applied voltage increasing from 0V to 10kV. The linear trend in Fig. 5.21(b) shows the EOM demonstrates little hysteresis,

compared to the piezo actuator. The phase offset is believed due to the temperature and environmental variation. The frequency response of the EOM was interrogated as in Section 5.3 and the results are shown in Fig. 5.21(c). The amplitude has a relatively smooth response (compared to that in Fig. 5.18) and shows a 3dB bandwidth of approximately 2.6kHz. The frequency response of the EOM determines the linearity of the optical control in the UV writing setup and is crucial in the method.

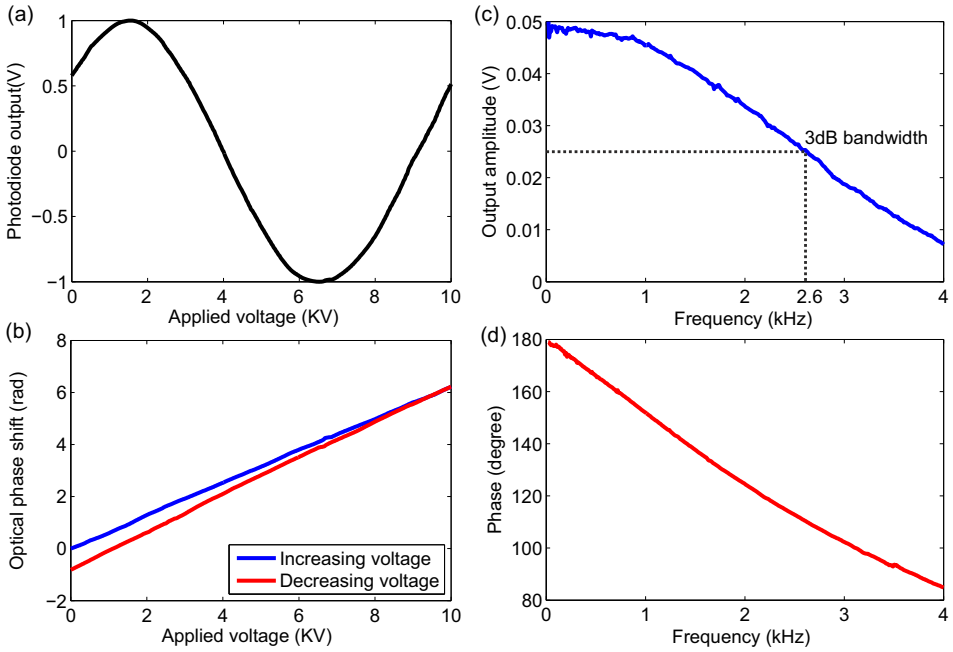

Figure 5.21: (a) The normalised photo receiver output voltage; (b) the corresponding optical phase shift with increasing (blue) and decreasing (red) driving voltage, with an effect of phase drift; (c) the amplitude response of the EOM; (d) the phase response of output signals as a function of drive frequency.

The KDP crystal (Fig. 5.22(a)) was removed from the original mounting (Fig. 5.20) and inserted into a in-house built mount shown in Fig. 5.22(b). This allowed anti-reflection coated UV windows to be used and a purge gas to prevent water ingress and degradation of the crystal. To confirm the suitability of this EOM for operation as the 244nm wavelength, a similar Michelson interferometer was constructed at 244nm wavelength and 2π phase modulation was observed, and an approximate calibration was obtained. The investigation also confirmed the crystal orientation.

The remounted EOM was placed in one arm of the interferometer within the UV writing system, as shown in Fig. 5.22(c). It should also be noted that the optical path lengths of the two arms of the interferometer were measured and equalised, accounting for relative refractive index, to minimise path imbalance. The integrator was modified as the offset voltage was no longer required.

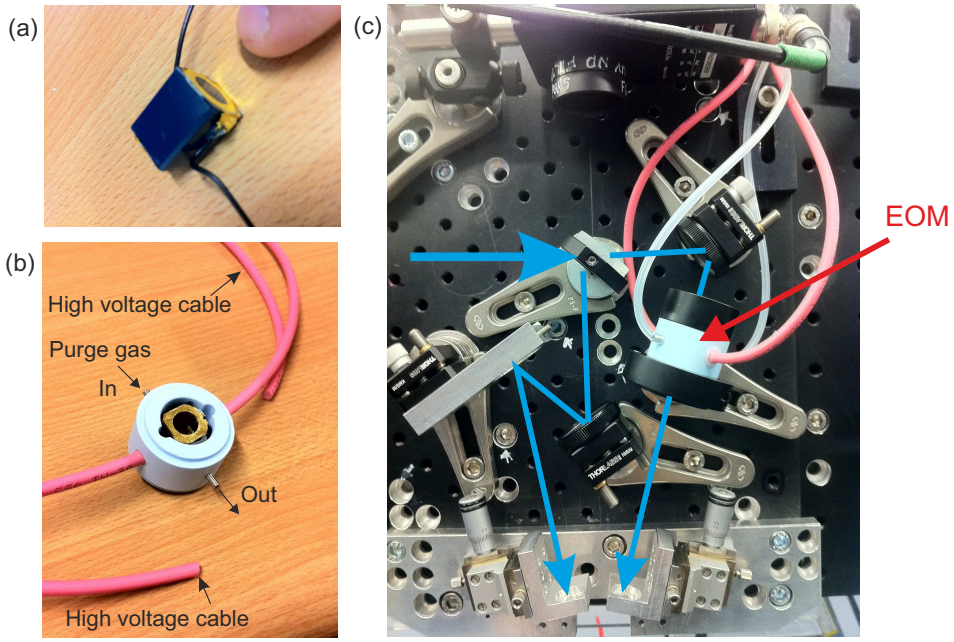

Figure 5.22: (a) The KDP crystal with electrodes;(b) the mounted EOM with purge gas ports;(c) the EOM mounted on the UV writing board with the interferometer structure, blue lines show the route of the UV laser beams.

5.4.3 High-voltage amplifier driving circuit configuration

The sawtooth signal from the integrator was fed to the high voltage amplifier (Trek™ 610E) to drive the EOM. The EOM capacity of 32 pF allows a sufficient slew rate. The insertion loss of the EOM at 244nm was measured to be 14% (0.75dB).

Negative over shoot was observed during the rapid high voltage operation (Fig. 5.23(a)), due to impendence mismatch and capacitive loads. The over shoot problem would potentially cause unwanted phase shift of the light and result in a nonlinear effect in the duty cycle. Through some investigations, this effect was reduced by a high voltage diode and load resist. The schematic circuit drawing is shown in Fig. 5.23(b).

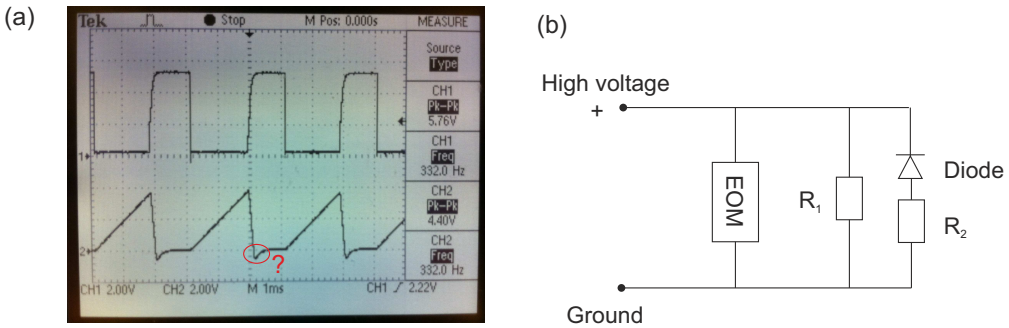

Figure 5.23: (a) The overshot issue observed from the oscilloscope; (b) the schematic circuit diagram to solve the problem.

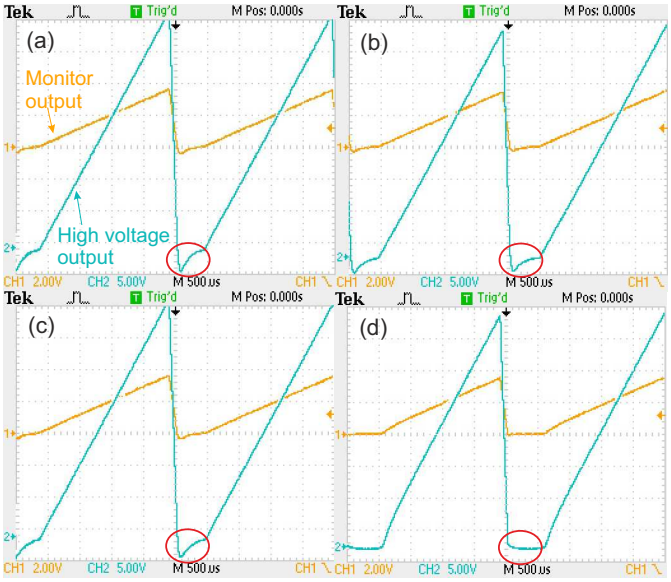

Figure 5.24: (a) The over shoot issue observed from the oscilloscope; (b) $10M\Omega$ resistance load R_1; (c) a diode in the circuit without R_1; (d) the outcome of the circuit configuration in Fig. 5.23(b).

Various configurations were investigated with some of corresponding responses for four configurations, shown in Fig. 5.24. After applying the configuration to the EOM driving circuit, the EOM based phase-control setup was utilised to fabricate Bragg gratings.

5.4.4 Direct UV grating writing with electro-optic phase modulation

After the electrical drive circuit was configured, trials of the direct UV grating writing with electro-optic phase modulation were conducted. A summary of results from this work in the following sections is the subject of a published journal paper [57].

A schematic of the phase control DGW setup is shown in Fig. 5.25(a) with the 3D illustrated in Fig. 5.25(b). Various Bragg gratings were fabricated via this method and the characterisation and analysis of grating responses are presented in the following subsections.

5.4.5 Grating responses analysis

In order to obtain the appropriate value for the EOM drive voltage for optimal grating response, a series of uniform and Gaussian apodised gratings were fabricated in a single chip (the W7 wafer) with increasing EOM drive voltage. A series of 1mm uniform gratings at 1550nm and 1mm Gaussian apodised gratings at 1565nm were fabricated, with the fluence of $12kJ/cm^2$. The waveguides were characterised to obtain the relevant grating parameters, in this case the maximum grating index contrast Δn. Figure 5.26(a)

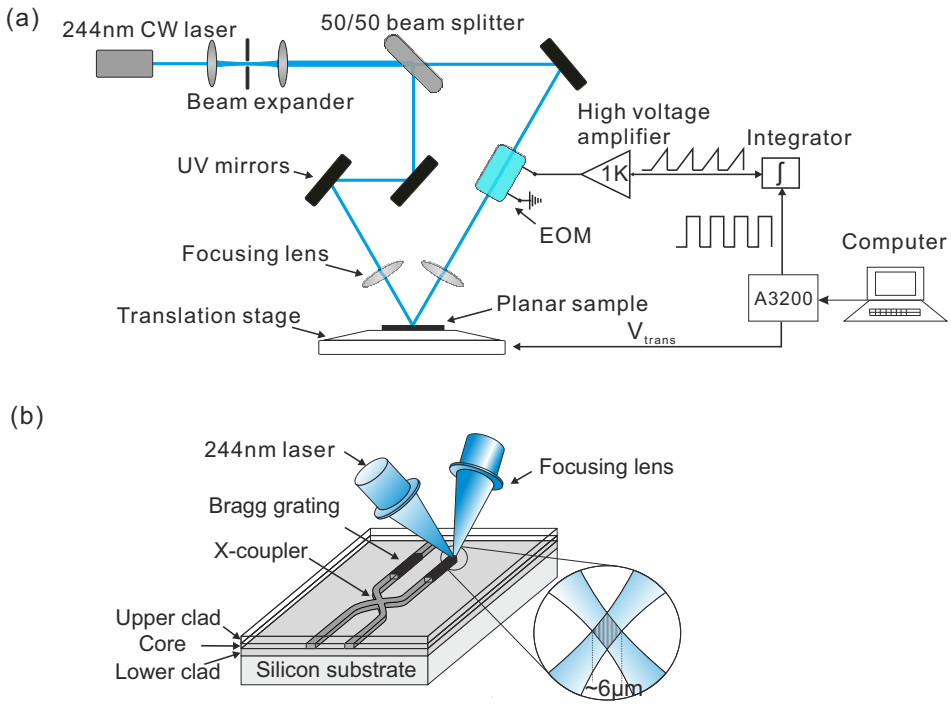

Figure 5.25: (a) The experimental setup of phase modulated direct UV grating writing technique; (b) the 3D illustration of the focused writing spot on the silica-on-silicon sample.

indicates that the peak refractive index change occurred at $V_p \approx 4.5kV$, which is the optimal voltage value for the process.

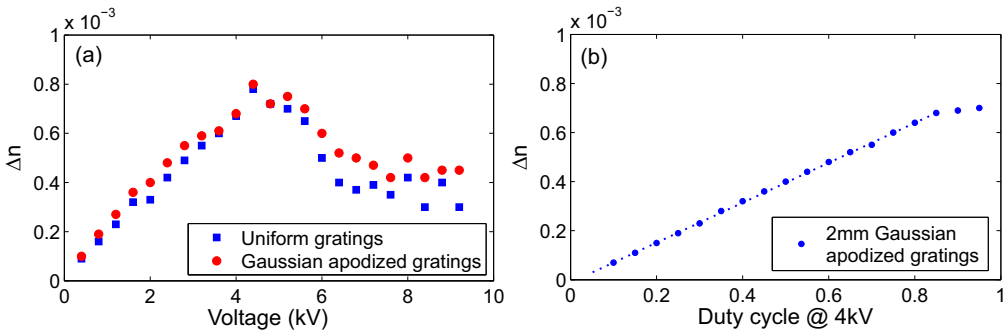

Figure 5.26: (a) EOM drive voltage test with uniform gratings (square) and Gaussian apodised gratings (circle); (b) Duty cycle linearity test using a maximum drive voltage of 4kV, with 2mm Gaussian apodised gratings.

When creating the apodised gratings, the duty cycle is altered throughout the grating to create the desired grating profile. In previously AOM or piezo actuator related DGW, the grating Δn did not track linearly with duty cycle value, due to thermal fluctuations and intrinsic nonlinearity of AOM (Fig. 5.3), or the hysteresis of piezo actuator (Fig. 5.13(b)). In Fig. 5.26(b), with the EOM based phase-control DGW system, the grating Δn behaves linearly with duty cycle variation between 0 and 0.8. The artifact above 0.8 is a result of the restricted slew rate of the high voltage amplifier. In the following data a duty cycle

of 0.8 is used at the maximum duty cycle. Using the same technique with $V_p = 4kV$, Δn of up to 1×10^{-3} have been observed in high photosensitivity samples.

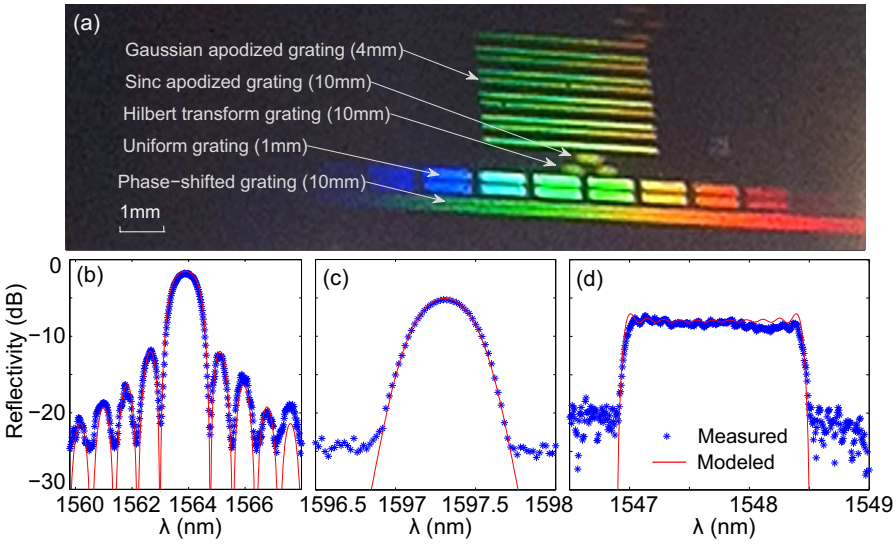

Figure 5.27: (a) A white-light source image of grating structures in a sample; (b) The reflectivity spectrum of the uniform grating: experimental data (star dot) and modelled data (red line); (c) Gaussian apodised grating; (d) sinc-apodised grating.

Figure 5.27(a) shows a photograph of the surface of a planar device containing about 20 waveguides with Bragg gratings, including uniform, Gaussian, sinc apodised, Hilbert transformers [123], and phase-shifted gratings [124]. The different colors are due to incident angle dependence of the white light scattered from the inscribed gratings. Figure 5.27(b)-(d) show the simulated reflectivity data (red line) and measured data (blue stars) of a 1mm uniform grating, 4mm Gaussian apodised grating and a 10mm sinc apodised grating respectively, with the maximum Δn of 6×10^{-4}. The gratings were characterised using an OSA and a broadband source, as described in Section 4.7.1. In Fig. 5.27(c), the Gaussian apodised grating has -5dB peak reflectivity and $> 20dB$ sidelobe suppression which is limited by the characterisation. In Fig. 5.27(d) the sinc-apodised Bragg grating compromises of multiple phase shifts along the grating structure and has a nearly flat-top reflection response with $\sim 200GHz$ bandwidth, sharp-cut edges and $\sim 1dB$ ripple on the top. Such gratings are used later to produce optical band pass filters [14].

5.5 Ultra-wide wavelength detuning

Centre wavelength detuning (simply referred to as detuning) is the process of introducing a differential in the distance between each stepped exposure of an interference pattern and the inherent period of target pattern of grating structures [111]. The maximum detuning only depends on the beam spot diameter where small spot sizes correspond to a

large detuning range [125]. The DGW process builds up a grating structure through successive exposure of a small spot interference pattern with diameter of $\sim 6\mu m$, with each single snapshot only contributing to a fraction of the overall exposure at any given point in the grating structure. The distinction permits fine tuning of the grating structure, allowing an ultra-wide Bragg wavelength detuning range while maintaining a significant refractive index change. Arbitrary Bragg grating devices can be made in desired central wavelength via the simple, flexible, affordable and reliable method.

Figure 5.28 shows the simulation of the phase controlled DGW process and the detuning effect. Figure 5.28(a) plots refractive index distribution along the grating section for three scenarios: the single interference fringe pattern with a $\sim 6\mu m$ diameter Gaussian spot (red line), the zero wavelength detuning pattern (dotted line) and a 100nm wavelength detuning pattern (blue line). The DGW technique intrinsically offers the zero dc refractive index change with fluence matching and the combination of grating length and refractive index modulation depth Δn determines the grating strength. Figure 5.28(b) shows the maximum refractive index change (Δn) as a function of wavelength detuning ($\Delta\lambda$). The highlighted data points (Δn_1, Δn_2) correspond to the zero detuning and 100 nm wavelength detuning scenarios in Fig. 5.28(a). Figure 5.28(c) shows the partially enlarged drawing of square region in Fig. 5.28(a) and indicates the wavelength detuning ($\Delta\lambda = 100nm$) and the grating period difference. Figure 5.28(d) shows a simulation of the maximum reflectivity of a 1mm long uniform Bragg grating s function of $\Delta\lambda$, while the maximum Δn is assumed to be 8×10^{-4}. By considering the writing spot intensity has a Gaussian distribution, Fig. 5.28(e) plots the detuning range full width at half maximum (FWHM) as a function of spot diameters. The Bragg grating reflectivity is over -20dB within a 700nm wavelength range and for a 3dB reflectivity degradation the wavelength detuning range is $\sim 250nm$.

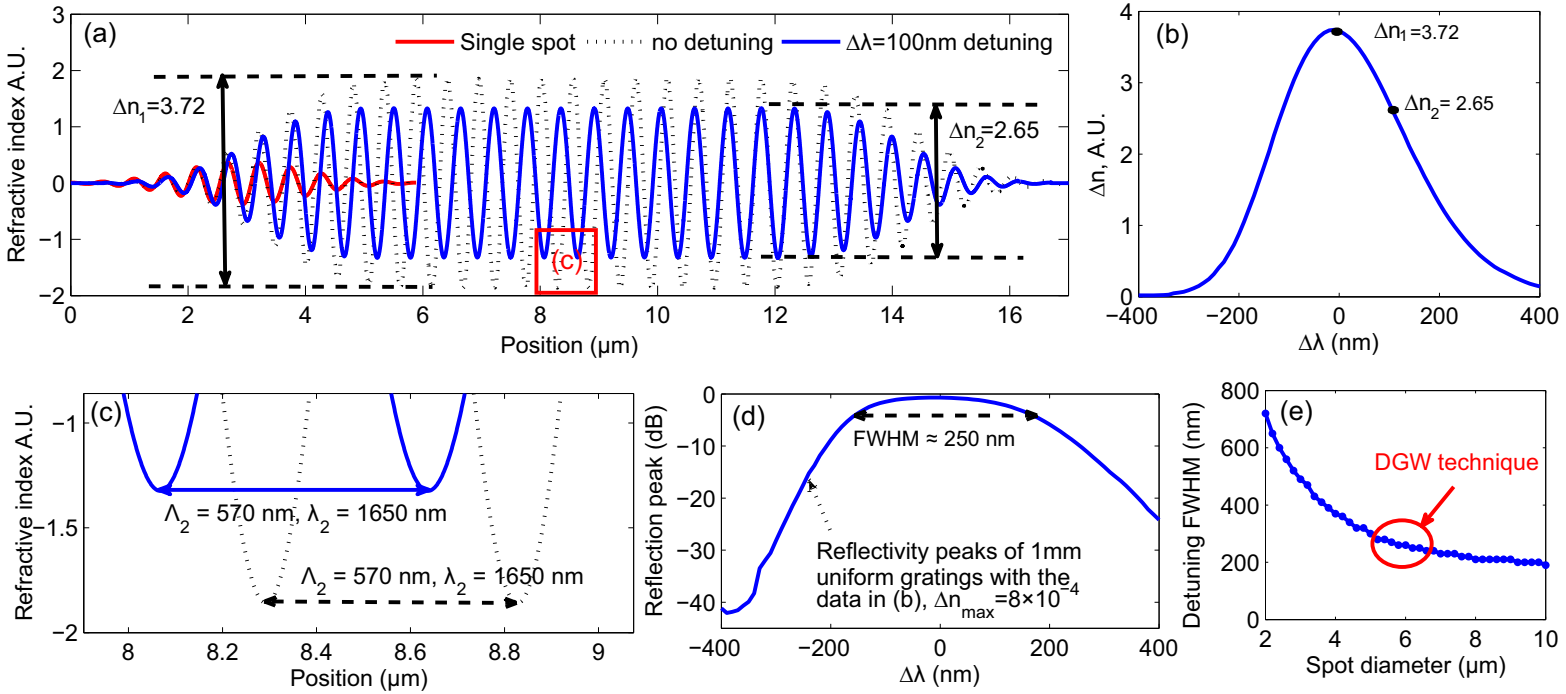

Figure 5.28: Modelling: (a) the refractive index pattern along the grating section; (b) maximum refractive index contrast (Δn) as a function of wavelength detuning ($\Delta\lambda$) with the phase-controlled method; (c) partial enlarged details in (a) present grating period variation showing the effect of wavelength detuning; (d) 1mm uniform grating reflection peaks variation as a function of ($\Delta\lambda$), showing 250nm FWHM (full width at half maximum); (e) the detuning FWHM in (d) as a function of the writing spot diameter.

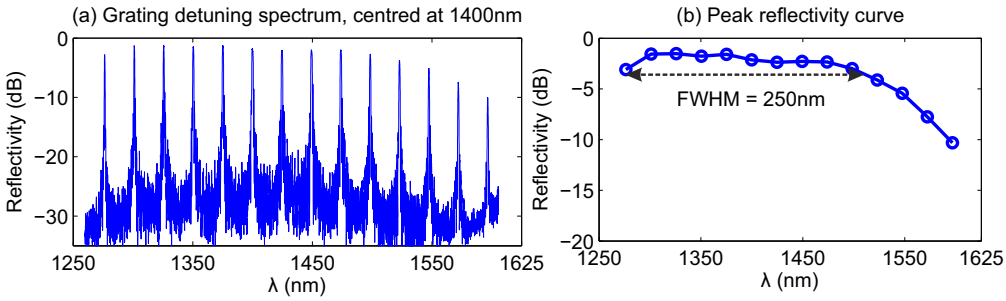

Figure 5.29: Experimental demonstration: (a) reflectivity spectrum of a series of 1mm uniform gratings from 1250nm to 1600nm, centred at around 1400nm; (b) grating peak reflectivity data (circle). In this case, the UV writing crossing angle was $\theta =\sim 31^{\circ}$, which leads to the centre of the spectral band being located at 1400nm.

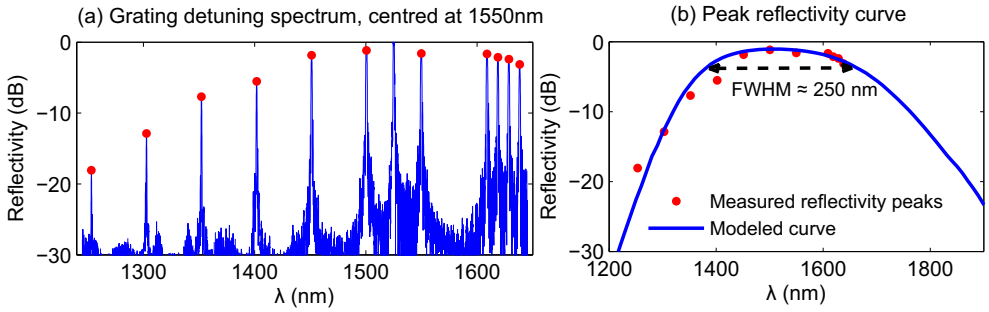

Figure 5.30: Experimental demonstration: (a) reflectivity spectrum of the gratings from 1250nm to 1650nm, centred at 1550nm;(b) grating peak reflectivity data (red dot) and modelled curve (solid line). The UV writing crossing angle was $\theta = 26^{\circ}$, which leads to the centre of the spectral band being located at 1550nm.

The simulations were experimentally tested using the system. A series of 1mm long uniform Bragg gratings with a wavelength interval of 25nm were fabricated in a single channel waveguide in a single process; the reflectivity spectrum is illustrated in Fig. 5.29(a). Figure 5.29(b) shows the peak reflectivity of the gratings (dots), demonstrating a 3dB bandwidth of $\sim 250nm$. The grating reflectivity varies slightly around 1400nm believed to be due to the hydroxyl ion absorption in the silica material. The angle between the laser beams is $\sim 31^{\circ}$, which causes the centre of the spectral band being located at 1400nm, agreeing with Eq. (5.1).

The crossing angle in the setup was changed to 26°, for optimal 1550nm operation, and a similar experiment was conducted, the data of which is shown in Fig. 5.30. Figure 5.30(a) shows the reflectivity spectrum of a series of 1mm long uniform Bragg gratings with a wavelength interval of 50 nm again fabricated in a single channel waveguide in a single process. The reference grating at 1525nm was a 3mm long uniform Bragg grating with a saturated reflection spectrum for characterisation calibration. Figure 5.30(b) shows the reflectivity of the gratings (stars) and the modelling curve (blue line) using the data in Fig. 5.28(d). The grating reflectivity degrades slightly around 1400nm again

believed to be due to the hydroxyl ion absorption. The experimental results suggest that gratings can be fabricated between 1200nm and 1900nm and demonstrate that the 3dB bandwidth range (FWHM) is $\sim 250nm$ (32THz), agreeing well with the modelling in Fig. 5.28(d). This ultra wide detuning range was achieved entirely through software control, without any perturbation or realignment. Gratings with Bragg wavelengths above 1650nm were not fabricated due to the limited bandwidth of the characterisation setup. In this data the strongest 1mm grating demonstrated $\sim$ 70% reflectivity and 1.4nm 3dB bandwidth, indicating Δn of 8×10^{-4}.

5.6 System linearity enhancement

5.6.1 Wafer specifications and fluence test

In the experiments of this thesis, three different kinds of FHD wafers were used: W5, W7 and NB17/18. The W5 and W7 wafers were fabricated by CIP. The NB17/18 wafer was made later at the ORC using the in-house FHD systems (recipe 17 for the core layer and recipe 18 for the overclad). The sample specifics are included in Appendix C. In summary, the W5 and W7 wafers are fabricated using the same recipe and with the same parameters, *e.g.* the same amount of dopant, 1.4461 core average refractive index and $5.6\mu m$ core thickness. The only difference lies in the wafer position on the turn table of the FHD setup and consolidation furnace, and the wafers are diced into different dimension chips. NB17/18 wafer has a higher germanium composition in the core layer ($6.8\mu m$ thick) for more increased UV photosensitivity. In the following sections the NB17 wafer was tested and used to make grating structures. The increase in effective index with raised UV fluence for the NB17/18 sample is depicted in Fig. 5.31.

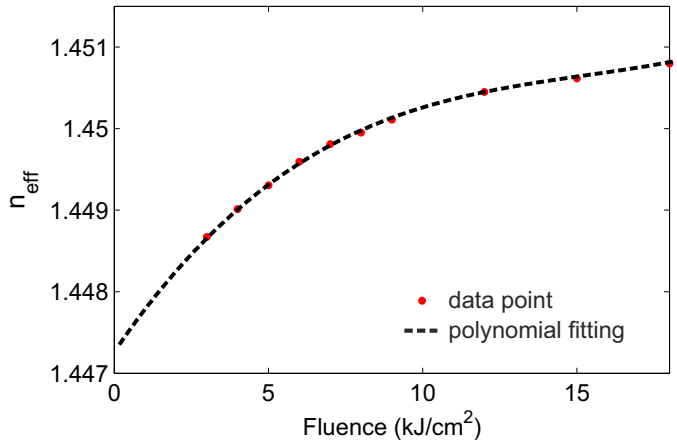

Figure 5.31: Effective indexes versus UV writing fluence, with the NB17/18 sample.

The polynomial fitting curve shown in Fig. 5.31 is as expected, and exhibits a similar behaviour described previously [84, 86, 92]. A fluence test allows measurements of Δn for a given fluence level, with the increase in index being reflected by the shift in peak Bragg wavelength, λ_B. It is expected that the trend will become flat at certain point, where increase in UV writing fluence would no longer have any effect in terms of index increase. This occurs when photosensitivity is completely saturated. The nature of the photosensitivity dependence intimately depends on the processing of the substrates. The fluence levels normally used for 1550nm operation are between $12 - 16kJ/cm^{-2}$ where the photosensitivity is not saturated [92]. When using the phase-control DGW technique to make waveguide structures with the typical operating UV laser beam power of 80mW and fluence of $12kJ/cm^{-2}$ (*e.g.* for W5 and W7 samples), the translation speed is $\sim 6mm/min$.

From the results for the NB17/18 samples in Fig. 5.31, a fluence level of $6kJ/cm^{-2}$ is chosen in fabrication, which leads to the translation speed of $\sim 12mm/min$.

5.6.2 Transfer function synthesis

The system transfer function refers to the relationship between the input apodisation profile and the grating response in terms of Δn. In most cases, while the fabrication speed $v_{trans} \leq 5mm/min$ for the EOM based phase-control DGW system, the grating Δn behaves linearly with duty cycle between 0 and 0.8, as previously demonstrated in Fig. 5.26(b), which means the transfer function is linear that is a beneficial feature for making high fidelity apodised gratings. When the UV writing system has some nonlinear response, possibly due to the high voltage amplifier's limited bandwidth and EOM bandwidth. The transfer function must be considered and compensated. A flow chart of the entire fabrication process is illustrated in Fig. 5.32.

When using the NB17/18 samples with the phase-control DGW technique, the fabrication speed ($\sim 12mm/min$) becomes twice as fast as used previously ($\sim 5mm/min$). It was observed that writing at these speeds ($12mm/min$), the relationship between Δn and the duty cycle becomes nonlinear. Figure 5.33(a) were obtained by characterising and normalising Δn of a series of 1mm uniform Bragg gratings fabricated with increasing duty cycles, and shows a nonlinear relationship. The data was obtained by spectrally multiplexing gratings with duty cycle increasing from 0.05 to 0.8 in a single waveguide channel. The ultra-wide detuning range of this fabrication technique ensures these gratings among a 100nm range have merely $\leq 1dB$ variation due to wavelength difference and the Δn value is sufficiently accurate.

Using the data in Fig. 5.33(a), a transfer function $Y(x)$ was calculated and is given as:

$$Y(x) = 2.6x^6 + 0.57x^5 - 10x^4 + 12x^3 - 6x^2 + 2.1x \tag{5.5}$$

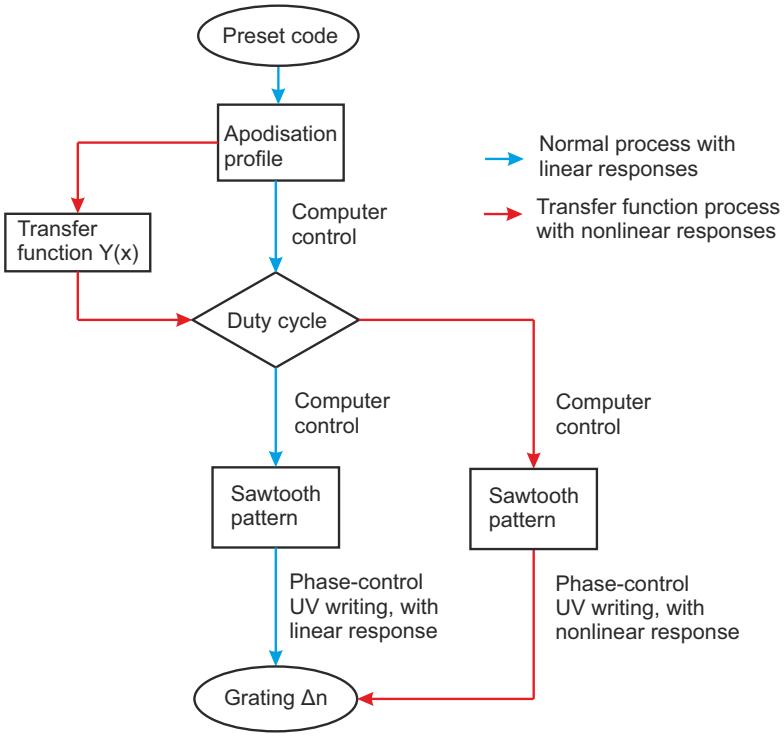

Figure 5.32: The flow chart of the phase-control direct UV grating writing technique, with the cases of normal linear process (blue arrow) and the transfer function process for nonlinear responses (red arrow).

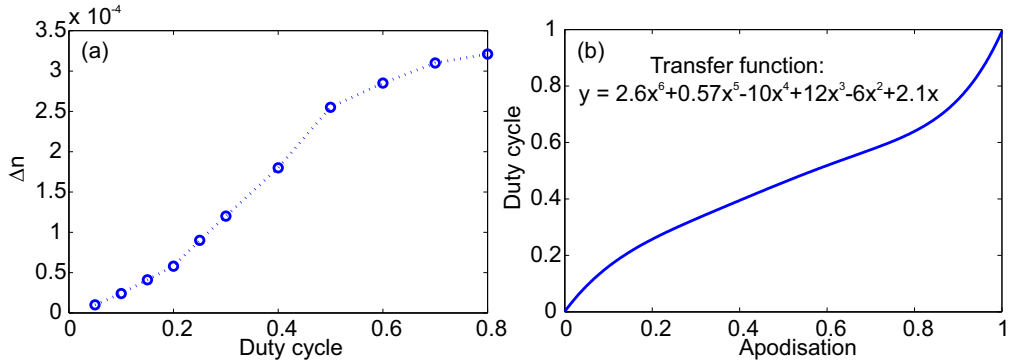

Figure 5.33: (a) The grating Δn as a function of duty cycle; (b) the transfer function curve of the entire fabrication system, which is the inverse function of the fitting curve in (a).

where Y is the duty cycle value and x denotes the input apodisation profile $(0-1)$. The transfer function was also plotted in Fig. 5.33(b). The transfer function was employed during the fabrication of Terahertz bandwidth PHTs. This concept was demonstrated and verified by the experimental results, which will be discussed in the next chapter.

The origin of the nonlinearity is in the limited slew rate of the EOM drive circuit. It is also possible that this nonlinearity is related to the mechanism of the photosensitivity. This could likely be improved but may be expensive and complicated to achieve. Nevertheless, transfer function compensation seems to provide a good solution.

5.7 Conclusion

Grating engineering using the direct UV grating writing technique is presented in this chapter. The chapter discusses the conventional AOM based system previously used to make planar Bragg grating structures with the concept of duty cycle control and fluence matching. The chapter highlights the limits of technique and the fabrication artifacts including the nonlinear grating response, low time/energy efficiency and the translation speed variation. The piezo actuator based phase-control method was firstly proposed and demonstrated. Due to the hysteresis of the piezoelectric effect, this method did not overcome the nonlinear grating response issue. The piezo actuator was characterised using a Michelson interferometer, showing an unfavorable hysteresis and strong resonance responses.

The EOM based phase-control method is proposed, demonstrated and analysed, with a near-linear relationship between maximum Δn and duty cycle achieved. Along with the unique micron-order writing spot, modulation linearity ensures the desired grating apodisation profile is achieved. Furthermore, the technique provides significant fringe visibility, thus the considerable refractive index change and ultra-wide wavelength detuning. The flexibility, simplicity, low cost, time/energy efficiency and stability of this technique make it a powerful and promising tool to fabricate arbitrary planar Bragg gratings. The use of transfer function compensation of the fabrication system was also discussed and demonstrated with experimental verification presented in the next chapter.

Chapter 6

Integrated photonics Hilbert transform devices

6.1 Introduction

Single-sideband (SSB) modulation is a well-known technique in telecommunications for improving performance in terms of required power, enhancing spectral efficiency and reducing fading. In the conventional electronic domain, Hilbert transform techniques have been widely used in SSB modulation applications, and devices have been implemented in both analogue and digital systems and geometries [20]. In the all-optical field, photonic Hilbert transformers (PHTs) offer potential for a wide range of applications as they provide operational bandwidths and speeds far beyond current electronic technologies. In addition they also reduce dispersion related artifacts such as signal power fading [43]. Several demonstrations of PHTs were presented and reviewed in Chapter 2. Previous works on all-optical SSB modulation such as those reported in the literature [38, 43] deal with complex fibre-based schemes comprising optical circulators, attenuators and optical delay lines. The complexity and scale of physically realising these schemes results in costly systems that lack the required mechanical and thermal stability for system applications.

In this chapter, photonics Hilbert transformers implementing monolithcally integrated all-optical SSB filters are proposed, modelled, fabricated and characterised. The initial proof-of-concept devices show sideband suppression ratios at microwave frequency. The PHT is further investigated to operate with Terahertz bandwidth and with fractional orders.

6.2 Photonic Hilbert transformer

The PHT was realised by using an apodised planar Bragg grating with a π phase shift within the grating; an example was previously shown in Fig. 3.9. During the fabrication of this device, some fabrication artifacts have been revealed. Modelled data of a few scenarios are shown in Fig. 6.1, including the designed grating response, a grating response with truncated apodisation profile, and truncated profile with a $\sim 5\%$ phase shift error.

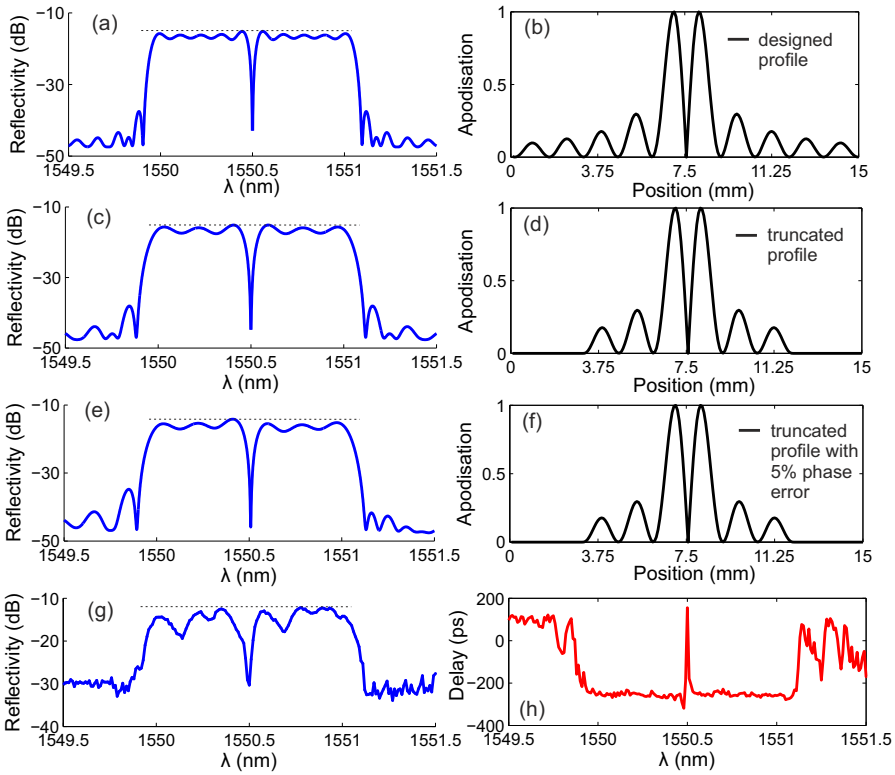

Figure 6.1: (a) Spectral simulation of a designed grating response, with the apodisation profile in (b); (c) spectral simulation of the truncated grating response, with the associated truncated apodisation profile in (d); (e) spectral simulation of the grating response with the truncated apodisation profile and 5% phase shift error, with apodisation profile shown in (f); the measured reflection response (g) and group delay (h) of the preliminary 15mm PHT device with 1550.5nm central wavelength.

The truncated apodisation profile in Fig. 6.1(d) leads to bigger ripples in the flat top of the reflectivity response in Fig. 6.1(c), compared to the response in Fig. 6.1(a) with the designed apodisation profile in Fig. 6.1(b). The asymmetric features of the reflectivity peak in Fig. 6.1(e) are characteristic of a small phase error in the π phase shift with the apodisation profile in Fig. 6.1(f). Modelled data has indicated that a $\sim 5\%$ error in the magnitude of the π phase shift produces similar features of the measured data in Fig. 6.1(g).

Figure 6.1(g) and (h) show the measured data of the fabricated PHT device that contains a π phase shift and apodisation profile using the following parameters: $L = 15mm$, $\Lambda = 535.467nm$, $n_{eff} = 1.4478$, and $\Delta f = 140GHz$. The reflectivity spectrum shows a flattop spectral response and a strong dip (-20 dB) due to the π phase shift. The Bragg grating operates at 1550.5 nm and has a bandwidth of $\sim 1.2nm$ ($\sim 150GHz$) bandwidth, both values agreeing with the target parameters.

Figure 6.1(h) illustrates the relative group delay of the reflected optical signal. It has a comparatively flat group delay within the operating bandwidth with an abrupt change in the centre, due to the phase shift. Both reflectivity and relative group delay were measured using the modulation phase-shift method. The restricted dynamic range of the reflectivity measurement (*i.e.*$\sim -32dB$) is a result of the limited sensitivity of the characterisation setup.

Ripples of $\sim 7dB$ in the top of the reflectivity spectrum and spectral asymmetric features were presented in the measured data shown in Fig. 6.1(g), believed due to the truncated apodisation profile and phase error. These unexpected truncation phenomenons and phase shift errors were observed in the devices fabricated by the amplitude modulated DGW technique using AOM. This analysis indicates an improved fabrication process is necessary to achieve high reflectivity and reduce these fabrication artifacts which likely result from the intrinsic nonlinearity in the amplitude modulated DGW technique. Hence, to overcome these artifacts, alternative methods using DGW with phase modulation concepts (discussed in Chapter 5) were proposed and utilised to fabricate the later PHTs in this work.

6.2.1 Improved grating responses

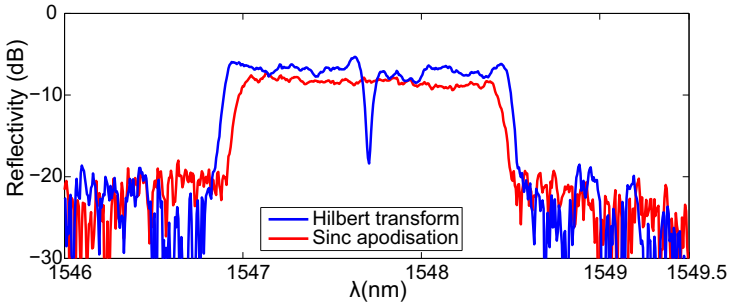

Figure 6.2: Experimental data: the reflectivity spectra of the planar Bragg grating implementing a Hilbert transformer (blue line) and that with a sinc apodisation profile(red line).

After implementing the phase-control DGW method, a series of Bragg gratings were produced including PHTs. Figure 6.2 shows the grating reflectivity spectra of the planar Bragg gratings implementing Hilbert transform (blue line) and gratings with sinc apodisation (red line). The operating bandwidth (3dB decay of the amplitude response)

of the PHT is approximately 8.5GHz-200GHz. Significant improvement in spectral quality was achieved by using this phase modulated DGW technique. Ripples in the top of reflectivity spectra are $\sim 2dB$, which also feature the sharp-cut edges. The data were obtained by using the characterisation technique in Section 4.7.1. Reflections just above the noise floor ($\sim -25db$) of the spectrum analyser are displayed. More devices implementing PHTs with fractional orders and Terahertz bandwidths are presented in the following sections.

6.3 All-optical SSB filters and microwave photonics operation

Considering the structures previously proposed in Fig. 3.10, the integrated photonic device is composed of an X-coupler [86], PHT, flattop reflector and a micro heater [123]. A sinc apodised Bragg grating was utilised as the flattop reflector; an example was shown in Figure 6.2. By applying DC voltages to the miniature Nichrome heater, the phase of the optical signal can be finely trimmed through thermal tuning. Modelled data of this device, also previously discussed in Section 3.6, are shown in Fig. 6.3.

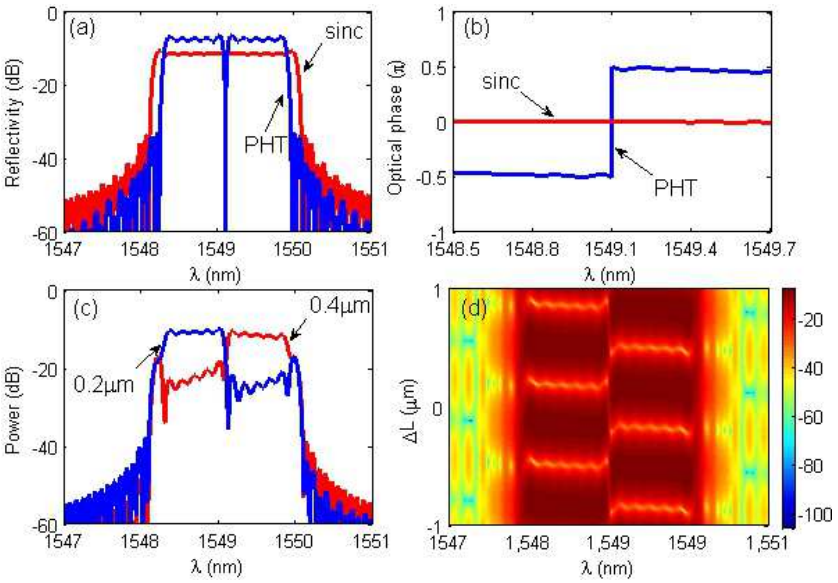

Figure 6.3: Simulation: (a) the PHT and sinc apodised gratings amplitude spectra; (b) normalized gratings phase spectra; (c) device outputs with ΔL at $0.2\mu m$ (red) and $0.4\mu m$ (blue); (d) the intensity color map of the output spectra as a function of ΔL.

Figure 6.3 illustrates the reflectivity spectra of individual Bragg gratings, the device output (with the path length imbalance ΔL of $0.2\mu m$ and $0.4\mu m$), and a pseudo color plot of the spectra as a function of ΔL. Figures 6.3(a) and (b) demonstrate the similarity of the sinc-apodised grating response to that of the PHT, except the π phase-shift at the central wavelength. Figure 6.3(c) shows the interfered output from the device for

two ΔL scenarios, where the opposite side lobes are suppressed and the single sideband switch could be realised. Figure 6.3(d) presents the effect of ΔL over an extended range showing a periodic variation.

The proposed planar structures were fabricated using the direct UV grating writing technique with electro-optical phase modulation [57]. The fabricated chip had dimensions of $20mm \times 10mm \times 1mm$ and the NB17/18 wafer with a fluence of $6kJ/cm^2$ was used. The two gratings were both 10mm long, the effective refractive index of the mode within the gratings was 1.447, and the maximum refractive index modulation depth was $\Delta n = 3 \times 10^{-4}$. The X-coupler length was $\sim 7.5mm$, with crossing angle 2.5 degrees, yielding $\sim 50:50$ coupling ratio. The spacing between the X-coupler arms was $250\mu m$ to provide coupling with a standard two port fibre v-groove assembly, shown in Fig. 6.4(a). The fibre v-groove assembly contained two pre-aligned single mode polarization maintaining (PM) fibres and was aligned to the waveguide channels and secured using a UV curing adhesive.

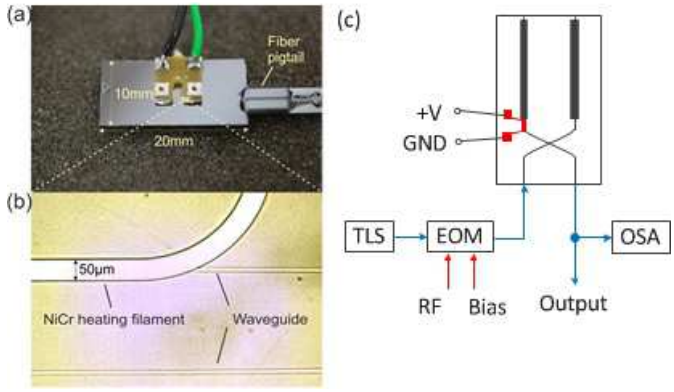

Figure 6.4: (a) The fabricated device with electro heating elements and a fibre pigtail; (b) the image of Nichrome heater ($50\mu m$ wide) on top of the waveguide; (c) the experimental setup of the optical SSB modulation system.

To deliver the thermal energy a $50\mu m$-wide by $210nm$-thick nichrome filament was deposited over a 1mm length of waveguide, as shown in Fig. 6.4(b), using electron beam metal evaporation and photolithography. The micro heater's resistance was measured to be 320Ω. The applied DC voltage was tuned between 0V and 22V by a power supply. The whole device was thermally bonded to a metal block to act as a simple thermal reservoir. The high thermal conductivity of the silicon substrate ensures that the gratings and surrounding waveguides away from the heater are substantially independent of the heater temperature [126].

Figure 6.4(c) shows the experimental setup of the all-optical SSB modulation system. To characterise the sideband suppression the output from a polarized CW tunable laser source was sent to an all-PM EOM which was amplitude modulated by the sinusoidal RF signal (without carrying any data) from the VNA. The double sideband (DSB) optical

signal from the EOM was launched into port A of the device and spectral characteristics were measured by an OSA from port B.

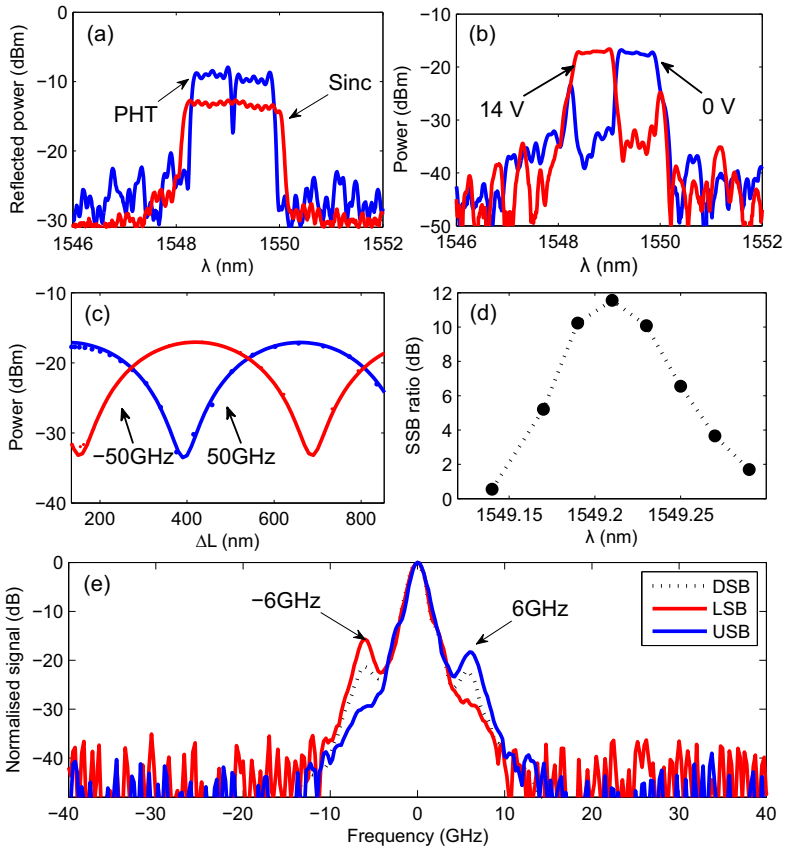

Figure 6.5: (a) Individual grating amplitude responses; (b) device output spectra with 0V (blue) and 14V (red) DC voltages; (c) modelled (line) and experimental data (dot) of output amplitude variations at 50GHz (blue) and -50GHz (red) frequency interval; (d) the SSB suppression ratio with wavelength detuning at 6GHz; (e) the input DSB signal without carrying any data (black dotted line), the output LSB signal (blue solid line) and the output USB signal (red solid line), the data is normalized for comparison.

The experimental performance of the fabricated device for microwave operation was investigated. Figure 6.5(a) shows the PHT (blue) and the sinc apodised grating (red) amplitude responses measured from ports C and D. Figure 6.5(b) shows the output spectra via thermal tuning at 0V (blue) and 14V (red), directly measured from port B of the device. Both figures (a) and (b) were measured using an OSA, 3dB coupler and an erbium doped fibre ASE source. Figure 6.5(c) shows the modelled data (solid line) and experimental data (dots) of the optical amplitude variation at 50GHz frequency interval (measured optically with the OSA) versus thermal tuning. Figure 6.5(d) shows the SSB suppression ratio (defined as the ratio between the power of suppressive sideband and that of another sideband [34]) with wavelength detuning at 6GHz. The maximum SSB suppression effect occurs when operating at the notch wavelength of the PHT spectrum, *i.e.* 1549.21nm. The notch wavelength shift was obtained if the entire chip was heated [126].

Figure 6.5(e) summaries the microwave performance of the device and shows the input DSB signal at 6GHz (black dotted line), the lower sideband signal (LSB, blue solid line) and the upper sideband signal (USB, red solid line). Selection between LSB and USB filters was achieved by thermally tuning the device with 0v (with the LSB signal) and 14v (with the USB signal). The measurements show a 12dB SSB suppression ratio for the filtered sideband. The optical carrier is still presented and could be suppressed if properly aligned to the notch of the amplitude spectrum. The modulation bandwidth of the RF signal presented (at 6GHz) is limited by the available characterisation equipment and not the device. The maximum operation bandwidth could be up to 100GHz according to the data shown in Fig. 6.5(b). The total insertion loss of the actual device was $\sim 20dB$ due to coupling loss, propagation loss in the X-coupler and low grating reflectivity. This can be reduced substantially by improving the X-coupler losses and using stronger gratings. Some results shown in this section were included and published [123].

6.4 Fractional order photonics Hilbert transformers

Fractional operations play an important role in information processing. They offer a new degree of freedom, the fractional order, which can be used for a better characterisation of a signal under test, or as an additional encoding parameter [29, 40, 50]. An example is provided by the fractional Hilbert transform (FrHT), which is a generalisation of the Hilbert transform. All-optical FrHTs were demonstrated, based on an asymmetrical uniform-period FBG with an apodisation profile operating in reflection [40, 42], and integrated optical ring resonators [46]. Using the similar concepts as the FBG devices, planar Bragg gratings implementing FrHT were investigated in this work. The devices implementing FrHT would have a fractional order of π phase shift in the frequency response while the amplitude response remains constant. As previously discussed, the conventional PHT can be realised by Bragg gratings with a π phase shift and proper apodisation profile (Fig. 3.9). It was also reported the phase shift could be continuously adjusted up to a maximum value of π, by varying the relative maximum index modulation depths (Δn) at both sides of the zero-crossing point in the apodisation profile, without affecting the flatness in the amplitude response [40]. The ratio of Δn at the two sides is denoted as ε. This behavior allows the direct design and fabrication of an FrHT by using planar Bragg grating structures. Using this concept, modelled data is shown in Fig. 6.6.

Figure 6.6(a)-(c) illustrates the left-side-halved apodisation profile of the Bragg grating for FrHT, the grating amplitude response, and the grating phase response, respectively. The Bragg grating is set to 15mm long, $n_{eff} = 1.4478$, and $\Delta f = 150GHz$. By reducing the maximum index modulation depth (Δn) on one side of the zero-crossing point in the apodisation profile, which is halved in Fig. 6.6(a), a fractional order π phase shift was achieved, *e.g.* $\sim 0.73\pi$ in Fig. 6.6(c), an essential feature of FrHT. Figure 6.6(d)-(f)

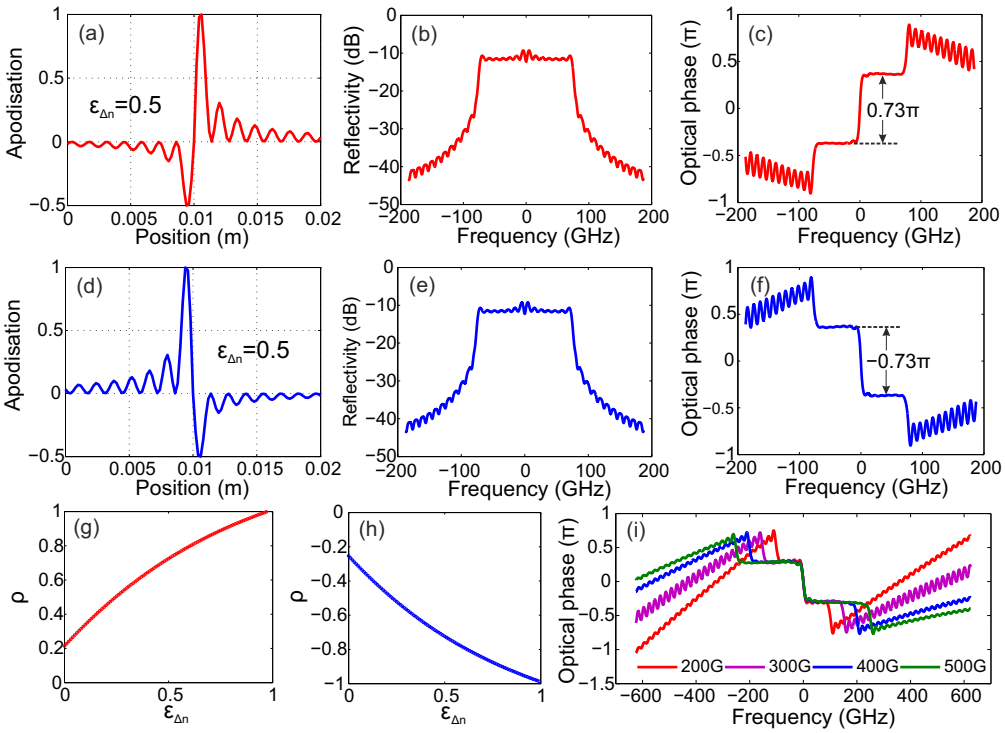

Figure 6.6: Simulation:(a)-(c) the left-side-halved apodisation profile of the grating for FrHT, the grating amplitude response, and the optical phase response, and ε denotes the ratio of the maximum index modulation depths Δn in the two sides of the zero-crossing point in the apodisation profile; (d)-(f) the right-side-halved apodisation profile, as well as the grating amplitude and optical phase response; (g) fractional order ρ as a function of the relative ratio ε for the addictive phase shift; (h) ρ as a function of ε for the subtractive phase shift; (i) the grating phase responses implementing same order FrHT but with different operating bandwidths. In the figures showing phase responses the average group-delay was not represented for illustration purposes.

illustrates the results for the right-side-halved scenario with same grating parameters, including the apodisation profile, the amplitude response and the grating phase response, respectively. In these two cases, the amplitude responses are identical while the phase shift in the phase responses are reversed to the similar extent.

When changing the ratio ε (defined as the ratio of the maximum index modulation depths (Δn) at the two sides of the apodisation profile), the factional order ρ of Hilbert transform would be adjusted as a function of ε, and the relationship is shown in Fig. 6.6(g) with the additive phase shift and in Fig. 6.6(h) with the subtractive phase shift.

If implementing the same order FrHT, the bandwidth effect on the grating performance in terms of phase responses is investigated, as shown in Fig. 6.6(i). It shows that if operating bandwidths vary for proposed grating structures implementing FrHT, the fractional order is generally constant. This feature is important to realise ultra-wide bandwidth devices in this thesis. In all figures showing phase responses, the average group-delay data were compensated for illustration purposes.

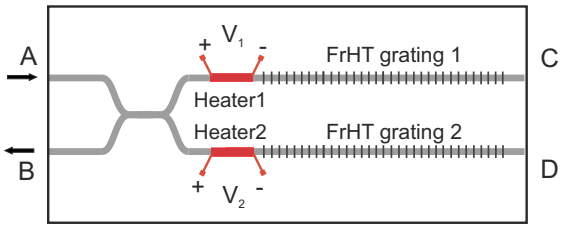

Figure 6.7: The proposed interferometric structure with FrHTs and push-pull thermal tuning elements.

After the modelling discussed above, some gratings implementing FrHTs were fabricated, characterised and integrated into interferometric structures with push-pull heating elements instead of a single micro-heater, shown in Fig. 6.7. This MachZehnder type structure with a pair of micro-heaters in Fig. 6.7 allows a more flexible thermal tuning choice. The NB17/18 wafer with a fluence of $6kJ/cm^2$ was used. The grating parameters are: $L = 10mm$, $\lambda_B = 1549.1nm$, $\Delta n = 3.6 \times 10^{-4}$, $\Delta f = 200GHz$ and the fractional order $\rho = 0.5$.

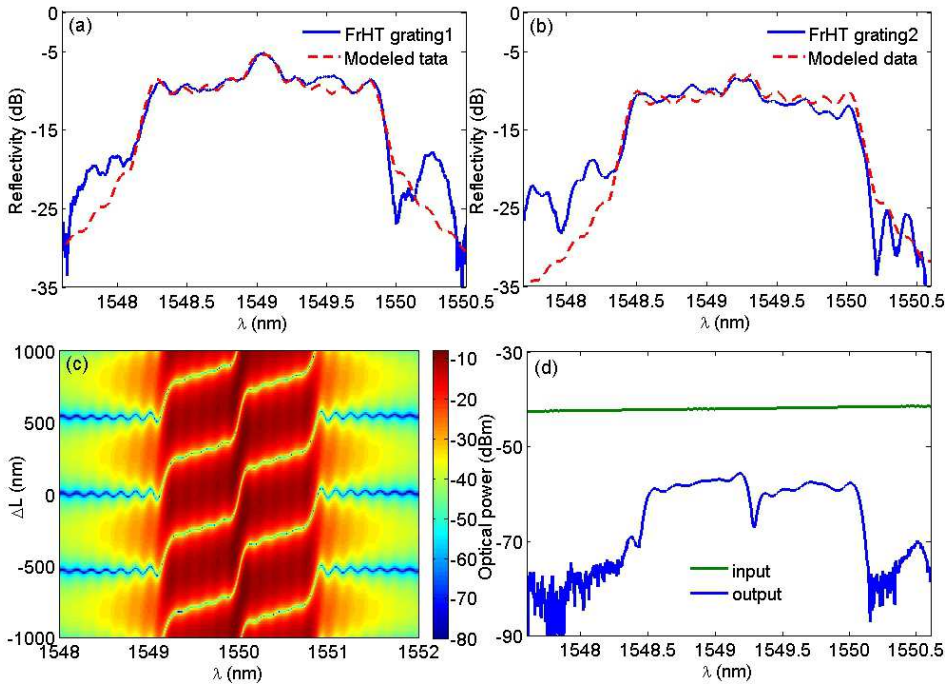

Figure 6.8: (a) Measured reflection data (blue solid line) and modelled data (red dashed line) of the grating measured via port C of the proposed structure; (b) measured reflection data (blue solid line) and modelled data (red dashed line) of the other grating measured via port D; (c) modelled data of the output spectra at port B, as a function of propagation length imbalance ΔL; (d) the measured output power spectra (blue line) at port B, with the input power (green line) at port A.

Figure 6.8(a) shows the modelled data (blue line) and the measured data (red dashed line) of the grating amplitude response for FrHT, directly measured from port C. Figure 6.8(b) illustrates the modelled data (blue line) and the measured data (red dashed

line) of the other grating amplitude response for FrHT, directly measured from port D. Both figures (a) and (b) were measured using an OSA, 3dB coupler and an erbium doped fibre ASE source. Figure 6.8(c) presents the modelled data of optical path difference ΔL over an extended range. Figure 6.8(d) shows the output spectra (blue line) of the device, directly measured from port B, and the input optical power spectrum (green line). The loss of the device comes from coupling loss, propagation loss in the X-coupler and low grating reflectivity.

Due to the substantial group delay difference of the two gratings located in the same position of each arm, optical signals reflected from the two gratings interact and generate a tiled top of the power spectrum in Fig. 6.8(c), different from that in Fig. 6.3.

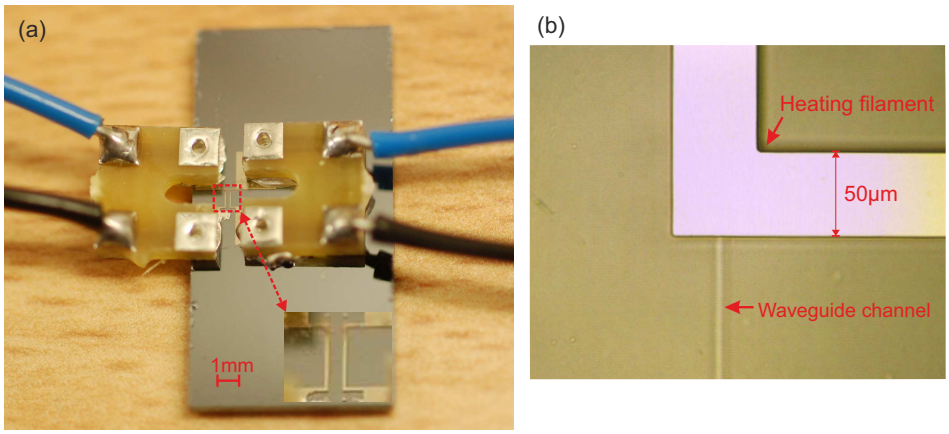

Figure 6.9: (a) The camera image of the device with heating elements; (b) the microscope image of the Nichrome filament deposited on top of the waveguide channel.

By using electron beam metal evaporation and photolithography, a pair of 200nm thick and 50μm wide Nichrome filaments was deposited in the same position on top of the two arms of the interferometric structures and connected with electric wires, shown in Fig. 6.9. By applying voltages to the Nichrome filaments, the optical phases of signals propagating along the waveguide channels would be tuned separately and a push-pull tuning effect could be achieved.

Figure 6.10 shows the modelled data (red line) and measured results (blue line) of the output optical power spectra from port B, with increased voltages applied to Heater1 in the device. Figure 6.10(b) shows that the system can be used to generate a bandpass notch filter with no sideband suppression.

Using the similar RF signal operation setup in Fig. 6.4(c), the all-optical SSB single filtering effect is characterised and shown in Fig. 6.11. Figure 6.11(a) and (b) show the measured optical power spectrum with 8V applied to Heater1 and the LSB suppression with 6GHz RF signals. If Heater2 is also applied with voltages, the spectra will be pulled or pushed to the adjacent state.

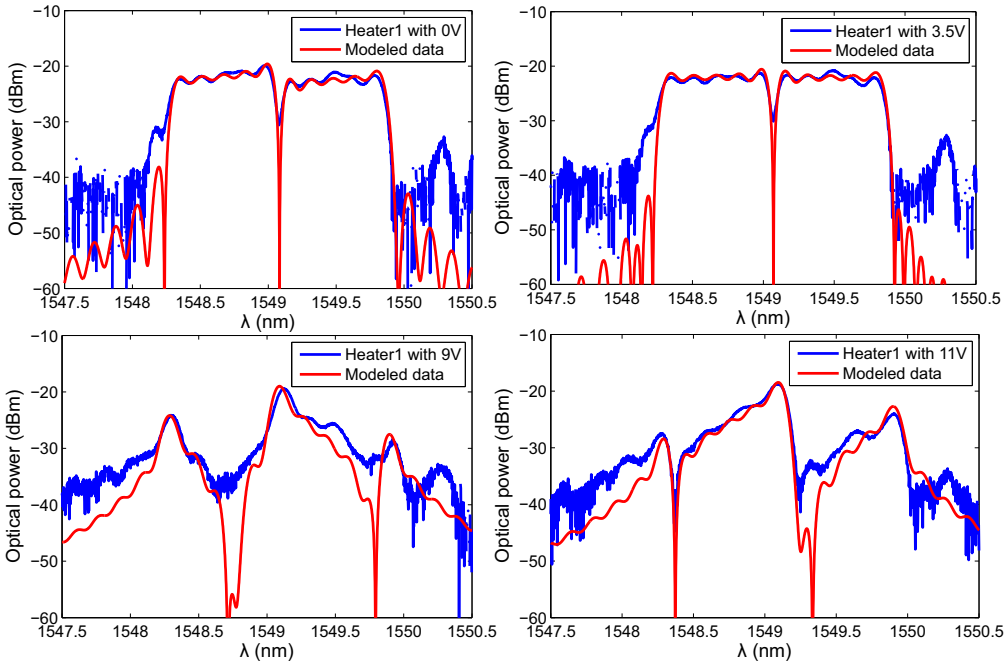

Figure 6.10: The modelled (red line) and measured (blue line) data of the device output power spectrum from port B, with the Heater1 applied with (a) 0V, (b) 3.5V, (c) 9V and (d) 11V DC voltages.

When Heater2 was applied with 7V, the optical spectrum altered into a flat top which results in a DSB signal, shown in Fig. 6.11(c) and (d). The optical spectrum in Fig. 6.11(c) is similar to that in Fig. 6.10(b). If the Heater1 thermal tuning was removed but Heater2 remained, the optical spectrum would become that in Fig. 6.11(e) and the SSB suppression ratio of $\sim 12dB$ in 6GHz RF frequency was obtained, as shown in Fig. 6.11(f). Signals $> 6GHz$ were not measured due to the lack of available microwave measurement equipment.

In this section, the photonic FrHT devices and their implementation in push-pull all-optical SSB filtering were presented and experimentally demonstrated. The device has a symmetrical structure in a silicon-on-silica substrate, comprising of a directional coupler with a micro heater and FrHT on each arm. FrHTs were realised by planar Bragg gratings with a π phase shift and an asymmetric apodisation profile, and the push-pull operation of the optical phase was realised by a pair of micro heaters on top of the waveguides. The fractional order of Hilbert transformers and fine thermal tuning and compensation of the symmetric micro heaters provide extra flexibility of the device.

6.5 Terahertz bandwidth photonics Hilbert transformers

Results discussed in this section has been summarised and published [127]. The references [44, 128] shows that the previous experimental approaches are limited to operation bandwidths $< 100GHz$ due to intrinsic complexity of approaches via discrete

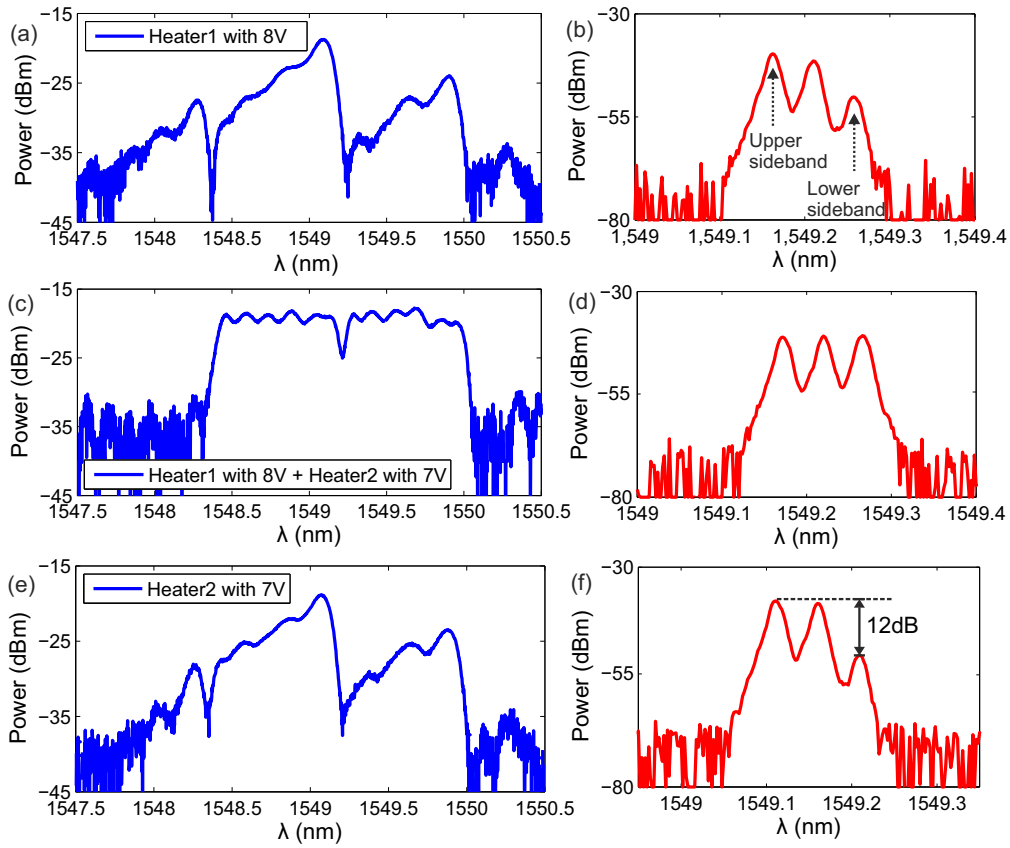

Figure 6.11: (a) The measured optical power spectrum with 8V applied to Heater1; (b) the LSB suppression with 6GHz RF signals, with the optical spectrum shown in (a); (c) the measured spectrum with 8V applied to Heater1 and 7V applied to Heater2; (d) the 6GHz RF DSB signals, with the optical spectrum shown in (c); (e) the measured spectrum with 7V applied to Heater2; (f) the 12dB LSB suppression of 6GHz RF signals, with the optical spectrum shown in (e).

components or the restrictions of current FBG fabrication. Terahertz bandwidth PHTs were numerically presented using long period gratings and core/cladding mode interaction [44], nevertheless, the complexity provides a significant challenge to practically realising such a device.

In this work, a direct and simple route to realise Bragg grating based PHTs has been experimentally demonstrated, with an operation bandwidth up to 2THz ($\sim 16nm$), over an order of magnitude larger than any previously reported experimental approaches. The phase-modulated direct UV grating writing in a NB17/18 wafer was used. This fabrication technique is further enhanced in terms of control linearity to improve spectral quality. The PHTs have also been integrated to implement ultra-wide band all-optical SSB filters. These devices have the benefits of processing Tbit/s serial optical communication signals, compact structures with fibre compatibility, long term thermal stability and could be used alongside etched silica-on-silicon devices.

For a physically realisable PHT, the practical grating apodisation profile has been given in Eq.(3.42); that is:

$$\Delta n(z) \propto \frac{\sin^2[\pi n_{eff}\Delta f(z-z_0)]}{n_{eff}\Delta f(z-z_0)}$$

where n_{eff} is the grating effective refractive index, c is the light speed in vacuum, z is the position in the grating section, z_0 is the zero-crossing point in the apodisation function, and Δf is the operating bandwidth. From Eq.(3.42), the full operation spectral bandwidth of the PHT is inversely proportion to the period of the apodisation profile Δz, also refers to the zero-to-zero width of the side-lobe in the apodisation profile [39], as shown in Fig. 6.12(a), given as:

$$\Delta f = \frac{c}{n_{eff}\Delta z} \tag{6.1}$$

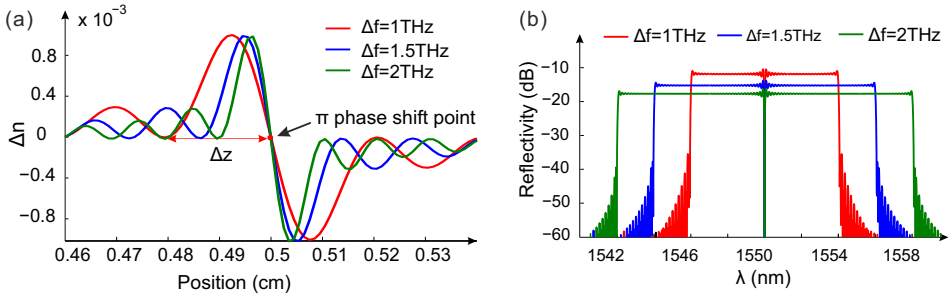

Figure 6.12: (a) The central apodisation profile of the Bragg grating for the THz bandwidth PHTs with increasing Terahertz bandwidths; (b) modelled amplitude responses of PHTs.

Therefore a broader processing bandwidth can be obtained using narrower apodisation sidelobes. A transfer matrix method was employed for modelling the device output with the proposed structure, assuming the grating length is $10mm$, $n_{eff} = 1.45$ and the maximum refractive index modulation depth was $\Delta n = 9 \times 10^{-4}$. Figure 6.12(a) presents the central section of the apodisation profile for the three THz bandwidth PHT scenarios, showing the sidelobe width Δz and the π phase shift point. Figure 6.12(b) illustrates the reflectivity spectra of the proposed Bragg gratings, with bandwidths of 1THz, 1.5THz and 2THz respectively; thus, the apodisation profile periods, Δz, were $207\mu m$, $138\mu m$ and $104\mu m$, according to Eq.(6.1).

For the current FBG fabrication technologies using phase masks, the UV writing spot allows writing grating apodisation profiles with spatial resolutions $\sim 100\mu m$ and hence the previous fabricated PHTs suffered the operation bandwidth limitations $< 100GHz$ [44]. Although these techniques may be able for the central lobe of such a Terahertz bandwidth device, they would struggle to control the phase shifts and apodisation in the remaining fluctuation, resulting in a non-flat top in the reflectivity spectrum. They would also struggle to yield the Δn required to fabricate a strong grating. To overcome

the restrictions and to obtain larger bandwidths, the alternative fabrication approach was utilised.

The proposed planar structures were fabricated using the direct UV grating writing technique with phase modulation [57], as shown in Fig. 5.25. This spot size is $\sim 6\mu m$ in diameter, providing the unique ability over traditional FBG to manipulate the grating's structure at the sub-10 micron level.

6.5.1 Linearity enhancement for grating synthesis

As mentioned in Section 5.6, the fabrication linearity is stringent requirement for planar Bragg gratings with complex structures. In the DGW fabrication technique, the grating refractive index change Δn is controlled by the duty cycle profile (proportional to the grating apodisation profile) and conventionally exhibits a linear response [57]. When using highly photosensitive samples and fabricating with a rapid translation speed for fluence matching [84], it results in fast operation and may exceed the bandwidth limitations of components in the fabrication setup, *e.g.* the high-voltage amplifier. If the Δn behaves nonlinearly as a consequence of bandwidth limitation (shown in Fig. 5.33), undesirable grating responses could occur and require be rectified. In this work, the linearity enhancement of the fabrication technique was investigated and verified with grating responses for Terahertz bandwidth PHTs [127].

Figure 6.13(a) shows modelled data (red dots) and measured spectrum (blue line) of the initial directly designed grating for 1THz PHT, which lacks of critical flattop features for Hilbert transform; Fig. 6.13(b) illustrates the corresponding duty cycle profile, which is not identical to the designed apodisation profile, due to the nonlinear effect in the grating fabrication. It is acknowledged that the sidelobe in the apodisation profile (also refers to the duty cycle profile) contributes to the flattop spectral features in PHTs. Hence an arbitrary step function was primarily introduced in the duty cycle profile, which doubles the duty cycle value once it is below 0.25. The modelled data (red dots), the measured grating response (blue line) and the adjusted duty cycle profile (black line) were shown in Fig. 6.13(c) and 6.13(d) respectively. To avoid abrupt jumps in the duty cycle profile in Fig. 6.13(d), another windowing function was used instead, which exclusively doubles the duty cycle value outside the two main peaks in the duty cycle profile, shown in Fig. 6.13(f). The modelled data and the measured grating response were also shown in Fig. 6.13(e).

Eventually, with synthesised design using linearity enhancement function in Fig. 5.33(b), the Terahertz bandwidth PHT responses are included in Fig. 6.14. The Bragg gratings sections were all 10 mm long, $n_{eff} = 1.447$, and the maximum $\Delta n = 9 \times 10^{-4}$. Grating reflectivity was measured using an OSA, 3dB coupler and an ASE source. Lack of equipment for the direct optical phase measurement, the modulation phase-shift method

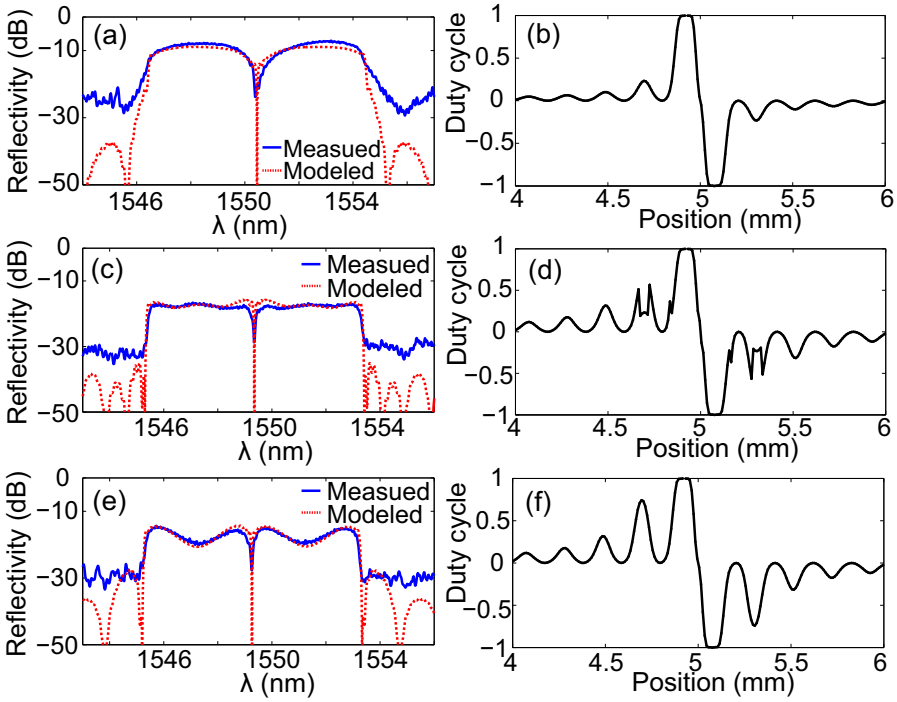

Figure 6.13: Demonstration of fabrication nonlinearity consequences on grating responses. The modelled data (red dot), measured data (blue line) and the corresponding duty cycle profile (black line) are illustrated. (a) shows the grating responses of the initial directly designed PHT with the duty cycle profile in (b); (c) shows the responses of the PHT designed with an arbitrary step function with the duty cycle profile in (d); (e) shows the responses of the PHT designed with a windowing function, with the duty cycle profile in (f).

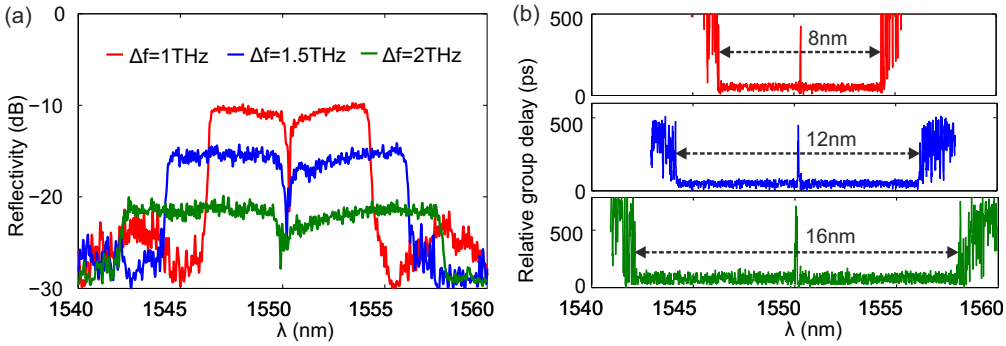

Figure 6.14: (a) The measured reflectivity spectra of the fabricated Bragg gratings implementing 1THz, 1.5THz and 2THz bandwidth PHTs; (b) Relative group delay data of the fabricated gratings.

was used to obtain relative group delay data, by comparing the change in phase of the received microwave waveform with the original modulated sinusoidal waveform using a vector network analyser.

The series of initial proof-of-concept devices demonstrate the 8nm (1THz), 12nm (1.5THz) and 16nm (2THz) maximum operation bandwidth PHTs respectively. In Fig. 6.14(a), the PHTs have flattop amplitude responses, with $< 1dB$ ripples for 1THz bandwidth.

The central spike in Fig. 6.14(b) indicates the $\sim \pi$ phase shift at the central dip of the amplitude spectra. For each device length, the minimum and maximum operation bandwidths (for a 3dB decay in the power spectral responses) are estimated. For the $1THz$ maximum bandwidth grating (red line) the minimum bandwidth is $\sim 30GHz$ while the minimum bandwidth is $\sim 55GHz$ for the $1.5THz$ maximum bandwidth grating (blue line).

The limited reflectively of the $\sim 2THz$ bandwidth device prevents detailed measurement of its optical properties and therefore the π phase shift is inferred and not directly measured. The data also highlights the current limitation of the approach; routes to overcome this limit will be discussed later. It should be noted that the fabrication tolerance of the phase shift in the DGW approach is identical for the three devices and as such would expect the same phase shift response.

6.5.2 Ultra-wide all-optical single sideband filters

To investigate the fabricated devices performance, the NB17/18 planar sample was employed for an all-optical SSB filter [123], composed of an X-coupler, flattop reflector, and the PHT. Sinc apodised Bragg grating was utilised as the flattop reflector with the same length and similar bandwidth to PHT. The reflected optical signal from the two gratings undergoes constructive and destructive interference, thereby suppressing one side band and enhancing the other. The relative optical phase difference of the two signals could be further fine-tuned by a small micro heater present on one arm of the device [123]. The X-coupler length was $\sim 7.5mm$, with crossing angle 1.8 degrees. The crossing angle of the X-coupler was adjusted, for an improved signal interaction, in terms of the intensity balance of signals reflected from the two arms. The spacing between the X-coupler arms was $250\mu m$ to provide coupling with a standard two-port fibre v-groove assembly. The interferometric structure is schematically shown in Fig. 6.15(a).

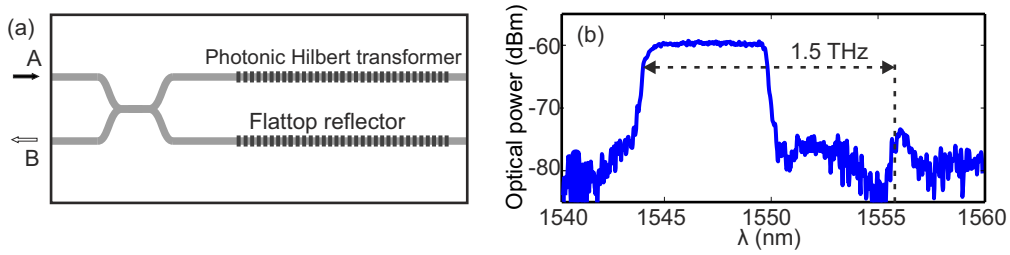

Figure 6.15: (a) The principle scheme of the integrated all-optical SSB filter device with the planar Bragg grating implementing 1.5THz bandwidth PHT; (b) the measured optical power output spectrum when optical broadband signal is coupled into port A and received from port B.

Figures 6.15(b) shows the output optical power spectra directly from port B of the device, incorporating the 1.5THz bandwidth PHTs, with input at port A, measured using an OSA and a broadband ASE source. Optical signals among the spectral band

below the central wavelength (1544-1550nm) have a ripple-less pass band while signals within the other band (1550-1556nm) are eliminated, with a suppression of $\sim 20dB$. The microwave signal measurement for SSB filtering is yet to be performed, due to the limitation of the available microwave characterisation setup and not the device. The total insertion loss of the actual devices were $\sim 20dB$ due to coupling loss, propagation loss in the X-coupler and low grating reflectivity. Although the coupling loss and X-coupler loss is improved, the reduced grating reflectivity results in a similar insertion loss as previously demonstrated.

In this section, a series of Terahertz bandwidth PHTs were proposed and experimentally demonstrated, using planar Bragg gratings. Devices implementing 1THz, 1.5THz and 2THz operation bandwidths PHTs were fabricated via the linearity enhanced direct UV grating writing technique. Significant improvement in terms of the spectral quality was achieved using this transfer function. This technique allows precise engineering of the amplitude and phase response of the gratings with complex structures at micron level. The PHTs were also integrated with directional couplers and flat top reflectors to perform ultra wide band all-optical SSB filters. This approach would allow implementing PHT devices for processing ultra wide-band optical signals with Terahertz bandwidth.

6.6 Conclusion

The photonics Hilbert transformers were experimentally demonstrated in this chapter. They were integrated with interferometric structures and flattop reflectors, which allowed them to work as all-optical single sideband filtering devices. RF signals operation performance of the devices was also presented. The design and responses of fractional order PHT were also discussed and characterised. Furthermore, the devices with Terahertz operation bandwidths were proposed and fabricated, via the linearity enhanced DGW technique. This linearity enhancement is extremely significant for synthesised gratings. The ultra wide-band all-optical single sideband filtering device was achieved in this work.

Chapter 7

Fibre Bragg grating fabrication

7.1 Introduction

This chapter presents some initial work on FBGs concluded at the end time of the PhD course. Gratings inscribed into the core of an optical fibre are well established, and have been developed into a number of important components for applications in fibre-optic communication and sensor systems. Advantages of fibre gratings over competing technologies include all-fibre geometry, low insertion loss, and commercially low cost [61]. They also have a distinguishing feature of flexibility for achieving the desired spectral characteristics. These are described in detail in several review papers and books [53, 99, 100]. Considering the fabrication platform in this work, the silica-on-silicon platform has similarities to optical fibres, such as the core dimension, material composite, and the photosensitivity behavior. It was considered worth extending the current planar waveguide fabrication technique to FBG inscription.

7.2 Fibre Bragg gratings

There are various techniques for FBG fabrication, such as the interferometric holographic technique [101], the phase mask related technique [129, 130], and the point-by-point writing technique [131]. In this work, the DGW technique was used and is similar to interferometric holography [101]. However the DGW approach uses small writing spots, improved writing stability and accuracy. Figure 7.1 shows the schematic of FBG fabrication method using DGW in this work. Since the writing spot is $\sim 6\mu m$ in diameter, the laser beam can be focused into the fibre core.

Figure 7.2 illustrates two types of groove structures made in silica, used to hold the fibres during fabrication. The fibre is placed in the groove underneath the beam and can be adjusted horizontally and vertically to be aligned to the writing spot, which is

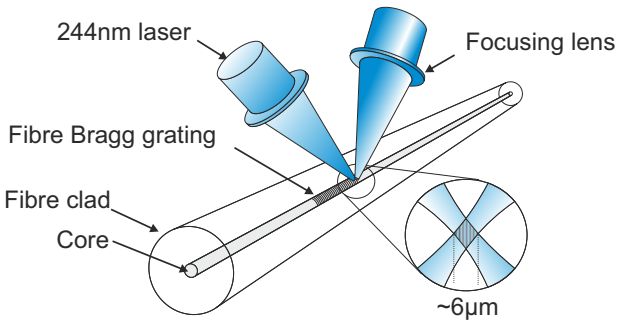

Figure 7.1: The schematic of fabricating fibre Bragg gratings using the direct UV grating technique, with the writing spot in $\sim 6\mu m$ diameter.

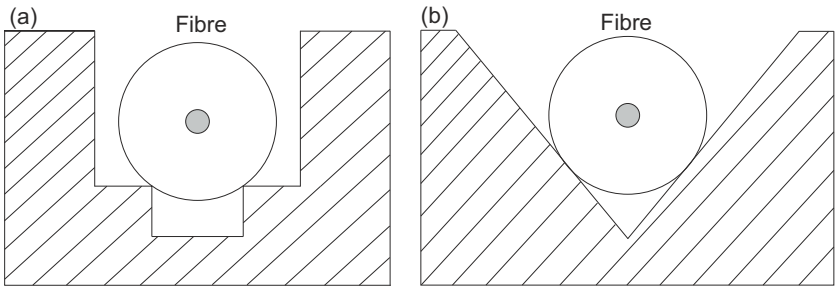

Figure 7.2: The schematics of (a) T-groove and (b) V-groove structures, diced within silica slides to hold bare fibres during fabrication.

similar to the planar samples alignment in this work. By using this setup, a number of FBGs were fabricated in this work.

Figure 7.3(a) shows the reflectivity spectra of a series of 5mm uniform FBGs fabricated in SMF28 fibre with increasing writing fluence (10-100kJ/cm^2). Figure 7.3(b) illustrates the uniform grating spectra with the fluence of 100, 150 and 200 kJ/cm^2 respectively. Figure 7.3(c) presents the maximum grating reflective index modulation depth Δn_{ac} of the FBGs with increasing fluence. The maximum Δn_{ac} is $\sim 10^{-5}$, this low figure could be improved by hydrogen loading or replacing the SMF28 with a highly photosensitive fibre.

The gratings shown in Fig. 7.3(b) were fabricated separately from the gratings in Fig. 7.3(a), with a fluence of of $100kJ/cm^2$, $150kJ/cm^2$ and $200kJ/cm^2$ respectively. The grating spectral quality degraded when made with the higher fluence. It was also found in Fig. 7.3(d) that the grating effective refractive index n_{eff} (calculated from the central wavelength) has a shift of $\sim 4 \times 10^{-4}$ for these high fluence gratings in this section of the fibre. It is believed to be due to an alignment issue in the FBG UV writing setup, the 'dc' refractive index change Δn_{dc} varied, altering the Bragg condition. Since the writing spot is much smaller then that of the phase mask technology(*e.g.* $\sim 100\mu m$), more effort and experience must be made to account for fibre alignment.

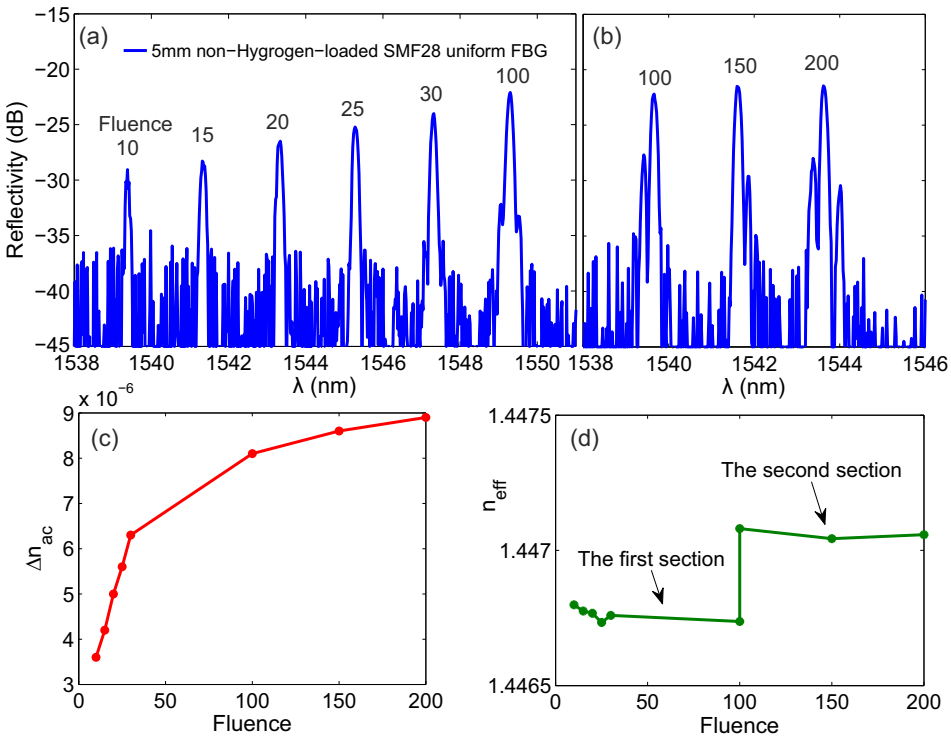

Figure 7.3: (a) Reflectivity spectra of a series of 5mm uniform FBGs in a single mode fibre with increased writing fluence (10-100kJ/cm^2); (b) the reflectivity spectra of 5mm uniform FBGs with writing fluence of 100kJ/cm^2, 150kJ/cm^2 and 200kJ/cm^2; (c) the maximum Δn_{ac} as a function of writing fluence; (d) the n_{eff} variation in the two separate sections of fabricated gratings, believed to be due to the different fibre alignment.

7.2.1 Bragg grating in multimode fibres

A multimode fibre (MMF) was used to make FBGs with the phase modulated UV grating writing technique. It is a Tm:Ge co-doped fibre fabricated in house, with the similar behaviour to a step index multimode fibre with a 10μm core diameter, 100μm outside diameter and a 0.18 numerical aperture (NA). The normalised frequency parameter (V number) of the MMF is $V \approx 3$.

Figure 7.4(a) shows the reflection spectrum of a 5mm uniform FBG in the MMF, with the writing fluence of 60kJ/cm^2. The fundamental mode LP_{01}, the higher order mode LP_{11} and the interaction between two modes LP_{01-11} are presented. With the increased writing fluence (60-80kJ/cm^2), the FBGs spectra were illustrated in Fig. 7.4(b). Fig. 7.4(c) and (d) show the characterised maximum grating reflective index modulation depth Δn_{ac} and the effective refractive index n_{eff} of the FBGs in the MMF. The differences of the value result from the modes distributions in the MMF.

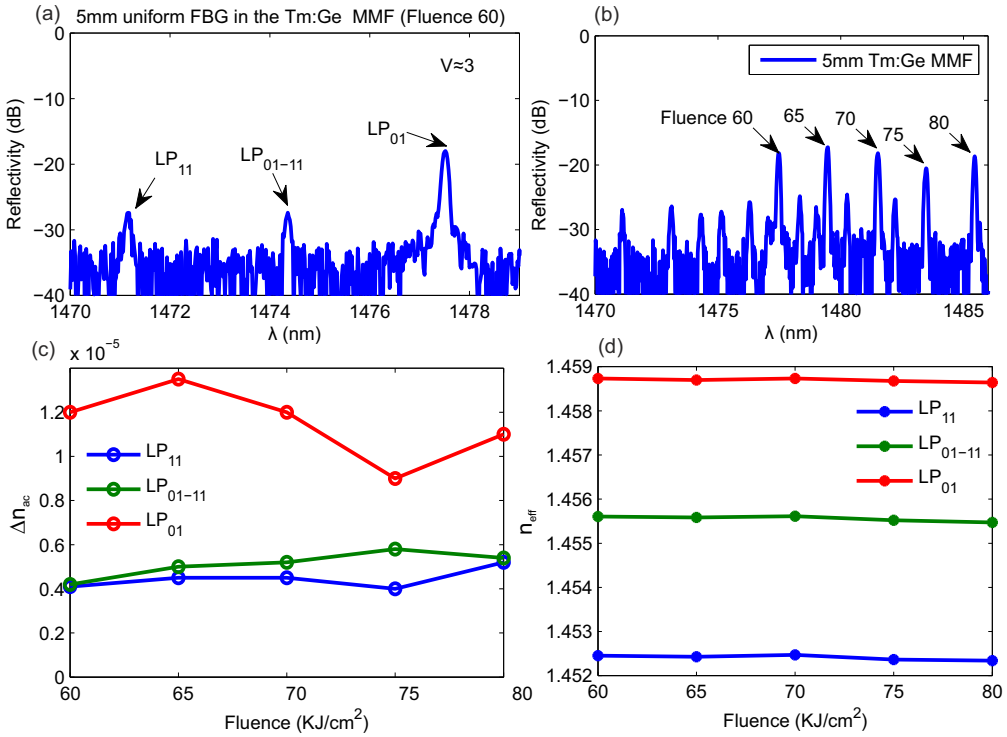

Figure 7.4: (a) The reflectivity spectrum of a 5mm uniform FBG fabricated in a Tm:Ge co-doped multimode fibre (MMF) with fluence of $60kJ/cm^2$, showing the higher order mode reflections; (b) the reflectivity spectra of a series of 5mm uniform FBGs in the MMF with increased writing fluence (60-80kJ/cm^2); (c) the maximum grating reflective index modulation depth Δn_{ac} of FBGs with increased fluence; (d) the effective refractive index n_{eff} of FBGs with increased fluence, corresponding to the different modes.

7.3 Grating engineering

7.3.1 Hydrogen loaded fibre

The SMF28 fibres were hydrogen loaded for 7 days at a pressure of 120bar at room temperatures before FBG fabrication. Uniform gratings were fabricated and characterised, and the maximum grating refractive index change Δn_{ac} is shown to approach 2×10^{-4} after hydrogen loading, a significant improvement compared to that of non-hydrogen-loaded SMF28 fibres.

7.3.2 Highly photosensitive fibre

The highly photosensitive fibres, Thorlab™ GF1 series of fibres, were used to make FBGs. These fibres are photosensitive fibres enabling high-reflectivity gratings to be written without the need to hydrogen-load. The reflectivity spectra of 1mm FBGs fabricated with increased writing fluence (5-35kJ/cm^2) were shown in Fig. 7.5. The maximum Δn of gratings in this fibre reaches 1.5×10^{-4} in this experiment.

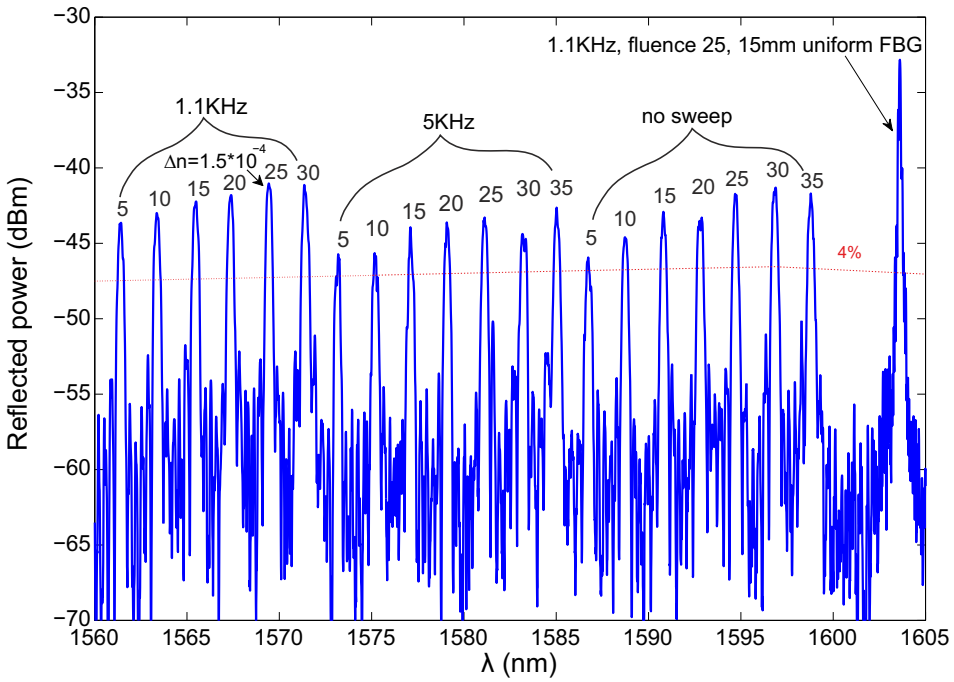

Figure 7.5: The reflectivity spectra of a series of 1mm uniform FBG fabricated in the photosensitive fibres with increased fluence (5-35kJ/cm^2) and different sweeping rates. The writing spot was simultaneously swept across $\sim 3\mu m$ distance in the perpendicular direction to the fibre core, with different repetition rates and controlled by a piezoelectric mirror in the UV writing setup.

7.3.3 Writing spot sweep

In the concept of writing spot sweeping, during the grating fabrication, the $\sim 6\mu m$ writing spot was simultaneously swept across the core of the fibre by a few microns in the perpendicular direction to the waveguide, with relatively high repetition rate and controlled by a piezoelectric mirror in the UV writing setup. The preliminary experimental data using the concept of sweeping the writing spot was illustrated in Fig. 7.5. The spot sweep would allow wider waveguides to be written in the core layer of planar samples, or FBGs inscribed into larger core fibres (*e.g.* multimode fibres). In Fig. 7.5, the reflection spectra of 1mm uniform FBGs were presented, using increasing fluence and different sweeping rates. The writing spot was observed to have a displacement of $\sim 3\mu m$ during this fabrication.

The sweeping frequency was 0Hz, 1.1kHz and 5kHz, and the corresponding grating spectra were illustrated in Fig. 7.5. Some degradation in the grating spectra occurred due to the alignment issue. The average reflectivity of gratings fabricated with increasing fluence indicates that the best sweeping rate is at 1.1kHz.

7.3.4 Thermal management

A strong thermal effect during FBG fabrication was revealed in this work. Figure 7.6 shows the realtime video capture of the grating reflection spectra from the OSA, during the fabrication of a series of 5mm uniform FBGs in the GF1 photosensitive fibre. The asymmetric spectral feature and the reflection peak shift were exhibited during the grating formation. Once the grating inscription completes and laser beam is simultaneously blocked (PSO signal preset by the computer), a sudden change of the spectrum occurs at around 36 seconds and 77 seconds (corresponding to the end times of the first and second gratings respectively), which leads to the anticipated normal symmetric uniform grating spectrum. This phenomenon recurred when beginning to fabricate the next FBG and are believed due to a laser induced thermal effect.

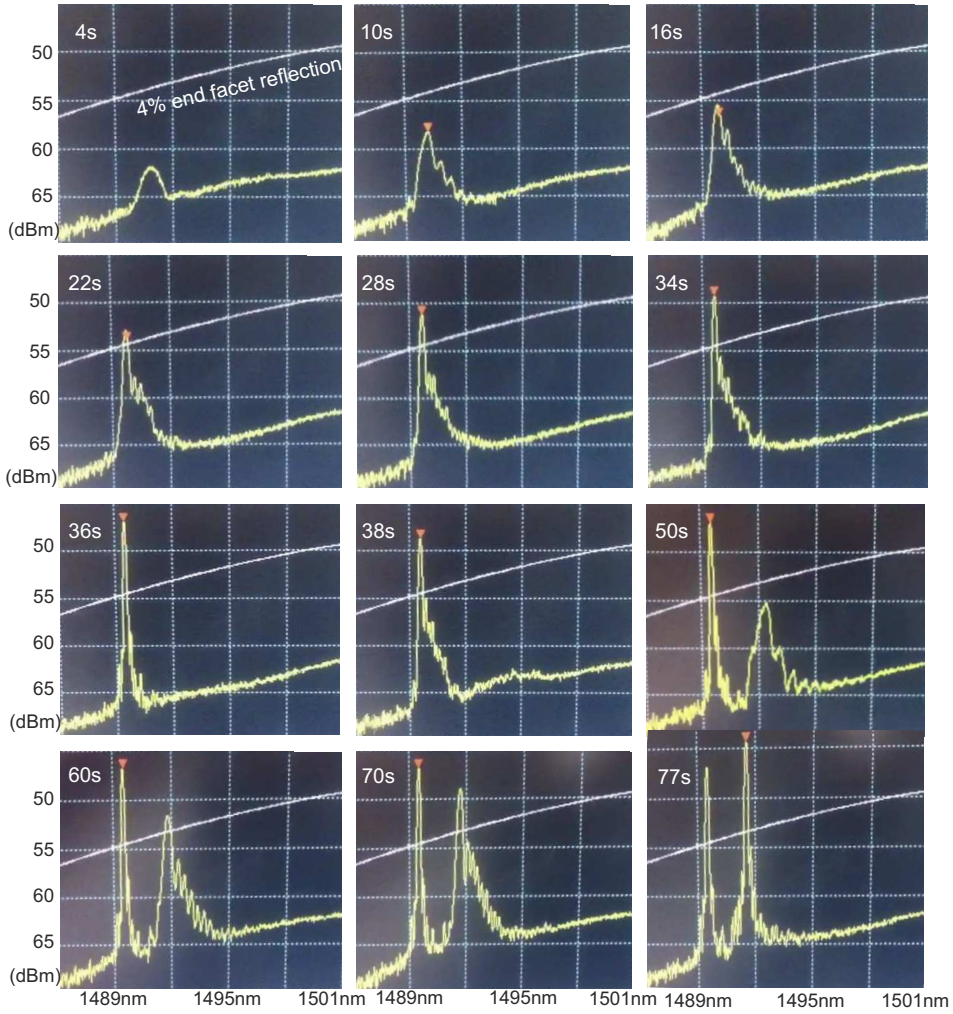

Figure 7.6: The realtime video capture of the grating reflection spectra (yellow line) compared to the end-facet reflection spectra of the source (white line) from the OSA, during the FBG fabrication in the GF1 photosensitive fibre. The grating spectrum has a sudden change at around 36 seconds (77 seconds as well). This abrupt behaviour and the grating asymmetric spectrum are believed due to the laser induced thermal effect.

To investigate the effect and reduce this artifact, a simple approach was proposed and experimentally demonstrated. It is known that water has a low UV absorption of $\sim 10^{-3}/cm$ at 244nm [132], a refractive index of ~ 1.38 at 244 nm at 21.5^oC [133], and much higher thermal conductivity as well as specific heat capacity than air. The grooves shown in Fig. 7.2 were filled with water to assist the UV laser inscription. The focused laser spot had less effect on the immersed fibre. As a result, the asymmetric spectrum and sudden change behaviour during fabrication disappeared, which was verified by the same realtime monitoring experiment of the reflection spectra.

To stabilise fibres during the stage translation, a thin glass slide was also put on top of grooves to cover the fibres, but, unfortunately, it caused more challenges in aligning the laser spot into the fibre core. Considering the alignment issue previously mentioned, the fibre holding stage needs to be further improved in the future work.

7.4 Conclusion

In this section, FBGs have for the first time been fabricated by using the small spot direct UV grating writing technique. FBGs within conventional single mode fibres, photosensitive fibres and multimode fibres have been fabricated and characterised. The piezoelectric sweep concept for making FBGs in fibres with large core sizes is also discussed. The in situ thermal management during the FBG fabrication are revealed and investigated. The fibre alignment is challenging and the experimental setup needs to be further improved. This UV grating writing technique with phase modulation shows potential for making arbitrary Bragg gratings in fibre structures.

Chapter 8

Conclusions

8.1 Conclusions

In this thesis, work has been presented on the theoretical understanding, design, modelling, fabrication and implementation of novel photonic Hilbert transform (PHT) devices for all-optical signal processing in advanced optical communication systems.

A transfer matrix model was developed initially for the analysis of planar Bragg grating based devices. Based on the coupled mode theory it can model a wide variety of Bragg grating structures, and devices containing Bragg gratings. The validity of the model has been verified through numerous analysis. Based on this modelling tool, a number of grating based Hilbert transform devices have been analysed. The gained understanding allowed the further optimization and design of novel high performance devices such as all-optical SSB filters. An inverse scattering method was also proposed for the optimal implementation of the PHT device. The inverse scattering method calculates grating parameters, based on the required grating reflectivity and phase responses.

The PHTs based on apodised and phase-shifted Bragg gratings were analysed in depth resulting to the development of an optimization process of three kinds of devices: conventional PHTs, FrHTs, and Terahertz bandwidth Hilbert Transformers (THTs).

A PHT designed accordingly to the proposed procedure can exhibit a relative flat-top amplitude response and a π (fractional π for FrHTs) phase shift at the central frequency. The manipulation of the grating apodisation profile was established and utilised, especially for the FrHTs and THTs. The properties of spectral response could be fully and independently tailored by employing a properly apodised Bragg grating. The system transfer function was also studied during the fabrication and the synthesised grating fabrication enhanced the grating spectral quality.

The class of full-coupler based interferometric filters for all-optical SSB modulation has been studied in detail. A novel monolithcally integrated SSB filtering configuration is

proposed for the first time, which composes of a PHT (FrHT or THT), flattop reflector, directional coupler (X-coupler) and micro heaters. This device exhibits fully integrated and tunable sideband suppression characteristics in contrast to the traditional discrete components or fibre based configuration. The flat top-hat spectral response characteristics of the proposed device allow ultra-wide bandwidth signal operation and improved suppression ratio. The device can be thermally tuned by localised micro heaters on top of waveguides, fabricated by the combination of E-beam metallic deposition and photolithography. A sideband suppression level of -12dB was achieved with the 6GHz RF signals operation.

A phase modulated DGW technique has been developed and its functionality has been confirmed through a number of experiments. A major problem towards the previously amplitude modulated DGW setup is lack of the linearity between the maximum grating refractive index change Δn_{ac} and the applied apodisation profile, which is critically necessary in the control and enhancement of grating responses. Linear control of the Δn_{ac} via the apodisation profile was achieved by using the electro-optical phase modulation in this work.

This phase-controlled method involves focusing two crossed laser beams into the photosensitive core of a planar sample. Constant translation of the sample and modulation of the fringe pattern defines the channel waveguide and simultaneously allows the creation of the grating structures. Phase modulation of one beam in the interferometer, achieved via an EOM, is used to manipulate the fringe pattern and thus control the parameters of the Bragg gratings and waveguides. This spot size is $\sim 6\mu m$ in diameter, providing the unique ability over traditional FBG to manipulate the grating's structure at the micron level. The method also offers significant time/energy efficiency as well as simplified optical layout and fabrication process. We have shown Bragg gratings can be made from 1200 nm to 1900nm exclusively under software control and the maximum peak reflectivity of 1mm uniform gratings only decreases by 3dB over a 250nm ($\sim 32THz$) bandwidth.

The FBG fabrication using this phase modulated DGW technique was also studied. FBGs in conventional single mode fibres, photosensitive fibres and multimode fibres were fabricated and characterised. The piezoelectric sweep concept for making FBGs in large core fibres was also discussed. A simple route for the in situ thermal management during the FBG fabrication was revealed and investigated, with the use of fibres immersed with water. The fibre alignment is challenging and the experimental setup needs to be further improved. This UV grating writing technique with phase modulation shows potential for making arbitrary Bragg gratings in fibre structures.

8.2 Future work

8.2.1 Direct phase measurement

In this work, optical phase responses of PHT devices were not measured directly, due to restrictions of the available characterisation setup. Nevertheless, interferometric structures with all-optical SSB filtering function were used to validate the phase shift of optical signals in this thesis. To evaluate the phase shift accuracy of the fabricated devices, there are some approaches to obtain optical phase spectra directly.

8.2.1.1 Optical vector analyser

The optical vector analyser (OVA) is based on swept-wavelength interferometry, using a interferometric network for spectral measurements of the transfer function of the device under test (DUT) [134].

An OVA was used to measure the reflection power and phase responses of the fabricated gratings in the references [43, 52]. This OVA can provide the DUT amplitude and phase characteristics in a single scan of a tunable laser. But this commercial product is expensive and was not available in our work.

8.2.1.2 Microwave photonics technique

Another approach is using the microwave photonics technique, discussed in detail as follows, with the discussion courtesy of Dr. L. Zhuang, University of Twente.

- One possible route is to use a CW laser with frequency-aligned in the passband of the PHT device and a dual-parallel MZI modulator to generate SSB frequency carrier modulation. The vector network analyser (VNA) could provide the S21 magnitude and phase measurement by sweeping through the RF frequency. The S21 parameter measurement in the VNA is a measure of the signal coming out one port relative to the RF stimulus entering the other port of the VNA [110]. Nevertheless, the measuring frequency bandwidth depends on the bandwidth of the VNA and is limited to tens of Gigahertz, and still not suitable for the widest bandwidth devices in the thesis.
- Another idea is to align the CW laser frequency to the notch point of the PHT device and use a regular intensity modulator for DSB frequency carrier modulation [46]. In this way with the VNA, the S21 magnitude and phase response of the right-hand side of the PHT could be achieved. The left-hand side response is in symmetric shape and shall give exactly the same contribution as the right-hand

side for the detected RF signal provided the CW laser frequency is well aligned at the notch point. However, besides the limited measuring bandwidth, it might be difficult to measure the PHT device with a deeper notch in the amplitude response, since the optical carrier in the notch frequency would be too heavily suppressed to be detected.

The proposed routes for obtaining grating phase responses are potential for the future work.

8.2.2 Direct UV grating writing technique

The phase modulated direct UV grating writing technique technique needs to be further refined. Considering the nonlinear effect of Δn observed during the duty cycle control, the transfer function of the entire system was utilised in this work to compensate for linearity enhancement. Recently we have started exploring alternative methods for Bragg grating writing, in order to allow grating writing processes more efficiently and controllably.

Replacing the EOM with a commercial device, as well as the high voltage amplifier with a unit with a higher frequency bandwidth, this should help reduce the nonlinear effect during the grating fabrication.

The combination of EOM and AOM could be employed synchronously during fabrication. In this work, duty cycle of 0.8 was chosen. In the remaining 0.2 amount of time, the laser spot still exposes to the moving sample, which could counteract the existed periodic pattern and affect the Δn. Hence an AOM could be introduced to block the laser beam during the 0.2 duty cycle interval and may increase the maximum Δn by additional 20% for the fabricated grating.

8.2.3 Applications of fractional Hilbert transformers

The general PHT and THT have been experimentally demonstrated in applications of all-optical SSB filtering. The FrHT has also been demonstrated based on optical ring resonators, achieving optical generation of microwave signals by means of optical heterodyning [46].

In the electronic field, FrHT was proposed in a secure SSB communication, in which the fractional order was used as a secret key for demodulation [135]. As the similar implementation in the optical domain, this concept of secure SSB communications using FrHTs is an interesting topic. But the initial idea of secure SSB communications using FrHTs has some challenges and needs more consideration. For example, the approach

to recover the key by trial and error or by monitoring the signals requires analysis, and the possible optical encryption schemes should be studied [136].

8.2.4 Fibre Bragg grating

The FBG fabrication was preliminarily demonstrated in this work. This work has significant potential for the fibre technology, and should be further investigated in the following areas.

8.2.4.1 Multimode fibre

With the small spot writing technique, by manipulating Bragg gratings structures and positions in some multimode fibres or large core fibres, optical modes selection, conversion or multiplexing/demultiplexing will be achieved [137, 138]. These concepts could also be realised in integrated planar geometries [139, 140].

8.2.4.2 Antireflection in high power fibre lasers

Another implementation of fabricated FBG is in the high energy delivery in fibres, such as high power fibre lasers. This technique could be used to prevent damages by the unwanted back reflection for a high power fibre laser or an amplifier system. Note that if the Fresnel reflection of $\sim 4\%$ from the fibre end facet is existed, the reflected power from the end facet of the fibre could approach 40W for 1kW system. This amount of optical power will cause serious thermal damages and also the efficiency degradation.

Recently, the power level of laser systems in industry area has reached a few tens of kW and beyond to MW. The demand for an efficient high-transmission and anti-reflection system has increased. Beside the current techniques such as the dielectric coating method, the use of FBG could be a simple and alternative solution compared to the dielectric coating at the end of a fibre. The principle is to inscribe a short FBG near the end of the fibre; when the amplitude and phase are properly matched, the reflected light from the grating and the end facet will interfere and cancel out to a subtle amount of power.

The uniform FBG has been initially demonstrated in a SMF28 fibre and resulted in a $\sim 1\%$ reflected power. The in situ realtime FBG interrogation is in consideration to obtain the optimised grating parameters for magnitude and phase matching. Moreover, the chirped FBG and sinc apodised FBG are also proposed and can allow arbitrary phase matching conditions and broadband spectral anti-reflections at the future.

Appendix A

Bragg grating derivation

The derivation begins from the material constitutive relations. The constitutive relations are:

$$\vec{D} = \varepsilon\vec{E} = \varepsilon_0 n^2 \vec{E}, \tag{A.1}$$

$$\vec{B} = \mu\vec{H} \tag{A.2}$$

where $\vec{E}$, $\vec{D}$, $\vec{B}$ and $\vec{H}$ denote the electric field, electric displacement, magnetic induction, and magnetic intensity, respectively. ε is the dielectric permittivity of the medium, μ is the magnetic permeability of the medium, n is the medium refractive index, ε_0 is the free space dielectric permittivity, and μ_0 represents the free space magnetic permeability.

For the nonmagnetic materials which normally constitute an optical waveguide, the magnetic permeability μ is rather similar to the free-space value μ_0, thus assuming $\mu = \mu_0$ for convenience.

For an isotropic ($\nabla\cdot\vec{D} = 0$), linear, nonconducting($\vec{J} = 0$), and non-magnetic ($\nabla\cdot\vec{B} = 0$) medium, **Maxwell's equations** are:

$$\nabla \times \vec{E} = -\frac{\partial\vec{B}}{\partial t} = (-\mu_0\frac{\partial\vec{H}}{\partial t}), \tag{A.3}$$

$$\nabla \times \vec{H} = \frac{\partial\vec{D}}{\partial t} = \varepsilon_0 n^2\frac{\partial\vec{E}}{\partial t}. \tag{A.4}$$

Take the curl of (A.3), substitute (A.4)with (A.2), we get

$$\begin{aligned}\nabla \times (\nabla \times \vec{E}) &= \nabla(\nabla \cdot \vec{E}) - \nabla^2 \vec{E} \\ &= \nabla \times (-\frac{\partial \vec{B}}{\partial t}) = \nabla \times (-\mu_0 \frac{\partial \vec{H}}{\partial t}) \\ &= -\mu_0 \frac{\partial(\nabla \times \vec{H})}{\partial t} = -\mu_0 \frac{\partial^2 \vec{D}}{\partial t^2} \\ &= -(\mu_0 \varepsilon_0 n^2 \frac{\partial^2 \vec{E}}{\partial t^2})\end{aligned}$$

Furthermore,

$$\begin{aligned}\nabla \cdot \vec{D} &= \varepsilon_0 \nabla \cdot (n^2 \vec{E}) = \varepsilon_0 (\nabla n^2 \cdot \vec{E} + n^2 \nabla \cdot \vec{E}) = 0. \\ \nabla \cdot \vec{E} &= -\frac{1}{n^2} \nabla n^2 \cdot \vec{E}.\end{aligned}$$

So we arrive at the **wave equation**:

$$\nabla^2 \vec{E} - \mu_0 \varepsilon_0 n^2 \frac{\partial^2 \vec{E}}{\partial t^2} + \nabla(\frac{1}{n^2} \nabla n^2 \cdot \vec{E}) = 0. \tag{A.5}$$

Similarly for the magnetic field,

$$\nabla^2 \vec{H} - \mu_0 \varepsilon_0 n^2 \frac{\partial^2 \vec{H}}{\partial t^2} + \frac{1}{n^2} \nabla n^2 \times (\nabla \times \vec{H}) = 0. \tag{A.6}$$

The scalar wave equation for the homogeneous medium,

$$\nabla^2 E - \mu_0 \varepsilon_0 n^2 \frac{\partial^2 E}{\partial t^2} = 0. \tag{A.7}$$

Expression for the electric field

When the electric field $\vec{E}$ is sinusoidal functions of time, it is often represented as complex amplitudes [14]. We do not consider the term $e^{i\beta r}$ for simplicity here. As an example, the electric field vector is expressed as:

$$\vec{E}(t) = |\vec{E}| \cos(\omega t + \phi) = Re\{\vec{E} e^{iwt}\} = \frac{1}{2}(\vec{E} e^{i\omega t} + \vec{E}^* e^{-i\omega t}) \tag{A.8}$$

where $|\vec{E}|$ is the amplitude, ϕ is the phase, and $*$ denotes the complex conjugate. Defining the complex amplitude of $\vec{E}(t)$ by $\vec{E} = |\vec{E}| e^{j\phi}$, we will represent $\vec{E}(t)$ by

$$\vec{E}(t) = \vec{E} e^{i\omega t} \tag{A.9}$$

instead of by (A.8).

This expression is not strictly correct; when using this phasor expression we should keep in mind that what is meant by (A.9) is the real part of $\vec{E}e^{i\omega t}$. In most mathematical manipulations, such as addition, subtraction, differentiation and integration, this replacement of (A.8) by the complex form (A.9) poses no problems [14].

However, we should be careful in the manipulations that involve the product of sinusoidal functions. In these cases we must use the real function or complex conjugates in (A.8). In Kashyap's book [53], $\vec{E}e^{i\omega t} + cc.$ is chosen for the field expression, which is the same as (A.8).

Electric Field in Planar Waveguide

As long as the core and cladding refractive indices are nearly equal (which is true for all practical fibres and planar Bragg gratings), the longitudinal components of the electric and magnetic fields are usually negligible in comparison to the corresponding transverse components, which is referred as **weakly guiding approximation**.

Consequently, for the refractive index varies only in the transverse direction, that is $n^2 = n^2(y)$ for planar geometry, the equations (A.5) and (A.6) can be separated out in the time and z part. Thus the solutions of equation (A.5) and (A.6) can be written as

$$\vec{E}(x, y, z, t) = \vec{E}(x, y, t)e^{-i\vec{\beta}z} \tag{A.10}$$

$$\vec{H}(x, y, z, t) = \vec{H}(x, y, t)e^{-i\vec{\beta}z} \tag{A.11}$$

Furthermore, the total electric field is

$$\vec{E}(x, y, z, t) = \vec{\Psi}(x, y, z)e^{i\omega t} = \vec{\psi}(x, y)e^{-i\vec{\beta}z}e^{i\omega t} \tag{A.12}$$

Substituting (A.12) into (A.3)and (A.4), and taking out the x, y and z components, we obtain the following equations

$$\begin{aligned}
i\beta E_y &= -i\omega\mu_0 H_x \\
\frac{\partial E_y}{\partial x} &= -i\omega\mu_0 H_z \\
-i\beta H_x - \frac{\partial H_z}{\partial x} &= i\omega\varepsilon_0 n^2 E_y \\
i\beta H_y &= i\omega\varepsilon_0 n^2 E_x \\
\frac{\partial H_y}{\partial x} &= i\omega\varepsilon_0 n^2 E_z \\
-i\beta E_x - \frac{\partial E_z}{\partial x} &= -i\omega\mu_0 H_y
\end{aligned}$$

The first three equations involve only E_y, H_x, and H_z. This set of equations corresponds to the modes with E_z vanishing and that means no electric field component along the

propagation direction, so called transverse electric(**TE**) modes. Similarly, the last three equations correspond to transverse magnetic(**TM**) modes in planar waveguides.

Substituting (A.12) into (A.7),

$$e^{-i\beta z}e^{i\omega t}\frac{\partial^2\psi(x,y)}{\partial x^2}+e^{-i\beta z}e^{i\omega t}\frac{\partial^2\psi(x,y)}{\partial y^2}+\beta^2e^{i\omega t}\psi(x,y)-\mu_0\varepsilon_0n^2\omega^2e^{-i\beta z}e^{i\omega t}\psi(x,y)$$
$$=e^{-i\beta z}e^{i\omega t}[(\nabla^2-\frac{\partial^2}{\partial z^2})\psi(x,y)+\mu_0\varepsilon_0n^2\omega^2\psi(x,y)-\beta^2\psi(x,y)]=0$$

So we'll find the transverse component $\psi(x,y)$ satisfies the following **scalar wave equation**

$$\nabla_t^2\psi+[k_0^2n^2(x,y)-\beta^2]\psi=0. \tag{A.13}$$

where $\nabla_t^2=\nabla^2-\partial^2/\partial z^2$, t is the transverse subscript, $k_0=\omega\sqrt{\mu_0\varepsilon_0}$ and $\omega=2\pi\nu$ is angular frequency.

$\vec{\beta}$ is the propagation vector constant and $\beta=|\vec{\beta}|$ is the phase propagation constant or the wave number.

$$\beta=|\vec{\beta}|=\frac{n\omega}{c}=\frac{2\pi}{\lambda}$$

where ν is the light frequency,and c is the light speed in vacuum.

Coupled-Mode Equations For Periodic Coupling.

Consider a planar waveguide with a refractive index profile $n(x,y)$ in which there is a periodic z-dependent perturbation $\Delta n(x,y,z)$.

$\psi_1(x,y)$ and $\psi_2(x,y)$ are two modes to be coupled in the waveguide with the same $n^2(x,y)$ and different propagation constant β_1, β_2. From (A.13), they satisfy the following equations.

$$\nabla_t^2\psi_1+[k_0^2n^2(x,y)-\beta_1^2]\psi_1=0 \tag{A.14}$$
$$\nabla_t^2\psi_2+[k_0^2n^2(x,y)-\beta_2^2]\psi_2=0 \tag{A.15}$$

The orthogonality condition is also satisfied

$$\int_{-\infty}^{\infty}\int_{-\infty}^{\infty}\psi_1^*(x,y)\psi_2(x,y)dxdy=0 \tag{A.16}$$

The total electric field in the waveguide at any value of z is given as

$$E(x,y,z,t)=\Psi(x,y,z)e^{i\omega t}=[A(z)\psi_1(x,y)e^{-i\beta_1z}+B(z)\psi_2(x,y)e^{-i\beta_2z}]e^{i\omega t} \tag{A.17}$$

where $A(z)$ and $B(z)$ are amplitudes of the two modes and are z-dependent. According to (A.7), the wave equation satisfied by $\Psi(x, y, z)$ is

$$\nabla^2\Psi + k_0^2[n^2(x, y) + 2n(x, y)\Delta n(x, y, z)]\Psi = 0 \tag{A.18}$$

To be noted, in Ghatak's book [60], the perturbation of permittivity was defined as $\varepsilon_r + \Delta\varepsilon = n^2(x, y) + \Delta n^2(x, y, z)$ and $\Delta n^2(x, y, z)$ was expressed in a periodic or almost-periodic function.

Nevertheless, in Kashyap's book [53], the perturbation of permittivity was defined as $\varepsilon_r + \Delta\varepsilon = [n(x, y) + \Delta n(x, y, z)]^2 = n^2(x, y) + 2n(x, y)\Delta n(x, y, z) + \Delta n^2(x, y, z)$ while $\Delta n(x, y, z)$, not $\Delta n^2(x, y, z)$ was expressed as a periodic or almost-periodic function. In this case, assuming $\Delta n(x, y, z) \ll n(x, y)$, ignoring $\Delta n^2(x, y, z)$, then $\varepsilon_r + \Delta\varepsilon \approx n^2(x, y) + 2n(x, y)\Delta n(x, y, z)$.

These two expressions will cause the same results , depending on the definitions of perturbation in propagation waveguide. Since it is more apparent for many papers and books on Bragg gratings [61], to use $\Delta n(x, y, z)$ for the refractive index perturbation, the second definition is employed in the derivation here.

Then substituting Equation (A.17) into (A.18), we get

$$\begin{aligned}
0 &= \nabla^2\psi + k_0^2[n^2(x, y) + 2n(x, y)\Delta n(x, y, z)]\Psi \\
&= A(z)e^{-i\beta_1 z}[\nabla_t^2\psi_1 + [k_0^2 n^2(x, y) - \beta_1^2]\psi_1] \quad \{\texttt{zero}\} \\
&\quad + B(z)e^{-i\beta_2 z}[\nabla_t^2\psi_2 + [k_0^2 n^2(x, y) - \beta_2^2]\psi_2] \quad \{\texttt{zero}\} \\
&\quad + [\frac{d^2A(z)}{dz^2}\psi_1(x, y)e^{-i\beta_1 z} + \frac{d^2B(z)}{dz^2}\psi_2(x, y)e^{-i\beta_2 z}] \quad \{\texttt{neglected}\} \\
&\quad - 2i\beta_1 e^{-i\beta_1 z}\psi_1(x, y)\frac{dA(z)}{dz} - 2i\beta_2 e^{-i\beta_2 z}\psi_2(x, y)\frac{dB(z)}{dz} \\
&\quad + k_0^2 2n(x, y)\Delta n(x, y, z)][A(z)\psi_1(x, y)e^{-i\beta_1 z} + B(z)\psi_2(x, y)e^{-i\beta_2 z}]
\end{aligned}$$

Using (A.14)and (A.15), the first and second components in the above equation are zero and , while the third component is neglected as the second derivatives of $A(z)$ and $B(z)$ over z with **slowly varying envelope approximation**.

Then equation (A.18) turns to

$$\begin{aligned}
&-2i\beta_1 e^{-i\beta_1 z}\psi_1(x, y)\frac{dA(z)}{dz} - 2i\beta_2 e^{-i\beta_2 z}\psi_2(x, y)\frac{dB(z)}{dz} \\
&+ k_0^2 2n(x, y)\Delta n(x, y, z)[A(z)\psi_1(x, y)e^{-i\beta_1 z} + B(z)\psi_2(x, y)e^{-i\beta_2 z}] \\
&= 0
\end{aligned} \tag{A.19}$$

Defining $\Delta\beta = \beta_1 - \beta_2$, multiplying equation (**??**) by $\psi_1^*(x,y)e^{i\beta_1 z}$ and integrating, we obtain

$$\begin{aligned}
&-2i\beta_1\frac{dA(z)}{dz}\int_{-\infty}^{\infty}\int_{-\infty}^{\infty}\psi_1(x,y)\psi_1^*(x,y)dxdy \\
&-2i\beta_2\frac{dB(z)}{dz}e^{i\Delta\beta z}\int_{-\infty}^{\infty}\int_{-\infty}^{\infty}\psi_2(x,y)\psi_1^*(x,y)dxdy \\
&+k_0^2\int_{-\infty}^{\infty}\int_{-\infty}^{\infty}2n(x,y)\Delta n(x,y,z)A(z)\psi_1(x,y)\psi_1^*(x,y)dxdy \\
&+k_0^2\int_{-\infty}^{\infty}\int_{-\infty}^{\infty}2n(x,y)\Delta n(x,y,z)B(z)\psi_2(x,y)e^{-i\Delta\beta z}\psi_1^*(x,y)dxdy = 0
\end{aligned}$$

where the second component is zero due to the orthogonality condition (A.16). Then simplifying the above equation

$$\frac{dA}{dz} = -ic_{11}A - ic_{12}Be^{i\Delta\beta z} \tag{A.20}$$

Similarly, multiplying equation (A.19) by $\psi_2^*(x,y)$ and integrating, we have

$$\frac{dB}{dz} = -ic_{22}B - ic_{21}Ae^{-i\Delta\beta z} \tag{A.21}$$

where $\Delta\beta = \beta_1 - \beta_2$,

$$\begin{aligned}
c_{11}(z) &= \frac{k_0^2}{\beta_1}\frac{\iint\psi_1^* n(x,y)\Delta n(x,y,z)\psi_1 dxdy}{\iint\psi_1^*\psi_1 dxdy} \\
c_{12}(z) &= \frac{k_0^2}{\beta_1}\frac{\iint\psi_1^* n(x,y)\Delta n(x,y,z)\psi_2 dxdy}{\iint\psi_1^*\psi_1 dxdy} \\
c_{22}(z) &= \frac{k_0^2}{\beta_2}\frac{\iint\psi_2^* n(x,y)\Delta n(x,y,z)\psi_2 dxdy}{\iint\psi_2^*\psi_2 dxdy} \\
c_{21}(z) &= \frac{k_0^2}{\beta_2}\frac{\iint\psi_2^* n(x,y)\Delta n(x,y,z)\psi_1 dxdy}{\iint\psi_2^*\psi_2 dxdy}
\end{aligned} \tag{A.22}$$

Equations (A.20) and (A.21) are the **coupled-mode equations** with the z-dependent perturbation.

Refractive index modulation

For Bragg grating geometries, the refractive index perturbation exists only in the core and is zero outside. In a periodic z-dependent perturbation, the refractive index modulation is given as

$$\Delta n(x,y,z) = \Delta n_{dc}(z) + \Delta n_{ac}(x,y)\bar{\Delta n}(z)\cos[\frac{2\pi}{\Lambda}z + \phi(z)] \tag{A.23}$$

- $\Delta n_{dc}(z)$: the average value of the refractive index change ('dc' offset)

- $\Delta n_{ac}(x, y)$: the maximum value of index change
- $\Delta\bar{n}(z)$: the grating apodisation profile (*e.g.* Gaussian, raise-cosine), $0 \sim 1$
- Λ : the perturbation period (grating period)
- $\phi(z)$: describes the grating chirp

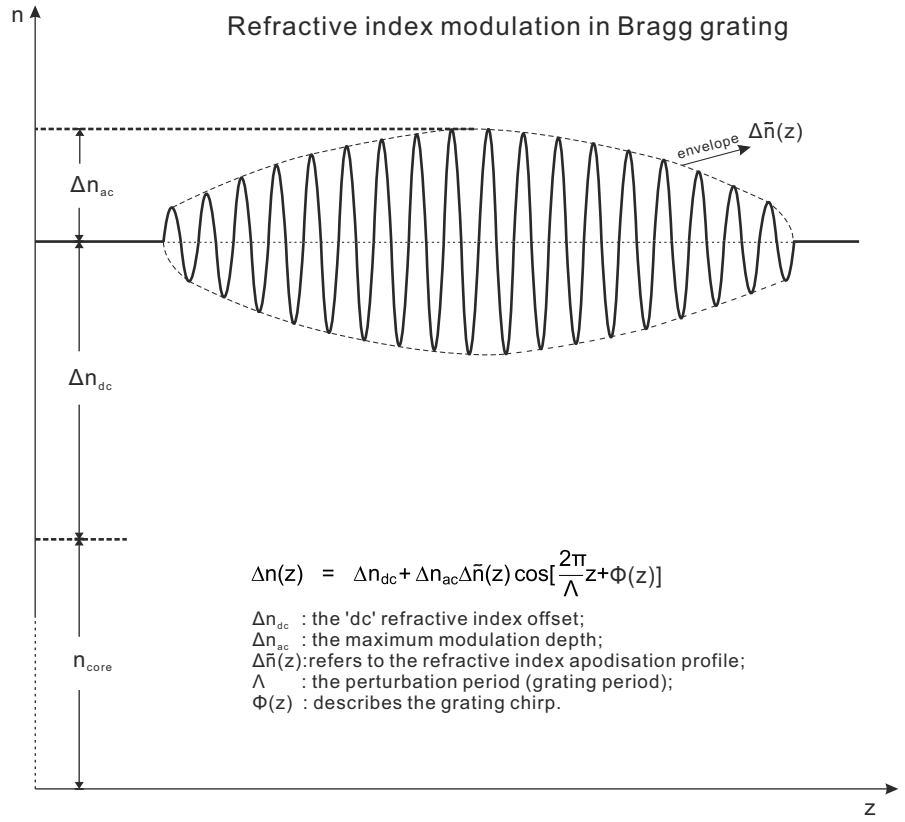

Figure A.1: Schematic diagram of the refractive index modulation in Bragg gratings. Dashed arrows are about fibre Bragg gratings and solid arrows are in planar Bragg gratings.

Then we discuss the components of the index modulation function relating to our direct UV grating writing fabrication technique.

1. The first component $\Delta n_{dc}(z)$ is the average index change of the grating section, unvarying part of index modulation. The planar Bragg gratings in our work are generally fluence matched, which means the average refractive index change is designed to be equal to the UV induced index increase $\Delta n_{dc}(z)$ of the grating channel.

   Once the fluence is fixed (*e.g.* $18kJ/cm^2$) ahead of fabrication, $\Delta n_{dc}(z) = \Delta n_{dc}$ remains constant. $\Delta n_{dc}(z)$ is always approximately zero in our planar Bragg gratings.

2. The second component of $\Delta n(x, y, z)$ has to do with duty cycle, which refers to the symmetry of the refractive index profile and the modulation depth, alternatively the grating strength.

   Analogous to the meaning of the term in electronics, duty cycle in this case represents the ratio between the time when the laser is on to the time when the laser is off over the space of a single exposure. Clearly, for the same writing translation speed setting, the grating plane modulation reduces with increase in duty cycle. As the duty cycle approaches 100%, channel waveguides are produced instead of gratings. Once duty cycle is chosen (*i.e.*, max value 50%), $\Delta n_{ac}(x, y)$ is considered to be constant as $\Delta n_{ac}(x, y) = \Delta n_{ac}$.

3. In Figure A.1, n_{core} could be constant for step index fibres, or (x, y) dependent (*e.g.* parabolic) for graded index fibres.

Hence, for our planar Bragg gratings, the refractive index modulation illustrated in Figure **??** becomes

$$\Delta n(z) \quad = \quad \Delta n_{dc} + \Delta n_{ac} \bar{\Delta n}(z) \cos[\frac{2\pi}{\Lambda} z + \phi(z)] \tag{A.24}$$

For fibre Bragg gratings, according to the discussion of refractive index modulation in Erdogan's paper [61], it's simplified to describe the perturbation to the effective refractive index n_{eff} of the guided mode(s) of interest as

$$\delta n_{eff}(z) = \overline{\delta n_{eff}}(z)\{1 + \nu \cos[\frac{2\pi}{\Lambda} z + \phi(z)]\}, \tag{A.25}$$

where ν is the fringe visibility of the index change, also shown in Fig. **??**.

Synchronous Approximation

Assuming the modes ϕ_1 and ϕ_2 are normalized to carry unit power, under the weakly guiding approximation we may write

$$\frac{\beta_1}{2\omega\mu_0} \int\int \psi_1^* \psi_1 dxdy = 1$$
$$\frac{\beta_2}{2\omega\mu_0} \int\int \psi_2^* \psi_2 dxdy = 1$$

and $|A|^2$ and $|B|^2$ give the power carried by both modes.

The coefficients c_{ij} in Eq.(A.22) can be re-written as

$$\begin{aligned}
c_{11}(z) &= \frac{k_0^2}{\beta_1} n_{eff}\{\Delta n_{dc} + \Delta n_{ac}\tilde{\Delta n}(z)\cos[\frac{2\pi}{\Lambda}z + \phi(z)]\} \\
c_{12}(z) &= \frac{\omega\varepsilon_0}{2}\iint \psi_1^* n(x,y)\Delta n(x,y,z)\psi_2 dxdy \\
&= \frac{\omega\varepsilon_0}{2} n_{eff}\{\Delta n_{dc} + \Delta n_{ac}\tilde{\Delta n}(z)\cos[\frac{2\pi}{\Lambda}z + \phi(z)]\}\iint_{core}\psi_1^*\psi_2 dxdy \\
c_{21}(z) &= \frac{\omega\varepsilon_0}{2}\iint \psi_2^* n(x,y)\Delta n(x,y,z)\psi_1 dxdy \\
&= \frac{\omega\varepsilon_0}{2} n_{eff}\{\Delta n_{dc} + \Delta n_{ac}\tilde{\Delta n}(z)\cos[\frac{2\pi}{\Lambda}z + \phi(z)]\}\iint_{core}\psi_2^*\psi_1 dxdy \\
c_{22}(z) &= \frac{k_0^2}{\beta_2} n_{eff}\{\Delta n_{dc} + \Delta n_{ac}\tilde{\Delta n}(z)\cos[\frac{2\pi}{\Lambda}z + \phi(z)]\}
\end{aligned}$$

Substituting (A.24), c_{11} and c_{12} into (A.20), deriving as follows:

$$\begin{aligned}
\frac{dA(z)}{dz} &= -i\frac{k_0^2}{\beta_1} n_{eff}\{\Delta n_{dc} + \Delta n_{ac}\tilde{\Delta n}(z)\cos[\frac{2\pi}{\Lambda}z + \phi(z)]\}A(z) \\
&\quad -i\{\frac{\omega\varepsilon_0}{2} n_{eff}\Delta n_{dc} + \Delta n_{ac}\tilde{\Delta n}(z)\cos[\frac{2\pi}{\Lambda}z + \phi(z)]\}\iint_{core}\psi_1^*\psi_2 dxdyB(z)e^{i\Delta\beta z} \\
&= -i\frac{k_0^2}{\beta_1} n_{eff}\Delta n_{dc}A(z) \\
&\quad -i\frac{k_0^2}{\beta_1} n_{eff}\Delta n_{ac}\tilde{\Delta n}(z)\cos[\frac{2\pi}{\Lambda}z + \phi(z)]\}A(z) \\
&\quad -i\frac{\omega\varepsilon_0}{2} n_{eff}\Delta n_{dc}\iint_{core}\psi_1^*\psi_2 dxdyB(z)e^{i\Delta\beta z} \\
&\quad -i\frac{\omega\varepsilon_0}{2} n_{eff}\Delta n_{ac}\tilde{\Delta n}(z)\cos[\frac{2\pi}{\Lambda}z + \phi(z)]\}\iint_{core}\psi_1^*\psi_2 dxdyB(z)e^{i\Delta\beta z}
\end{aligned}$$

With $\cos(x) = \frac{e^{ix}+e^{-ix}}{2}$, continuing the derivation

$$\begin{aligned}
&\frac{dA(z)}{dz} = -i\frac{k_0^2}{\beta_1} n_{eff}\Delta n_{dc}A(z) \\
&-i\frac{k_0^2}{\beta_1} n_{eff}\Delta n_{ac}\tilde{\Delta n}(z)A(z)\cos[\frac{2\pi}{\Lambda}z + \phi(z)] \\
&-i\frac{\omega\varepsilon_0}{2} n_{eff}\Delta n_{dc}\iint_{core}\psi_1^*\psi_2 dxdyB(z)e^{i\Delta\beta z} \\
&-i\frac{\omega\varepsilon_0}{4} n_{eff}\Delta n_{ac}\tilde{\Delta n}(z)\iint_{core}\psi_1^*\psi_2 dxdyB(z)e^{i[(\Delta\beta-\frac{2\pi}{\Lambda})z-\phi(z)]} \\
&-i\frac{\omega\varepsilon_0}{4} n_{eff}\Delta n_{ac}\tilde{\Delta n}(z)\iint_{core}\psi_1^*\psi_2 dxdyB(z)e^{i[(\Delta\beta+\frac{2\pi}{\Lambda})z+\phi(z)]} \qquad \text{(A.26)}
\end{aligned}$$

Then we begin to derive Synchronous Approximation. For weak perturbations, the coupling coefficients are small. If we integrate above equation over distance L, small compared with the distance over which A and B change appreciably. Now we consider about the contribution on the mode amplitude change from the components in (A.27).

Because $\Delta\tilde{n}(z)$ and $e^{i\phi(z)}$ have the same influence on the 2nd , 4th and 5th components in (A.27), we could ignore integrating $\Delta\tilde{n}(z)$ and $e^{i\phi(z)}$ for simplicity and then obtain

$$
\begin{aligned}
&A(z+\frac{L}{2}) - A(z-\frac{L}{2}) = \\
&-i\frac{k_0^2}{\beta_1} n_{eff} \Delta n_{dc} AL \\
&-i\frac{k_0^2}{\beta_1} n_{eff} \Delta n_{ac} \Delta\tilde{n}(z) * A * \underbrace{[\frac{\sin[\frac{2\pi}{\Lambda}z + \phi(z)]}{\frac{2\pi}{\Lambda} + \frac{d\phi(z)}{dz}}|_{z-\frac{L}{2}}^{z+\frac{L}{2}}]}_{} \\
&-\frac{i\omega\varepsilon_0}{2} n_{eff} \Delta n_{dc} \iint_{core} \psi_1^* \psi_2 dxdy * B * \underbrace{[\frac{e^{i\Delta\beta z}}{\Delta\beta}|_{z-\frac{L}{2}}^{z+\frac{L}{2}}]}_{} \\
&-\frac{\omega\varepsilon_0}{4} n_{eff} \Delta n_{ac} \Delta\tilde{n}(z) \iint_{core} \psi_1^* \psi_2 dxdy * B e^{-i\phi(z)} * \underbrace{[\frac{e^{i(\Delta\beta - \frac{2\pi}{\Lambda})z}}{\Delta\beta - \frac{2\pi}{\Lambda}}|_{z-\frac{L}{2}}^{z+\frac{L}{2}}]}_{} \\
&-\frac{\omega\varepsilon_0}{4} n_{eff} \Delta n_{ac} \Delta\tilde{n}(z) \iint_{core} \psi_1^* \psi_2 dxdy * B e^{i\phi(z)} * \underbrace{[\frac{e^{i(\Delta\beta + \frac{2\pi}{\Lambda})z}}{\Delta\beta + \frac{2\pi}{\Lambda}}|_{z-\frac{L}{2}}^{z+\frac{L}{2}}]}_{}
\end{aligned}
$$

For the components with under brace in the integral above, we get

$$
\left|\frac{\sin[\frac{2\pi}{\Lambda}z + \phi(z)]}{\frac{2\pi}{\Lambda} + \frac{d\phi(z)}{dz}}|_{z-\frac{L}{2}}^{z+\frac{L}{2}}\right| = 2\left|\frac{\cos[\frac{2\pi}{\Lambda}z + \phi(z)]}{\frac{2\pi}{\Lambda} + \frac{d\phi(z)}{dz}}\right|
$$

$$
\left|\frac{e^{i\Delta\beta z}}{\Delta\beta}|_{z-\frac{L}{2}}^{z+\frac{L}{2}}\right| = \left|2i\sin(\frac{\Delta\beta L}{2})e^{i\Delta\beta z}\right| = 2\left|\frac{\sin(\frac{\Delta\beta L}{2})}{\Delta\beta}\right|
$$

$$
\left|\frac{e^{i(\Delta\beta - \frac{2\pi}{\Lambda})z}}{\Delta\beta - \frac{2\pi}{\Lambda}}|_{z-\frac{L}{2}}^{z+\frac{L}{2}}\right| = \left|2ie^{i(\Delta\beta - \frac{2\pi}{\Lambda})z}\right| \left|\frac{\sin(\Delta\beta - \frac{2\pi}{\Lambda})\frac{L}{2}}{\Delta\beta - \frac{2\pi}{\Lambda}}\right| = 2\left|\frac{\sin(\Delta\beta - \frac{2\pi}{\Lambda})\frac{L}{2}}{\Delta\beta - \frac{2\pi}{\Lambda}}\right|
$$

$$
\left|\frac{e^{i(\Delta\beta + \frac{2\pi}{\Lambda})z}}{\Delta\beta + \frac{2\pi}{\Lambda}}|_{z-\frac{L}{2}}^{z+\frac{L}{2}}\right| = \left|2ie^{i(\Delta\beta + \frac{2\pi}{\Lambda})z}\right| \left|\frac{\sin(\Delta\beta + \frac{2\pi}{\Lambda})\frac{L}{2}}{\Delta\beta + \frac{2\pi}{\Lambda}}\right| = 2\left|\frac{\sin(\Delta\beta + \frac{2\pi}{\Lambda})\frac{L}{2}}{\Delta\beta + \frac{2\pi}{\Lambda}}\right|
$$

Now,

$$
\Delta\beta = \frac{2\pi}{\lambda_0}\Delta n_{eff}
$$

where Δn_{eff} is the effective index difference between the modes. As a typical value, Δn_{eff} is approximately the index difference between the core and cladding, assumed to be 0.005, gives for $\lambda_0 = 1.5\mu m$

$$
\Delta\beta \approx 2 \times 10^4 m^{-1}
$$

If $\frac{2\pi}{\Lambda}$ is chosen as $\frac{2\pi}{\Lambda} \approx \Delta\beta$ and $L \approx 10^{-2}m$, then

$$\left|\frac{\cos[\frac{2\pi}{\Lambda}z+\phi(z)]}{\frac{2\pi}{\Lambda}+\frac{d\phi(z)}{dz}}\right| \leqslant \frac{1}{\frac{2\pi}{\Lambda}+\frac{d\phi(z)}{dz}} \approx \frac{1}{\frac{2\pi}{\Lambda}} \approx \frac{1}{\Delta\beta} = 5\times10^{-5}m$$
$$\left|\frac{\sin(\frac{\Delta\beta L}{2})}{\Delta\beta}\right| \leqslant \frac{1}{\Delta\beta} = 5\times10^{-5}m$$
$$\left|\frac{\sin(\Delta\beta-\frac{2\pi}{\Lambda})\frac{L}{2}}{\Delta\beta-\frac{2\pi}{\Lambda}}\right| \approx \frac{L}{2} = 5\times10^{-3}m$$
$$\left|\frac{\sin(\Delta\beta+\frac{2\pi}{\Lambda})\frac{L}{2}}{\Delta\beta+\frac{2\pi}{\Lambda}}\right| \leqslant \frac{1}{\Delta\beta+\frac{2\pi}{\Lambda}} \approx \frac{1}{2\Delta\beta} = 2.5\times10^{-5}m$$

It is reasonable that $L(in10^{-3}m)$ is lager than $\Delta\beta^{-1}(in10^{-6}m)$ by several orders of magnitude for Bragg gratings. Thus, the effect from $e^{i(\Delta\beta+\frac{2\pi}{\Lambda})z}$ term is negligible compared with $e^{i(\Delta\beta-\frac{2\pi}{\Lambda})z}$ term and $e^{i(\Delta\beta+\frac{2\pi}{\Lambda})z}$ term can be ignored. It's similar when $\Delta\beta \approx -\frac{2\pi}{\Lambda}$ $e^{i(\Delta\beta-\frac{2\pi}{\Lambda})z}$ term is dismissed. So (A.26) becomes

$$\begin{aligned}&\frac{dA(z)}{dz} = -i\frac{k_0^2}{\beta_1}n_{eff}\Delta n_{dc}A(z)\\&-i\frac{\omega\varepsilon_0}{4}n_{eff}\Delta n_{ac}\tilde{\Delta n}(z)\iint_{core}\psi_1^*\psi_2 dxdyB(z)e^{i[(\Delta\beta-\frac{2\pi}{\Lambda})z-\phi(z)]}\end{aligned} \tag{A.27}$$

So, in the presence of a period perturbation, coupling takes place mainly among modes for which $\Delta\beta$ is close to either $\frac{2\pi}{\Lambda}$ or $-\frac{2\pi}{\Lambda}$. This justifies the two-term expansion of (A.17). The approximation retaining either $e^{i(\Delta\beta+\frac{2\pi}{\Lambda})z}$ or $e^{i(\Delta\beta-\frac{2\pi}{\Lambda})z}$ term in (A.27) is called **synchronous approximation** and corresponds to the rotating wave approximation used in time-dependent perturbation theory in quantum mechanics.

Predominant coupling occurs only between those modes with propagation constant β_1 and β_2 satisfying

$$\beta_1 - \beta_2 \approx \pm\frac{2\pi}{\Lambda}$$

and coupling to other modes is negligible. For the counter-propagating identical modes in Bragg gratings, $\beta_1 = -\beta_2 = \frac{2\pi n_{eff}}{\lambda_c}$, it is simplified to be

$$\lambda_B = 2n_{eff}\Lambda \tag{A.28}$$

which is called Bragg wavelength.

Coupling coefficient and solutions

As for c_{ij} parameters and same order (identical) modes in coupled mode equations (A.20) and (A.21), if we define two new coefficients [61]

$$\begin{aligned}\kappa_{dc}(z) &= \frac{\omega\varepsilon_0}{2} n_{eff}\Delta n_{dc} \\ \kappa_{ac}(z) &= \frac{\omega\varepsilon_0}{4} n_{eff}\Delta n_{ac}\Delta\tilde{n}(z)\iint_{core}\psi_1^*\psi_2 dxdy\end{aligned}$$

where κ_{dc} is a 'dc' (period-averaged) coupling coefficient and κ_{ac} is an 'AC' coupling coefficient, the general coupling coefficient c_{12} and c_{21} become

$$\begin{aligned}c_{12}(z) &= \kappa_{dc}(z)\underbrace{\iint_{core}\psi_1^*\psi_2 dxdy} + 2\kappa_{ac}(z)\cos[\frac{2\pi}{\Lambda}z + \phi(z)] \\ c_{21}(z) &= c_{21}^*(z)\end{aligned}$$

Hence, (A.27) could be written as

$$\frac{dA(z)}{dz} = -i\kappa_{dc}A(z) - i\kappa_{ac}B(z)e^{i[(\Delta\beta-\frac{2\pi}{\Lambda})z-\phi(z)]} \tag{A.29}$$

Similarly, we have

$$\frac{dB(z)}{dz} = i\kappa_{dc}B(z) + i\kappa_{ac}^*A(z)e^{i[(\Delta\beta-\frac{2\pi}{\Lambda})z-\phi(z)]} \tag{A.30}$$

Although the mode amplitude functions $A(z)$ and $B(z)$ vary slowly, the two exponential functions may fluctuate rapidly. To minimize the effect of rapid fluctuations, we introduce two auxiliary functions $R(z)$ and $S(z)$:

$$\begin{aligned}R(z) &= A(z)e^{\frac{-i}{2}[(\Delta\beta-\frac{2\pi}{\Lambda})z-\phi(z)]} \\ S(z) &= B(z)e^{\frac{i}{2}[(\Delta\beta-\frac{2\pi}{\Lambda})z-\phi(z)]}\end{aligned}$$

These auxiliary functions are different from those in [61],but the same with those in [62] which is more logical. Then substituting

$$A(z) = R(z)e^{\frac{i}{2}[(\Delta\beta-\frac{2\pi}{\Lambda})z-\phi(z)]} \tag{A.31}$$

$$B(z) = S(z)e^{\frac{-i}{2}[(\Delta\beta-\frac{2\pi}{\Lambda})z-\phi(z)]} \tag{A.32}$$

into the coupled mode equations and defining

$$\delta = \frac{1}{2}(\Delta\beta - \frac{2\pi}{\Lambda}) + \kappa_{dc} - \frac{1}{2}\frac{d\phi}{dz}$$

We have

$$\begin{aligned} \frac{dR(z)}{dz} &= -i\delta R(z) - i\kappa_{ac} S(z) \\ \frac{dS(z)}{dz} &= i\delta S(z) + i\kappa_{ac}^* R(z) \end{aligned}$$

The equations are unlike the equations in Erdogan's paper [61], with the ± difference but same results [53]. For the boundary conditions $R(0) = 1$, $S(L) = 0$ and $\kappa = \kappa_{ac} = \kappa_{ac}^*$, with $\cosh(x) = \frac{e^x + e^{-x}}{2}$ and $\sinh(x) = \frac{e^x - e^{-x}}{2}$, the solutions of the coupled-mode equations are

$$R(z) = \frac{i\delta \sinh[\sqrt{\kappa^2 - \delta^2}(L - z)] + \sqrt{\kappa^2 - \delta^2}\cosh[\sqrt{\kappa^2 - \delta^2}(L - z)]}{i\delta \sinh(\sqrt{\kappa^2 - \delta^2}L) + \sqrt{\kappa^2 - \delta^2}\cosh(\sqrt{\kappa^2 - \delta^2}L)} \tag{A.33}$$

$$S(z) = \frac{-i\kappa \sinh[\sqrt{\kappa^2 - \delta^2}(L - z)]}{i\delta \sinh(\sqrt{\kappa^2 - \delta^2}L) + \sqrt{\kappa^2 - \delta^2}\cosh(\sqrt{\kappa^2 - \delta^2}L)} \tag{A.34}$$

The reflection coefficient $\rho = \frac{A(0)}{B(0)}$ is

$$\rho = \frac{S(0)}{R(0)} e^{-i\phi(0)} = \frac{-i\kappa \sinh[\sqrt{\kappa^2 - \delta^2}L] e^{-i\phi(0)}}{\sqrt{\kappa^2 - \delta^2}\cosh[\sqrt{\kappa^2 - \delta^2}L] + i\delta \sinh[\sqrt{\kappa^2 - \delta^2}L]} \tag{A.35}$$

The reflectivity $r = |\rho|^2$ is

$$r = \frac{\sinh^2(\sqrt{\kappa^2 - \delta^2}L)}{\cosh^2(\sqrt{\kappa^2 - \delta^2}L) - \frac{\delta^2}{\kappa^2}} \tag{A.36}$$

If we denote $\theta_\rho = phase(\rho)$, the time delay τ_ρ (in picoseconds) for the light reflected off of a grating is

$$\tau_\rho = \frac{d\theta_\rho}{d\omega} = -\frac{\lambda^2}{2\pi c}\frac{d\theta_\rho}{d\lambda} \tag{A.37}$$

The grating group delay is also related to the dispersion parameter d_ρ in optical fibre communications, which is used to describe the chromatic dispersion in units of picoseconds per nanometer and kilometer (ps/(nm*km)). We get

$$d\rho = \frac{d\tau_\rho}{d\lambda} = \frac{2\tau_\rho}{\lambda} - \frac{\lambda^2}{2\pi c}\frac{d^2\theta_\rho}{d\lambda^2} = -\frac{2\pi c}{\lambda^2}\frac{d^2\theta_\rho}{d\omega^2} \tag{A.38}$$

Appendix B

Matlab code

B.1 Transfer matrix method

```
clc;clear;
c=3e8;%light velocity in vacuum
L=16*1e-3;% the grating length (mm)
neff=1.45;% the effective refractive index
M=100;% the number of grating sections
step=1e-2*1e-9;%wavelength step (nm)
wb = 36*1e-9; % wavelength bandwidth (nm)
lambdaD=1550*1e-9;%the designed central wavelength (m)
lambda=(lambdaD-0.5*wb:step:lambdaD+0.5*wb);% the wavelength range (m)
period= lambdaD/(2*neff); %Bragg grating period(nm)
DL = L/M; % length of each grating section
z = (0:DL:L);
z0= L/2; % phase shift point
z01 =0; z02= L;  % grating section strat point
%% Refractive Index mudalation parameters
eta = 1;    %mode/core overlap integral
dneff = 0.0006;%the ac refactive index change
Δ=2*pi*neff*(1./lambda-1/lambdaD);  % local wavelength number
%% chirp parameters
chirp = 0.0*1e-9;   % the linear chirp coefficient (m)
C1 = -(2*pi*chirp)/(L*period^2);
C2 = +(pi*chirp)/period^2;
%% apodisation function
% apod = ones(1,M); % set no apodisation
%  for s=1:M
% apod(s) = sinc(22*(-z0+s*L/M)/L);
% %      apod(s) = exp(-((-z0+s*L/M)/L)^2*30);%     Gaussion
% %     if abs(apod(s))≤0.02
```

```
% %         apod(s)= (apod(s)/abs(apod(s)))*0.02;
% %     end
%  end
%% Hilbert transform variabes
% apod = ones(1,M); % set no apodisation
△f=4000e9; % the operation bandwidth (Hz)
△N=zeros(1,M);
O=zeros(1,M);
% for k=1:M
%        O(k)=sin(pi*neff*△f*(z(k)-z0)/c);
%        △N(k)=O(k)^2./(z0-z(k));
%        if z(k)==z0
%            △N(k)=1e-6;
%        end
% end
% apod = △N/max(△N);
% apod = zeros(1,M);
% for k =1:M
%     apod(k) = apod(M+1-k);
% end
order = 0.25;%FrHT order
for k=1:M
       O(k)=sin(pi*neff*△f*(z(k)-z0)/c);
       △N(k)=O(k)^2./(z0-z(k));
       if z(k)==z0
           △N(k)=1*1e-12;
       end
end
apod = (△N/max(△N));
for k=1:M
       if z(k)≥z0
       apod(k)=apod(k);
       else
           apod(k)= order*apod(k);
       end
end
%% coulpe coefficient(q) construction
ze = zeros(1, M);
qmod = zeros(1, M);
f0 = zeros(1, M);
qphase = zeros(1, M);
q = zeros(1, M);

for n=1:M
   ze(n)=z01+(n-1)*DL;
   qmod(n)=eta*pi*dneff/lambdaD;            %coupling constant modulus
   qmod(n)=qmod(n)*apod(n);                 %apodised coupling constant ...
    modulus
   qphase(n)=0.5*C1*ze(n)^2+C2*ze(n);       %coupling constant spatial phase
   q(n)=qmod(n)*exp(1i*qphase(n));          %coupling constant
end
```

```
rcoef = zeros(length(lambda),1);
tcoef = zeros(length(lambda),1);
rimag = zeros(length(lambda),1);
rreal = zeros(length(lambda),1);
Ref = zeros(length(lambda),1);
Trans = zeros(length(lambda),1);
Rphase = zeros(length(lambda),1);
rmod = -tanh(qmod*DL);          %local reflection coeff. modulus
rphase = -qphase;                   %local reflection coeff. phase
r = rmod.*exp(1i*rphase);           %local reflection coeff.
tmod = sqrt(1-rmod.^2);         %local transmission coeff. modulus

for k = 1:(length(lambda))
    F = [1,0;0,1];
    for t = M:-1:1
F = F*[exp(1i*Δ(k)*DL)/tmod(t),conj((-r(t)*exp(-1i*Δ(k)*DL))/tmod(t));
(-r(t)*exp(-1i*Δ(k)*DL))/tmod(t),exp(-1i*Δ(k)*DL)/tmod(t)];
    end
    rcoef(k)=-F(2,1)/F(2,2);
    tcoef(k) = 1/F(2,2);
    rreal(k) = real(rcoef(k));
    rimag(k) = imag(rcoef(k));
    Ref(k) = (abs(rcoef(k)))^2;
    Rphase(k) = angle(rcoef(k));
    Trans=(abs(tcoef)).^2;
end
UnwrapRphase = unwrap(2*Rphase)/2;
%% Group delay
dtr = zeros(length(lambda));
dtr(1)= (neff*L/c)*1e12;
for m = 2:(length(lambda))
   dfl = (UnwrapRphase(m)-UnwrapRphase(m-1))/step;
   dtr(m) = -((lambda(m)^2)/(2*pi*c))*dfl*1e12;         %time delay (in ps)
   if abs(dtr(m)) ≥ 2000
      dtr(m) = dtr(m-1);
   end
end
%% output graph
figure
subplot(2,2,1)
plot(lambda*1e9,10*log(Ref));% reflectivity in dB
title('Grating amplitude responses')
xlabel('Wavelength (nm)')
ylabel('Reflectivity')
hold on
grid on
subplot(2,2,2)
plot(lambda*1e9,UnwrapRphase); %unwrap reflection phase
title('Phase')
xlabel('Wavelength (nm)')
ylabel('Phase(rad)')
```

```
hold on
grid on
subplot(2,2,3)
plot(lambda*1e9,dtr(:,1),'-m');
title('Relative group delay ')
xlabel('Wavelength (nm)')
ylabel('Delay(ps)')
hold on
grid on
subplot(2,2,4)
plot(ze,apod,'-k');
title('Apodisation profile')
xlabel('Positions (mm)')
ylabel('Apodisation')
hold on
grid on
```

B.2 Inverse scattering method

```
Δ = 2*pi*neff*((1./lambda)-1/lambdaD);   % wavenumber detuning
dz = L/M;
lambdap = (Δf/(10^(12)*0.125))*10^(-9);
order1 = 1;
Rmax = sqrt(0.5); %peak reflectivity
rcoef1 = ((0.5*1./sqrt(1+((lambda-lambdaD)/(lambdap/2)).^(16))).^(0.5))';
timeref = (2*L)/(c/neff);
N = length(lambda);
realRphase = zeros(N,1);
realRphase(1) = 0;
for k = 2:N
    if (k == ceil(N/2))
   realRphase(k) = ...
    -1*(-(neff*L*2*pi)/(lambda(k))+(neff*L*2*pi)/(lambda(k-1)))+ ...
    realRphase(k-1)- order1*pi;
       else
        realRphase(k) = ...
    -1*(-(neff*L*2*pi)/(lambda(k))+(neff*L*2*pi)/(lambda(k-1)))+realRphase(k-1);
    end
end
ref = (Rmax/max(abs(rcoef)))*rcoef;
NΔ = length(ref);                       % spretrum wavelength range
ro1 = 1/NΔ*sum(ref);                    % reflection coefficient
ro0 = zeros(M,1);
ro0(1) = ro1;

for t=2:M                                   % 2 to Mth layer
    r2 = exp(-1i*2*(Δ)'*dz).*(ref-ro1)./(1-conj(ro1).*ref);
```

```
    ro2 = 1/N△*sum(r2);
    ro0(t) = ro2;
    ref = r2;
    ro1 = ro2;
end
qq = (-atan(abs(ro0))/dz).*conj(ro0)./(abs(ro0));  %caculate the coupling
couple = qq;
save('couplecoef.mat','qq');
%% extra phasefunc to plot the real apodisation function
phasefunc = ones(length(couple),1);
for s=1:length(couple)
    if angle(couple(s))<0
        phasefunc(s)= -1;
    end
end
realcouple = phasefunc.*abs(couple);
ze0 = zeros(M,1);
for n1=1:M
   ze0(n1)=(n1-1)*dz;
end
ze = ze0;
figure
subplot(2,2,1)
plot(ze*1e2,dneff*apod,'k');%apod
title('Original apodisation profile')
xlabel('Grating Length (cm)')
ylabel('dn')

subplot(2,2,3)
plot(ze*1e2, realcouple);
title('Coupling coefficient calculated by layer peeling');
xlabel('Grating Length (cm)');
ylabel('Coupling coefficient(q)');
hold on
%% use the IS data to caculate the reflectivity and group delay
rcoeftemp = ones(length(lambda),1);
rimag = ones(length(lambda),1);
rreal = ones(length(lambda),1);
Ref2 = ones(length(lambda),1);
Rphase2 = ones(length(lambda),1);
qmod = abs(qq);
qphase = angle(qq);
rmod = -tanh(qmod*DL);              %local reflection coeff. modulus
rphase = -qphase;                   %local reflection coeff. phase
r = rmod.*exp(1i*rphase);           %local reflection coeff.
tmod = sqrt(1-rmod.^2);             %local transmission coeff. modulus
for k = 1:(length(lambda))
    F = [1,0;0,1];
    for t = M:-1:1
F = F*[exp(1i*△(k)*DL)/tmod(t),conj((-r(t)*exp(-1i*△(k)*DL))/tmod(t));
(-r(t)*exp(-1i*△(k)*DL))/tmod(t),exp(-1i*△(k)*DL)/tmod(t)];
```

```
77      end
78      rcoeftemp(k) =- F(2,1)/F(2,2);
79      tcoef(k) = 1/F(2,2);
80      rreal(k) = real(rcoeftemp(k));
81      rimag(k) = imag(rcoeftemp(k));
82      Ref2(k) = (abs(rcoeftemp(k)))^2;
83      Rphase2(k) = angle(rcoeftemp(k));
84  end
85  UnwrapRphase2 = unwrap(2*Rphase2)/2;
86  %% Group delay
87  dtr2 = zeros(length(lambda));
88  dtr2(1)= (neff*L/c)*1e12;
89  for m = 2:(length(lambda))
90     dfl2 = (UnwrapRphase2(m)-UnwrapRphase2(m-1))/step;
91     dtr2(m) = -((lambda(m)^2)/(2*pi*c))*dfl2*1e12;       %time delay (in ps)
92     if abs(dtr2(m)) ≥ 2000
93        dtr2(m) = dtr2(m-1);
94     end
95  end
96  subplot(2,2,2)
97  plot(lambda*1e9,10*log10(Ref),':b',lambda*1e9,10*log10(Ref2),'b');
98  legend('original ','after layer peeling ');
99  xlabel('Wavelength (nm)');ylabel('Reflectivity (dB)');
100 title('Reflectivity');
101 subplot(2,2,4)
102 plot(lambda*1e9,dtr(:,1),':r',lambda*1e9,dtr2(:,1),'r');
103 legend('original','after layer peeling ')
104 title('Group delay');xlabel('Wavelength (nm)');ylabel('group delay (ps)');
105 hold on
```

Appendix C

Wafer parameters

The various wafers used to fabricate the waveguides and Bragg gratings described in this thesis have different chemical and physical properties, having been produced via different recipes. This appendix details the properties of fabrication of each slab waveguide layer, prior to UV writing, in an effort to compare the typical composition with the optical behaviour observed.

Wafers W5 and W7 were fabricated at CIP, whilst wafer NB17/18 was fabricated at the ORC. Thus the recipes used to achieve similar refractive index layers are marginally different, given the differing gas flows and extract conditions at each site. The gas flows given here are pressure compensated, given the air pressure and humidity of the lab environment on different days. The gas flows, shown here in litres per minute, cannot be directly compared for the different precursors, as the pressure at operating temperature for each is different. However, as a means of comparison between different wafers, the presence of more or less gas flow can be interpreted as a greater or lesser amount of precursor reaching the torch. The detailed fabrication parameters for each wafer are given as follows.

Wafer W5 Fabricated at CIP			
Underclad	TY468, 16-17 μm thermal oxide		
Core	Date	22/07/2008	
	Deposition Program	0deltacore	
	Run number	ORC 2-1	
	Wafer position	2	
	Consolidation Program	CoreORC2	
	Average Refractive Index	**1.4461**	
	Average Thickness	**5.64** μm	
	Torch gas flows	H_2	5
		O_2	5
		Ar	8
	Process gas flows	$SiCl_4$	142
		$GeCl_4$	51
		PCl_3	0
		BCl_3	76
	Furnace gas flows	He	1.9
		O_2	0.9
Overclad	Date	23/07/2008	
	Deposition Program	CIP Clad 1	
	Run number	ORC-2-Clad2	
	Wafer position	2	
	Consolidation Program	Clad ORC	
	Average Refractive Index	**1.4448**	
	Average Thickness	**16.4** μm	
	Torch gas flows	H_2	6.5
		O_2	2
		Ar	8
	Process gas flows	$SiCl_4$	139
		$GeCl_4$	0
		PCl_3	31
		BCl_3	70
	Furnace gas flows	He	1.9
		O_2	0

Wafer W7 Fabricated at CIP			
Underclad	TY468, 16-17 μm thermal oxide		
Core	Date	22/07/2008	
	Deposition Program	0deltacore	
	Run number	ORC 2-1	
	Wafer position	3	
	Consolidation Program	CoreORC2	
	Average Refractive Index	**1.4461**	
	Average Thickness	**5.64** μm	
	Torch gas flows	H_2	5
		O_2	5
		Ar	8
	Process gas flows	$SiCl_4$	142
		$GeCl_4$	51
		PCl_3	0
		BCl_3	76
	Furnace gas flows	He	1.9
		O_2	0.9
Overclad	Date	23/07/2008	
	Deposition Program	CIP Clad 1	
	Run number	ORC-2-Clad2	
	Wafer position	3	
	Consolidation Program	Clad ORC	
	Average Refractive Index	**1.4448**	
	Average Thickness	**16.4** μm	
	Torch gas flows	H_2	6.5
		O_2	2
		Ar	8
	Process gas flows	$SiCl_4$	139
		$GeCl_4$	0
		PCl_3	31
		BCl_3	70
	Furnace gas flows	He	1.9
		O_2	0

Wafer NB17/18 Fabricated at ORC			
Underclad	TY471, 17.1 μm thermal oxide		
Core	Date	13/07/2011	
	Deposition Program	0deltacore	
	Run number	NB17	
	Wafer position	2	
	Consolidation Program	Core3	
	Average Refractive Index	**1.4456**	
	Average Thickness	**6.764** μm	
	Torch gas flows	H_2	5
		O_2	5
		Ar	8
	Process gas flows	$SiCl_4$	140
		$GeCl_4$	50
		PCl_3	0
		BCl_3	60
	Furnace gas flows	He	1.9
		O_2	0.9
Overclad	Date	14/07/2011	
	Deposition Program	ORC Clad2A	
	Run number	NB18	
	Wafer position	5	
	Consolidation Program	Clad	
	Average Refractive Index	**1.4447**	
	Average Thickness	**17.01** μm	
	Torch gas flows	H_2	6.5
		O_2	1.9
		Ar	8.0
	Process gas flows	$SiCl_4$	137
		$GeCl_4$	0
		PCl_3	31
		BCl_3	71
	Furnace gas flows	He	1.9
		O_2	0

Appendix D

Publications

D.1 Journals

1. **C. Sima**, J. C. Gates, H. L. Rogers, P. L. Mennea, C. Holmes, M. N. Zervas, and P. G. R. Smith. "Phase controlled integrated interferometric single-sideband filter based on planar Bragg gratings implementing photonic Hilbert transform". *Optics Letters*, 38(5): 727-729, 2013.

2. **C. Sima**, J. C. Gates, H. L. Rogers, P. L. Mennea, C. Holmes, M. N. Zervas, and P. G. R. Smith. "Ultra-wide detuning planar Bragg grating fabrication technique based on direct UV grating writing with electro-optic phase modulation". *Optics Express*, 21(13): 15747-15754, 2013.

3. **C. Sima**, J. C. Gates, P. L. Mennea, C. Holmes, M. N. Zervas, and P. G. R. Smith. "Terahertz bandwidth photonic Hilbert transformers based on synthesized planar Bragg grating fabrication". *Optics Letters*, 38(17): 3448-3451, 2013.

4. **C. Sima**, J. C. Gates, M. N. Zervas, and P. G. R. Smith. "Review of photonic Hilbert transformers". *Frontiers of Optoelectronics*, 6(1): 78-88, 2013.

5. J. C. Gates, **C. Sima**, C. Holmes, and P. G. R. Smith. "UV direct writing of planar waveguides: basics and applications". *SPIE Newsroom*, August, 2013. DOI:10.1117/2.1201307.005036. (Invited)

D.2 Conference Contributions

1. C. Holmes, **C. Sima**, P. L. Mennea, L. G. Carpenter, J. C. Gates, and P. G. R. Smith. "Fabricating fiber Bragg gratings using phase modulated direct UV

writing". *SPIE Photonics West 2014*, San Francisco, USA, 2014. (Submitted)

2. **C. Sima**, J. C. Gates, M. N. Zervas, and P. G. R. Smith. "Bragg grating based integrated photonic Hilbert transformers". *MWP 2013*, 2013 IEEE International Topical Meeting on Microwave Photonics, Alexandria, Virginia, USA, 2013.

3. **C. Sima**, J. C. Gates, P. L. Mennea, P. A. Cooper, C. Holmes, M. N. Zervas, and P. G. R. Smith. "Experimental demonstration of terahertz bandwidth photonic Hilbert transformers and implementations in interferometric all-optical single sideband filter". *ECOC 2013*, the 39th European Conference and Exhibition on Optical Communication, London, UK, 2013.

4. J. C. Gates, S. G. Lynch, P. L. Mennea, P. A. Cooper, S. Ambran, H. L. Rogers, L. G. Carpenter, **C. Sima**, D. J. Wales, C. Holmes, and P. G. R. Smith. "UV written planar Bragg grating sensors - an overview of fabrication geometries and applications". *Advanced Photonics 2013*, 2013 OSA Advanced Photonics Congress, Rio Grande, Puerto Rico, 2013. (Invited)

5. **C. Sima**, J. C. Gates, H. L. Rogers, P. L. Mennea, C. Holmes, M. N. Zervas, and P. G. R. Smith. "Phase modulation technique for high modulation wide band planar Bragg". *CLEO/Europe-EQEC 2013*, the European Conference on Lasers and Electro-Optics and the International Quantum Electronics Conference, Munich, Germany, 2013.

6. J. C. Gates, S. Lynch, C. Holmes, **C. Sima**, and P. L. Mennea. "Integrated planar Bragg grating stabilized diode lasers". *CLEO/Europe-EQEC 2013*, the European Conference on Lasers and Electro-Optics and the International Quantum Electronics Conference, Munich, Germany, 2013.

7. P. A. Cooper, C. Holmes, L. G. Carpenter, **C. Sima**, P. L. Mennea, J. C. Gates and P. G. R. Smith. "Micro-beams for tuneable Bragg gratings and resettable optical devices". *CLEO/Europe-EQEC 2013*, the European Conference on Lasers and Electro-Optics and the International Quantum Electronics Conference, Munich, Germany, 2013.

8. C. Holmes, H. L. Rogers, K. R. Daly, L. G. Carpenter, **C. Sima**, P. L. Mennea, J. C. Gates, G. D'Alessandro, and P. G. R. Smith. "Tilted Planar Bragg Grating Refractometers". *CLEO/Europe-EQEC 2013*, The European Conference on Lasers and Electro-Optics and the International Quantum Electronics Conference, Munich, Germany, 2013.

9. **C. Sima**, J. C. Gates, H. L. Rogers, P. L. Mennea, C. Holmes, M. N. Zervas, and P. G. R. Smith. "Phase modulated direct UV grating writing technique for ultra wide spectrum planar Bragg grating fabrication". *SPIE Photonics West 2013*, San Francisco, USA, 2013. (*SPIE-Newport Research Excellence Award*)

10. **C. Sima**, J. C. Gates, H. L. Rogers, P. L. Mennea, C. Holmes, M. N. Zervas, and P. G. R. Smith. "Interferometric integrated planar Bragg filter for all-optical single-sideband suppression". *ECIO 2012*, the 16th European Conference on Integrated Optics, Barcelona, Spain, 2012.

11. **C. Sima**, J. C. Gates, B. D. Snow, H. L. Rogers, C. Holmes, M. N. Zervas, and P. G. R. Smith. "All-optical signal processing using planar Bragg gratings". *POEM 2011*, the 4th International Photonics and Opto-Electronics Meetings, Wuhan, China, 2011. (*Best student paper award*)

12. H. L. Rogers, L. G. Carpenter, S. Ambran, **C. Sima**, D. J. Wales, R. M. Parker, C. Holmes, J. C. Gates, and P. G. R. Smith. "Direct grating writing: single-step Bragg grating and waveguide fabrication for telecommunications". *IONS NA-3*, the International OSA Network of Students in North America, Stanford, USA, 2011.

13. **C. Sima**, J. C. Gates, H. L. Rogers, C. Holmes, M. N. Zervas, and P. G. R. Smith. "Integrated all-optical SSB modulator using photonic Hilbert transformer with planar Bragg gratings". *CLEO/Europe-EQEC 2011*, the European Conference on Lasers and Electro-Optics and the International Quantum Electronics Conference, Munich, Germany, 2011.

14. H. L. Rogers, L. G. Carpenter, S. Ambran, **C. Sima**, B. D. Snow, R. M. Parker, C. Holmes, J. C. Gates, and P. G. R. Smith. "Direct grating writing: Single-step Bragg grating and waveguide fabrication for telecommunications and sensing applications". *IONS-9*, the International OSA Network of Students in North America, Salamanca, Spain, 2011.

15. **C. Sima**, J. C. Gates, B. D. Snow, H. L. Rogers, C. Holmes, M. N. Zervas, and P. G. R. Smith. "Simple planar Bragg grating devices for photonic Hilbert transform". *POEM 2010*, the 3th International Photonics and Opto-Electronics Meetings, Wuhan, China, 2010. (*Best student paper award*)

16. **C. Sima**, J. C. Gates, B. D. Snow, H. L. Rogers, M. N. Zervas, and P. G. R. Smith. "Realisation of photonic Hilbert transformer with a simple planar Bragg grating". *Photon 10*, Southampton, UK, 2010. (*Highly commended poster prize*)

17. **C. Sima**, J. C. Gates, B. D. Snow, H. L. Rogers, M. N. Zervas, and P. G. R. Smith. "Realization of a planar Bragg grating for all-optical Hilbert transformer". *ECIO 2010*, the 15th European Conference on Integrated Optics, Cambridge, UK, 2010.

18. B. D. Snow, H. L. Rogers, C. Holmes, J. C. Gates, **C. Sima**, M. Kaczmarek, and P. G. R. Smith. "UV-written planar chirped Bragg gratings for use in dispersion management". *ECIO 2010*, the 15th European Conference on Integrated Optics, Cambridge, UK, 2010.

References

[1] A. W. Lohmann, D. Mendlovic, and Z. Zalevsky, "Fractional Hilbert transform," *Optics Letters*, vol. 21, no. 4, pp. 281–283, 1996.

[2] K. Takano, N. Hanzawa, S. Tanji, and K. Nakagawa, "Experimental demonstration of optically phase-shifted SSB modulation with fiber-based optical Hilbert transformers," in *Optical Fiber Communication Conference*, Optical Society of America, 2007.

[3] H. Emami, N. Sarkhosh, L. A. Bui, and A. Mitchell, "Wideband RF photonic in-phase and quadrature-phase generation," *Optics Letters*, vol. 33, no. 2, pp. 98–100, 2008.

[4] X. Wang, M. Hanawa, K. Nakamura, K. Takano, and K. Nakagawa, "Sideband suppression characteristics of optical SSB generation filter with sampled FBG based 4-taps optical Hilbert transformer," in *Communications, 2009. APCC 2009. 15th Asia-Pacific Conference on*, pp. 622–625, IEEE, 2009.

[5] M. Li and J. Yao, "All-fiber temporal photonic fractional Hilbert transformer based on a directly designed fiber Bragg grating," *Optics Letters*, vol. 35, no. 2, pp. 223–225, 2010.

[6] Z. Li, H. Chi, X. Zhang, and J. Yao, "Optical single-sideband modulation using a fiber-Bragg-grating-based optical Hilbert transformer," *Photonics Technology Letters, IEEE*, vol. 23, no. 9, pp. 558–560, 2011.

[7] L. Zhuang, W. Beeker, A. Leinse, R. Heideman, and C. Roeloffzen, "Continuously tunable photonic fractional Hilbert transformer using ring resonators for on-chip microwave photonic signal processing," in *Microwave Photonics (MWP), 2012 International Topical Meeting on*, pp. 22–25, 2012.

[8] J. Skaar, *Synthesis and characterization of fiber Bragg gratings*. PhD thesis, Norwegian University of Science and Technology, 2000.

[9] F. R. M. Adikan, *Direct UV-written waveguide devices*. PhD thesis, University of Southampton, 2007.

[10] A. Othonos and K. Kalli, *Fiber Bragg gratings: fundamentals and applications in telecommunications and sensing*. Boston, MA: Artech House, 1999.

[11] S. P. Watts, *Flame hydrolysis deposition of photosensitive silicate layers suitable for the definition of waveguiding structures through direct ultraviolet writing*. PhD thesis, University of Southampton, 2002.

[12] B. D. Snow, *Liquid crystal adaptive planar optical devices*. PhD thesis, University of Southampton, 2010.

[13] S. E. Miller, "Integrated optics: an introduction," *the Bell System Technical Journal*, vol. 48, no. 7, pp. 2059–2069, 1969.

[14] J. B. Spring, B. J. Metcalf, P. C. Humphreys, W. S. Kolthammer, X. M. Jin, M. Barbieri, A. Datta, N. Thomas S Peter, N. K. Langford, D. Kundys, *et al.*, "Boson sampling on a photonic chip," *Science*, vol. 339, no. 6121, pp. 798–801, 2013.

[15] J. Yao, "Microwave photonics," *Lightwave Technology, Journal of*, vol. 27, no. 3, pp. 314–335, 2009.

[16] J. Capmany and D. Novak, "Microwave photonics combines two worlds," *Nature Photonics*, vol. 1, no. 6, pp. 319–330, 2007.

[17] H. Al-Raweshidy and S. Komaki, *Radio over fiber technologies for mobile communications networks*. Artech House, 2002.

[18] G. H. Smith, D. Novak, and Z. Ahmed, "Technique for optical SSB generation to overcome dispersion penalties in fibre-radio systems," *Electronics Letters*, vol. 33, no. 1, pp. 74–75, 1997.

[19] K. Ennser, R. Laming, and M. Zervas, "Analysis of 40 Gb/s TDM-transmission over embedded standard fiber employing chirped fiber grating dispersion compensators," *Journal of lightwave technology*, vol. 16, no. 5, p. 807, 1998.

[20] "Cloud-ready data center reference architecture." `http://www.juniper.net/us/en/local/pdf/reference-architectures/8030001-en.pdf`, 2013.

[21] M. Hogan, F. Liu, A. Sokol, and J. Tong, "Nist cloud computing standards roadmap," *NIST Special Publication*, p. 35, 2011.

[22] R. Hunsperger, *Integrated optics*. Advanced texts in physics, Springer-Verlag New York, 2009.

[23] R. W. Tkach, "Scaling optical communications for the next decade and beyond," *Bell Labs Technical Journal*, vol. 14, no. 4, pp. 3–9, 2010.

[24] E. A. Limited, "Telecommunications network maintenance services: key trends in Asia." http://www.emerging-asia.com/wp-content/uploads/2010/09/Telecom-Network-Maintenance-Services-Emerging-Asia-Whitepaper-October-2008.pdf, 10 2008.

[25] G. Lifante, *Integrated photonics: fundamentals*. J. Wiley, 2003.

[26] K. Okamoto, *Fundamentals of optical waveguides*. Academic press, 2010.

[27] G. H. Smith, D. Novak, and Z. Ahmed, "Overcoming chromatic-dispersion effects in fiber-wireless systems incorporating external modulators," *Microwave Theory and Techniques, IEEE Transactions on*, vol. 45, no. 8, pp. 1410–1415, 1997.

[28] J. Park, W. Sorin, and K. Lau, "Elimination of the fibre chromatic dispersion penalty on 1550 nm millimetre-wave optical transmission," *Electronics Letters*, vol. 33, no. 6, pp. 512–513, 1997.

[29] S. Blais and J. Yao, "Optical single sideband modulation using an ultranarrow dual-transmission-band fiber Bragg grating," *Photonics Technology Letters, IEEE*, vol. 18, no. 21, pp. 2230–2232, 2006.

[30] G. J. Ockenfuss, N. A. O'Brien, and E. Williams, "Ultra-low stress coating process: an enabling technology for extreme performance thin film interference filters," in *Optical Fiber Communication Conference and Exhibit, 2002. OFC 2002*, pp. FA8–1, IEEE, 2002.

[31] T. Erdogan and V. Mizrahi, "Thin-film filters come of age," *Photonics Spectra*, vol. 37, no. 7, pp. 94–96, 2003.

[32] S. L. Hahn, *The transforms and applications handbook*. No. 7, Boca Raton: CRC Press LLC, 2 ed., 2000.

[33] N. Thrane, J. Wismer, H. Konstantin-Hansen, and S. Gade, "Practical use of the Hilbert transform," *Brüel and Kjær Sound & Vibration Measurement A/S Application Note*, 1995.

[34] A. Kastler, "A system of high-contrast diffraction fringes," *Review Optik*, vol. 29, no. 6, pp. 307–314, 1950.

[35] H. Wolter, "Die Minimumstrahlkennzeichnung als Mittel zur Genauigkeitssteigerung optischer Messungen und als methodisches Hilfsmittel zum Ersatz des Strahlbegriffes," *Annalen der Physik*, vol. 442, no. 7-8, pp. 341–368, 1950.

[36] D. Hauk and A. W. Lohmann, "Minimumstrahlke.nnich- nung bei Gitterspektrographen," *Optik*, vol. 15, pp. 275–281, 1958.

[37] S. Lowenthal and Y. Belvaux, "Observation of phase objects by optically processed Hilbert transform," *Applied Physics Letters*, vol. 11, no. 2, pp. 49–51, 1967.

[38] J. Eu and A. Lohmann, "Isotropic Hilbert spatial filtering," *Optics Communications*, vol. 9, no. 3, pp. 257–262, 1973.

[39] B. R. Brown and A. W. Lohmann, "Complex spatial filtering with binary masks," *Applied Optics*, vol. 5, no. 6, pp. 967–969, 1966.

[40] A. W. Lohmann and D. Paris, "Binary Fraunhofer holograms, generated by computer," *Applied Optics*, vol. 6, no. 10, pp. 1739–1748, 1967.

[41] A. Lohmann, E. Tepichin, and J. Ramirez, "Optical implementation of the fractional Hilbert transform for two-dimensional objects," *Applied Optics*, vol. 36, no. 26, pp. 6620–6626, 1997.

[42] J. A. Davis, D. E. McNamara, D. M. Cottrell, and J. Campos, "Image processing with the radial Hilbert transform: theory and experiments," *Optics Letters*, vol. 25, no. 2, pp. 99–101, 2000.

[43] C. S. Guo, Y. J. Han, J. B. Xu, and J. Ding, "Radial Hilbert transform with Laguerre-Gaussian spatial filters," *Optics Letters*, vol. 31, no. 10, pp. 1394–1396, 2006.

[44] N. Bokor and Y. Iketaki, "Laguerre-Gaussian radial Hilbert transform for edge-enhancement Fourier transform x-ray microscopy," *Optics Express*, vol. 17, no. 7, pp. 5533–5539, 2009.

[45] H. Emami, N. Sarkhosh, L. Bui, and A. Mitchell, "Amplitude independent RF instantaneous frequency measurement system using photonic Hilbert transform," *Optics Express*, vol. 16, no. 18, pp. 13707–13710, 2008.

[46] Z. Li, Y. Han, H. Chi, X. Zhang, and J. Yao, "A continuously tunable microwave fractional Hilbert transformer based on a nonuniformly spaced photonic microwave delay-line filter," *Journal of Lightwave Technology*, vol. 30, no. 12, pp. 1948–1953, 2012.

[47] M. H. Asghari and J. Azaña, "All-optical Hilbert transformer based on a single phase-shifted fiber Bragg grating: design and analysis," *Optics Letters*, vol. 34, no. 3, pp. 334–336, 2009.

[48] C. Cuadrado-Laborde, "Proposal and design of a photonic in-fiber fractional Hilbert transformer," *Photonics Technology Letters, IEEE*, vol. 22, no. 1, pp. 33–35, 2010.

[49] M. Li and J. Yao, "Experimental demonstration of a wideband photonic temporal Hilbert transformer based on a single fiber Bragg grating," *Photonics Technology Letters, IEEE*, vol. 22, no. 21, pp. 1559–1561, 2010.

[50] R. Ashrafi and J. Azaña, "Terahertz bandwidth all-optical Hilbert transformers based on long-period gratings," *Optics Letters*, vol. 37, no. 13, pp. 2604–2606, 2012.

[51] K. Tanaka, K. Takano, K. Kondo, and K. Nakagawa, "Improved sideband suppression of optical SSB modulation using all-optical Hilbert transformer," *Electronics Letters*, vol. 38, no. 3, pp. 133–134, 2002.

[52] L. Zhuang, M. R. Khan, W. Beeker, A. Leinse, R. Heideman, and C. Roeloffzen, "Novel microwave photonic fractional Hilbert transformer using a ring resonator-based optical all-pass filter," *Optics Express*, vol. 20, no. 24, pp. 26499–26510, 2012.

[53] C. Sima, J. Gates, H. Rogers, C. Holmes, M. Zervas, and P. Smith, "Integrated all-optical SSB modulator using photonic Hilbert transformer with planar Bragg gratings," in *The European Conference on Lasers and Electro-Optics*, Optical Society of America, 2011.

[54] T. X. Huang, X. Yi, and R. A. Minasian, "Microwave photonic quadrature filter based on an all-optical programmable Hilbert transformer," *Optics Letters*, vol. 36, no. 22, pp. 4440–4442, 2011.

[55] "Hilbert transform." `http://en.wikipedia.org/wiki/Hilbert_transform`, 2013.

[56] F. W. King, *Hilbert transforms*, vol. 1. Cambridge: Cambridge University Press, 2009.

[57] J. Proakis, *Digital signal processing: principles, algorithms, and applications*. Pearson Education, 2007.

[58] R. Slavík, Y. Park, M. Kulishov, R. Morandotti, *et al.*, "Ultrafast all-optical differentiators," *Optics Express*, vol. 14, no. 22, pp. 10699–10707, 2006.

[59] R. Kashyap, *Fiber bragg gratings*. Academic Press, 2 ed., 2009.

[60] R. Feced, M. Zervas, and M. A. Muriel, "An efficient inverse scattering algorithm for the design of nonuniform fiber Bragg gratings," *Quantum Electronics, IEEE Journal of*, vol. 35, no. 8, pp. 1105–1115, 1999.

[61] G. Emmerson, S. Watts, C. Gawith, V. Albanis, M. Ibsen, R. Williams, and P. Smith, "Fabrication of directly UV-written channel waveguides with simultaneously defined integral Bragg gratings," *Electronics Letters*, vol. 38, no. 24, pp. 1531–1532, 2002.

[62] C. Sima, J. Gates, H. Rogers, P. Mennea, C. Holmes, M. Zervas, and P. Smith, "Ultra-wide detuning planar Bragg grating fabrication technique based on direct

UV grating writing with electro-optic phase modulation," *Optics Express*, vol. 21, no. 13, pp. 15747–15754, 2013.

[63] A. Yariv, "Coupled-mode theory for guided-wave optics," *Quantum Electronics, IEEE Journal of*, vol. 9, no. 9, pp. 919–933, 1973.

[64] W. P. Huang, "Coupled-mode theory for optical waveguides: an overview," *Journal of the Optical Society of America A*, vol. 11, no. 3, pp. 963–983, 1994.

[65] A. Ghatak and K. Thyagarajan, *An introduction to fiber optics*. Cambridge University Press, 1998.

[66] T. Erdogan, "Fiber grating spectra," *Journal of Lightwave Technology*, vol. 15, no. 8, pp. 1277–1294, 1997.

[67] H. Kogelnik, "Theory of dielectric waveguides," in *Integrated Optics*, pp. 13–81, Springer, 1975.

[68] M. Yamada and K. Sakuda, "Analysis of almost-periodic distributed feedback slab waveguides via a fundamental matrix approach," *Applied Optics*, vol. 26, no. 16, pp. 3474–3478, 1987.

[69] K. Ennser, M. Zervas, and R. Laming, "Optimization of apodized linearly chirped fiber gratings for optical communications," *Quantum Electronics, IEEE Journal of*, vol. 34, no. 5, pp. 770–778, 1998.

[70] "Apodization function." `http://en.wikipedia.org/wiki/Apodization_function`, 2013.

[71] W. H. Southwell, "Using apodization functions to reduce sidelobes in rugate filters," *Applied Optics*, vol. 28, no. 23, pp. 5091–5094, 1989.

[72] I. Sparrow, P. Smith, G. Emmerson, S. Watts, and C. Riziotis, "Planar Bragg grating sensorsFabrication and applications: A review," *Journal of Sensors*, vol. 2009, 2009.

[73] S. Watts, "Bragg gratings: optical microchip sensors," *Nature Photonics*, vol. 4, no. 7, pp. 433–434, 2010.

[74] M. Ibsen, M. K. Durkin, M. J. Cole, and R. I. Laming, "Sinc-sampled fiber Bragg gratings for identical multiple wavelength operation," *Photonics Technology Letters, IEEE*, vol. 10, no. 6, pp. 842–844, 1998.

[75] G. P. Agrawal and A. H. Bobeck, "Modeling of distributed feedback semiconductor lasers with axially-varying parameters," *Quantum Electronics, IEEE Journal of*, vol. 24, no. 12, pp. 2407–2414, 1988.

[76] G. P. Agrawal and S. Radic, "Phase-shifted fiber Bragg gratings and their application for wavelength demultiplexing," *Photonics Technology Letters, IEEE*, vol. 6, no. 8, pp. 995–997, 1994.

[77] J. Skaar, L. Wang, and T. Erdogan, "On the synthesis of fiber Bragg gratings by layer peeling," *Quantum Electronics, IEEE Journal of*, vol. 37, no. 2, pp. 165–173, 2001.

[78] J. Skaar and O. H. Waagaard, "Design and characterization of finite-length fiber gratings," *Quantum Electronics, IEEE Journal of*, vol. 39, no. 10, pp. 1238–1245, 2003.

[79] A. Rosenthal and M. Horowitz, "Inverse scattering algorithm for reconstructing strongly reflecting fiber Bragg gratings," *Quantum Electronics, IEEE Journal of*, vol. 39, no. 8, pp. 1018–1026, 2003.

[80] M. Zervas and R. Feced, "Synthesis of fiber gratings," in *Optical Fiber Communication Conference*, vol. 1, pp. 112–114, Optical Society of America, 2000.

[81] I. Gelfand and B. Levitan, "On the determination of a differential equation from its spectral function," *American Mathematical Society Translations: Series 2*, vol. 1, pp. 253–304, 1955.

[82] B. Berger, Naumand Levit, B. Fischer, M. Kulishov, D. Plant, and J. Azaña, "Temporal differentiation of optical signals using a phase-shifted fiber Bragg grating," *Optics Express*, vol. 15, no. 2, pp. 371–381, 2007.

[83] G. Miller, R. Batchko, W. Tulloch, D. Weise, M. Fejer, and R. Byer, "42%-efficient single-pass cw second-harmonic generation in periodically poled lithium niobate," *Optics Letters*, vol. 22, no. 24, pp. 1834–1836, 1997.

[84] J. Wang, J. Sun, and Q. Sun, "Single-PPLN-based simultaneous half-adder, half-subtracter, and OR logic gate: proposal and simulation," *Optics Express*, vol. 15, no. 4, pp. 1690–1699, 2007.

[85] L. Eldada and L. W. Shacklette, "Advances in polymer integrated optics," *Selected Topics in Quantum Electronics, IEEE Journal of*, vol. 6, no. 1, pp. 54–68, 2000.

[86] G. D. Emmerson, *Novel direct UV written devices.* PhD thesis, University of Southampton, 2003.

[87] I. J. G. Sparrow, *Development and applications of UV written waveguides.* PhD thesis, University of Southampton, 2005.

[88] M. Svalgaard, C. Poulsen, A. Bjarklev, and O. Poulsen, "Direct UV writing of buried singlemode channel waveguides in Ge-doped silica films," *Electronics Letters*, vol. 30, no. 17, pp. 1401–1403, 1994.

[89] J. Batey and E. Tierney, "Low-temperature deposition of high-quality silicon dioxide by plasma-enhanced chemical vapor deposition," *Journal of Applied Physics*, vol. 60, no. 9, pp. 3136–3145, 1986.

[90] G. T. Reed, *Silicon photonics*. Wiley Online Library, 2008.

[91] G. Grand, J. Jadot, H. Denis, S. Valette, A. Fournier, and A. Grouillet, "Low-loss PECVD silica channel waveguides for optical communications," *Electronics Letters*, vol. 26, no. 25, pp. 2135–2137, 1990.

[92] J. M. Ruano, V. Benoit, J. S. Aitchison, and J. M. Cooper, "Flame hydrolysis deposition of glass on silicon for the integration of optical and microfluidic devices," *Analytical Chemistry*, vol. 72, no. 5, pp. 1093–1097, 2000.

[93] H. L. Rogers, *Direct UV-written Bragg gratings for waveguide characterisation and advanced applications*. PhD thesis, University of Southampton, 2013.

[94] J. Bautista and R. Atkins, "The formation and deposition of SiO2 aerosols in optical fiber manufacturing torches," *Journal of Aerosol Science*, vol. 22, no. 5, pp. 667–675, 1991.

[95] H. Limberger, P. Fonjallaz, R. Salathé, and F. Cochet, "Compaction-and photoelastic-induced index changes in fiber Bragg gratings," *Applied Physics Letters*, vol. 68, no. 22, pp. 3069–3071, 1996.

[96] M. Douay, W. Xie, T. Taunay, P. Bernage, P. Niay, P. Cordier, B. Poumellec, L. Dong, J. Bayon, H. Poignant, *et al.*, "Densification involved in the UV-based photosensitivity of silica glasses and optical fibers," *Journal of Lightwave Technology*, vol. 15, no. 8, pp. 1329–1342, 1997.

[97] M. Kristensen, "Bragg gratings white paper." `http://www.ibsen.dk/phasemasks/tutorials/bragggratingswhitepaper`, 2005.

[98] K. Hill, Y. Fujii, D. Johnson, and B. Kawasaki, "Photosensitivity in optical fiber waveguides: Application to reflection filter fabrication," *Applied Physics Letters*, vol. 32, p. 647, 1978.

[99] K. O. Hill and G. Meltz, "Fiber Bragg grating technology fundamentals and overview," *Journal of Lightwave Technology*, vol. 15, no. 8, pp. 1263–1276, 1997.

[100] A. Othonos, "Fiber bragg gratings," *Review of scientific instruments*, vol. 68, no. 12, pp. 4309–4341, 1997.

[101] G. Meltz, W. Morey, and W. Glenn, "Formation of Bragg gratings in optical fibers by a transverse holographic method," *Optics Letters*, vol. 14, no. 15, pp. 823–825, 1989.

[102] P. J. Lemaire, R. Atkins, V. Mizrahi, and W. Reed, "High pressure H2 loading as a technique for achieving ultrahigh UV photosensitivity and thermal sensitivity in GeO2 doped optical fibres," *Electronics Letters*, vol. 29, no. 13, pp. 1191–1193, 1993.

[103] B. Poumellec, P. Guenot, I. Riant, P. Sansonetti, P. Niay, P. Bernage, and J. Bayon, "UV induced densification during Bragg grating inscription in Ge: SiO2 preforms," *Optical Materials*, vol. 4, no. 4, pp. 441–449, 1995.

[104] S. Thibault, J. Lauzon, and F. Ouellette, "Influence of Ge concentration on UV-excited luminescence in a graded-index fibre preform," *Electronics Letters*, vol. 30, no. 6, pp. 517–518, 1994.

[105] J. Archambault, L. Reekie, and P. S. J. Russell, "100% reflectivity Bragg reflectors produced in optical fibres by single excimer laser pulses," *Electronics Letters*, vol. 29, no. 5, pp. 453–455, 1993.

[106] C. Holmes, *Direct UV written planar devices for sensing and telecommunication applications*. PhD thesis, University of Southampton, 2009.

[107] M. Svalgaard, K. Færch, and L. U. Andersen, "Variable optical attenuator fabricated by direct UV writing," *Journal of Lightwave Technology*, vol. 21, no. 9, p. 2097, 2003.

[108] H. L. Rogers, S. Ambran, C. Holmes, P. G. Smith, and J. C. Gates, "In situ loss measurement of direct UV-written waveguides using integrated Bragg gratings," *Optics Letters*, vol. 35, no. 17, pp. 2849–2851, 2010.

[109] H. Rogers, C. Holmes, J. Gates, and P. Smith, "Analysis of dispersion characteristics of planar waveguides via multi-order interrogation of integrated Bragg gratings," *Photonics Journal, IEEE*, vol. 4, no. 2, pp. 310–316, 2012.

[110] R. Hui and M. O'Sullivan, *Fiber optic measurement techniques*. Academic Press, 2009.

[111] G. Emmerson, C. Gawith, R. Williams, P. Smith, S. McMeekin, J. Bonar, and R. Laming, "Ultra-wide planar Bragg grating detuning and 2D channel waveguide integration through direct grating writing," in *ECOC-IOOC 2003 (29th European Conference on Optical Communication - 14th International Conference on Integrated Optics and Optical Fibre Communication)*, 2003. Invited paper.

[112] J. Sipe, L. Poladian, and C. Sterke, "Propagation through nonuniform grating structures," *Journal of the Optical Society of America A*, vol. 11, no. 4, pp. 1307–1320, 1994.

[113] I. Petermann, B. Sahlgren, S. Helmfrid, A. T. Friberg, and P.-Y. Fonjallaz, "Fabrication of advanced fiber Bragg gratings by use of sequential writing with a

continuous-wave ultraviolet laser source," *Applied Optics*, vol. 41, no. 6, pp. 1051–1056, 2002.

[114] Y. Liu, J. J. Pan, C. Gu, F. Zhou, and L. Dong, "Novel fiber Bragg grating fabrication method with high-precision phase control," *Optical Engineering*, vol. 43, no. 8, pp. 1916–1922, 2004.

[115] M. GagnÚ, L. Bojor, R. Maciejko, and R. Kashyap, "Novel custom fiber Bragg grating fabrication technique based on push-pull phase shifting interferometry," *Optics Express*, vol. 16, no. 26, pp. 21550–21557, 2008.

[116] A. Manbachi and R. S. Cobbold, "Development and application of piezoelectric materials for ultrasound generation and detection," *Ultrasound*, vol. 19, pp. 187–196, 2011.

[117] "Fundamentals of piezoelectricity." `http://www.physikinstrumente.com/en/products/prdetail.php?sortnr=400600.00`, 2013.

[118] G. B. Clayton and S. Winder, *Operational amplifiers*. Newnes, 2003.

[119] "Buffer amplifier." `http://en.wikipedia.org/wiki/Buffer_amplifier`, 2013.

[120] J. Wilson and J. F. Hawkes, *Optoelectronics: an introduction*. Prentice Hall, 1998.

[121] A. Yariv and P. Yeh, *Optical waves in crystals*, vol. 5. Wiley New York, 1984.

[122] "Application notes: Pockels cells for Q-switching." `http://www.eoc-inc.com/leysop/app_notes_pockels_cells_q_switching.htm`.

[123] C. Sima, J. Gates, H. Rogers, P. Mennea, C. Holmes, M. Zervas, and P. Smith, "Phase controlled integrated interferometric single-sideband filter based on planar Bragg gratings implementing photonic Hilbert transform," *Optics Letters*, vol. 38, no. 5, pp. 727–729, 2013.

[124] C. Sima, J. Gates, H. Rogers, B. Snow, C. Holmes, M. Zervas, and P. Smith, "All-optical signal processing using planar Bragg gratings," in *Photonics and Optoelectronics Meetings 2011*, pp. 833309–833309, International Society for Optics and Photonics, 2011.

[125] M. Cole, W. Loh, R. Laming, M. Zervas, and S. Barcelos, "Moving fibre/phase mask-scanning beam technique for enhanced flexibility in producing fibre gratings with uniform phase mask," *Electronics Letters*, vol. 31, no. 17, pp. 1488–1490, 1995.

[126] C. Holmes, D. Kundys, J. Gates, C. Gawith, and P. Smith, "150 Ghz of thermo-optic tuning in direct UV written silica-on-silicon planar Bragg grating," *Electronics Letters*, vol. 45, no. 18, pp. 954–956, 2009.

[127] C. Sima, J. Gates, P. Mennea, C. Holmes, M. Zervas, and P. Smith, "Terahertz bandwidth photonic Hilbert transformers based on synthesized planar Bragg grating fabrication," *Optics Letters*, vol. 38, no. 17, pp. 3448–3451, 2013.

[128] C. Sima, J. Gates, M. Zervas, and P. Smith, "Review of photonic Hilbert transformers," *Frontiers of Optoelectronics*, vol. 6, no. 1, pp. 78–88, 2013.

[129] K. Hill, B. Malo, F. Bilodeau, D. Johnson, and J. Albert, "Bragg gratings fabricated in monomode photosensitive optical fiber by UV exposure through a phase mask," *Applied Physics Letters*, vol. 62, no. 10, pp. 1035–1037, 1993.

[130] D. Anderson, V. Mizrahi, T. Erdogan, and A. White, "Production of in-fibre gratings using a diffractive optical element," *Electronics Letters*, vol. 29, no. 6, pp. 566–568, 1993.

[131] K. Hill, B. Malo, K. Vineberg, F. Bilodeau, D. Johnson, and I. Skinner, "Efficient mode conversion in telecommunication fibre using externally written gratings," *Electronics Letters*, vol. 26, no. 16, pp. 1270–1272, 1990.

[132] "Optical absorption of water compendium." `http://omlc.ogi.edu/spectra/water/abs/index.html`, 1998.

[133] "Refractive index database." `http://refractiveindex.info/`.

[134] D. K. Gifford, B. J. Soller, M. S. Wolfe, and M. E. Froggatt, "Optical vector network analyzer for single-scan measurements of loss, group delay, and polarization mode dispersion," *Applied optics*, vol. 44, no. 34, pp. 7282–7286, 2005.

[135] C. C. Tseng and S. C. Pei, "Design and application of discrete-time fractional Hilbert transformer," *Circuits and Systems II: Analog and Digital Signal Processing, IEEE Transactions on*, vol. 47, no. 12, pp. 1529–1533, 2000.

[136] J. M. Castro, I. B. Djordjevic, and D. F. Geraghty, "Novel super structured Bragg gratings for optical encryption," *Journal of Lightwave Technology*, vol. 24, no. 4, p. 1875, 2006.

[137] J. U. Thomas, C. Voigtländer, S. Nolte, A. Tünnermann, N. Jovanovic, G. D. Marshall, M. J. Withford, and M. Steel, "Mode selective fiber Bragg gratings," in *LASE*, pp. 75890J–75890J, International Society for Optics and Photonics, 2010.

[138] R. G. Krämer, C. Voigtländer, E. Freier, A. Liem, J. U. Thomas, D. Richter, T. Schreiber, A. Tünnermann, and S. Nolte, "Femtosecond pulse inscription of a selective mode filter in large mode area fibers," in *SPIE LASE*, pp. 86010S–86010S, International Society for Optics and Photonics, 2013.

[139] J. M. Castro, D. F. Geraghty, S. Honkanen, C. M. Greiner, D. Iazikov, T. W. Mossberg, *et al.*, "Demonstration of mode conversion using anti-symmetric waveguide Bragg gratings," *Optics Express*, vol. 13, no. 11, pp. 4180–4184, 2005.

[140] Y. Ding, J. Xu, F. Da Ros, B. Huang, H. Ou, and C. Peucheret, "On-chip two-mode division multiplexing using tapered directional coupler-based mode multiplexer and demultiplexer," *Optics Express*, vol. 21, no. 8, pp. 10376–10382, 2013.